The Dissertation Committee for James Christopher Sanders Certifies that this is the approved version of the following dissertation:

Terawatt Raman Laser System for Two-Color Laser Plasma Interactions

Committee:

_____
Michael Downer, Supervisor

_____
Todd Ditmire

_____
Manfred Fink

_____
Gennady Shvets

_____
Greg Sitz

_____
Philip Varghese

Terawatt Raman Laser System for Two-Color Laser Plasma Interactions

by

James Christopher Sanders, B.S.

Dissertation

Presented to the Faculty of the Graduate School of
The University of Texas at Austin
in Partial Fulfillment
of the Requirements
for the Degree of

Doctor of Philosophy

The University of Texas at Austin

August, 2014

Dedication

This work is dedicated
First to my wife Rebecca,
Then to our children present and future,
And next to my mother and father.
It is also dedicated to the head of my order, Dominic,
And my patrons therein, Thomas and Albert
Finally but foremost to God—
Father, Son and Holy Spirit—
Who made this possible.

Acknowledgments

Many people helped me in this work both behind the scenes and in front of them, and so there are many people whom I must thank. First of all is my wife, Rebecca Sanders, whose mostly patient support has helped me through the stresses and disappointments which come with the territory of experimental research, and who has been there to share the excitement of those successes I have enjoyed. I am ever thankful that she has been willing to share the sacrifices of long work hours and low pay which are inflicted upon graduate students and their families: I hope the hard work and sacrifices will finally pay off. Thanks for standing by me through thick and thin, for being loving and patient and supportive all his time.

Second, I thank my adviser, Pr. Mike Downer. He's had the patience to allow me to grow as a physicist, and the persistence to ensure that the end result will be my graduation rather than my growing to be a permanent fixture of the university. He's taught me to be a scientist and has encouraged me in the few moments of panic or despair that I've encountered along the way. I am not certain that I would have stuck through graduate school under a more driving and less patient adviser, but then again I am not sure I would have finished in time under one who failed to step in and push me to complete my research later on when it seemed to have stalled.

Thirdly, I would like to thank the other members of my committee. Each of you have helped me along the way, from Pr. Greg Sitz's friendly conversations to Pr. Gennady

young age, and who occasionally rekindled this work ethic during the various stages of burn-out that I've suffered over the years. I really hate UT's bureaucracy.

James Christopher Sanders, O.P.

The University of Texas at Austin

May 25, 2014

Feast of Venerable St. Bede

Terawatt Raman Laser System Two-Color Laser Plasma Interactions

James Christopher Sanders, Ph.D.
The University of Texas at Austin, 2014

Supervisor: Michael Downer

In some high-field laser-plasma experiments, it is advantageous to accompany the main high-energy (~1 J) laser with a second high-energy pulse (~0.1 J) which has been frequency-shifted by ~10-20%. Such a pulse-pair would have a low walk-off velocity while remaining spectrally distinct for use in two-color pump-probe experiments. Moreover, by shifting the second pulse by ~plasma frequency, it is theoretically possible to exercise some amount of control over a variety of laser-plasma instabilities, including forward Raman scattering, electromagnetic cascading, and relativistic self-focusing. Alternatively, the two pulses may be counter-propagated so that the collide in the plasma and create a slowly-propagating beatwave which can be used to inject electrons into a laser wakefield accelerator.

The design, characeterization, and performance of a hybrid chirped-pulse Raman amplifier (CPRA)/Ti-Sapphire amplifier are reported and discussed. This hybrid system allows for the generation of a high-energy (>200 mJ), broadband (15-20 nm bandwidth FWHM), short duration (>100 fs duration) laser sideband. When amplified and compressed, the Raman beam's power exceeds 1 TW. This sideband is combined with the primary laser system to create a bi-color terawatt laser system which is capable of performing two-color high-field experiments. This two-color capability can be added to any commercial terawatt laser system without compromising the energy, duration or

beam quality of the primary system.

Preliminary two-color laser-plasma experiments are also discussed.

Table of Contents

List of Tables

List of Figures

xviii

Chapter 1

Laser Wakefield Acceleration: Background Motivation for High-Intensity Laser-Plasma Interactions

1.1 INTRODUCTION: A BRIEF HISTORY OF PARTICLE ACCELERATION

Particle acceleration in general and electron acceleration by laser-driven plasma wakefield in particular are discussed in this chapter. This chapter forms the background motivation for the research presented in this dissertation. Some of the points in this chapter (in particular the advanced article injection schemes) suggest potential applications for the two-color terawatt laser system which is the principle new instrument that this work introduces to the field of plasma-based particle acceleration.

Particle acceleration typically involves the acceleration of a charged particle via an applied electromagnetic field. The oldest accelerators use a static electric field, as in the cathode ray tubes used in older television sets[i] and oscilloscopes, or the Van de Graaff generators—historically developed to investigate atomic nuclei[1], but which today are found in fun-houses and physics classrooms the world over. These static accelerators are

---

i   It is strange to refer to these as "old" or "obsolete" technologies, but CRT monitors and television sets are obsolete, having been replaced with various flatscreen technologies based on liquid crystal displays, etc. It is strange to think that 10 years from now, this example will no longer be well-known or common for young readers. It may be worth noting here as trivia that oscilloscopes use electrostatic deflection and televisions use magnetic deflection of the charged particles.

fundamentally limited by electrical breakdown of material, though they have successfully been used to accelerated charged particles across a potential difference of up to 20 MV[2].

The first "advanced" particle accelerators were developed in the 1920s-1930s, and used an oscillating radio-frequency (RF) electromagnetic field to accelerate charged particles. The first linear accelerator (linac) to use this technology was built in 1928[3], and accelerate particles along a ~ straight line path. This linac and was soon followed by the first Betatron (developed in 1932 but first built in 1940[4],[5]), which accelerated particles in a circular-torroidal path, and by the first cyclotron (1932[6]) which accelerated particle along a spiraling path. These schemes initially achieved particles energies in the 10's of MeVs. However, larger and more power linear accelerators have been built, most notably SLAC, which has achieved particle energies of approximately 50 GeV in its standard configuration. A more advanced cyclotron—the synchrotron, in which the oscillating EM field is synchronized in time with the accelerating particle—has become the basis for the most powerful particle accelerators in the world: Fermi Lab's Tevatron, Brookhaven's Relativistic Heavy Ion Collider (RHIC[7], up to 250 GeV observed), and CERN's Large Hadron Collider (LHC, 7 TeV per nucleon energies projected, or 574 TeV for a lead nucleus; 4 TeV beams observed).

These high-energy accelerators are used primarily for high-energy/particle physics research and (in the case of synchrotrons) for the generation of synchrotron radiation. However, a number of lower-energy accelerators are used for industrial and biomedical research. According to one estimate[8], there are approximately 26,000 "advanced" particle accelerators worldwide (this is excluding simple accelerators like

CRTs and Van de Graaff generators), of which approximately 1% are used for basic scientific research, and the rest are used for such diverse processes[9] as ion implantation (for manufacturing integrated circuits), radiotherapy for cancer treatment, radiosurgery (e.g. for the treatment of brain tumors), nondestructive inspection (e.g. in material sciences), radioisotope production (e.g. for cancer detection), electron beam material processing, and synchrotron radiation production.

The high-energy accelerators in particular suffer from one great problem: size. The linear accelerator at SLAC is 3km long and cost ~$126 million to build (1966), Tevatron is 6.86 km long and was built for a cost of $120 million (1983), and the LHC has a circumference of 27 km and cost 7.5 billion Euros (~$9 billion, 2008). This large size is because these conventional RF accelerators are also limited by dielectric breakdown of the accelerating tube, which imposes an upper gradient limit of $~10^7$ V/cm[10].

1.2 WAKEFIELDS

Laser wakefield acceleration was first proposed by Tajima and Dawson[11] as a means of accelerating electrons to high energy. Wakefield acceleration has the advantage of allowing a high potential gradient as compared to conventional accelerator methods. In laser wakefield acceleration, a high-intensity wave electromagnetic wave packet is injected into a plasma, thereby exciting an electrostatic wake behind the photons.

Electrons injected into the wake can then be accelerated to high energy, with acceleration gradients of ~GeV/cm.

A nonhomogeneous electric field—such as an oscillating electromagnetic wave packet—will exert a ponderomotive force of

$$F_P = \frac{-e^2}{4m\omega^2} \nabla E^2 \qquad (1.2.1)$$

In a laser pulse, the electric field will be transverse to the direction of pulse propagation, and therefore some of the electrons will be expelled transversely behind the pulse. As the laser pulse passes an electron in the plasma, the electron is displaced in the transverse direction by $\Delta x = \Delta v_x \tau$, where τ is the length (duration) of the laser pulse. On the other hand, the ponderomotive force itself will push electrons in the front part of the pulse forward and the ponderomotive force in the back part of the pulse will push the electron backward.

The much heavier ions will meanwhile remain undisplaced, resulting in a space charge. After the laser pulse has passed, the space charge will pull the electron back, and a plasma oscillation is set up: this is the plasma wake. In the linear regime ($|a| \ll 1$), the laser ponderomotive force is $F_p = -m_e c^2 \nabla (a^2/2)$, where a is the normalized vector potential,

$$a = \frac{eA}{m_e c^2} = \frac{e^2 \Omega_0 \lambda_L^2 I}{4\pi^2 (mc^2)^2} = 0.85 \times 10^{-9} \lambda_L (\mu m) I^{1/2} (W \cdot cm^{-2}) \qquad (1.2.2)$$

In the nonlinear regime ($|a| \sim 1$), the ponderomotive force is more difficult to model in 3 dimensions, though a 1-D analytic solution does exist[12]:

$$F_{pz} = -\left(\frac{m_e c^2}{2\gamma}\right)\frac{\partial a_{\perp}^2}{\partial z} \qquad (1.2.3)$$

As this ponderomotvive force is applied to electrons in the plasma, the electrons will be pushed out of the path of the laser pulse, much as water is pushed out of the path of a boat. Once the laser pulse has passed, the electrons rush back into the now positively charged region in the laser's wake, much as water rushes back into the region behind a boat. And, just as the water's oscillations then create a series of waves—the wake behind the boat—the electrons collectively begin to oscillate and create a series of waves in the field left in the wake of the laser pulse.

Electrons trapped by this wake will experience a strong longitudinal accelerating gradient,

$$E_o = \frac{m_e \omega_p c}{e} = c\sqrt{\frac{m_e n_e}{\epsilon_o}} \qquad (1.2.4)$$

where n_e is the electron density and $\omega_p = \sqrt{\frac{n_e e^2}{\epsilon_0 m_e}}$ is the plasma frequency. Therefore, the primary determining factor of the accelerating gradient is the plasma density, so that a plasma with density $\sim 10^{18}$ cm^{-3} would give an accelerating gradient of ~ 100 GeV/m, meaning that an electron accelerated by this gradient for 1 cm would attain an energy of 1 GeV. Thus, while the plasma itself makes a transverse wave in the wake of the laser pulse, the electrons trapped by the wave are accelerated longitudinally, much like a surfer riding an ocean wave is accelerated "forward" while the water in the wave is moving "up" and "down."

5

There are three basic regimes of interest for wakefield accelerators: linear, nonlinear, and bubble (sometimes also called "blowout" or "total cavitation"). I will briefly discuss each of these regimes in turn.

1.2.1 Wakefields in the Linear Regime

In the linear regime, the plasma oscillation is essentially sinusoidal with frequency ω_p and $E_{max} \ll E_0$, where E_0 is the nonrelativistic wave-breaking field

$$E_o = e m_e \omega_p / e \rightarrow E_0 [V/cm] = 0.96 n_o^{1/2} [cm^{-3}] \qquad (1.2.5)$$

This wave breaking limit describes the maximum amplitude of an electrostatic standing wave which can be sustained by the plasma within the fluid model. The generation of a linear wakefield can be described using the cold fluid equations[12]. A plasma wave generated by a laser pulse (e.g. LWFA) and a charged particle beam (e.g. PWFA) in an initially uniform plasma is described by

$$\left(\frac{\partial^2}{\partial t^2} + \omega_p^2 \right) \frac{\delta n}{n_0} = - \omega_p^2 \frac{n_b}{n_0} + c^2 \nabla^2 \frac{a^2}{2} \qquad (1.2.6)$$

where n_b/n_0 is the density of the driving particle beam (n.b. this term vanishes in LWFA), a is the normalized intensity of the laser pulse (n.b. this term vanishes in PWFA), and $\delta n/n_0$ is the perturbed density of the plasma. The linear regime functions under the conditions that $n_b/n_0 \ll 1$ PWFA) and a $\ll 1$ (LWFA). The solution to (1.2.6) in the linear regime laser-driven plasma wave is then

$$\frac{\delta n}{n_o} = \frac{1}{\omega_p} \int_0^t dt' \sin[\omega_p(t' - t)] c^2 \nabla^2 \frac{a^2}{2} \qquad (1.2.7)$$

This describes the actual electron density perturbation of the plasma wake. The electric field of these waves is given by

$$\vec{E}(\vec{r},t) = -\left(m_e c^2 \omega_p / e\right) \int_0^t dt' \sin\left[\omega_p(t'-t)\right] c^2 \nabla \frac{a^2(\vec{r},t)}{2}$$

(1.2.8)

The actual plasma wakefield will have an axial component E_z and transverse components E_r and B_θ, which are related to each other by the Panofsky-Wenzel theorem[12],[13]:

$$\frac{\partial E_z}{\partial r} = \frac{\partial\left(E_r - B_\theta\right)}{\partial \zeta}$$

(1.2.9)

where $\zeta = z - ct$. If the laser wakefield is generated using linearly polarized light with an intensity profile given by $a^2 = (a_0^2/2)\exp(-2r^2/r_s^2)\sin^2(\pi\zeta/L)$, then the axial electric field and the density perturbation behind the laser pulse will be given by[12],[14]:

$$\frac{E_z}{E_0} = \frac{-\pi a_0^2}{8} \exp\left(-\frac{2r^2}{r_s^2}\right) \cos\left(k_p \zeta\right)$$

(1.2.10)

$$\frac{\delta n}{n_0} = \frac{-\pi a_0^2}{8}\left[1 + \frac{8}{k_p^2 r_s^2}\left(1 - \frac{2r^2}{r_s^2}\right)\right]\exp\left(\frac{-2r^2}{r_s^2}\right)\sin\left(k_p \zeta\right)$$

(1.2.11)

It should be noted here that if the driving laser is circularly polarized instead of linearly polarized, (1.2.10) and (1.2.11) can be corrected by replacing $a_0^2/2$ with a_0^2. Both the electron density oscillation and the actual wake-field are sinusoidal, and both have transverse profiles which essentially match the initial Gaussian profile of the driving pulse.
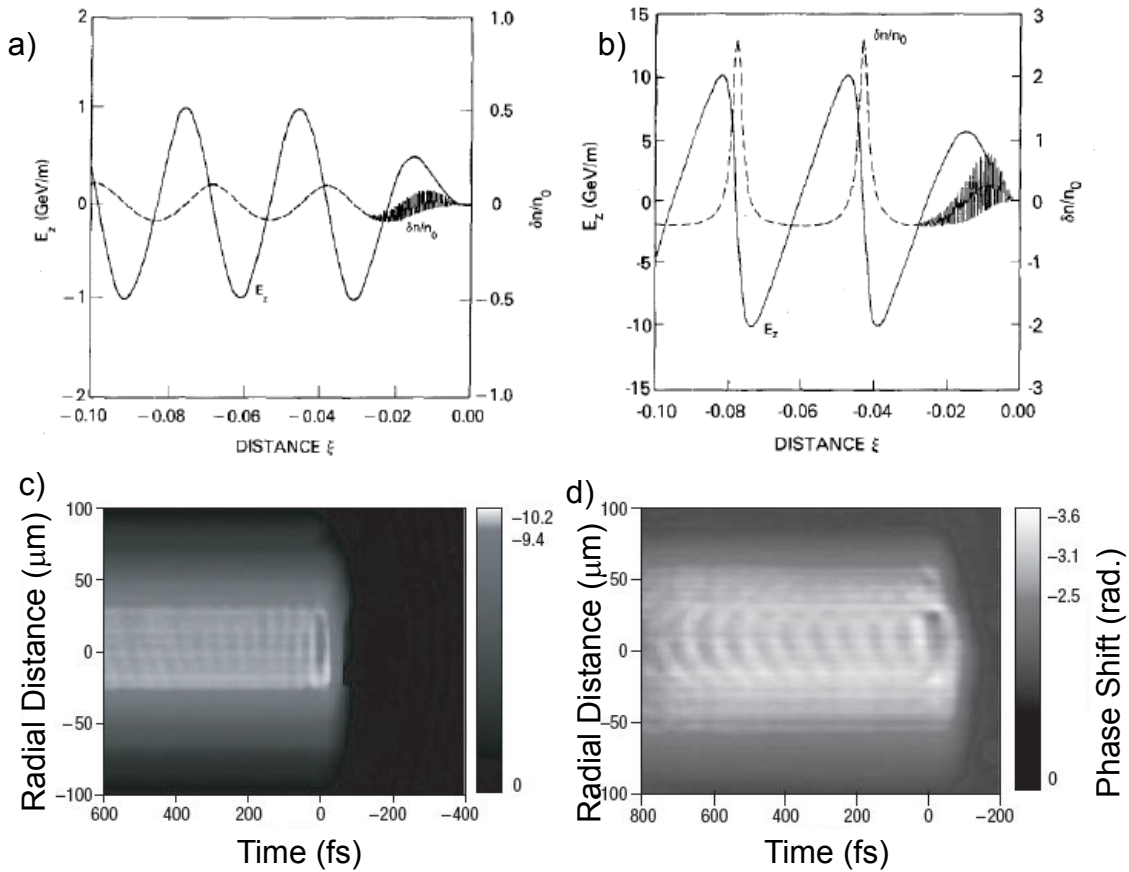
Figure 1.1: Laser wakefields in the linear and nonlinear regimes[12],[15],[16]. The upper two plots are the electron density variation $dn/n_0 = n/n_0$ -1 and the axial electric field E_z in a LWFA. The LWFA is driven by a laser pulse which is moving from left to right in the region $L = \lambda_p = 0.03$ cm for a) the linear regime where $a_0 = 0.5$ and b) the nonlinear regime where $a_0 = 2$. The lower two images are holographic snapshots via probe phase shift of c) linear and d) nonlinear laser wakefields.

It is also possible to estimate the peak electric field amplitude of a plasma wave in the linear regime using Poisson's equation, $\nabla \cdot E = 4\pi e (n_0 - n_e)$, which gives a maximum sustainable[ii] field amplitude of $E_{max} = E_0$ for a plasma in which all the electrons

---

ii It is, of course, possible to exceed this field by udergoing wavebreaking. This is in fact a technique used in many accelerator schemes, especially in the bubble regime which will be discussed in section 1.2.3. It is worth noting, however, that wavebreaking implies the breaking of the plasma wave (as implied by the name), and so is not really a sustainable field.

oscillate with wavenumber $k_p = \omega_p/c$. In other words, the electric field amplitude in the linear regime is limited to the non-relativistic wavebreaking field given by (1.2.5). However, in the nonlinear (highly relativistic) regime this limit may be sustainably exceeded, that is, $E_{max} > E_0$. An example of laser wakefields in the linear and nonlinear regimes is shown in Figure 1.1[15],[16].

1.2.2 Wakefields in the Nonlinear Regime

In the nonlinear regime, it is possible to obtain a maximum sustainable field strength for a cold plasma[12],[17] using the 1-D cold fluid equations:

$$E_{WB} = \sqrt{2(\gamma_p - 1)} E_0 \tag{1.2.12}$$

where $\gamma_p = (1 - v_p^2/c^2)^{-1/2}$ is the relativistic factor associated with the plasma wave's phase velocity. The plasma waves' phase velocity is approximately equal to the drive laser's group velocity, $\gamma_p \simeq \omega_L/\omega_p$ where ω_L is the laser's frequency. As an example, in a LWFA with a background plasma density of $n_0 = 1 \times 10^{17}$ cm^{-3} and a laser wavelength of 1μm, the relativistic Lorentz factor associated with the phase velocity of the plasma wave is $\gamma_p \simeq 100$, and the wavebreaking limit is $E_{WB} = 14E_0$.

This new limit E_{WB} is the relativistic wave-breaking limit for a cold-fluid plasma; for a warm-fluid plasma, this is further modified[18] to

$$E_{th} = (m_e c^2/3T)^{1/4} f_{th}(\gamma_p, T) E_0 \tag{1.2.13}$$

where $f_{th}(\gamma_p, T)$ is a slowly-varying function of the relativistic factor γ_p and the temperature T, whose magnitude is ~1. The maximum sustainable field is limited by either Eqn. (1.2.12) if $E_{th} > E_{WB}$ or (1.2.13) if $E_{th} < E_{WB}$.

Plasma wakefields in the nonlinear regime can be solved analytically in 1-D, and they can be approached using a quasi-static approximation in 2-D but for the most part require numerical simulations (e.g. PIC codes and fluid simulations). However, they require numerical simulations to be treated in 3-D, and so full 3-D treatments are less common (and more recent) than the simpler 1-D and 2-D regimes. The linear limit requires that the normalized vector potential $|a| \ll 1$, and therefore that the electron density perturbation $\delta n/n_0 \ll 1$. However, highly relativistic electrons require $a_0 \geq 1$ and hence operation in the nonlinear regime and beyond.

The 1-D nonlinear regime applies to broad drivers, $k_p r_t \gg 1$, where r_t is the transverse spot size of the driving pulse, and begin with the assumption that the driving beam (electron or laser) is non-evolving. In this case, the cold-fluid equations—momentum, continuity, and Poisson's equation—yield[12],[19]

$$k_p^{-2}\frac{\partial^2 \phi}{\partial \zeta^2} = \frac{n_b}{n_o} + \gamma_p^2 \left[\frac{v_p}{c}\left(1 - \frac{1+a^2}{\gamma_p^2(1+\phi)^2}\right)^{-1/2} - 1\right] \tag{1.2.14}$$

In the highly-relativistic limit where $\gamma_p \gg 1$, Eqn. (1.2.14) simplifies via Taylor expansion of the term in parenthesis to

$$k_p^{-2}\frac{\partial^2 \phi}{\partial \zeta^2} = \frac{n_b}{n_o} + \frac{1+a^2}{2(1+\phi)^2} - \frac{1}{2} \tag{1.2.15}$$

10

The first term on the right hand side is used for PWFA, which uses a charged particle beam instead of a laser as the driver driver; thus, for our purposes this term is 0. The second term is used for for LWFA. In the region behind the driving pulse (e.g. the region in which a = 0 for LWFA), the electrostatic potential will oscillate between a minimum value ϕ_{min} and a maximum value ϕ_{max}, which are given by

$$\phi_{min} = \frac{E_{max}^2}{2E_0^2} - \frac{v_p}{c}\left[\left(1 + \frac{E_{max}^2}{2E_0^2}\right)^2 - 1\right] \tag{1.2.16}$$

and

$$\phi_{max} = \frac{E_{max}^2}{2E_0^2} + \frac{v_p}{c}\left[\left(1 + \frac{E_{max}^2}{2E_0^2}\right)^2 - 1\right] \tag{1.2.17}$$

Esarey notes[12] here that the electric field departs from a sinusoidal form and takes on a sawtooth profile instead. Furthermore the period of the nonlinear wave increases along with the wave's amplitude, such that the nonlinear plasma wavelength is $\lambda_{Np} = (2/\pi)E_{max}\lambda_p/E_0$ in the limit where $E_{max}/E_0 \gg 1$ (the other limit, $E_{max}/E_0 \ll 1$, is the linear regime and the plasma wavelength is just λ_p).

This lengthening wavelength produces another limit on accelerators, in particular those which are driven by beat-waves (PBWA) or self-modulating pulses (sm-LWFA), or by LWFA and PWFA schemes utilizing multiple drive pulses. For example, the PBWA driven by a constant beat frequency equal to the initial plasma frequency, $\Delta\omega_{12} = \omega_p$, will no longer be beating resonantly with the plasma once the plasma waves grow, since the

11

effective plasma frequency will change. The driver will therefore be out of phase with the plasma waves, and the plasma wave amplitude then becomes saturated as a result.

The 2-D nonlinear regime has not been solved analytically, though the quasi-static approximation (QSA) is useful here, as are 2-D PIC simulations. The QSA assumes that the time over which the laser pulse evolves τ_E is very long compared to the pulse's actual duration $\tau_L = L/c$: $\tau_L \ll \tau_E$. Having made this assumption—which essentially means that an electron in the plasma sees a ~static, time-independent electric field—the time derivatives $\partial/\partial\tau$ can be neglected in the plasma fluid equations (though not in the wave equation which describes the evolution of the laser itself). The laser-plasma interaction can then be approximately calculated in an iterative fashion, first by solving the fluid equations (1.2.12) in the 1-D limit and then using this fluid response with the wave equation to move the laser pulse forward one iteration, and repeating the process. This wave equation might be written[12],[20],[21] as

$$\left(\nabla_{\perp}^{2} + \frac{2 v_g}{c^2} \frac{\partial^2}{\partial\zeta\,\partial\tau} + \frac{1}{\gamma_g} \frac{\partial^2}{\partial\zeta^2} - \frac{1}{c^2} \frac{\partial^2}{\partial\tau^2} \right) a \simeq k_p^2 \rho\, a \tag{1.2.18}$$

where $\rho = n/\gamma n_0$, $\zeta = z - v_g t$, $\tau = t$, and v_g is the group velocity of the laser pulse. The fluid quantity ρ is determined from the quasi-static fluid equations.

It was earlier stated in the discussion of nonlinear waves in the 1-D regime that the plasma waves tend to distort from sinusoidal to sawtooth. Moreover, the period between the waves is dependent on the amplitude of the waves, and therefore on the driving laser's intensity and electric-field amplitude. In the 2-D regime, this becomes even more important, because the laser pulse's intensity typically has a non-constant

radial profile. Typically, the pulse tends to be focused on a gas-jet or gas-cell target to achieve sufficiently high-intensity for these experiments. For example, a 1 J, 20 fs (50 TW) laser with a Gaussian transverse (radial) profile would require a spot size of ~12.5 μm to achieve a peak intensity of 1×10^{19} W/cm^2, but might initially require a spot size of several centimeters to avoid damaging most optics, whose damage thresholds may range from 10 J/cm^2 for a CVI-Melles Griot TLM1 (high energy, broadband) mirror to ~0.3 J/cm^2 for most gold-coated optics (e.g compressor gratings, large off-axis parabola mirrors, etc).

A focused beam will have a radial profile which is the Fourier transform of its farfield profile. Thus, a farfield Gaussian beam will have a Gaussian focus and a farfield flat-top (or top-hat) profile will focus to a sinc profile. This means that a laser in use for experiments will have a higher intensity on-axis than off-axis. This in turn means a larger plasma wave amplitude and hence a larger plasma period on-axis than off-axis: $\lambda_{Np} = \lambda_{Np}(r)$. The plasma wavefronts will therefore become curved, with this curvature becoming greater for waves farther back in the plasma wave train, as shown in Fig.1.2.1d.

1.2.3 Electron Cavitation and the Blowout/Bubble Regime

Another regime of interest is alternatively called the blow-out or bubble regime[iii]. This regime was discovered in simulations for PWFA in 1991[22] and in LWFA in 2001[23]. The

---

iii Since bubble regime is more commonly used to refer to LWFA and blow-out regime is often used when referring to PWFAs[32], I shall adopt this nomenclature unless otherwise noted.

bubble regime generally requires short pulses, $\lambda_L < \lambda_p$, and high intensities $a_0 > 1$, which exceed the intensity for which the linear regime of wake-fields is valid, and indeed is more intense than generally treated in the nonlinear regime discussed above. In this regime, the laser is sufficiently intense to expel all of the electrons from it path: the electron density along the axis of propagation for some region behind the laser is $n_e/n_0 \sim 0$. This effect is sometimes referred to as electron cavitation.
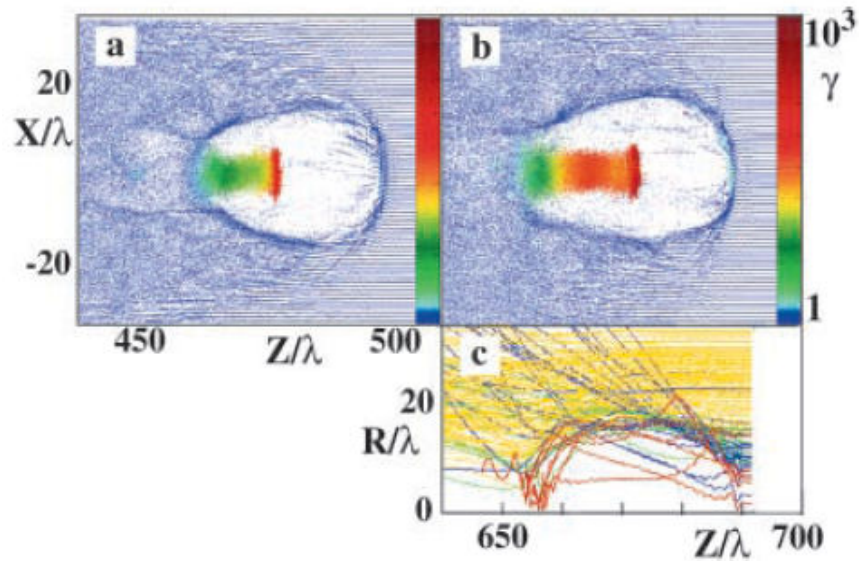
Figure 1.2: Simulation of a plasma wakefield in the bubble regime[23]. The bubble is produced by a 12 J, 33 fs laser pulse incident on a plasma of density 10^{19} cm^{-3}. (a) shows the electron density after $ct/\lambda = 500$, and (b) shows the electron density after $ct/\lambda = 700$. The colors in (a) and (b) represent electron energy (in terms of relativistic γ), and the dots are every 100th electron. (c) represents electron trajectories, and color in this plot is to distinguish between electrons with different initial distances from the laser pulse propagation axis.

The development of the bubble behind the driving laser pulse is shown in Fig. 1.2. The laser used for the simulation which resulted in Fig. 1.2 is a_0=10, laser pulse duration τ = 33 fs, laser pulse energy 12 J, spot size σ = 12λ, and plasma density n_e=10^{19} cm^{-3}. The driving pulse's intensity is sufficiently large so as to blow-out all electrons from the region behind the pulse (which has traveled from left to right and is not shown in the figures). The dots in Fig. 1.2(a) and (b) each represent an electron, and only every 100th electron has been plotted. Therefore the "dot density" represents electron density, and the absence of dots behind the pulse means that electrons have been completely blown out of that region, forming a bubble. Fig. 1.2(c) shows electron trajectories for this pulse, with the trajectory colors being used to distinguish between different initial distances from the axis.

Most of the electrons are far from the laser axis and thus are unperturbed (or only slightly perturbed) by its passage. For those which are more drastically affected, one of two things happens: i) they are scattered outwards never to return to the cavity region; or ii) for electrons which are closest to the axis, the trajectory describes a sort of semi-circle out to the edge of the bubble (the high electron-density sheath) and then along this to the rear vertex, from which they may be injected back into the cavity, where they form a "stem." As time progresses, the bubble stretches and the stem elongates. Ultimately these injected numbered approximately 3.5×10^{10} with an energy spread of 300 ± 30 MeV, so that the accelerated electrons had a total energy of ~1.2J, or 15% of the initial laser pulse energy, a result which has been confirmed by additional simulations[24] and

experimentally[25] (Faure *et al.* attained 10% laser driver to electron beam energy conversion). It is also worth noting here that only a single bubble formed behind the laser pulse, with any additional waves being washed out.

Pukhov and Meyer-ter-Vehn report the scaling laws for the bubble regime. The number of laser cycles N (which determines pulse duration for a given laser frequency) effectively determines the other parameters, with the constraint that the pulse duration should be shorter than the plasma wavelength: $N \propto \omega_0/\omega_p \propto n_o^{-1/2}$. The second requirement which must be met is that wavebreaking must occur, so using $E_{max}/E_{WB} =$ constant gives that the laser field strength (and thus intensity) scales as $I\lambda_L^2 \propto a_0^2 \propto \omega_0/\omega_p \propto N$. If the laser itself is to have plane-like behavior in the bubble, then its diameter at focus should be $r_0 \sim \lambda_p$, which leads to the scaling laws for laser power and energy ($\sim N^3$ and $\sim N^4$, respectively). Finally, the maximum accelerated electron energy scales like $W_{max} = eE_{max}L_{ph} \propto a_0(\omega_0/\omega_p)^2 \propto N^{5/2}$, where L_{ph} is the detuning (or dephasing) length, which will be discussed in Sec. 1.2.5 of this dissertation. Pukhov and Meyer-ter-Vehn conclude that short pulses with few cycles are best-suited for accessing the bubble regime, and indeed that the optimum drive-pulse duration is $\lambda_p/2$ or shorter[24].

Of course, longer pulses with many cycles have entered the bubble regime readily enough provided that the intensity was sufficiently large to induce self-focusing and self-compression[26]. To give a few examples, the Lund Laser Centre experiment by Mangles *et al.*[26] used 35 fs (FWHM) pulse durations and plasma densities of $n_e = 2.1\times10^{19}$ cm^{-3}-3.0×10^{19} cm^{-3}, which gives a plasma wavelength of 7.23-6.05 μm and a pulse length of

10.5 μm; and Faure *et al.*[25] used a 30 fs pulse in a plasma of density $n_e = 2 \times 10^{19}$ cm^{-3}, which gives a plasma wavelength of 7.41 μm and a pulse length of 8.99 μm. On the other hand, the Texas Petawatt accelerator experiment[27],[28],[29],[30] uses densities of $n_e = $ 1.7-6.2×10^{17} cm^{-3} and a pulse duration of 170 fs, which corresponds to a plasma wavelength of 74.1-52.3 μm and a pulse length of 50.9 μm, meaning that the laser pulse is initially shorter than the plasma wavelength. Plasma blowout can occur in the long-pulse sm-LWFA regime, but again electron blowout is optimized for short pulses whose length is half the plasma's wavelength.

The bubble regime is a 3-D effect in which the plasma is driven at intensities which exceed the 1D wavebreaking limit. The result of this driving beyond wavebreaking is that only a single wake rather than a train of wakes is formed, and moreover that many electrons ($\sim$ nC) will self-trap and be accelerated without interacting with the drive pulse directly. Self-injection in the bubble-regime will be further discussed in Sec. 1.2.4 of this dissertation. Although the intensity of the laser must be sufficiently large that wave-breaking occurs in order to form a bubble, the bubble regime can be accessed for slightly lower intensities because the nonlinear laser-plasma interaction has a tendency "shape" laser pulses so that they can fit into the first wake[24].

There are many regimes in which a plasma bubble can form for laser drivers, though the most efficient is the short-pulse regime. For longer pulses, e.g. in the self-modulated regime, blowout of electrons can occur. If the laser is a long pulse with a slowly-varying axial profile, then the plasma density profile can be determined by

balancing the space charge force against the ponderomotive force. In the long long-pulse adiabatic limit, for a linearly-polarized laser pulse, the plasma density is given by the equation[31]

$$n/n_0 = 1 + k_p^{-2} \nabla_\perp^2 \left(1 + \frac{a^2}{2}\right)^{1/2} \tag{1.2.19}$$

As an example, a Gaussian pulse has the profile $a^2 = a_0^2 \exp(-2r^2/r_0^2)$, so the on-axis plasma density profile will be $n(0)/n_0 = 1 - (4/k_p^2 r_0^2)(a_0^2/2)/(1 + a_0^2/2)^{1/2}$. This means that complete electron cavitation will occur on-axis for a laser pulse whose intensity satisfies

$$(a_0^2/2)/(1 + a_0^2/2) \geq k_p^2 r_0^2/4.$$

For short intense pulses, $L < \lambda_p$ and $a^2 > 1$, the bubble regime is characterized by an accelerating field which varies ~linearly as a function of distance behind the laser and which is ~constant as a function of radius inside of the bubble[31]. An analytic model[32] of wake generation in the bubble regime yields an axial electric field in the wake of
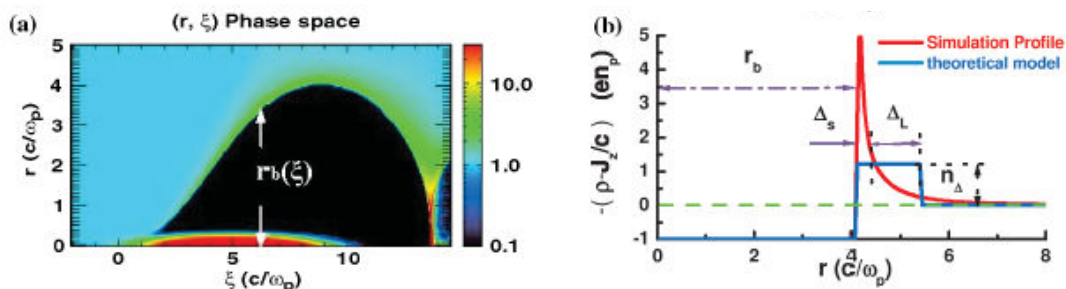
Figure 1.3 Bubble regime charge and current profiles[32]. (a) Electron density with blowout radius defined and (b) -(ρ – J_z/c) profile, which defines Δ_S and Δ_L for (1.2.21), from a PIC simulation.

$$E_z = \frac{\partial}{\partial \xi} \psi(r_\perp, \xi)$$ (1.2.20)

where $\xi = ct - z$ and the pseudopotential ψ is obtainable from the Poisson-like equation

$$- \nabla_\perp^2 \psi = 4\pi(\rho - J_z/c)$$ (1.2.21)

The axial field in Eqn. (1.2.20) is the accelerating field parallel to the axis of propagation of the laser experienced by an electron inside the bubble.

The source term depends on the ion charge density (which is constant as a function of r); on the charge and current of a thin sheath of blown-out electrons which travel around the bubble, at radius $r_b(\xi)$, defined in Figure 1.3(a); and on the charge and current of any electrons which are within a skin depth beyond this sheath. The electrons in the narrow sheath will move almost tangentially to the ion column boundary, which means that the "trajectory" of the bubble boundary, $r_b(\xi)$, can be determined from the equation of motion of an electron in the sheath[32]:

$$A(r_b)\frac{d^2 r_b}{d\xi^2} + B(r_b)r_b\left(\frac{dr_b}{d\xi}\right)^2 + C(r_b)r_b = -\frac{\frac{1}{4}\frac{d|a|^2}{dr}}{1 + \frac{\beta}{4}r_b^2}$$ (1.2.22a)

$$A(r_b) = 1 + \left(\frac{1}{4} + \frac{\beta}{2} + \frac{r_b}{8}\frac{d\beta}{dr_b}\right)r_b^2$$ (1.2.22b)

$$B(r_b) = \frac{1}{2} + \frac{3}{4}\beta + \frac{3}{4}r_b\frac{d\beta}{dr_b} + \frac{1}{8}r_b^2\frac{d^2\beta}{dr_b^2}$$ (1.2.22c)

$$C(r_b) = \frac{1}{4}\left(1 + \frac{1}{(1+\beta r_b^2/4)^2}\right) \tag{1.2.22d}$$

with

$$\beta[r_b(\xi), \Delta_L, \epsilon] = \frac{(1+\alpha)^2 \ln(1+\alpha)^2}{(1+\alpha)^2 - 1} - 1 \tag{1.2.23a}$$

$$\alpha \equiv \Delta/r_b = \Delta_L/r_b + \epsilon \tag{1.2.23b}$$

The term $\Delta = \Delta_S + \Delta_L$ is defined in Fig. 1.2.3(b). Essentially, Δ_S is the sheath thickness, and Δ_L is the width of the region over which the plasma electrons respond similarly to the way they would in the linear wakefield theory. Moreover, very accurate results for the accelerating field can be obtained by assuming a constant electron density profile $n_\Delta = r_b^2/[(r_b + \Delta)^2 - r_b^2]$ over the sheath and linear regions. A comparison of the results of PIC simulation to these analytic models is shown in Fig. 1.2.4.

In the high-intensity limit ($a_0 > 4$), the optimum spot size for wake generation is $k_p r_0 \approx 2\sqrt{a_0}$. In this limit, the blow-out bubble will approximate a sphere with a radius $r_b \approx (2/k_p)\sqrt{a_0}$, which is similar to the result obtained from balancing between ponderomotive and space-charge forces. The bubble diameter is also nearly equal to the 1D nonlinear plasma wavelength[32]:

$$2r_b \approx \lambda_{NL} \approx (2/\pi)(E_{max}/E_0)\lambda_p \approx (2\sqrt{a_0}/\pi)\lambda_p \tag{1.2.24}$$

where λ_p is the linear plasma wavelength and E_{max} is the maximum electric field amplitude of the wake, $E_{max} \approx \sqrt{a_0} E_0$.
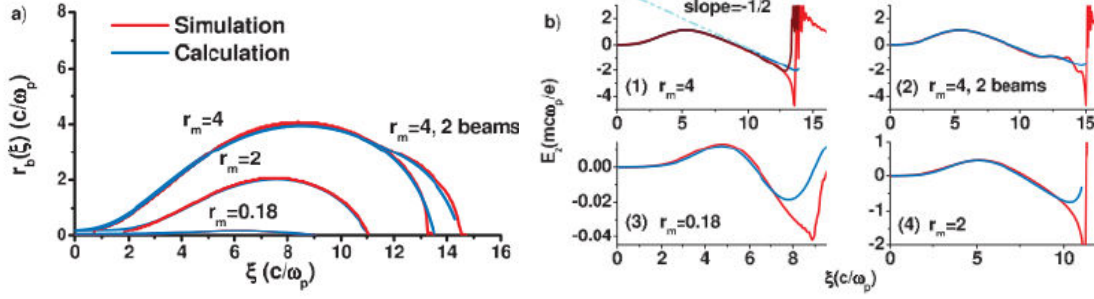
Figure 1.4: Some comparisons between the bubble regime theory in (1.2.18)-(1.2.21) and PIC simulation[32]. (a) Trajectories of $r_b(\xi)$, and therefore of the electron sheath at the boundary of the bubble, with beam center at $\xi = 5$, and r_m is the maximum bubble radius. (b) Comparison of accelerating field in the bubble for each of the bubble plotted in (a). The red curves are from PIC simulation, the blue curves are calculated assuming a constant sheath density profile, and the brown curve in (b)(1) assumes that $\Delta_L = 1$ for $1<\xi<8$ and then decreases linearly to 0.2 at $\xi = 15$.

1.3 SHORT-SCALE ELECTRON-INJECTION SCHEMES

Electron-injection is also a topic of some interest. If wavebreaking does not occur, then the electrons oscillating in the plasma wake itself will not be accelerated by the wakefield because they are out of phase with it. Thus, electrons must be injected through (or from) the plasma wave into the wakefield such that they are in phase with the field itself if they are to be accelerated.

Early experiments focused on accelerating an injected electron bunch which was pre-accelerated to a few MeV[33],[34]. The electron bunches in these early experiments had a length of much greater than the plasma's wavelength, with only a small number of the electrons from these bunches being accelerated. Similarly, the early self-injection

experiments in which electrons from the plasma itself are accelerated involve the injection of many electrons over many plasma wavelengths, more-or-less at random[35]. The result is that the electrons which are accelerated have a Maxwellian-like energy distribution, and thus are not ~monoenergetic.

In order to improve the quality (e.g. energy distribution) of the accelerated electron beams, an injection scheme would ideally inject electrons into the wakefield accelerator over a very short distance: $\lambda_{inj} < \lambda_p$. There are several schemes of injecting electrons over such short distances which have been successfully demonstrated. These include[36] (transverse) self-injection in the bubble and blowout regimes, longitudinal self-injection, density gradient injection, ionization injection, and colliding pulse injection.

1.3.1 Transverse Self-Injection in the Bubble Regime

In the bubble or blow-out[32] regime, electrons are self-injected via transverse wavebreaking. The high-intensity laser expels electrons radially from its path via the ponderomotive force. This creates a cavity which is mostly empty of electrons and thus is positively charged (the ions are not similarly expelled). This cavity is surrounded by a region of high electron-density, particularly in the region just behind the cavity. Some of the electrons are injected from this high-density region into the cavity. This is shown schematically in Fig. 1.3.1.
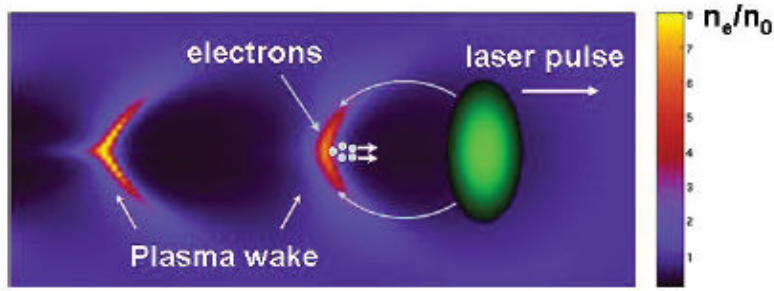
Figure 1.5: Schematic-representation of the principle of self-injection in the bubble regime[36]. The laser pulse is propagating left-to-right, and the electrons are expelled radially from its path, forming a low-electron-density, positively charged, ion-cavity. The electrons flow along the cavity boundary and collect at the rear of the bubble, and are then injected from there into the cavity.

Because the high-density region is highly-localized, the injected electrons will have similar initial properties in phase-space, meaning that they will largely experience the same acceleration and hence will largely end with the same energy: a quasi-monoenergetic beam.

Recall that the plasma wavelength depends inversely on the plasma density, $\lambda_p \sim n_e^{1/2}$. Since the cavitated bubble/blowout region's length is $\sim \lambda_p$, a plasma with relatively low density will trap and inject electrons relatively far behind the laser pulse, meaning that these injected electrons will have little further interaction with the pulse itself, thus further improving electron beam quality.

It should be worth reiterating here that not all of the electrons which are blown out of the bubble will get trapped and injected. Indeed, the majority will not. It is also worth noting one other disadvantage to self-injection via transverse-wavebreaking. Because the process happens naturally as a consequence of the laser's expulsion of the

electrons from its path, it is not easily fine-tuned or otherwise controlled. Also, transverse self-injection is very sensitive to changes in the laser's focal spot[36].

Scaling laws for the maximum accelerating field, the acceleration length, and hence the peak electron energy ($W_{peak} \propto E_z l_{acc}$) show that these parameters depend on both the laser intensity and the laser spot size. A theory developed by Gordienko and Pukhov[37] yields a relativistic similarity parameter S which allows them to derive non-trivial power-law scalings for the energy of accelerated electrons in both overdense and underdense plasmas:

$$S = \frac{n_e}{a_o n_{cr}} \tag{1.3.1}$$

They then obtain the following scaling laws: transverse bubble radius $r_b \propto S^{-1/2} \propto a_0^{1/2}$; acceleration length $l_{acc} \propto S^{-3/2}(c\tau_0/r_b) \propto a_0$; peak electron number $N_{e,peak} \propto n_0 r_b^3 \propto a_0^{3/2}$; bubble electric field $E_z \propto n_0 r_b \propto a_0^{1/2}$; and peak electron energy $W_{peak} \propto E_z l_{acc} \propto a_0^{3/2}$. On the other hand, scalings obtained by Geissler, Schreiber, and Meyer-ter-Vehn via PIC simulation yield[15] $r_b \approx w_0 a_0^{0.25}$ and $l_{acc} \approx 40\sqrt{w_0 a_0}$, which can be combined to obtain for peak electron energy:

$$W_{peak} \approx 0.3\, E_z l_{acc} \rightarrow W_{peak}[MeV] \approx n_0[10^{19} cm^{-3}](w_0[\mu m])^{1.5} a_0^{0.75} \tag{1.3.2}$$

Despite the difference in scaling laws with respect to the intensity, both agree that acceleration length and thus final electron energy scales with the drive pulse's spot size, and thus will be affected by changes in laser mode. Indeed, since the normalized vector potential a_0 also depends on the spot size (and quality), transverse self-injection becomes

24

very sensitive to mode evolution. Therefore, it would be advantageous to be able to control the evolution of the laser's spot size when using this injection method.
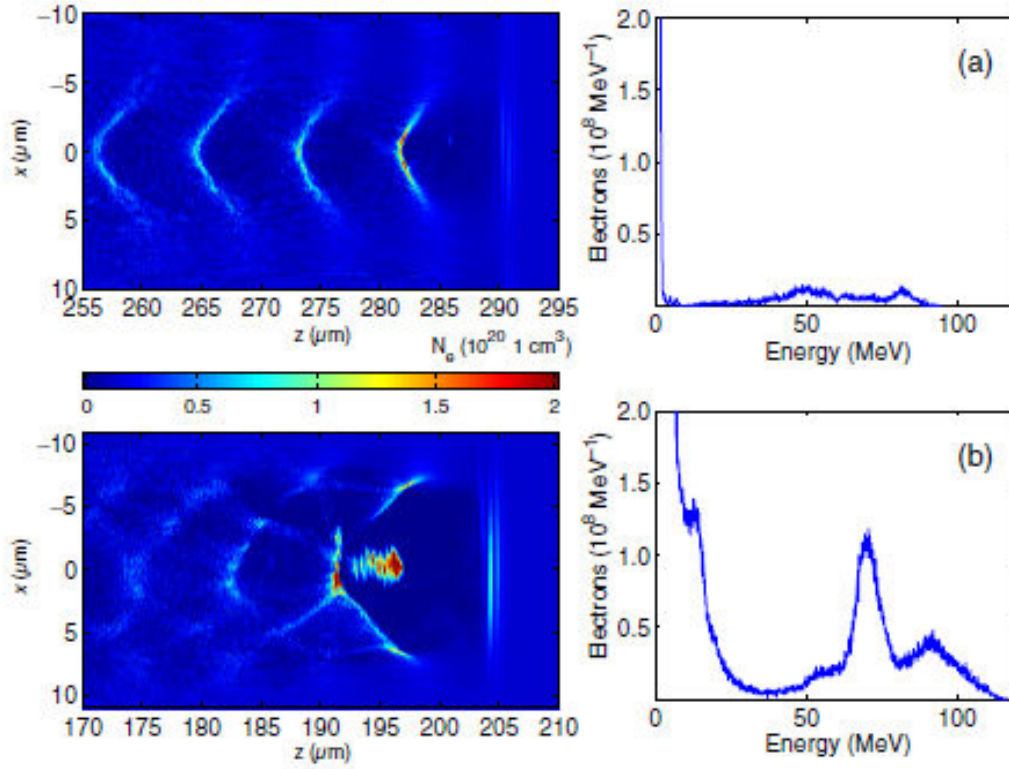
Figure 1.6: Simulated snapshots of electron density (left) and electron energy spectrum (right) after the acceleration has saturated[24] such that further propagation no longer increases either the maximum electron energy nor the position of the spectral peak. These show (a) a_0 = 3, which is below the bubble regime's threshold for the laser in question, meaning the wakefield is in the nonlinear regime; and (b) a_0 = 5, which is intense enough for a bubble to form. These are obtained using PIC code ILLUMINATION for a laser with Gaussian radial and temporal profiles and centered at λ = 800 nm, and a plasma of density n_0 = 1.745×10^19 cm^-3. It's worth noting the relatively small energy spread of the bubble regime as compared to the nonlinear non-bubble regime.

1.3.2 Longitudinal Self-Injection

Longitudinal self-injection[38] does away with the sensitivity to transverse mode evolution. In longitudinal self-injection, the electrons are injected from near the laser's propagation-axis when they cross over the laser pulse. These electrons are injected while the laser's spot size is still relatively large (e.g. before the laser's focus) and thus has a small radial ponderomotive force. These electrons are therefore not pushed very far from the laser's propagation-axis, and thus remain where the accelerating field is largest. Since the laser spot is relatively large as compared to transverse self-injection, electrons which are injected longitudinally remain relatively symmetric in distribution and are not as drastically affected by small fluctuations in the laser's spot. It should be noted, however, that longitudinal self-injection largely occurs in the nonlinear regime and not in the bubble regime.

1.3.3 Electron Injection via Plasma Density Ramping

One method for controllable electron injection is to use a plasma whose density ramps downward over scales longer than the plasma wavelength[39]. If the plasma density decreases as the laser propagates through it, then plasma wave's phase-velocity will also decrease, which in turn lowers the threshold for trapping electrons in the wave. This leads to wave-breaking in the density ramp: the result is that wave-breaking can be made to occur in a localized spatial region of the plasma.

There are several schemes under which this has been done:

1. the density ramp can occur at the end of a gas jet.

2. the ramp can be placed earlier in the beam's propagation.

3. The ramp can be created by inserting a thin wire or knife edge or other obstacle into the gas jet, thereby creating a series of shock fronts.

The first method[40] produces relatively stable electron beams, but has the disadvantage of having low-energy beams which blow up quickly once they exit the plasma thanks to the space-charge effect. Since the gradient is at the back end of the gas jet—where the gas density and thus the eventual plasma density slowly taper off anyway—the acceleration length would be very small and hence would produce very low-energy beams (0.4 MeV), although at relatively high charges (> 300 pC). These beams would therefore break apart in a relatively small propagation distance as compared to a higher energy (faster) and lower charge (meaning, less "break-up" force) beam.

The second density-gradient scheme requires a more specialized set-up, and essentially attempts to circumvent the problem of beam break-up by placing the density gradient earlier on in the beam's propagation through the plasma[41]. The result is that the electrons can attain relativistic energies. This scheme produces a much more collimated beam (~4 mrad observed), though the energy distribution of these beams tends to fluctuate from shot to shot.

The third density-gradient injection scheme involves creating a shock in the gas jet by placing a knife-edge[42],[43] or thin wire[44] into the gas jet. The former (knife-edge) experiments yielded a reduction in energy spread by a factor of 2 over bubble-regime self-injection, but also a reduction in charge by a similar factor. The shocks generated in

the latter (wire) experiment generates three distinct stages: laser self-compression, then electron injection, and finally electron acceleration in the second period of the plasma wave.

1.3.4 Ionization Injection

Ionization injection[45],[46],[47] involves doping a low-Z background plasma with high-Z atoms. These dopant atoms will have a higher ionization threshold for electrons in lower orbitals. The barrier suppression[48],[49] (or above-threshold ionization) intensity is given by

$$I_{BS}[W/cm^2] \approx 4 \times 10^9 \frac{E_{bound}^4[eV]}{q_i^2}$$
(1.3.3)

where q_i is the charge-state of the ion and E_{bound} is the binding energy in eV of the electron to be ionized.

Barrier suppression intensities are plotted for a variety of gases in Fig. 1.7. As a pair of examples[iv], the first ionization of helium has a barrier suppression intensity of ~1.46×10^{15} W/cm², and the second is ~8.77×10^{15} W/cm²; whereas for nitrogen, the barrier suppression ionization occurs at ~ 1.78×10^{14} W/cm² for the first electron, 7.68×10^{14} W/cm² for the second electron, 2.25×10^{15} W/cm² for the third electron, 9.01×10^{15} W/cm² for the fourth electron, 1.47×10^{16} W/cm² for the fifth electron, 1.03×10^{19} W/cm² for the sixth electron, and 1.62×10^{19} W/cm² for the seventh electron. Note the large jump in

---

iv Calculated using (1.2.17) and the binding energies obtained from NIST.
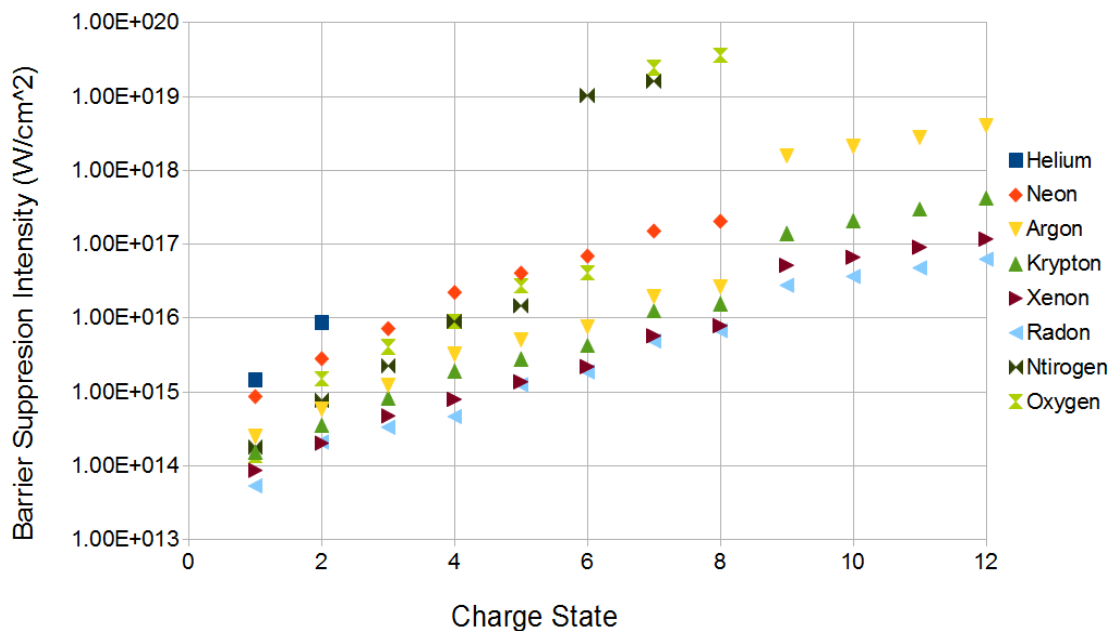
Figure 1.7: Barrier suppression ionization intensities for nitrogen, oxygen, and the noble gases. This plot only shows to the 12th ionization (where applicable),which is sufficient to show where ionization energy makes a sudden "jump" for various elements as we pass from one electron shell to another. For example, there is a large jump from the 5th and 6th electrons in nitrogen, and between the 6th and 7th electrons in oxygen.

ionization suppression intensity from the 5th electron to the 6th electron in nitrogen: this is the difference between ionizing an electron in the 1s orbital as opposed to one in the 2s orbital, that is between ionization of an electron in the outer shell and the inner one, which is due to the charge shielding between shells.

The leading edge of the laser pulse therefore ionizes the low-Z atoms and/or the low-energy level electrons (upper orbitals in the high-Z atoms), thereby creating the plasma. As the laser pulse passes through this plasma, it drives the plasma waves, but the

29

higher-energy electrons are not ionized until they pass the high-intensity peak of the laser, which means that these inner-level electrons are ionized only after the plasma waves have already been generated. These electrons are therefore immediately trapped and accelerated by the plasma's waves. On the other hand, because the beam's intensity can change due to self-focusing (discussed in Chapter 3), ionization injection can take place over a long propagation distance, which in turn results in a more inhomogeneous electron beam.

1.3.5 All-Optical Electron Injection: Colliding Pulses

The first all-optical injection scheme was proposed by Umstadter *et al.*[50] This early all-optical scheme made use of two laser pulses: one high-intensity pulse to drive the plasma wave, and then a second lower-intensity pulse which injects electrons into the plasma wake of the first pulse. The two pulses would propagate orthogonally to each other, that is, if the driving pulse is propagating along the z-axis, then the injector pulse will propagate along the y-axis, and the injector pulse intersects the plasma wake behind the pump. The resulting ponderomotive drift velocity of an electron injected by the second pulse will cause the electron to either counter-propagate or co-propagate with the driver pulse and the plasma wake. If the latter, then the electron is injected into the wakefield, and dephased with respect to it so that it can be trapped and accelerated by the wakefield. The axial ponderomotive force of the injection pulse scales as

$$F_z = -\left(m_e c^2 / \tilde{\gamma}\right)\left(\partial / \partial z\right) a_1^2 / 2 \sim \left(m_e c^2 / \tilde{\gamma}\right) a_1^2 / r_1 \qquad (1.3.4)$$

The alignment and timing of this cross-propagating ponderomotive injection scheme is difficult to realize in an actual experimental setting. Furthermore, both the pump and injector pulses require high intensities, $a_{pump} \simeq a_{inj} \simeq 2$. However, a second all-optical injection scheme was proposed shortly thereafter by Esarey *et al.*[51] which utilizes three co-axial pulses[52],[53],[54]: a large-amplitude pump pulse ($a_0 > 1$) and two low-intensity injector pulses. If the direction of propagation of the pump pulse (subscript 0) is chosen to be forwards, then one injector pulse (subscript 1) will be forwards moving and thus co-propagating with the pump, and delayed behind the pump; the other injector pulse (subscript 2) will be backwards propagating and thus counter-propagating with respect to both the pump and the first injector pulse.

A 1D profile of colliding pulse injection is shown in Fig. 1.8. The pump drives a plasma wave whose phase velocity is near the speed of light. The laser wave numbers (k) and the frequencies (ω) satisfy the relations $k_1 \simeq k_0, k_2 \simeq - k_1, \Delta k = k_1 - k_2 \simeq 2k_0$ and $\omega_1 - \omega_2 = \Delta\omega \gg \omega_p$. When the injection pulses collide behind the pump pulse, they generate a ponderomotive beatwave which takes on the form $F_{pb} = a_1 a_2 \cos(\Delta kz - \Delta\omega t)$. The phase velocity of this beatwave is slow, $v_{pb} \simeq |\Delta\omega|/2k_0 \ll c$, which has an axial force which scales as[31]

$$F_z = - \left(m_e c^2 / \tilde{\gamma} \right)\left(\partial / \partial z \right) a_1 a_2 \cos\left(2k_0 z - \Delta\omega t \right) \sim \left(m_e c^2 / \tilde{\gamma} \right) a_1 a_2 \qquad (1.3.5)$$

Note that in the monochromatic limit (both injector pulses are single-color) this beatwave becomes a standing wave, $v_{pb} \sim 0$, $F_{pb} \propto 2a_1 a_2 / \lambda_1$, where λ_1 is the central wavelength of the injector pulses.
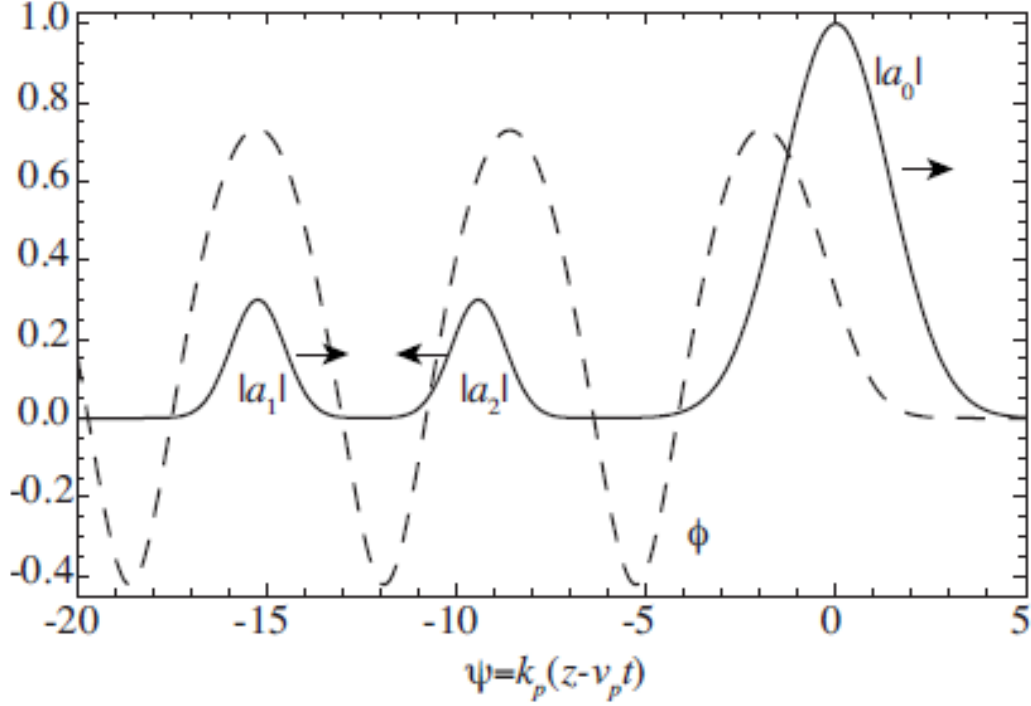
Figure 1.8: Conceptual profiles plot of the laser pulses (a_0 = pump pulse, a_1 = co-propagating injector pulse, a_2 = counter-propagating injector pulse) and the plasma wake ϕ of the in the 3-pulse colliding pulse injection scheme[31]. In the $\psi = k_p(z-v_pt)$ frame, the pump, wake, and forward-propagating injector pulse are all ~stationary, and the backward propagating pulse moves to the left at ~2c.

Another useful scaling law is the ratio of the axial force of a beatwave in a colliding pulse scheme as compared to the cross-propagation ponderomotive injection scheme:

$$F_{z,pb}/F_{z,env} \sim 2k_0 a_1 a_2/\left(a_s^2/r_s\right) \tag{1.3.6}$$

where the subscript s is for the single injection pulse in the cross-propagation scheme, whose ponderomotive injection owes to the gradient in the single pulse's laser intensity envelope. That is, the cross-propagating pulse moves across the wake behind the pump

32

pulse so that the wake will see different injection envelope intensities at each axial position x (due to propagation in time) and in z (due to the injection pulse's transverse profile, which would be oriented along the pump pulse's propagation direction). For comparable pulse injection intensities, $a_1 \simeq a_2 \simeq a_p$, Eqn. (1.3.4) reduces to $F_{z,pb}/F_{z,env} \sim 4\pi r_p/\lambda_0 \gg 1$. In other words, the colliding-pulse injection will work at considerably lower intensities than the cross-propagating injection scheme. Moreover, the colliding-pulse scheme can be realized as significantly lower densities than the cross-propagating scheme, which results in higher single-stage energy gains due to the longer dephasing length of the accelerator.

Colliding pulse injection does not actually require three pulses: it is possible to realize colliding pulse injection experimentally using only two pulses[55],[56]. The two-pulse colliding pulse injector is actually easier to realize in an experiment[57],[58],[59], but it sacrifices some detailed control of the trapping process. A schematic representation of the two-color colliding injector is illustrated in Fig. 1.9. The two-pulse colliding injector has been successfully demonstrated experimentally, as will be discussed in Chapter 2 (Sec. 2.2) of this dissertation.

A major advantage of the colliding-pulse injection scheme is that the LWFA is now broken into two stages: an injection stage and an acceleration stage. This offers more control and flexibility as compared with (for example) self-injection in the bubble regime. Essentially, there are more initial parameters which can be controlled: intensities of each of the beams; relative polarizations of the injector pulses; in the three-beam case,

delay between pump and co-propagating injector pulse, or in the two-beam case, position inside the plasma at which the two pulses collide, and the duration of the colliding injector pulses (which controls injection time). For example, changing the amplitude of the injector pulse allows control of the heating and pre-acceleration of the electrons to be injected without changing the structure of the accelerating plasma wave. Similarly, controlling the location inside the plasma in which the two pulses collide also controls the acceleration length of the injected electrons and thus their final energy.

For example, in the case of 3-pulse colliding injection, it is desirable for the counter-propagating injector pulse to not beat with the pump pulse, so the two injector pulses are polarized orthogonally to the main pulse. On the other hand, in a simpler 2-pulse colliding pulse scheme for which the tail of the pump pulse acts as co-propagating injector, it is desirable for both pulses to have parallel polarization. However, stochastic heating processes may induce injection even when the two injector pulses are cross-polarized[60],[61],[62]. When the laser becomes sufficiently intense that the electron motion becomes relativistic, the $\mathbf{v} \times \mathbf{B}$ force introduces a significant longitudinal field which makes the heating of electrons possible. Thus, the two laser fields are able to couple through the relativistic longitudinal motion of the electrons even though the fields themselves are perpendicular to each other. By tuning the intensity of the injector pulses or changing their relative polarization, it is possible to control the heating level and hence also the number and initial energy of electrons injected.
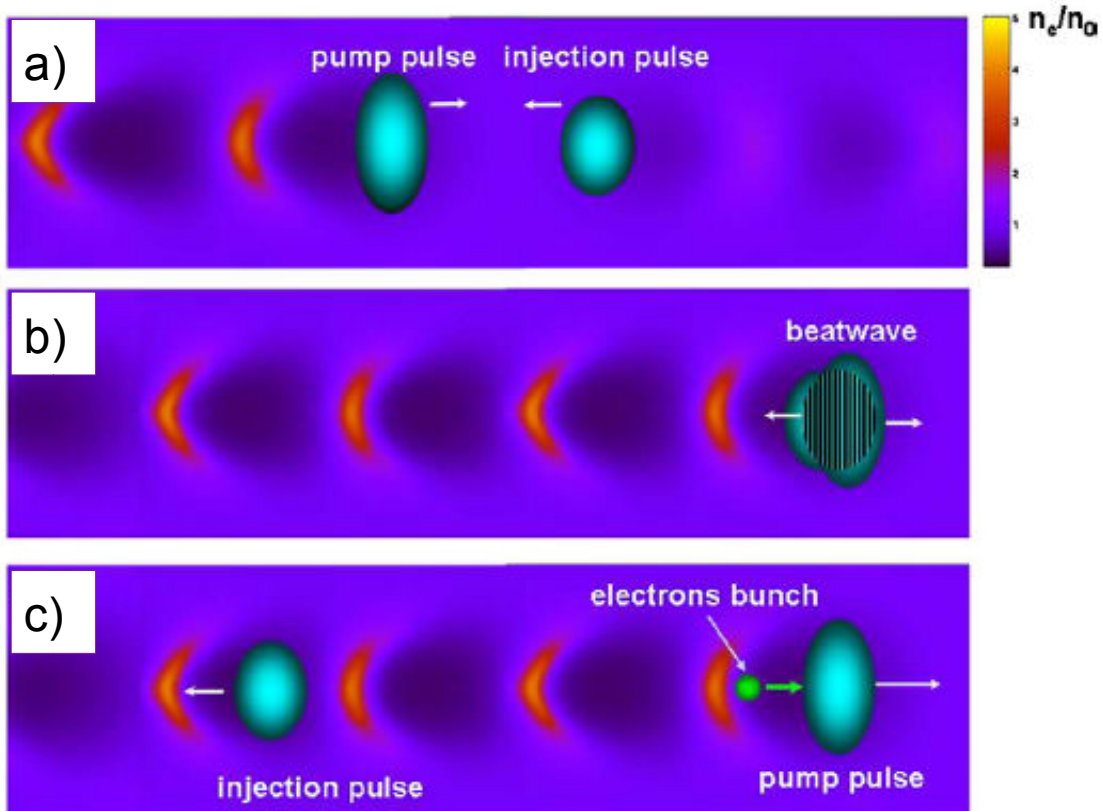
Figure 1.9: Illustrated principle of colliding pulse injection using two laser pulses[61]. (a) A large-amplitude laser pulse drives the plasma wave, while a smaller-amplitude injector pulse counterpropagates with it. (b)At some point, the two pulses collide and interfere, generating a beatwave which per-accelerates some electrons from the background plasma. (c) these per-accelerated electrons are then trapped and further accelerated by the plasma wake behind the pump pulse.
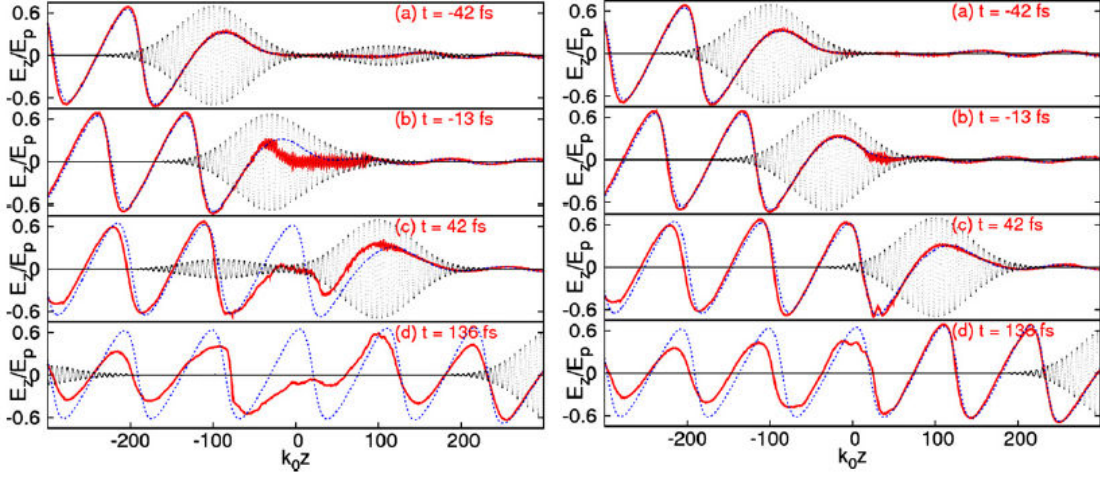
Figure 1.10: Comparison of the electric fields for colliding pulse injection using two pulses which are parallel-polarized (left a-d) or cross-polarized (right a-d)[61]. The solid red curves are the longitudinal fields obtained at different times (a-d) from 1D PIC simulations, the dotted blue curves are the longitudinal fields at the same times obtained from simulations based on the fluid model, and the thin dotted line is the laser pulses' transverse fields. Parameters are $a_{pump} = 2$, $a_{inj} = 0.4$, 30 fs FWHM duration for each pulse, pulses both centered around 800 nm wavelength, and background plasma density $n_e = 7 \times 10^{18}$ cm^{-3}.

Figure 1.10 shows a comparison of the evolution of the longitudinal E-field for both the parallel- and the crossed-polarization cases in the two-beam injection scheme. It is worth noting that the curve in Figs. 1.10 obtained from only the fluid model remains the same for both the parallel-polarized and the cross-polarized cases, whereas the curve from 1D PIC codes varies between the two cases.

In the parallel-polarized case, the electrons become spatially trapped in the beatwave and are unable to sustain the collective plasma oscillation (wave). This inhibits the plasma wave behind the collision—as shown in Figs. 1.10(c-d, left)—and so changes the waves behavior as compared to the fluid model even long after the collision. On the

other hand, because cross-polarized pulses do not generate a standing beatwave, this effect is marginal in the case of cross-polarized colliding pulse injection, as shown in Figs. 1.10(c-d, right), and so the plasma wave behavior deviates little from that predicted by the fluid model. The result is that whereas crossed-polarization induces less efficient stochastic heating as compared to parallel-polarization (making injection and trapping less efficient), it also does not inhibit the wakefield to the same extent (making trapping more efficient). These two effects counter-balance each other, making trapping possible in the crossed-polarization case.

A comparison of electrons injected into the accelerator using parallel- and cross-polarized beams is shown in Fig. 1.11. In both cases, the parallel-polarized injector pulse is more effective than the cross-polarized injector by a factor of ~5. Furthermore, the threshold for trapping an injected charge is also a factor of ~5 higher for the crossed-polarized injection pulse: whereas the parallel-polarized injector pulse only required $a_{inj,par} > 0.05$, the crossed-polarized pulse required approximately $a_{inj,perp} > 0.25$. This is a factor of ~25 increase in threshold intensity from the parallel-polarized scheme to cross-polarized scheme.

The colliding-pulse injector ultimately shows improvement in stability when compared to other injection schemes like bubble-regime self-injection. Perhaps more importantly, it allows for more control over such electron beam parameters as energy, relative energy spread, and charge.
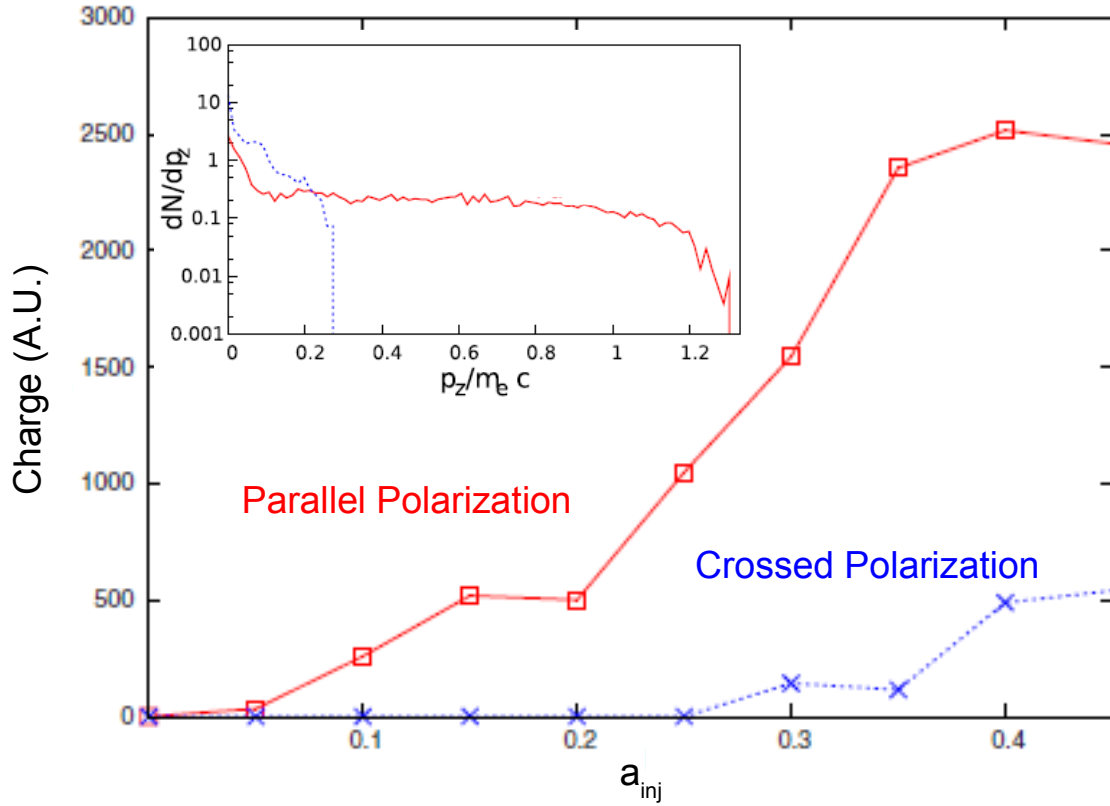
Figure 1.11: Comparison of 1D PIC results for accelerated electron beam charge in a colliding-pulse injector for parallel polarization (solid red) and crossed polarization (dotted blue). The inset shows a comparison of electron longitudinal momenta. Image from [62].

1.4 SOME FUNDAMENTAL LIMITATIONS OF LASER WAKEFIELD ACCELERATORS

The laser-plasma accelerator has three fundamental length limitations[63]: dephasing length, diffraction length, and pump depletion length. The shortest of these three lengths then becomes the limiting length of the accelerator. Tajima and Dawson considered the dephasing length by stating that an electron (or other accelerated particle) reaches its maximum energy just before its acceleration is reversed. The time that the electron is

accelerated before reaching maximum energy is the dephasing time (sometimes also called "detuning" time), and the distance it travels is referred to as the dephasing length ($L_{ph} \sim ct_{ph}$)[11],[31]:

$$L_{ph} = \frac{\lambda_p^3}{2\lambda_l^2} \times \begin{Bmatrix} 1, & for\ a_0^2 \ll 1 \\ (\sqrt{2}/\pi)\,a_0/N_p, & for\ a_0^2 \gg 1 \end{Bmatrix} \tag{1.4.1}$$

where N_p is the number of plasma periods behind the drive pulse; this factor of $1/N_p$ for $a_0^2 \gg 1$ is due to the plasma period's increasing as discussed in Sec. 1.2.2.

As for the diffraction length, the laser spot size will evolve due to Rayleigh diffraction according to

$$w_s(z) = w_0(1 + z^2/Z_R^2)^{1/2} \tag{1.4.2}$$

for a Gaussian pulse, where Z_R Rayleigh range and $w_0 = w_s(0)$ is the laser's spot waist. Thus, a looser focus will result in a greater acceleration length (because of a longer diffraction length), but also a smaller intensity and thus ultimately in a smaller accelerating gradient. A tighter focus will yield a larger accelerating gradient, but a much shorter diffraction length. The Rayleigh range is a good measure of diffraction length, and for a Gaussian pulse is given by

$$z_R = \frac{\pi\,\eta(w_0)^2}{\lambda_L} \tag{1.4.3}$$

where w_0 is the $1/e^2$ intensity waist of the laser at focus and η is the refractive index of the plasma. This particular limit typically affects LWFA in the linear regime as described by Tajima and Dawson, but can be mitigated by using self-focusing to guide the beam, e.g. in self-modulating laser-wakefield schemes[64],[65].

39

The final fundamental limit is pump depletion. Essentially, driving the plasma wake requires energy which is drawn from the pump photons. These are typically non-resonantly absorbed and scattered into longer wavelengths at lower energy, though a proposal of using CO_2 lasers to resonantly drive plasma waves has been made[66],[67],[68], primarily to accelerate ions (or proton bunches). As photons are scattered or absorbed from the laser, the energy available to drive the plasma wake is decreased—as is the ponderomotive force of the laser—and thus the wave gradually grows weaker again. One estimate[31],[69],[70],[71] of the depletion length is[v]

$$L_{dep} \simeq \frac{\lambda_p^3}{\lambda_L^2} \times \begin{cases} 2/a_0^2, & for\ a_0^2 \ll 1 \\ (\sqrt{2}/\pi)a_0, & for\ a_0^2 \gg 1 \end{cases} \tag{1.4.4}$$

This is the length over which half of the laser pulse's initial energy is depleted.

A fourth limitation is the growth of various laser-plasma instabilities which can disrupt the laser or the plasma wave. These will be discussed in the next chapter.

These various limitations can be related to the plasma density. In the case of the pump depletion length and the dephasing length, the density of the plasma affects the plasma wavelength term: $\lambda_p = 2\pi c/\omega_p \sim n_e^{-1/2}$. On the other hand, the maximum longitudinal field strength $E_{max} \simeq \sqrt{a_0} E_0 \simeq (0.96 n_e^{1/2}) \sqrt{a_0}$. Therefore, the accelerating field strength of a plasma wake increases like the square root of the plasma density, $n_e^{1/2}$,

---

v   On the other hand, Bulanov *et al.*[71] give a different estimate for depletion length. Their estimate of depletion length is

$$L_{dep} = \frac{8}{3} \frac{\lambda_p}{\pi^{2/3} a^2 k_p \sigma_z} \left(\frac{\lambda_p}{\lambda_l}\right)^2$$

for a long laser pulse with short leading edge, where σ_z is the spot size of the laser pulse.

but the dephasing length and pump depletion length both decrease with $n_e^{-3/2}$. These scaling laws therefore suggest that for an accelerator limited by either dephasing length or pump depletion length, the energy gain actually decreases inversely with the plasma density. The ideal energy gain in a LWFA might be estimated as $\Delta W = eE_zL_{acc}$, where L_{acc} is the acceleration length. Assuming a flat-top, linearly polarized laser field in the 1D limit, E_z becomes[31] $E_z = E_0(a_0^2/s)(1 + a_0^2/2)^{-1/2}$, so that if the acceleration length is limited by dephasing, the energy gained by an electron is

$$\Delta W_{ph}[MeV] \simeq \frac{630\, I\, [W/cm^2]}{n_e[cm^{-3}]} \times \begin{cases} 1, & for\, a_0^2 \ll 1 \\ 2/(\pi N_p), & for\, a_0^2 \gg 1 \end{cases} \tag{1.4.5}$$

Similarly, if the accelerator length is limited by pump depletion, the energy gain is

$$\Delta W_{dep}[MeV] \simeq \frac{1}{n_e[cm^{-3}]} \times \begin{cases} 3.4\times10^{21}/\lambda_L[\mu m], & for\, a_0^2 \ll 1 \\ 400\, I\, [W/cm^2], & for\, a_0^2 \gg 1 \end{cases} \tag{1.4.6}$$

These two scaling laws hold for a LWFA in the regime $L\sim\lambda_p$ for broad laser pulses ($k_p^2 r_0^2 \gg 1$) propagating in a density channel which provides guiding. The scaling laws will be different in highly non-linear regimes such as the bubble regime. Two alternative scaling laws obtained through numerical analysis for the bubble regime of LWFA are

$$\gamma_f \propto a_0^2 k_0^2/k_p^2 = a_0^2 n_c/n_e$$ [37] and, in a regime with lower plasma densities and wider spot sizes and ~constant intensities[72], $\Delta W[MeV] \simeq 0.1(c\tau_L/\lambda_L)\sqrt{P[GW]}$.

The plasma density also affects the diffraction length (albeit more weakly), because the plasma refractive index is $\eta = 1- (\omega_L/\omega_p)^2 \sim 1-1/n_e$. In this case, the idealized energy gain is

$$\Delta W_{diff,R} \simeq \frac{740 \, \lambda_L P[TW]}{\lambda_p \sqrt{1 + a_0^2/2}} \tag{1.4.7}$$

These estimates are based on idealized conditions which neglect laser-plasma interactions such as relativistic self-focusing, ionization defocusing, etc. In some cases, these other effects can improve these limitations, as when self-focusing and optical guiding overcome diffraction, though they come with their own set of limitations (such as when a self-focusing laser filaments).

Chapter References

[1] R.A. Van de Graaff, *Phys. Rev.*, Vol. **38**, 1919 (1931).

[2] I.D. Smith and H. Aslin, "Pulsed Power for EMP Simulators," *IEEE Trans. Antennas and Prop.*, Vol. **AP-26**, No. 1, pp. 53-59 (1978).

[3] R. Widerøe, (17 December 1928). "Ueber Ein Neues Prinzip Zur Herstellung Hoher Spannungen". Archiv fuer Elektronik und Uebertragungstechnik 21 (4): 387.

[4] D.W. Kerst, "Acceleration of Electrons by Magnetic Induction," Phys. Rev. Vol. **58**, No. 9 (1940).

[5] D.W. Kerst, "The Acceleration of Electrons by Magnetic Induction," *Phys. Rev.*, Vol. **60**, 47–53 (1941).

[6] Ernest O. Lawrence, "Method and apparatus for the acceleration of ions," US patent 1948384, issued 1934-02-20.

[7] Anonymous, "The Relativistic Heavy Ion Collider Run-9: 250 GeV Polarized Proton Operation," *Brookhaven National Laboratory, Collider-Accelerator Department*, 02 April, 2009.
http://www.agsrhichome.bnl.gov/AP/Spin2009/

[8] Hamm, Robert W.; Hamm, Marianne E. (2012). Industrial Accelerators and Their Applications. World Scientific. ISBN 978-981-4307-04-8.

[9] Anonymous, "File:Breakdown of the cumulative number of industrial accelerators according to their applications.png," *Wikipedia*, 21 February 2013.
http://en.wikipedia.org/wiki/File:Breakdown_of_the_cumulative_number_of_indu strial_accelerators_according_to_their_applications.png

[10] B. Bernstein and I. Smith, "Aurora, an electron accelerator," *IEEE Trans. Nucl. Science* Vol. **3**, 294-300 (1973).

[11] T. Tajima and J. M. Dawson, "Laser Electron Accelerator," *Phys. Rev. Let.*, Vol. **43** No. 4 (1979).

[12] E. Esarey, P. Sprangle, J. Krall, and A. Ting, "Overview of Plasma-Based Accelerator Concepts," *IEEE Trans. Plasma Sci.*, Vol. **24**, No. 2 (1996).

[13] R. Keinigs and M.E. Jones, "Two-dimensional dynamics of the plasma wakefield accelerator," *Phys. Fluids*, Vol. **30**, pp. 252-263 (1987).

[14] P. Sprangle, E. Esarey, A. Ting, and G. Joyce, "Laser wakefield acceleration and relativistic optical guiding," *Applied Phys. Letters*, Vol. **53**, pp 2146-2148 (1988).

[15] P. Sprangle, E.Esarey, and A. Ting, "Nonlinear interaction of intense laser pulses in plasmas," *Phys. Rev. A.*, Vol. **41**, pp. 4463-4469 (1990).

[16] N.H. Matlis, S. Reed, S.S. Bulanov, V. Chvykov, G. Kalintchenko, T. Matsuoka, P. Rousseau, V. Yanovsky, A. Maksimchuk, S. Kalmykov, G. Shvets, and M.C. Downer, "Snapshots of laser wakefields," *Nature Physics*, Vol. **2**, 749-753 (2006).

[17] A.I. Akheizer and R.V. Polovin, "Theory of wave motion of an electron plasma," *Sov. Phys. JETP,* Vol. **3**, pp 696-705 (1956).

[18] T. Katsouleas and W.B. Mori, "Wave-breaking amplitude of relativistic oscillations in a thermal plasma," *Phys. Rev. Lett.,* Vol. **61**, pp 90-93 (1988).

[19] E. Esarey and M. Pillof, "Trapping and acceleration in nonlinear plasma waves," *Phys. Plas.* Vol. **2**, 1432 (1995).

[20] P. Sprangle, E. Esarey. J. Krall, and G. Joyce, "Interaction of ultrahigh laser fields with beams and plasmas," *Phys. Fluids B*, Vol. **4**, pp. 2241-2248 (1992).

[21] P. Sprangle, E. Esarey. J. Krall, and G. Joyce, "Propagation and guiding of intense laser pulses in plasmas," *Phys. Rev. Lett.*, Vol. **69**, pp. 2200-2203 (1992).

[22] J. B. Rozenzweig, B. Breizman, T. Kasouleas, and J. J. Su, "Acceleration and focusing of electrons in two-dimensional nonlinear plasma wake fields" *Phys. Rev. A*, Vol. **44**, No. 10, R6189-R6192 (1991).

[23] A. Pukhov and J. Meyer-ter-Vehn, "Laser wake field acceleration: the highly non-linear broken-wave regime," *Appl. Phys. B*, Vol. **74**, 355-361 (2002).

[24] M. Geissler, J. Schreiber, and J. Meyer-ter-Vehn, "Bubble acceleration of electrons with few-cycle laser pulses," *New J. of Phys.*, Vol. **8**, 186, (2006).

[25] J. Faure, Y. Glinec, A. Pukhov, S. Kiselev, S. Gordienko, E. Lefebre, J.-P. Rousseau, F. Burgy, and V. Malka, "A laser-plasma accelerator producing monoenergetic electron beams," *Nature*, Vol. **431**, 541-544 (2004).

[26] S.P.D. Mangles, A.G.R. Thomas, M.C. Kaluza, O. Lundh, F. Lindau, A. Persson, F.S. Tsung, Z. Najmudin, W.B. Mori, C.-G. Wahlstrom, and K. Krushelnick, "Laser-Wakefield Acceleration of Monoenergetic Electron Beams in the First Plasma-Wave Period," *Phys. Rev. Lett.*, Vol. **96**, 215001 (2006).

[27] S. Y. Kalmykov, S.A. Reed, S.A. Yi, A. Beck, A.F. Lifschitz, X. Davoine, E. Lefebvre, V. Khudik, G. Shvets, P. Dong, X. Wang, D. Du, S. Bedacht, Y. Zhao, W. Henderson, A. Bernstein, G. Dyer, M. Martinez, E. Gaul, T. Ditmire, and M.C. Downer, "Laser wakefield electron acceleration on Texas Petawatt facility: Towards multi-GeV electron energy in a single self-guided stage," *High Energy Density Physics*, Vol. **6**, no. 2, pp. 200-206 (2010).

[28] X. Wang et. al., "Self-injected Petawatt Laser-driven Plasma Electron Acceleration in 10^{17} cm^{-3} Plasma," *Las. Appl. Phot. Application*, *OSA Conf. Proc, Quant. El. and Las. Sci. Conf*, QMJ3 (2011).

[29] X. Wang, D. Du, S.A. Yi, S. Kalmykov, E. D'avignon, N. Fazel, R. Zgadzaj, S. Reed, P. Dong, W. Henderson, G. Dyer, A. Bernstein, E. Gaul, M. Martinez, G. Shvets, T. Ditmire, and M. Downer, "Multi-GeV Electron Generation Using Texas Petawatt Laser," *AIP Conf. Proc.* **1299**, 209 (2010).

[30] X. Wang, R. Zgadzaj, W. Henderson, N. Fazel, Y.-Y. Chang, R. Korzekwa, A.S. Yi, V. Khudik, H.-E. Tsai, Z. Li, H. Quevedo, G. Dyer, E. Gaul, M. Martinez, A. Bernstein, T. Borger, M. Spinks, M. Donovan, G. Shvets, T. Ditmire, and M.C. Downer, "Generation of Dark-current-free Quasi-monoenergetic 1.25 GeV Electrons by Laser Wakefield Acceleration," *Quant. Elect. And Laser Sci. Conf. Proc.*, QW3F (2012).

[31] E. Esarey, C.B. Schroeder, and W.P. Leemans, "Physics of laser-driven plasma-based electron accelerators," *Rev. Mod. Phys.*, Vol. **81**, No. 3, pp. 1229-1285 (2009).

[32] W. Lu, C. Huang. M. Zhou, W.B. Mori, and T. Katsouleas, "Nonlinear Theory for Relativistic Plasma Wakefields in the Blowout Regime," *Phys. Rev. Lett.*, Vol **96**, 165002 (2006).

[33] C. E. Clayton, K. A. Marsh, A. Dyson, M. Everett, A. Lal, W. P. Leemans, R. Williams, and C. Joshi, "Ultrahigh-gradient acceleration of injected electrons by

laser-excited relativistic electron plasma waves," *Phys. Rev. Lett.* Vol. **70**, No. 1, 37-40 (1993).

[34] F. Amiranoff, M. Laberge, J.R. Marques, F. Moulin, E. Fabre, B. Cros, G. Matthieussent, P. Benkheiri, F. Jacquet, J. Meyer, Ph. Mine, C Stenz, and P. Mora, "Observation of Modulational Instability in Nd-Laser Beat-Wave Experiment," *Phys. Rev. Lett*. Vol. **68**, No. 25, pp. 3710-3713 (1992).

[35] A. Moderna, Z. Najmudn, A.E Danger, C.E. Clayton, K.A Marsh, C. Joshi, V. Malka, C.B. Darrow, C. Danson, D. Neely, and F.N. Walsh, Electron acceleration from the breaking of relativistic plasma waves," *Nature*, Vol. **377**, 606 (1995).

[36] V. Malka, "Review of Laser Wakefield Accelerators," *Proceedings of IPAC* (2013).

[37] S. Gordienko and A Pukhov, "Scalings for ultrarelativistic laser plasmas and quasimonoenergetic electrons", *Phys. Plasmas*, Vol. **12**, 043109 (2005).

[38] S. Corde, C. Thaury, A. Lifschitz, G. Lambert, K Ta Phuoc, X. Davoine, R. Lehe, D. Douillet, A. Rousse, and V. Malka, "Observation of longitudinal and transverse self-injection in laser-plasma accelerators," *Nature Communications*, Vol. **4**, 1501 (2013).

[39] S. Bulanov, N. Naumova, F. Pegoraro, and J. Sakai, "Particle injection into the wave acceleration phase due to nonlinear wake wave breaking," *Phys. Rev. E*, Vol. **58**, R5257 (1998).

[40] C. G. R. Geddes, K. Nakamura, G. R. Plateau, Cs. Toth, E. Cormier-Michel, E. Esarey, C. B. Schroeder, J. R. Cary, and W. P. Leemans, "Plasma-Density-Gradient Injection of Low Absolute-Momentum-Spread Electron Bunches," *Phys. Rev. Lett.*, Vol. **100**, 215004 (2008).

[41] J. Faure, C. Rechatin, O. Lundh, L. Ammoura, and V. Maka, "Injection and acceleration of quasimonoenergetic relativistic electron beams using density gradients at the edges of a plasma channel," *Phys. of Plasmas,* Vol. **17**, 083107 (2010).

[42] K. Koyamaa, A. Yamazakia, A. Maekawaa, M. Uesakaa, T. Hosokaib, M. Miyashitac, S. Masudad, E. Miura, "Laser-plasma electron accelerator for all-optical inverse Compton X-ray source," *Nucl. Instrum. Methods A*, Vol. **608**, S51 (2009).

[43] K. Schmid, A. Buck, C.M.S. Sears, J.M. Mikhailova, R. Tautz, D. Herrmann, M. Geissler, F. Krausz, and L. Veisz, "Density-transition based electron injector for laser driven wakefield accelerators," *Phys. Rev. STAB*, Vol. **13**, 091301 (2010).

[44] M. Burza, A. Gonoskov, K. Svensson, F. Wojda, A. Persson, M. Hansson, G. Genoud, M. Marklund, C.-G. Wahlstro and O. Lundh, "Laser wakefield acceleration using wire produced double density ramps,", *Phys. Rev. STAB*, Vol. **16**, 011301 (2013).

[45] C. Rechatin, J. Faure, A. Ben-Ismail, J. Lim, R. Fitour, A. Specka, H. Videau, A. Tafzi, F. Burgy, and V. Malka, "Controlling the Phase-Space Volume of Injected Electrons in a Laser-Plasma Accelerator," *Phys. Rev. Lett.*, Vol. **102**, No. 16, 164801 (2009).

[46] T. P. Rowlands-Rees, C. Kamperidis, S. Kneip, A. J. Gonsalves, S. P. D. Mangles, J. G. Gallacher, E. Brunetti, T. Ibbotson, C. D. Murphy, P. S. Foster, M. J. V. Streeter, F. Budde, P. A. Norreys, D. A. Jaroszynski, K. Krushelnick, Z. Najmudin, and S. M. Hooker, "Laser-Driven Acceleration of Electrons in a Partially Ionized Plasma Channel," *Phys. Rev. Lett.*, Vol. **100**, 105005 (2008).

[47] A. Pak, K. A. Marsh, S. F. Martins, W. Lu, W. B. Mori, and C. Joshi, "Injection and Trapping of Tunnel-Ionized Electrons into Laser-Produced Wakes," *Phys. Rev. Lett.*, Vol. **104**, 025003 (2008).

[48] S. Augst, D.D. Meyerhofer, D. Strickland, and S.L. Chin, "Laser ionization of noble gases by Coulomb-barrier suppression," *J. Opt. Soc. Am. B*, Vol. **8**, No. 4, pp. 858-867 (1991).

[49] L. V. Keldysh, "Ionization in the field of a strong electromagnetic pulse," *Sov. Phys. JETP*, Vol. **20**, 1307 (1965).

[50] D. Umstadter, J.K. Kim, and E. Dodd, "Laser Injection of Ultrashort Electron Pulses into Wakefield Plasma Waves," *Phys. Rev. Lett.*, Vol. **76**, No. 12, 2073-2076 (1996).

[51] E. Esarey, R.F. Hubbard, W.P. Leemans, A. Ting, and P. Sprangle, "Electron Injection into Plasma Wake Fields by Colliding Laser Pulses," *Phys. Rev. Lett.* Vol. **79**, No. 14, 2682-2685 (1997).

[52] W.P. Leemans, P. Volbeyn, K.X. Guo, S. Chattopadhyay, C.B. Schroeder, B. A. Shadwick, P. B. Lee, J.S. Wurtele, and E. Esarey, "Laser-driven plasma-based

accelerators: Wakefield excitation, channel guiding, and laser-triggered particle injection," *Phys. of Plasmas*, Vol. **5**, 1615 (1998).

[53] E. Esarey, C.B. Schroeder, W.P. Leemans, and B. Hafizi, "Laser-Induced electron trapping in plasma-based accelerators," *Phys. of Plasmas*, Vol. **6**, 2262 (1999).

[54] C.B. Schroeder, P.B. Lee, J.S. Wurtele, E. Esarey, and W.P. Leemans, "Generation of ultrashort electron bunches by colliding laser pulses," *Phys. Rev. E*, Vol. **59**, pp. 6037-6047 (1999).

[55] H. Kotaki, S. Masuda, M.Kando, J.K. Koga, N. Nakajima, "Head-on injection of a high quality electron beam by the interaction of two laser pulses," *Phys. Plasmas*, Vol. **11**, 3296 (2004).

[56] G. Fubiani, E. Esarey, C.B. Schroeder, and W.P. Leemans, "Beat wave injection of electrons into plasma waves using two interfering laser pulses," *Phys. Rev. E*, Vol. **70**, No. 1, 016402 (2004).

[57] J. Faure, C. Rechatin, A. Norlin, A. Lifschitz, Y. Glinec, and V. Malka, "Controlled injection and acceleration of electrons in plasma wakefields by colliding laser pulses," *Nature*, Vol. **444**, 737-739 (2006).

[58] J. Faure, C. Rechatin, A.F. Lifschitz, X. Davoine, E. Lefebre, and V. Malka, "Experiments and Simulations of the Colliding Pulse Injection of Electrons in Plasma Wakefields," *IEEE Trans. Plasma. Phys.,* Vol. **36**, No. 4, pp. 1751-1759, 2008.

[59] H. Kotaki, I. Daito, M. Kando, Y. Hayashi, M. Jinglong, L.-M. Chen, T. Z. Esirkepov, Y. Fuduka, T. Homma, A. Pirozhkov, J.K. Koga, K. Nakajima, H. Daido, and S.V. Bulanov, "Improvement of the Quality and Stability of Electron Bunch Using Countercrossing Laser Beam," *IEEE Trans. Plasma Phys.*, Vol. **36**, No. 4, pp. 1760-1764, 2008.

[60] X. Davoine, E. Lefebre, J. Faure, C. Rechatin, A. Lifschitz, and V. Malka, "Simulation of quasimonoenergetic electron beams produced by colliding pulse wakefield acceleration," *Phys. of Plasmas*, Vol. **15**, 113102 (2008).

[61] V. Malka and P. Mora, "Principles of Laser-Plasma Accelerators," *C.R. Physique*, Vol. **10**, pp 106-115, 2009.

[62] V. Malka, J. Faure, C. Rechatin, A. Ben-Ismail, J.K. Lim, X. Davoine, and E. Lefebre, "Laser-driven accelerators by colliding pulses injection: A review of simulation and experimental results," *Phys. of Plasmas*, Vol. **16**, 056703 (2009).

[63] A. Ogata, "Status and Problems of Plasma Accelerators," *ICFA Beam Dynamics Newsletter*, No. 11, August 1996.

[64] C. Joshi, T. Tajima, J.M. Dawson, H.A. Baldis, and N.A. Ebrahim, "Forward Raman Instability and Electron Acceleration," *Phy. Rev. Lett.*,Vol. **47**, 1285 (1981).

[65] K. Nakajima, D. Fisher, T. Kawakubo, H Nakanishi, A. Ogata, Y. Kato, Y. Kitagawa, R. Kodama, K. Mima, H. Shiraga, K. Suzuki, K. Yamakawa, T. Zhang, Y. Sakawa, T. Shoji, Y. Nishida, N. Yugami, M. Downer, and T. Tajima, "Observation of Ultrahigh Gradient Electon Acceleration by a Self-Modulated Intense Short Pulse," *Phys. Rev. Let.* Vol. **74**, Number 22, May 1995.

[66] S. Totchitsky, J. Pigeon, D. Haberberger, and C. Joshi, "Amplification of High-Power Picosecond 10-μm Pulses in Atmospheric CO_2 laser," *Conf. Proc.* CLEO 2012.

[67] I.V. Pogorelshy, V. Yakimenko, M. Polyanskiy, P. Sholnikov, M. Ispiryan, D. Neely, P. McKenna, D. Carrol, Z. Najmudin, L. Willingale, "Ultrafast CO2 laser technology--Application in ion acceleration," *Nuclear Instruments and Methods in Physics Research A*, Vol. **620**, No. 1, pp. 67-70 (2010).

[68] Z. Najmudin, C.A.J. Palmer, N.P. Dover, I. Pogerelsky, M. Babzien, A.E. Dangor, G.I. Dudnikova, P.S. Foster, J.S. Gree, M. Ispiriyan, D. Neely, M.N. Polyanskiy, J. Schreiber, P. Shkolnikov, and V. Yakimenko, "Observation of impurity free monoenergetic proton beams from the interaction of a CO_2 laser with a gaseous target," *Phys. Plasmas*, Vol. **18**, 056705 (2011).

[69] B.A. Shadwick, C.B. Schroeder, and E. Esarey, "Nonlinear laser energy depletion in laser-plasma accelerators," *Phys. of Plasmas*, Vol. **16**, 056704, 2009; Paper D12 3, *Bull. Am. Phys. Soc.*, Vol. **53**, 77 (2008).

[70] B.A. Shadwick, C.B. Schroeder, E. Esarey, and W.P. Leemans, "Nonlinear Pump Depletion and Electron Dephasing in Laser Wakefield Accelerators," *Proceedings of the Advanced Accelerator Concepts Workshop*, *AIP Conf. Proc.* Vol. **737**, 578 (2004).

[71] S.V. Bulanov, I. N. Inovenkov, V.I. K.M. Naumova, and S.A. Sakharov, "Nonlinear depletion of ultrashort and relativistically strong laser pulses in an underdense plasma" Phys. Fluids B4 1935 (1992).

49

[72] W. Lu, M. Tzoufras, C. Joshi, F.S. Tsung, W.B. Mori, J. Vieira, R.A. Fonseca, and L.O. Silva, "Generating multi-GeV electron bunches using single laser wakefield acceleration in a 3D nonlinear regime," *Phys. Rev. STAB*, Vol. **78**, 061301 (2007).

Chapter 2

Review of Experimental Progress in Laser-Wakefield Acceleration

Laser technology was not yet ripe for creating a laser wakefield accelerator (LWFA) at the time of Tajima and Dawson's proposal, so other methods such as the plasma wakefield accelerator (PWFA)[73],[74] and the laser beatwave accelerator (LBWA)[75],[76] were used in early wakefield accelerator experiments. However, with the advent of chirped pulse amplification[77] (CPA) and the table-top terrawatt laser, research laboratories were able to achieve sufficient intensities to conduct LWFA experiments.

2.1   FIRST OBSERVATION OF LASER WAKEFIELD AND ACCELERATION

The first laser-driven wakefield was observed a few years after the advent of the CPA laser[78], and a LWFA proof-of-concept experiment was conducted soon thereafter[79]. In the proof-of-concept experiment, electrons were injected into a laser-induced wakefield and accelerated by a gradient of 0.7 GeV/m, a factor of ~7 times greater than the gradient attainable by an RF accelerator. A later experiment observed the acceleration of injected electrons by a simple (linear regime) LWFA[80] in which the electrons experienced a maximum energy gain of 1.6 MeV.
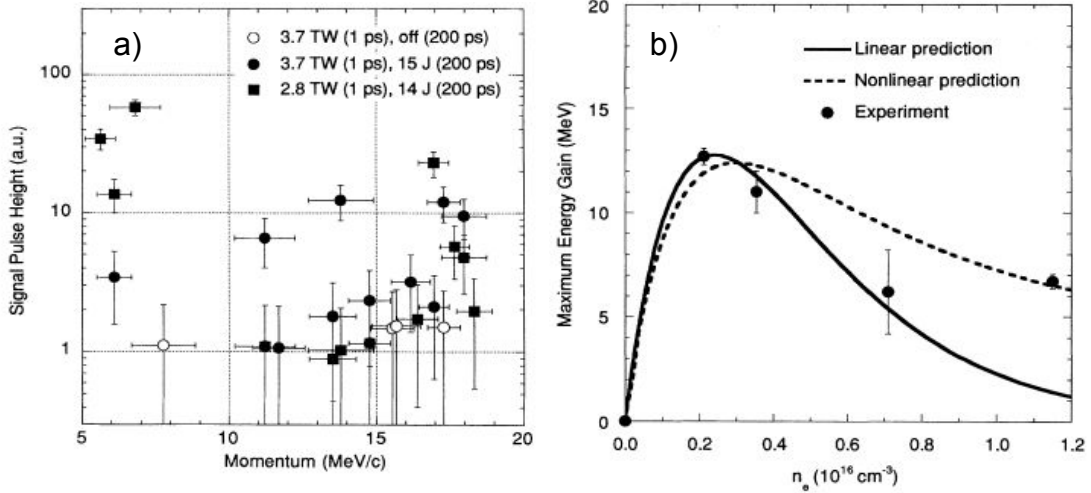
Figure 2.1: Results from the first self-modulated laser wakefield acceleration experiment[81]. The observed momenta spectra (a) for the accelerated electrons shows that electrons were accelerated to a maximum momentum of ~18 MeV/c. Electrons are injected by irradiating an aluminum solid target with a 200 ps pulse (either 14 J for black circles or 15 J for black squares), or when this target is removed a small number (~100) are self-injected (white circles). The maximum observed energies are compared to the theoretical values (b) predicted by the nonlinear fluid model (solid line) and the nonlinear fluid model (dashed line).

However, most early LWFA experiments were actually sm-LWFA. These relied on the self-modulation of the laser pulse as it propagated through the plasma to break the single pulse (duration $\tau_{laser} > \tau_{plasma}$) into a train of pulses which can resonantly excite the plasma wave and thus drive a large wake field. The first acceleration of electrons by a self-modulated laser wakefield was observed[81], shortly after the initial proof-of-principle experiment.

The results of this sm-LWFA experiment are displayed in Fig. 2.1, which shows the results of acceleration at high density (a) and a density scan compared to theory (b). In this experiment, a helium gas jet was ionized by a 1 ps laser with an 8 TW peak power,

which generated the wakefield. Electrons of initial momentum 1 MeV/c were injected into the wakefield by irradiating an aluminum target with a 200 ps laser pulse, and the plasma density was varied by changing the backing pressure of the gas jet, and then the maximum energy was compared to the values predicted by the linear and nonlinear fluid models (described in Secs. 1.2.1 and 1.2.2). The linear model's predictions were in agreement with the experimental results at lower plasma densities, but for densities $> 10^{16}$ cm^{-3}, the maximum energy agrees more strongly with the nonlinear model.

The accelerations of the electrons shown in Fig. 2.1a were obtained at relatively high plasma density (1.5×10^{19} cm^{-3}) with a 2.8 TW (black squares) or 3.7 TW (circles) pulse. The maximum momentum gain by the accelerated electrons was 18 MeV, and this acceleration occurred over a maximum distance of 0.6 mm (limited by dephasing), which yields a maximum acceleration gradient of 30 GeV/m. This is a factor of 300 larger than dielectric breakdown-limited maximum gradient obtainable by a conventional RF accelerator.

A third acceleration experiment operated in the forced laser wakefield (FLWF) regime[82] in which the laser pulse duration (30 fs) was of approximately the same length as the plasma wavelength. In this regime, the laser will not self-modulate: a process which typically grows from some small-signal (effectively, background) seed requiring instabilities (e.g. Raman Scattering) for its creation, and which as a result both requires time to develop and has large shot-to-shot fluctuations. This lack of instabilities also

results in a lower plasma temperature, which means that the wakefield will approach the cold wave-breaking limit, as discussed in Chapter 1 (Sec. 1.2.2) of this dissertation.

The energy spectrum and angular distribution obtained in this experiment are shown in Fig. 2.2. The accelerated electrons more-or-less obey an inverse exponential, though the lower energy (<130 MeV) electrons obey a nearly linear distribution; an effective temperature of 18 MeV can be obtained using the exponential fit. While most of the electrons are in this low-energy part of the spectrum—and have a relatively high angular distribution—there is a well-collimated "hot tail" of electrons whose energy extends beyond 200 MeV and whose angular distribution is < 2º.
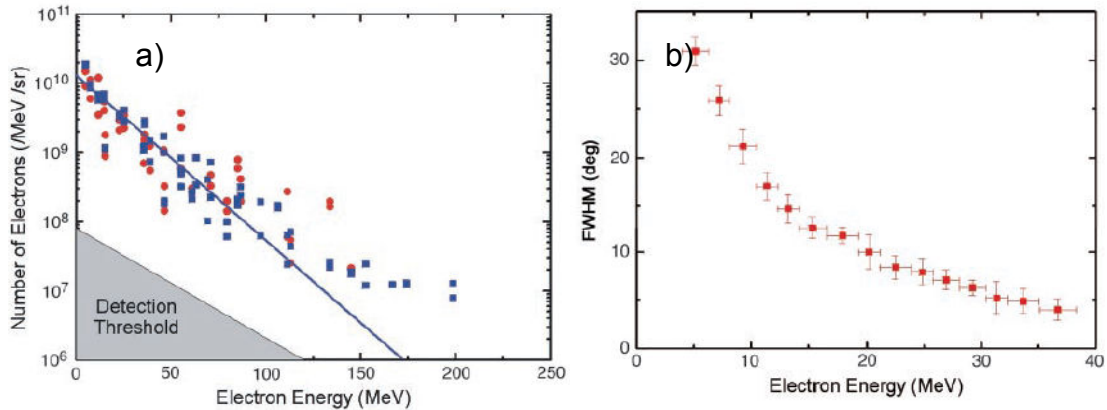
Figure 2.2: Electron spectra from an early FLWF experiment[82]. a) Electron spectra at two plasma densities, $n_e = 2.5 \times 10^{19}$ cm^{-3} (blue squares) and $n_e = 6 \times 10^{19}$ cm^{-3} (red circles). The line represents electrons of energy <130 MeV, for which an effective temperature of 18 MeV is obtained via exponential fit. b) Angular distribution of the accelerated electrons as a function of energy.

2.2 SHORT-SCALE INJECTION SCHEMES AND THE "DREAM BEAM"

Most of the early experiments involving electron acceleration by LWFAs (including self-modulated LWFAs) produced what might be called "low quality" electron bunches. The typical accelerated electron bunch might have total charge ~nC, but the energy spectrum itself was characterized by an exponential distribution whose tail might achieve 10's of MeV but whose typical energy was ~1's of MeV. For example, Fig. 2.2a shows a typical energy spectrum for accelerated electrons prior to the advent of the various short-scale injection schemes discussed in Chapter 1 (Sec. 1.3): the electron energy distribution is approximated by an exponential distribution. The effective temperature of this distribution is 18 MeV, but the tail of the measured electrons' spectrum reached >200 MeV, and the total energy spread exceeds 100%.

However, several experiments which utilized short-scale injection schemes (e.g. self-injection in the bubble regime) were published simultaneously in *Nature* in 2004. These experiments produced relatively high-energy collimated electron beams with low energy spread and high charge: the "dream beam" had arrived.

2.2.1 Bubble Regime Acceleration at RAL

The first (by page order) of these experiments took place at Rutherford's Appleton Laboratory[83] ("RAL"). The laser in question (Astra) was a 40 fs, 0.5 J laser which was focused to a relatively large spot size, $w_0 = 25$ μm ($Z_R \sim 2.5$ mm) so that the acceleration would be limited by dephasing length rather than diffraction. They used a plasma of

length 2 mm and density 3×10^{19} cm^{-3} < n_e < 5×10^{19} cm^{-3}, so the pulse duration was comparable to the plasma wavelength: 0.33 τ_{LC} < λ_P < 2 τ_{LC}. They were therefore operating in the FLWF regime, and in fact achieved bubble-regime self-injection (see Chapter 1, Sec. 1.3.1), which resulted in a very low electron energy spread, as shown in Fig. 2.3. Although this experiment achieved the lowest peak electron energy—varying between 50 and 80 MeV peak due to fluctuations in the laser parameters—of the three experiments, it is especially noteworthy for its small energy spread, which was ±3 % of the peak electron energy. This small energy spread was obtained when the laser pulse
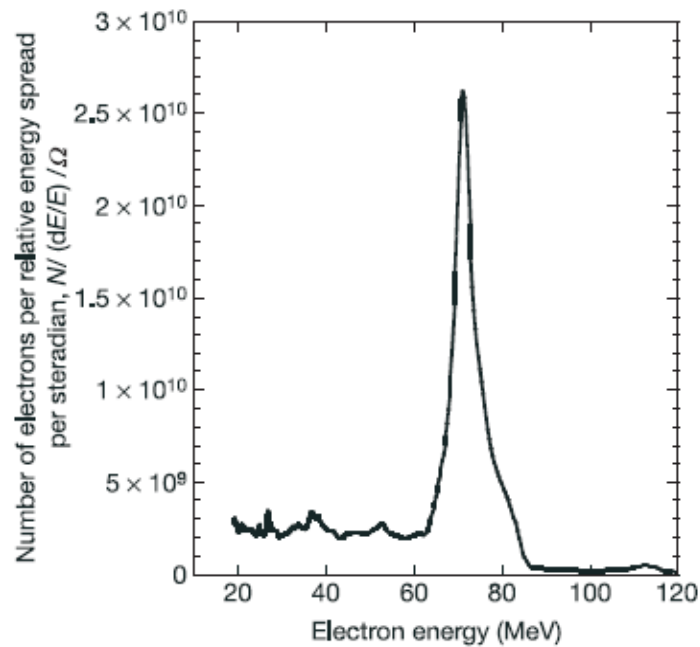
Figure 2.3: The measured electron spectrum of the bubble-regime experiment at the Rutherford Appleton Laboratory[83]. A 500 mJ, 40 fs laser was focused to a spot size of 25 mm on a plasma of density 2×10^{19} cm^{-3}, resulting in an electron beam energy of 75 MeV with an energy spread of 3%.
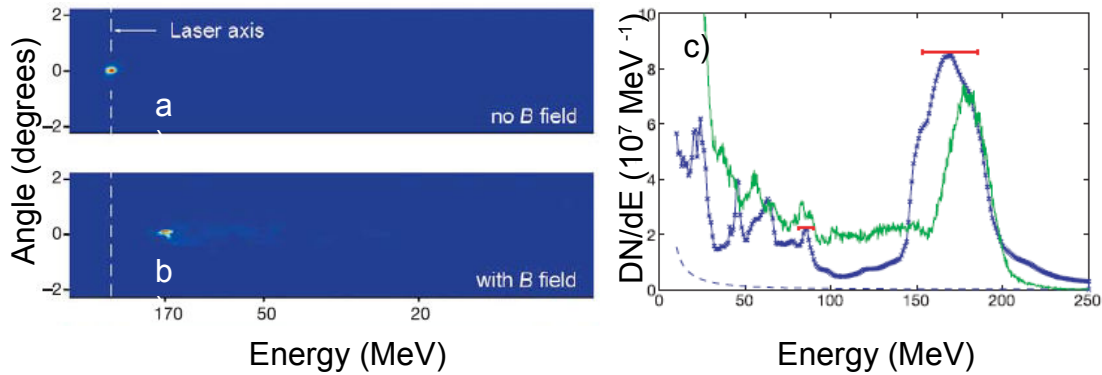
Figure 2.4: Images obtained on a LANEX screen[84] of a) the electron beam spatial distribution with no magnetic field applied, b) the energy distribution of the electron beam under the same conditions with a magnetic field applied, corresponding to 170 MeV, and c) an energy spectrum (lineout) of the beam in b), where the blue line is the experimentally obtained result, the green line is a result obtained from a 3D PIC simulation, and the red horizontal bars are error bars imposed by the resolution of the energy spectrometer used. The dashed line in this case is the estimated background level. In b) the horizontal axis represents electron energy, and the vertical axis represents the electron beam's divergence.

length was less than the plasma wavelength—a condition for bubble regime self-injection.

2.2.2 Bubble Regime Acceleration at LOA

The group operating at the Laboratoire d'Optique Appliquee[84] ("LOA") also utilized the bubble-regime to generate quasi-monoenergetic electron beams. The LOA experiment used a 1J, 33 fs laser centered at 820 nm and focused to 21 μm FWHM, which was focused onto a 3 mm long gas jet producing a plasma density of $6 - 7.5 \times 10^{18}$ cm^{-3}. The laser duration was thus shorter than the plasma wavelength.

The electron energies obtained in this experiment are shown in Fig. 2.4. The energy of the beam ~2 times greater than that of the RAL experiment—170 MeV as per Fig. 2.4b and c—but it also has a higher energy spread, nearly 25% FWHM as per Fig 2.4c. The estimated total electron energy is 100 mJ, which means a conversion efficiency of 10% from laser energy to electron energy.

2.2.3 Plasma Channel Guiding and Quasi-Monoenergetic Electrons at LBNL

The third group of the "dream beam" trio was at Lawrence Berkeley National Laboratory (LBNL)[85], and utilized pre-formed plasma channels to realize quasi-monoenergetic electron bunches. This experiment used a 9 TW laser centered at 810 nm and focused to a smaller spot size, 8.5 μm FWHM, which was focused on the entrance of a 1.7 mm long pre-formed plasma channel whose minimum density was on-axis of axial density 1.9×10^{19} cm^{-3}. In this experiment, the electron peak energy was up to 150 MeV, though the spectrometer could not resolve the energy spectrum of the electrons at this energy. A lower-energy shot is shown in Fig. 2.5, along with a comparison between a guided and an unguided pulse. This experiment was the first demonstration of the guiding of a laser pulse by a plasma channel, with the exit spot size being 24 μm after $z \sim 6Z_R$ when the preformed channel was present. The spot size was significantly larger than this without the channel, as a comparison between Figs. 2.5 a-d demonstrates. The electron bunch energy in this case was centered at 86 MeV with an energy spread of 2% (Fig. 2.5e); shot-to-shot energy fluctuations of roughly 15% were reported, due to fluctuations in the laser's initial parameters.
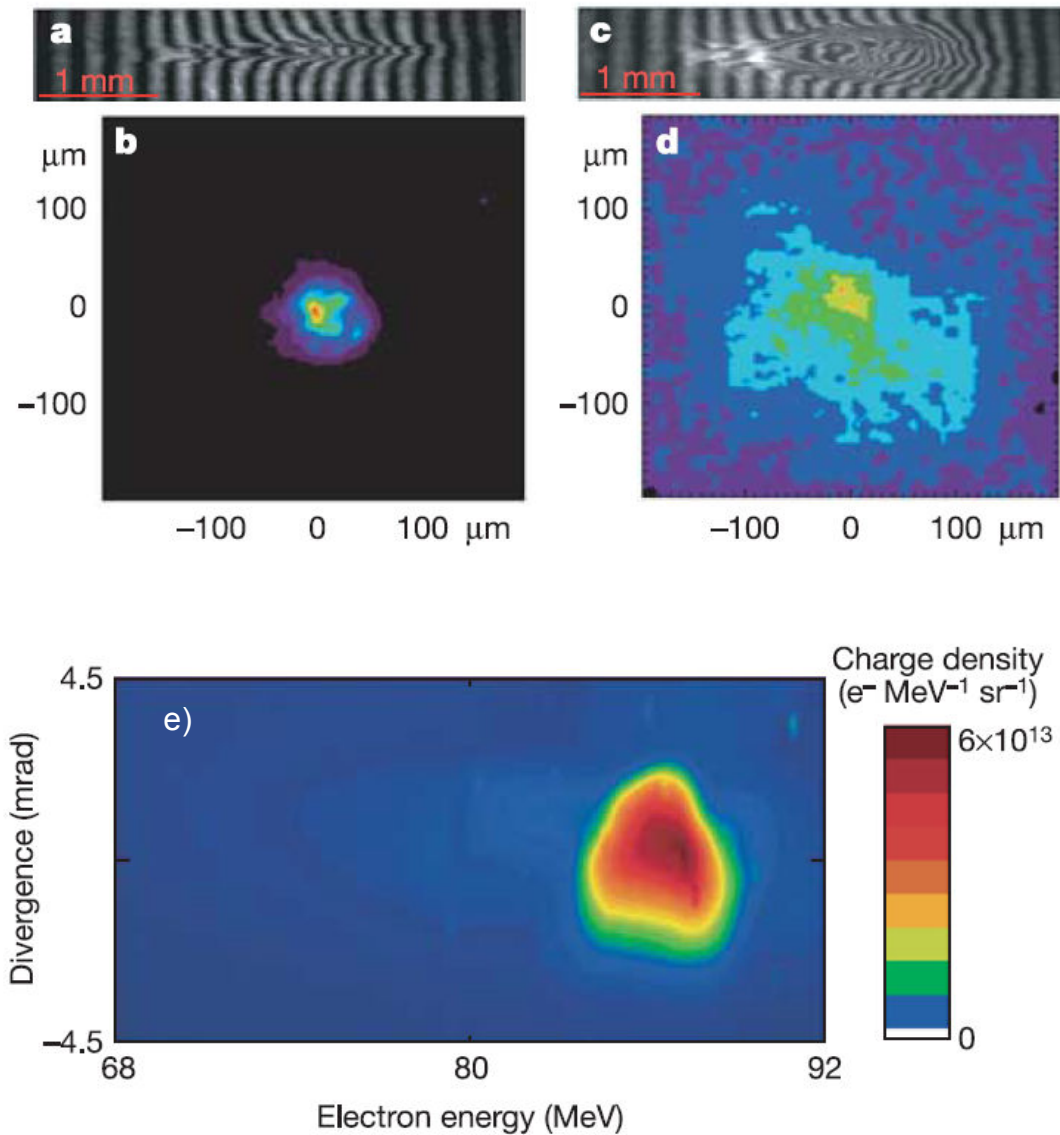
Figure 2.5: Guiding of the laser pulse and resultant electron beam energy[85]. a) Interferogram and b) laser exit mode when guided by a preformed channel; the laser spot at exit is nearly circular, indicating a cylindrically-shaped guiding channel. The mode here is well-defined with a FWHM of 24 µm. When the channel is off, c) the interferogram shows drive pulse blowout after ~few hundred microns, and d) the exiting laser mode is diffuse and several times larger than the guided mode. The channel also generates a well-defined and nearly monoenergetic electron beam e) as detected by a LANEX. The electron beam energy is centered in this case at 8 MeV with a spread of $\pm 2\%$. However, the electron beam energy could vary by $\pm 15\%$ from shot to shot.

59

2.3   COLLIDNG PULSE INJECTION

Another successful method of generating high-quality electron bunches was realized by the LOA group two years after the original "Dream Beam" trio[86] with the first demonstration of colliding pulse injection. The pump laser parameters in this experiment are 720 mJ at 820 nm with 30 fs pulse duration focused to a slightly elliptical 21 μm x 16 μm FWHM spot for an intensity of $I_{peak} = 3.4 \times 10^{18}$ W/cm² ($a_0 = 1.3$). The injection laser was similar, but with only 250 mJ and a larger more circular spot size of 31 μm FWHM, and a resulting peak intensity of 4×10^{17} W/cm² ($a_0 = 0.4$). In order to remove self-injection, the gas jet backing pressure was decreased so that the plasma density fell below the threshold for self-injection: $n_e \sim 7.3 \times 10^{18}$ cm⁻³.

When the injector pulse was orthogonally polarized with respect to the pump pulse, no electron injection was observed, though the LANEX image shows a low charge and high energy spread of accelerated electrons. Although the theory of colliding pulse injection discussed above (Chapter 1, Sec. 1.3.5) suggests that some electrons may be injected due to stochastic heating processes, the expected electron peak energy and charge are much lower for orthogonally polarized pump and injection beams, as shown in Fig. 1.10 (Chapter 1, Sec. 1.3.5). The injection pulse intensity in the LOA group's experiment does, however, exceed the threshold intensity for electron injection according to the theory discussed above.

On the other hand, if the injection pulse is parallel polarized with respect to the pump pulse, then electrons are injected and achieve peak energies as high as 250 MeV with energy spreads as low as 5% (the resolution limit of the spectrometer). However, the

electron beam charge is relatively low, from as high as 60-80 pC when the peak electron energy is < 100 MeV to as low as only 4-5 pC when the peak energy exceeds 200 MeV, an effect which will be briefly explained below.

This is falls far short of the charge produced in the quasi-monoenergetic self-injected bubble-regime accelerators reported in the earlier "dream beam" papers. The LOA group, for example, reported[84] charges of $0.5 \pm 02 \, nC$ at $170 \pm 20 \, MeV$: two orders of magnitude more charge than in the colliding pulse injection experiment. However, this charge far exceeds the charge of electrons of comparable energy obtained before the introduction of short-scale injection schemes, in which the entire energy spectrum would contain ~nC of charge, well over 99% of which is typically distributed among electrons of energy < 10 MeV.

A typical energy spectrum and a plot of the peak energy and energy spread as functions of collision position within the gas jet obtained are shown in Fig. 2.6. These results are obtained using parallel-polarization. The energy spectrum is centered at 115 MeV with a spread of 9%, which resulted from a collision of the pump and injector pulses in the middle of the gas jet. Both the peak energy obtained and the quality of the beam improve for earlier injection times, with a maximum beam energy of 250 MeV with spread 5% (at the resolution limit of the spectrometer) being observed when collision and injection occur near the entrance of the gas jet. The detection threshold of the spectrometer used to collect the data shown in Fig. 2.6b was 50 MeV. Another

spectrometer with lower resolution for high energy electrons was able to detect quasi-monoenergetic electron with energies as low as 15 MeV.

Controlling the position at which the two pulses collide in the gas jet therefore gives control of output electron energy. Thus, the colliding pulse injection scheme yields an electron beam whose energy is more easily tunable than the bubble self-injection accelerator. A collision and injection early in the gas jet means that the injected electrons will be accelerated for nearly the whole length of the gas jet, and thus will achieve higher energy than electrons injected near the exit of the gas jet, which have a comparatively short acceleration length. Provided that the gas jet is not longer than the dephasing, diffraction, or depletion lengths, the length of the gas jet remaining after the point of
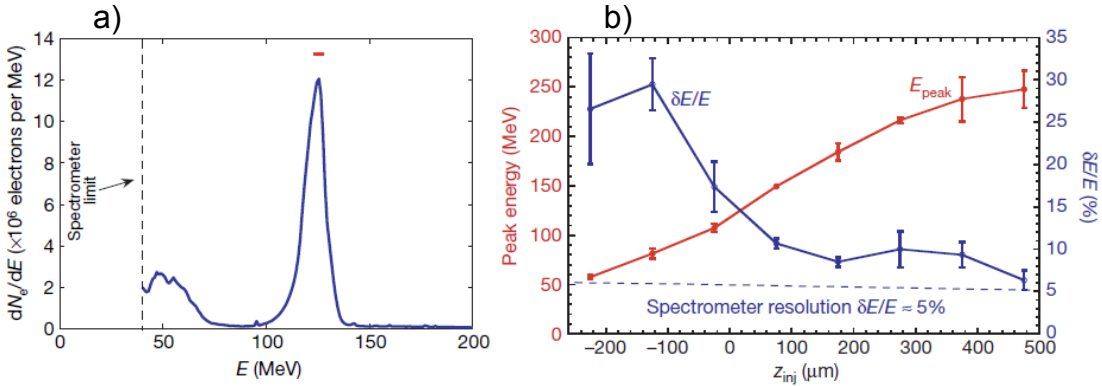
Figure 2.6: Energies of electrons accelerated in a colliding-pulse-injected LWFA[87]. a) A typical quasi-monoenergetic electron beam energy spectrum obtained by colliding the two pulses in the middle of the gas jet. The electron bunch energy is centered around 125 MeV with a spread of 9%, and results from the pulses' colliding in the center of the gas jet, corresponding to z_{inj} = 0 in b). The red line corresponds to the spectrometer resolution, which is 4% here. b) The electron energy spread (blue) and peak energy (red) are plotted as functions of the position at which the two pulses collide and injection takes place (z_{inj}) in the gas jet. The left side of the graph (z_{inj} < 0) is late injection, and the right side (z_{inj} > 0) is early injection. The gas jet is 1 mm long, with each point representing the average of 3-5 shots and the error bars representing the standard deviation.
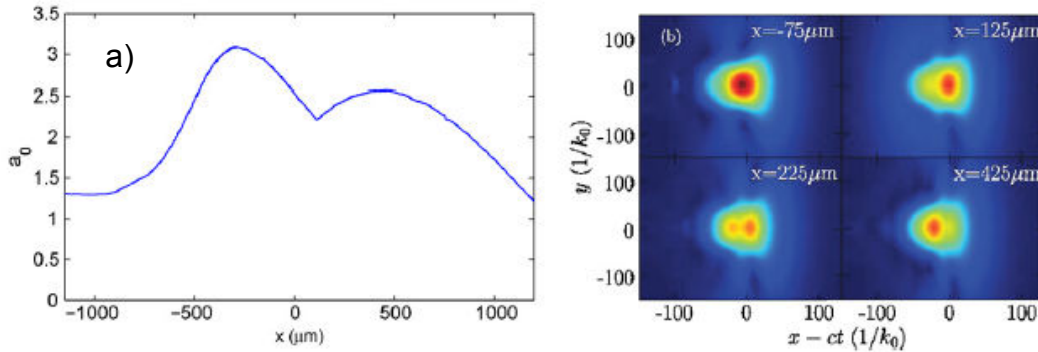
Figure 2.7: Pump pulse evolution in the plasma accelerator[87]. a) 3D PIC simulation of the pump pulse's normalize vector potential a_0 as a function of the pulse's propagation distance through the plasma. The pulse undergoes some self-guiding. b) The spatio-temporal evolution of the laser pulse as it propagates.

injection becomes the determining parameter of the electrons' acceleration length, and hence of their final energy.

In more recent experiments by the LOA group[87], the charge of the higher energy electron bunches were improved from ~4 pC at 200 MeV to ~13 pC at the same energy level. In this more recent experiment, the 2 mm gas jet was replaced with a 3 mm gas jet, and the counterpropagating injection pulse was shifted from being collinear with the ump pulse to counterpropagating but at a small angle, 4° with respect to the pump.

The decrease in electron bunch charge for earlier times and increase for bunch charge at later times can be explained by the laser pulses' spatial-temporal evolution. Initially, the pump pulse undergoes self-focusing, then it self-guides with a modulated amplitude. The result is that the maximum intensity slips backwards in the pulse as it propagates. This in turn leads to the laser's driving a wakefield which is distorted in such

63

a way that its potential well is steeper over a larger radius, thus in turn allowing it to trap more electrons. These effects in the laser pulse are shown in Fig. 2.7. The left plot, Fig. 2.7a, shows that the pulse undergoes self-focusing in the first part of the plasma, with the vector potential increasing from 1.3 to 3, and then thereafter the pulse defocuses slightly but is otherwise guided through the plasma. The right plots, Fig. 2.7b, show the mode's actual spatial-temporal evolution, with the peak intensity shifting backwards (to the left on the horizontal axis) in the pulse as it propagates.

2.4   ACCELERATION TO 1 GeV AND BEYOND

Achieving high-quality electron bunches is one important benchmark for tabletop accelerators to be practical. However, if they are to be useful for particle physics research, they must also produce high-energy electrons (and eventually, other types of particle clusters). In particular, free-electron lasers and synchotron facilities both need electrons with ~GeV energies. For example, the wavelength of a free-electron laser is given by[88]

$$\lambda_L = \frac{\lambda_u}{2\gamma^2}(1 + K^2)$$

(2.4.1)

where λ_u is the magnetic undulater spacing, K is the wiggler strength parameter, and γ is the relativistic Lorentz factor. Since K is typically small and the undulator spacing is of order 1 cm, a 1 nm x-ray laser requires $\gamma \sim 2000$, corresponding to an electron energy of ~1 GeV. The experiments so far described have produced electrons with energies of up to

250 MeV. However, higher electron energies have been obtained using tabletop accelerators.

There are three broad approaches which have been suggested for generating GeV-scale electrons in a LWFA, all of which seek to overcome the limitation imposed on accelerators by diffraction (see Chapter1, Sec. 1.4). The first is operating with petawatt-scale lasers with larger spot sizes. Since the Rayleigh range scales with the inverse of the minimum spot size, a larger spot size means a longer diffraction length; however, the larger spot size requires a much higher laser power to effectively drive the wakefield and access the bubble regime of self-injection. The second approach is to use self-guiding of the laser (e.g. relativistic self-focusing, which will be discussed in the next chapter) to overcome diffraction. However, if not controlled, this self-guiding instability can cause problems such as the filamentation of the laser mode. The third approach is to to use a waveguide for the laser pulse—for example, channel-guiding of the laser pulse, which can be accomplished over centimeter-scale channels.

2.4.1 Plasma Channel Guiding over Centimeter-Scales and Acceleration to 1 GeV

By using the third of the methods described above, the same group at LBNL which first demonstrated channel-guiding in the production of high-quality electron beams was then able to produce GeV electrons[89]. They used a 40 TW in 40 fs laser centered at 810 nm
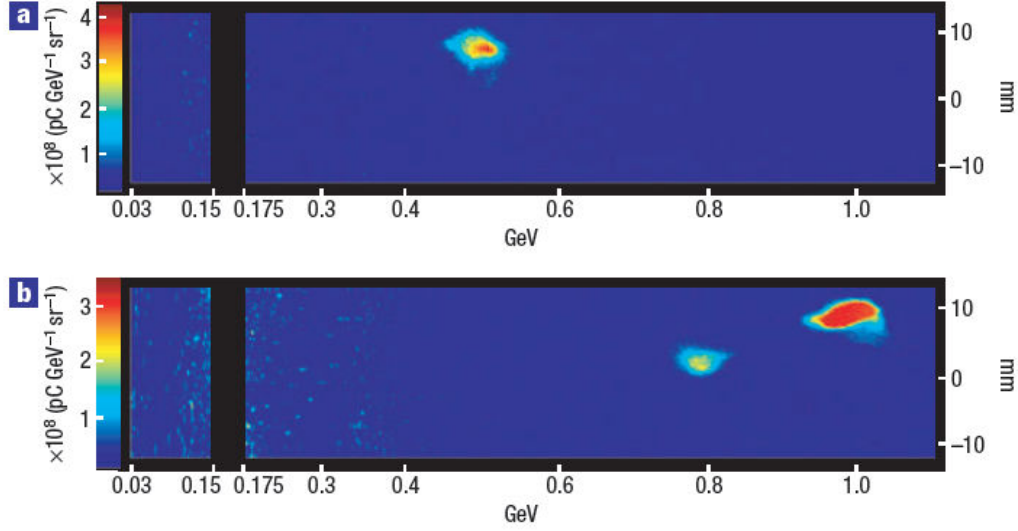
Figure 2.8: Single-shot electron beam spectra for a capillary-guided wakefield accelerator[89]. a) Electrons accelerated to 0.5 GeV with < 6% r.m.s. energy spread, 2.0 mrad divergence, and ~50 pC charge. b) Electrons accelerated to 1.0 GeV with < 3% r.m.s. energy spread, 1.6 mrad divergence, and ~30 pC charge. A second beam at 0.8 GeV is visible to the left of the main beam at 1.0 GeV, though it contains less charge than te main beam. Color indicates the amount of charge, horizontal axis the electron energy, and vertical axis the electron beam size from which the divergence can be obtained. The black band is the energy range not measured by the spectrometer.

and focused to a spot size of 25 μm at the entrance of a gas-filled capillary-discharge waveguide[90][91] to do this. The reason for this is that a lower-density plasma was needed to increase the dephasing length as per Eqn. (1.3.7): $L_{ph} \propto \lambda_P^3 \propto n_e^{-3/2}$.

However, the plasma channel itself was produced by using two pre-pulses—one to ionize the gas to form a plasma and the other to heat the plasma and form the channel. This process is inefficient at lower densities, and the LBNL group could not produce plasma channels without densities $n_e > 10^{19}$ cm^{-3}, which would then result in a shorter-than-desired dephasing length. The gas was therefore ionized and heated via electrode-discharge at the capillary ends, resulting in a parabolic plasma-channel in the capillary.

The resultant plasma had a density of 2.7-4.3×10^{18} cm^{-3}, and the electron acceleration took place over centimeter-scale lengths (the capillary was 3.3 cm long).

The electron spectra from two single shots are shown in Fig. 2.8. When using a capillary entrance diameter of 225 μm and a laser power of 12 TW (73 fs)-18 TW (40 fs) with a plasma density of 3.2-3.4×10^{18} cm^{-3}, the result was a beam of ~monoenergetic (<6% energy spread) 0.5 GeV electrons. When the laser peak power was increased to 40 TW and the capillary entrance diameter to 310 μm with a 4.2×10^{18} cm-3 density, the energy of the electrons increased to 1 GeV. These had a measured spread of 2.5%, though the actual energy spread may be possibly lower, since this was approximately the resolution limit of the spectrometer. Also, at this power level, the peak electron energy fluctuated significantly from shot to shot with changes in the laser and plasma parameters: injection and self-trapping are sensitive to both as the plasma approaches the bubble regime as discussed in Chapter 1 (Secs. 1.2.3 and 1.3.1).

Other groups using similar set-ups (gas-channel guiding) have also attained GeV-scale electrons[92],[93],[94],[95].

2.4.2 Petawatt-Driven Acceleration to 2 GeV

Petawatt-driven laser wakefields have also been used to accelerate electrons to high energy[96]. The Texas Petawatt (TPW)[97],[98] laser has been used to successfully demonstrate the acceleration of electrons to multi-GeV energies[99]. The TPW at peak capacity delivers one shot per hour of energy 170 J and duration 150 fs (1.1 PW power)

at a wavelength of 1057 nm, and is focused by a spherical mirror tilted 1° off-axis onto a

gas cell; the target plasma has a low density, 2.1×10^{17} cm^{-3} < n_e < 6.0×10^{17} cm^{-3}, an
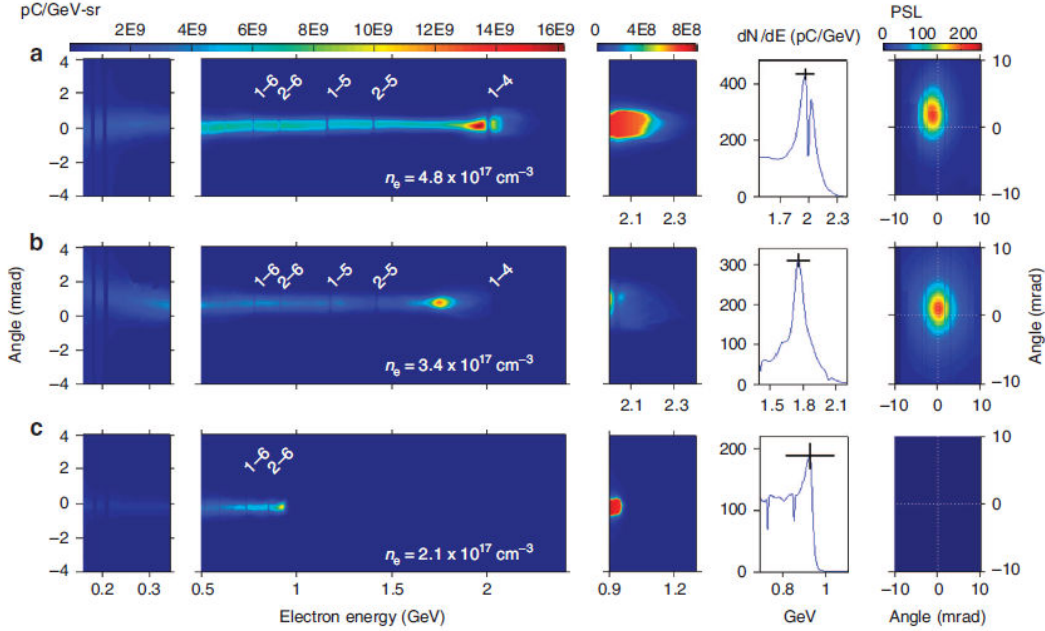
Figure 2.9: Single-shot electron spectra and betatron profiles for three different plasma densities on the TPW[99]. These are recorded on a set of imaging plates (one for high-energy electrons and x-rays, the other for low-energy electrons) to which the electrons are deflected in the presence of a magnetic field. Density is decreased in descending order: a) $n_e = 4.8 \times 10^{17}$ cm^{-3}, b) $n_e = 3.4 \times 10^{17}$ cm^{-3}, and c) $n_e = 2.1 \times 10^{17}$ cm^{-3}. The columns represent low energy < GeV electron spectra (first column), higher energy > GeV electron spectra (second column), a detailed view of the high-energy tail in the electron spectrum (third column), a vertically integrated lineout of the electron energy peak (fourth column), and the betatron angular distribution. The shadows in the electron spectra are from fiducial wires, which are labeled, and which are used to help determine the trajectory of the electrons (and hence their energy). In the first three columns, vertical axis represents angular distribution, with 0 mrad being the average position of GeV electron for a 30-shot sequence and horizontal axis represents electron energy. Unlike the electrons, the betatron x-rays do not deflect from the axis of propagation in the presence of a magnetic field, so the horizontal and vertical axis in the fifth column represent horizontal and vertical divergence of the x-rays.

order of magnitude lower than the density in the previous GeV electrons experiment. The effects of this low-density plasma are that the laser is sufficiently short to access the bubble regime and its self-injection, and also that the dephasing length of the plasma accelerator is very long.

This experiment produced a number of results. The most significant are shown in Fig. 2.9. These include the acceleration of electrons to peak energies of up to 2 GeV, and the observation of collimated transverse betatron x-ray radiation at ~25 keV which are produced by the oscillations of the accelerating electrons. Additionally, the electrons were highly collimated, with a typical FWHM divergence of < 1 mrad and shot-to-shot pointing stability of 1.4 mrad r.m.s. over dozens of shots. Furthermore, this self-injection and acceleration to high energy occurs despite a poor laser focus: as discussed in Chapter 1 (Secs. 1.2.3-1.3.1), the focal profile and beam spot evolution can drastically affect the dynamics of bubble formation and self-injection.

The electron energy was determined as in previous experiments by electron deflection in the presence of a strong magnetic field. However, because high-energy electrons will have a small deflection, and because electrons can leave the accelerator at a variety of angles, an additional step was necessary to separate the effects of of beam pointing, beam divergence, and beam deflection. One method of separating these parameters is to use two image plates rather than one[95][100]: the image plates are separated by a known distance, so that electrons' trajectory can then be tracked by noting position on each plate and solving for the relativistic equations of motion in the presence of a

strong magnetic field. This two-plate method assumes that all electrons originate from the laser axis at the gas jet axis—the initial deflection angle of the electron can then be solved for, and then the energy determined based on further deflection by the magnet.

The TPW experiment modified this two-plate measurement by replacing the first plate (between plasma exit and second image plate) with a pair of arrays of thin tungsten-wire fiducials. These cast identifying shadows on the detecting image plate (see Fig. 2.9; fiducial shadows are labeled in second column). These fiducial wires allow for determination of both initial deflection at the exit from the accelerator, as well as actual initial transverse position of the electrons, thus eliminating the need for the assumption that electron originate on the laser's axis at plasma exit. With this information, the electron energies can be determined. Therefore, the electron peak energy was determined to be as high as 2 GeV with a high-energy tail up to 2.3 GeV.

2.5   DOUBLING SLAC: 85 GEV ELECTRONS FROM A WAKEFIELD ACCELERATOR

Achieving 2.3 GeV maximum electron energy and the 2 GeV peak energy are both records for LWFA, but it is worth noting another experiment which achieved higher energy still. A group at the Stanford Linear Accelerator (SLAC) used an electron beam accelerated to 42 GeV by a a convention 2-mile long RF accelerator to drive a plasma wakefield, which then accelerated the tail of that drive beam to as much at 85 GeV[101]. This experiment makes use of a plasma wakefield accelerator (PWFA), meaning that the

wakefield is driven by a charged cluster rather than a laser—but it illustrates nicely the capabilities of plasma-based accelerators. It also begs the question: why not with LWFA?

2.5.1 The Experiment at SLAC: Doubling the Output of a Conventional RF Accelerator with PWFA

In this experiment, the driving electron beam exits the RF accelerator with a nominal duration of 50 fs, an energy of 45 ± 1.5 GeV, and a total of ~1.8×10^{10} particles. It then enters a lithium vapor plasma of density $n_e = 2.7\times10^{17}$ cm^{-3}. The electrons exiting the plasma were then imaged in two planes to resolve energy (measured via magnetic spectrometer) effects from initial divergence angles (see Sec. 2.4.2 and references[95],[100]). The observed energy spectrum is shown in Fig. 2.10. The image was taken at the second image plane, at which the energy dispersion is higher and the camera lens has a greater magnification compared to plane 1: in other words, this image is taken in the plane with greater energy resolution.

Both the peak energy (the head of the beam, which is not accelerated) and the highest energy electrons are resolved in this image. However, the core of the pulse loses energy in driving the plasma wake, and so many electrons are not present on the image plate in this second plane. The minimum energy measured on the earlier plate was 5-7 GeV. The high-energy tail of the accelerated electrons reached 100 GeV, with the highest energy reported as $85\pm7\,\mathrm{GeV}$, more than double the 41 GeV of the accelerated electrons in the pulse's trailing tail.
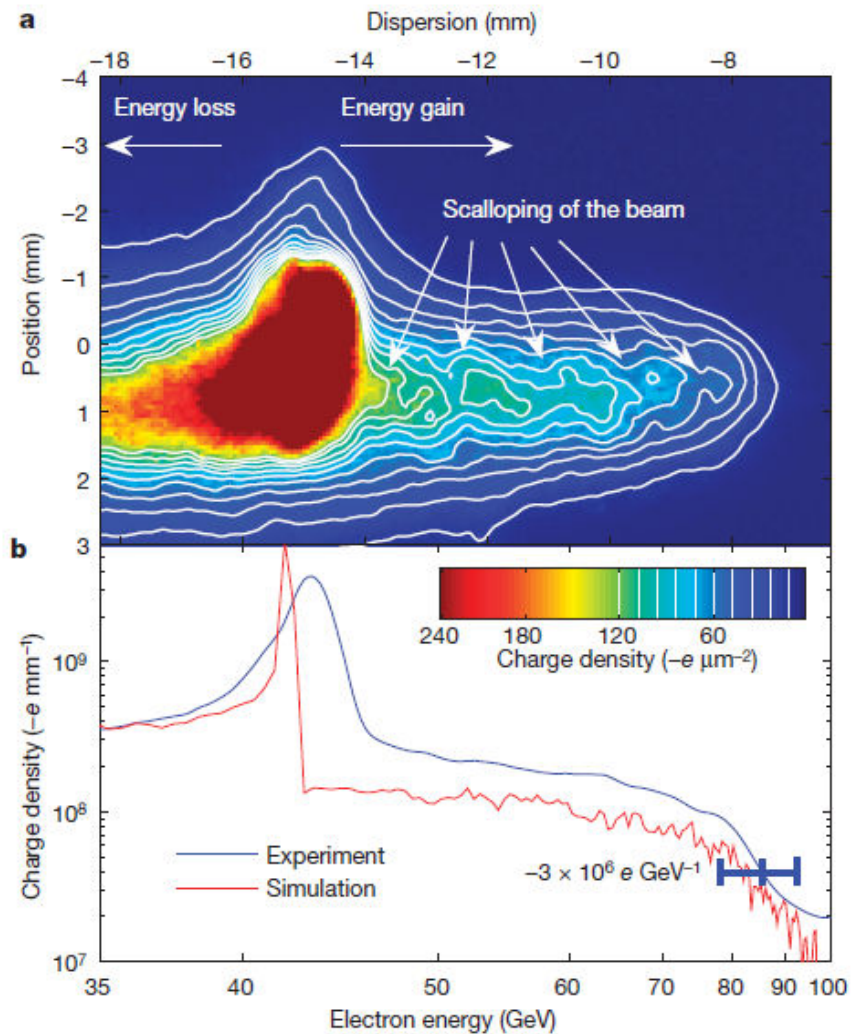
Figure 2.10: The energy spectrum of the electrons after the PWFA[101]. a) Energy spectrum of the electrons in the 35-100 GeV range. Dispersion (top axis) is inversely proportional to particle energy (bottom axis): high-energy electrons are deflected less by the magnet than low-energy electrons. The head of the pulse is mostly unaffected, and is centered at 43 GeV. The core of the pulse has lost much of its energy and is dispersed out of the field of view of the camera. The particles at the back of the bunch are accelerated by the PWFA, and obtain energies of up to 85 GeV. The pulse scalloping is consistent with an energy-dependent betatron phase advance. b) Energy lineout of the image in a), shown in blue. The red curve is the simulated energy spectrum, which does not take into account the initial energy spread of 1.5 GeV. The horizontal error bar is due to uncertainty in initial deflection angle and beam spot size.

72

This PWFA is operating in the blowout regime, which behaves almost exactly the same as the bubble regime described in Chapter 1 (see, Secs. 1.2.3 and 1.3.1). The density of the electrons in the driving pulse exceeds that of the background plasma, so electrons are blown out radially from the region surrounding the electron pulse. The heavier ions remain in this region, and some of the expelled electrons move along the the blowout sheath to the rear of the region, from which they are injected. The ion column, for its part, acts to keep these injected electrons focused. However, there is a key difference between the blowout regime of a PWFA and the bubble regime of a LWFA: in the PWFA blowout regime, the driving pulse is a high-density electron cluster. The reason that this is significant is that the injected electrons experience a varying longitudinal field due both to the presence of the electron pulse driving the wake and the high-density electron "wall" at the back of the blowout.

The result is that the core of the electron pulse is decelerated, but its tail (trailing edge) is accelerated. Furthermore, the accelerated electrons are focused by the ion column, but attempt to defocus (analogous to diffraction), which sets up a transverse oscillation in the size of the accelerated electron beam as it propagates through the plasma—this is betatron oscillation, from which come the x-rays mentioned in the TPW experiment (Sec. 2.4.2).

The length of the plasma accelerator was in this case 85 cm; when it was increased to 113 cm, the maximum energy decreased from 85 GeV to only 71 GeV. The reason for this is that in the early stages of propagation, the electrons are effectively self-

focused: the PWFA operates in the blowout regime, such that the main electron pulse is in a region essentially devoid of other electrons, but filled with ions. These ions provide a focusing force for the electrons of the drive pulse. However, as the pulse propagates, the head of the electron pulse erodes. Because the head is not focused by the ion column, which is behind it, the head expands as it propagates; this expansion decreases the beam density and hence its resulting electric field, so that the electric field of the leading edge of the electron pulse falls below the threshold necessary for ionization. In essence, acceleration is being limited due to diffraction, and so the 85 cm length over which the maximum energy is obtained is equivalent to the Rayleigh range which limits an optical pump (see Eqn. 1.3.9 in Chapter 1).

The increased size of the electron head leads to a distortion of the ionization front and then to a "blurring" of the position at which the electrons to be injected arrive on-axis, an effect known as "phase-mixing." This both reduces the peak accelerating field and causes some defocusing of the most highly accelerated electrons. Therefore, the energy of the accelerated electrons increases more-or-less linearly with accelerator length until it reaches an energy of 80 GeV at 70 cm; phase-mixing causes the energy to saturate at about 85 GeV after 85 cm, and then as the head of the electron pulse erodes the highest-energy electrons are lost and the maximum electron energy begins dropping. After about 104 cm, simulations show that the core of the electrons has been completely eroded away so that no wakefield remains. It is worth noting again that this is an effect of beam erosion: this limit is equivalent to reaching an acceleration limit due to diffraction and not pump depletion, since the electron pulse energy is still considerable at this point.

2.5.2 Considerations, Challenges, and Obstacles to Using a LWFA

There are a number of challenges to duplicating this "booster" accelerator using a LWFA. These include overcoming diffraction, dephasing, and depletion; and synchronizing the arrival of the electrons to be accelerated with the phase of the accelerating wakefield. The first three challenges effectively limit the length of the LWFA, and the fourth must be resolved if the accelerator is to further accelerate the injected electrons rather than decelerating them.

As has been mentioned above (see Sec. 2.4.2, and Chapter 1, Sec. 1.5), the dephasing length can be extended by decreasing the plasma density. However, this also will decrease the accelerating electric field of the wakefield (see Chapter 1, Sec. 1.2). Furthermore, guiding of a laser pulse become difficult over long distances without self-focusing (see Chapter 3, Sec. 3.3.2 for more details), the critical power for which is:

$$P_{cr} = 16.2 \times \left(\frac{\omega_L}{\omega_p} \right)^2 [GW] \qquad (2.5.1)$$

Thus, at the plasma density used in the original PWFA experiment, $n_e = 2.7 \times 10^{17}$ cm^{-3}, and assuming a Ti:Sapph laser (800 nm), the critical power for self focusing would be ~105 TW. This is not an unreasonable laser power, and can easily be attained by commercially available laser systems. However, such a laser would tend to both defocus due to ionization and deplete over such a long propagation distance. The ionization defocusing could be mitigated by pre-ionizing the plasma, and the beam depletion by

increasing the laser's available power. However, the self-focusing would almost certainly lead to filamentation and beam break-up (see Chapter 3, Sec. 3.3) over length scales of 100 cm.

On the other hand, a high-density plasma offers the advantages of requiring a lower laser power to self-guide (e.g. by self-focusing), and furthermore will have a larger accelerating field. For example, a plasma with density $n_e = 1.25 \times 10^{19}$ cm^{-3} will have a critical power for self-focusing of only 2.3TW. On the other hand, pump depletion and the dephasing length will both decrease.

As an alternative to self-focusing (which is an instability whose behavior is dependent on small variations in the laser phase front), the laser can be given a slower focus with a correspondingly larger spot size. However, the laser power would then need to be increased to maintain intensity (and thus a_0), which in turn makes the likelihood of catastrophic self-focusing even greater.

One possible solution to the dephasing problem is to borrow a concept from nonlinear optics: quasi-phasematching. Rather than using a single LWFA, in which the electrons will dephase over a long length scale (not too mention that the laser will diffract), the electrons could be accelerated in several shorter stages with higher plasma densities. Provided that each stage is independently pumped and that the electrons are injected in-phase with each, the electrons will gain a small amount of energy with each stage.

There are a few remaining drawbacks to this approach. The first is that it would require that the pump beam be split into several lines, one for each stage, and thus would

either require many pump lasers or a single very high power laser; for example, a channel-guided laser accelerator in the style of Leemans *et al.* (Sec. 2.4.1 and reference [89]) could use a system of 100 x 15 TW beam lines—a total of 1.5 PW—to achieve ~50 GeV worth of acceleration (0.5 GeV per line). The second is that it would likely require a fairly complex system to guide both the accelerated electrons and the pumping beam to each sequential stage; either a series of magnets could be used to steer the electrons (in which case the lowest energy electrons would be constantly culled: expect a low charge yield), or the laser and hence the accelerating field could be slightly nonlinear with the electrons, or the laser could be steered using mirrors with holes.

The third drawback is that the injected electrons would still need to be phase-matched with the accelerating plasma structure. One possible method for doing this will be discussed at the end of the next chapter.

Chapter References

[73] P. Chen, J.M. Dawson, R.W. Huff, and T. Katsouleas, "Acceleration of Electrons by the Interaction of a Bunched Electron Beam with a Plasma," *Phys. Rev. Lett.*, Vol. **54**, 693 (1985).

[74] J.B. Rosenzweig, D.B. Cline, H. Figueroa, W. Gai, R. Konecny, J. Norem, P. Schoessow, and J. Simpson, "Experimental Observation of Plasma Wake-Field Acceleration," *Phys. Rev. Lett.*, Vol. **61** No. 1 (1988).

[75] T. Tajima and J. M. Dawson, "Laser Electron Accelerator," *Phys. Rev. Lett.,* Vol. **43** No. 4 (1979).

[76] Y. Kitagawa, T. Matsumoto, T. Minamihata, K. Sawai, K. Matsuo, K. Mima, K. Nishihara, H. Azechi, K.A. Tanaka, H. Takabe, and S. Nakai, "Beat-Wave Exceitation of plasma Wave and Observation of Accelerated Electrons," *Phys. Rev. Lett.*, Vol. **68**, No. 1 (1992).

[77] P. Maine, D. Strickland, P. Bado, M. Pessot, and G. Mourou, "Generation of Ultrahigh Peak Power Pulses by Chirped Pulse Amplification" *IEEE J. Quantum Electron.*, Vol. **24** No. 2, 398 (1988).

[78] H. Hamster, A. Sullivan, S. Gordon, W. White, and R.W. Falcone, "Subpicosecond, electromagnetic pulses from intense laser-plasma ineteraction," *Phys. Rev. Lett.*, Vol. **71**, No. 17, 2725-2728 (1993).

[79] K. Nakajima, T. Kawakubo, H Nakanishi, A Ogata, Y Kato, Y Kitagawa, R Kodama, K Mima, H Shiraga, K Suzuki, T Zhang, Y Sakawa, T Shoji, Y Nishida, N Yugami, M Downer, D Fisher, B Newberger and T Tajima, "A proof-of-principle experiment of laser-wakefield acceleration" *Physica Scripta*, **T52**, 61 (1994).

[80] F. Amiranoff, S. Baton, D. Bernard, B. Cros, D. Descamps, F. Dorchies, F. Jacquet, V. Malka, J.R. Marques, G. Matthieussent, P. Mine, A. Modena, P. Mora, J. Morillo, and Z. Najmudin, "Observation of Laser Wakefield Acceleration of Electrons," *Phys. Rev. Lett.*, Vol. **81**, No. 5 (1998).

[81] K. Nakajima, D. Fisher, T. Kawakubo, H. Nakanishi, A. Ogata, Y. Kato, Y. Kitagawa, R. Kodama, K. Mima, H. Shiraga, K. Suzuki, K. Yamakawa, T. Zhang, Y. Sakawa, T. Shoji, Y. Nishida, N. Yugami, M. Downer, and T. Tajima,

"Observation of Ultrahigh Gradient Electron Acceleration by a Self-Modulated Intense Short Laser Pulse," *Phys. Rev. Lett.*, Vol. **74**, No. 22 (1995).

[82] V. Malka, S. Fritzler, E. Lefebvre, M.-M. Aleonard, F. Burgy, J.-P. Chambaret, J.-F. Chemin, K. Krushelnick, G. Malka, S. P. D. Mangles, Z. Najmudin, M. Pittman, J.-P. Rousseau, J.-N. Scheurer, B. Walton, A. E. Dangor, "Electron Acceleration by a Wake Field Forced by an Intense Ultrashort Laser Pulse," *Science*, Vol. **298**, 1596-1600 (2002).

[83] S. P. D. Mangles, C. D. Murphy, Z. Najmudin, A. G. R. Thomas, J. L. Collier, A. E. Dangor, E. J. Divall, P. S. Foster, J. G. Gallacher, C. J. Hooker, D. A. Jaroszynski, A. J. Langley, W. B. Mori, P. A. Norreys, F. S. Tsung, R. Viskup, B. R. Walton & K. Krushelnick, "Monoenergetic beams of relativistic electrons from intense laser–plasma interactions," *Nature*, Vol. **431**, 535-538 (2004).

[84] J. Faure, Y. Glinec, A. Pukhov, S. Kiselev, S. Gordienko, E. Lefebre, J.-P. Rousseau, F. Burgy, and V. Malka, "A laser-plasma accelerator producing monoenergetic electron beams," *Nature*, Vol. **431**, 541-544 (2004).

[85] C.G.R. Geddes, Cs. Toth, J. van Tilborg, E. Esarey, C.B. Schroeder, D. Bruhwiler, C. Nieter, J. Cary, and W.P. Leemans, "High-quality electron beams from a laser wakefield accelerators using plasma-channel guiding," *Nature,* Vol. **431**, 538-541 (2004).

[86] J. Faure, C. Rechatin, A. Norlin, A. Lifschitz, Y. Glinec, and V. Malka, "Controlled injection and acceleration of electrons in plasma wakefields by colliding laser pulses," *Nature*, Vol. **444**, 737-739 (2006).

[87] J. Faure, C. Rechatin, A. Ben-Ismail, J. Lim, X. Davoine, E. Lefebvre, V. Malka, "Physics of colliding laser pulses in underdense plasmas," *C. R. Physique,* Vol. **10**, 148–158 (2009).

[88] G. Neil and L. Merminga, "Technical approaches for high-average-power free-electron lasers," *Rev. Mod. Phys.*, Vol. **74**, 685-701 (2002).

[89] W.P. Leemans, B. Nagler, A.J. Gonsalves, Cs. Toth, K. Nakamura, C.G.R. Geddes, E Esarey, C.B Schroeder, and S.M. Hooker, "GeV electron beams from a centimetre-scale accelerator," *Nature Physics*, Vol. **2**, 696-699 (2006).

[90] D.J. Spence and S.M. Hooker, "Investigation of a hydrogen plasma waveguide," *Phys. Rev. E*, Vol. **63,** 015401 (2001).

[91] A. Buter, D.J. Spece, and S.M. Hooker, "Guiding of high-intensity laser pulses with a hydrogen-filled capillary discharge waveguide," *Phys. Rev. Lett.*, Vol. **89,** 185003 (2002).

[92] S. Karsch, J. Osterhoff, A. Popp, T.P. Rowlands-Rees, Zs. Major, M. Fuchs, B. Marx, R. Horlein, K. Schmid, L. Veisz, S. Becker, U. Schramm, B. Hidding, G. Pretzler, D. Habs, F. Gruner, F. Krausz, and S.M. Hooker, "GeV-scale electron acceleration in a gas-filled capillary discharge waveguide," *New J. of Phys.*, Vol. **9**, No. 11, 415 (2007).

[93] S. Kneip, S.R. Nagel, S.F. Martins, S.P.D. Mangles, C. Bellei, O. Chekhov, R.J. Clarke, N, Delerue, E.J. Divall, G. Doucas, K. Ertel, F. Fiuza, R. Fonseca, P. Foster, S.J. Hawkes, C.J. Hooker, K. Krushelnick, W.B. Mori, C.A.J Palmer, K. Ta Phuoc, P.P. Rajeev, J.Schreiber, M.J.V. Streeter, D. Urner, J. Vieira, L.O. Silva, and Z.Najmudin, "Near-GeV Acceleration of Electrons by a Nonlinear Plasma Wave Driven by a Self-Guided Laser Pulse," *Phys. Rev. Lett.,* Vol. **103**, No. 3, 035002 (2009).

[94] T.P.A. Ibbotson, N. Bourgeois, T.P. Rowlands-Rees, L.S. Caballero, S.I. Bajlekov, P.A. Walker, S. Kneip, S.P.D. Mangles, S.R. Nagel, C.A.J. Palmer, N. Delerue, G. Doucas, D. Umer, O. Chekhlov, R.J. Clarke, E. Divall, K. Ertel, P.S. Foster, S.J. Hawkes, C.J. Hooker, B. Parry, P.P. Rajeev, M.J.V. Streeter, and S.M. Hooker, "Laser-wakefield acceleration of electron beams in a low density plasma channel," *Phys. Rev. STAB*, Vol. **13**, No.3 031301 (2010).

[95] C.E. Clayton, J.E. Ralph, F. Albert, R.A. Fonseca, S.H. Glenzer, C. Joshi, W. Lu, K.A. Marsh, S.F. Martins, W.B. Mori, A. Pak, F.S. Tsung, B.B. Pollock, J. S. Ross, L.O. Silva, and D.H. Froula, "Self-guided laser wakefield acceleration beyond 1 GeV using ionization-induced injection," *Phys. Rev. Lett*. Vol. **105**, 105003 (2010).

[96] X.Wang, R. Zgadzaj, N. Fazel, S. A. Yi, X. Zhang, W. Henderson, Y.-Y. Chang, R. Korzekwa, H.-E. Tsai, C.-H. Pai, Z. Li, H. Quevedo, G. Dyer, E. Gaul, M. Martinez, A. Bernstein, T. Borger, M. Spinks, M. Donovan, S. Y. Kalmykov, V. Khudik, G. Shvets, T. Ditmire and M. C. Downer, "Petawatt-laser-driven wakefield acceleration of electrons to 2 GeV in 1017cm-3 plasma," *AIP Conf. Proc. AAC*, **1507**, 341-344 (2012).

[97] E. W. Gaul, T. Ditmire, M. D. Martinez, S. Douglas, D. Gorski, G. R. Hays, W. Henderson, A. Erlandson, J. Caird, C. Ebbers, I. Iovanovic, and W. Molander, "Design of the Texas Petawatt Laser," *OSA/QELS Conf. Proc.*, JFB2 (2005).

[98] Erhard W. Gaul, Mikael Martinez, Joel Blakeney, Axel Jochmann, Martin Ringuette, Doug Hammond, Ted Borger, Ramiro Escamilla, Skylar Douglas, Watson Henderson, Gilliss Dyer, Alvin Erlandson, Rick Cross, John Caird, Christopher Ebbers, and Todd Ditmire, "Demonstration of a 1.1 petawatt laser based on a hybrid optical parametric chirped pulse amplification/mixed Nd:glass amplifier," *J. Appl. Optics*, Vol. **49**, No. 9, 1676-1681 (2010).

[99] Xiaoming Wang, Rafal Zgadzaj, Neil Fazel, Zhengyan Li, S. A. Yi, Xi Zhang, Watson Henderson, Y.-Y. Chang, R. Korzekwa, H.-E. Tsai, C.-H. Pai, H. Quevedo, G. Dyer, E. Gaul, M. Martinez, A. C. Bernstein, T. Borger, M. Spinks, M. Donovan, V. Khudik, G. Shvets, T. Ditmire & M. C. Downer, "Quasi-monoenergetic laser-plasma acceleration of electrons to 2 GeV," *Nature Communications*, Vol. **4**, 2988 (2013).

[100] B.B. Pollock, J.S. Ross, G.R. Tynan, L. Divol, S.H. Glenzer, V. Leurent, J.P. Palastro, J.E. Ralph, D.H. Froula, C.E. Clayton, K.A. Marsh, A.E. Pak, T.L. Wang, and C. Joshi, "Two-screen method for determining electron beam energy and deflection from laser wakefield acceleration," *Proceedings of the 2009 Particle Accelerator Conference* (Vancouver, 2009).

[101] Ian Blumenfeld, Christopher E. Clayton, Franz-Josef Decker, Mark J. Hogan, Chengkun Huang, Rasmus Ischebeck, Richard Iverson, Chandrashekhar Joshi, Thomas Katsouleas, Neil Kirby, Wei Lu, Kenneth A. Marsh, Warren B. Mori, Patric Muggli, Erdem Oz, Robert H. Siemann, Dieter Walz, and Miaomiao Zhou, "Energy doubling of 42 GeV electrons in a metre-scale plasma wakefield accelerator," *Nature*, Vol. **445**, 05538, 741-744 (2007).

Chapter 3

A Survey of Laser-Plasma Instabilities and Other Nonlinear Interactions

Laser-plasma accelerators have a number of instabilities which can variously either enhance or disrupt the plasma wake and thus the particle accelerator. Such instabilities typically grow from background noise in the plasma but then couple to the laser-plasma interaction in such a way that they begin to grow exponentially. Additionally, many of these interactions find analogues in nonlinear optics.

3.1   RAMAN SCATTERING AND SELF-MODULATION

A photon which is not resonant with the plasma frequency cannot excite a plasma wave by direct absorption. Rather, it scatters from an electron in the plasma such that it is frequency-shifted by the plasma's frequency. If it excites further oscillation by the electron, then it undergoes a redshift $\omega_s = \omega_0 - \omega_p$. Therefore, a laser pulse propagating through a plasma will excite a wave via Raman scattering. The shifted photons can then beat with the unshifted photons at the plasma's resonant frequency, thus creating a positive feedback loop in which the plasma is further excited and the pulse further scattered. The laser pulse undergoes modulation and breaks up into shorter pulses whose

duration is that of the plasma length. Raman scattering is observed in other nonlinear media as a $\chi^{(3)}$ effect.

3.1.1 Raman Scattering in Nonlinear Media

Raman scattering was first predicted in 1923 by Adolf Smekal[102] and in 1928 it was independently observed and reported by C.V. Raman and K.C. Krishnan[103],[104], and by Grigory Landsberg and Leonid Mandelstam[105]. It is a nonlinear (χ_3) optical effect. Raman scattering may be spontaneous (random) or stimulated[106][107][108][109].

The basic physics of Raman scattering is straightforward: light is incident on a molecule which has energy levels l_1, l_2, and l_3. The light excites a transition from l_1 to a virtual level associated with l_2, which then relaxes to l_3. During this process, the exciting light is scattered in such a way that its frequency is shifted. If the level l_3 is higher than l_1, then the light's frequency is decreased (Stokes' shift), but if the level l_3 is lower than l_1, then the light's frequency is increased (anti-Stokes' shift).

The actual mechanism of this shift is the excitation (Stokes) or relaxation (anti-Stokes) of a molecular vibration. If the vibrational frequency is ω_v, then the corresponding frequency shifts will be $\omega_s = \omega_L - \omega_v$ for Stokes-shifts, and $\omega_s = \omega_L + \omega_v$ for anti-Stokes shift. Stimulated Raman scattering is a $\chi^{(3)}$ process which is automatically phase-matched, $\omega_S = \omega_S + \omega_L - \omega_L$.

83

Spontaneous Raman scattering can be understood in terms of the nonlinear polarization of the molecules in the Raman medium. A single molecule in an electric field is polarized according to

$$\tilde{p}(t)=\epsilon_0\alpha^{(1)}\tilde{E}(t), \ \chi^{(1)}=n\alpha^{(1)} \tag{3.1.1a}$$

where $\alpha^{(1)}$ is the linear molecular polarizability, $\chi^{(1)}$ is the linear susceptibility, and n is the number of molecules per unit volume. In a molecule which vibrates with frequency ω_v, the polarizability will have a component which similarly oscillates. This modification to the polarizability can be expressed as

$$\tilde{\alpha}(t)=\alpha_0+\left(\frac{\partial\alpha}{\partial q}\right)_0\tilde{q}(t) \tag{3.1.1b}$$

$$\tilde{q}(t)=qe^{-i\omega_v t}+q^*e^{i\omega_v t} \tag{3.1.1c}$$

where the motion of the vibrations has been expressed in (3.1.1c) as a deviation of internuclear distances at equilibrium spacing q_0. The upshot is that if Eqs. (3.1.1) are combined, then the polarization induced by an incident EM field at frequency ω_L will have Fourier components[110] $\omega_L + \omega_v$ and $\omega_L - \omega_v$:

$$\tilde{p}(t)=\epsilon_0\alpha_0 E e^{-i\omega_L t}+\epsilon_0\left(\frac{\partial\alpha}{\partial q}\right)_0 E\left(qe^{-i(\omega_L+\omega_v)t}+q^*e^{i(\omega_L-\omega_v)t}\right)+c.c. \tag{3.1.2}$$

In addition to the polarizability due to vibrations described in Eqn. (3.1.1c), the molecule may have an additional permanent dipole moment p_p due to its being asymmetric:

$$p_p(q)=\mu_p^0+\left(\frac{\partial p_p}{\partial q}\right)_0 q \tag{3.1.3}$$

84

The perturbation Hamiltonian for transitions between vibrational levels is then given by[111]

$$H'=-\vec{p}\circ\vec{E}=-\left[p^0_p+\left(\frac{\partial p_p}{\partial q}\right)_0+\epsilon_0\alpha_0 E_p+\epsilon_0\left(\frac{\partial \alpha}{\partial q}\right)_0 qE_p\right]E_p \tag{3.1.4}$$

where E_p is the component of the electric field which is parallel to the dipole moment. The second term in Eqn. (3.1.4) gives rise to direct infrared absorption, and the fourth term gives rise to Raman scattering. In other words, infrared scattering requires a change in the dipole moment of the molecule, and cannot occur in symmetrical molecules such as N_2 or O_2. Raman scattering, on the other hand, requires a change in the polarizability of the molecule:

$$H'_{Raman}=\epsilon_0\left(\frac{\partial \alpha}{\partial q}\right)_0 qE^2_\mu \tag{3.1.5}$$

Although spontaneous Raman scattering occurs from many laser modes into many Raman modes, it is easier to describe the process using a single Stokes mode. Spontaneous Raman scattering from a single laser mode into a single Stokes mode is governed by[111][112]

$$\frac{dm_S}{dt}=DP_a m_L(m_S+1)- DP_b m_S(m_L+1) \tag{3.1.6}$$

where m_s and m_L are the number of photons in the Stokes and laser modes (respectively), P_a and P_B are the probabilities of finding the Raman-active molecule in the ground or excited states (respectively), and D is a proportionality constant whose value depends on the physical properties of the Raman medium. The Stokes mode can considered as a wave

traveling in the z-direction with a velocity of c/η, where η is the refractive index. Alternatively, the Stokes' wave can be considered as the decay of the photons in the laser wave (total number of photons is conserved). Thus, the spatial growth rate of the Stokes wave and the spatial decay rate of the laser photon density can be written

$$\frac{dm_S}{dz} = \frac{-\ dm_L}{dz} = \frac{\eta}{c}\frac{dm_S}{dt} = \frac{\eta}{c}Dm_L(m_S+1) \tag{3.1.7}$$

In the limit where $m_S \ll 1$, there is a low occupation number of the Stokes mode, and Eqn. (3.1.4) becomes

$$\frac{dm_S}{dz} = \frac{1}{c/\eta}Dm_L z \tag{3.1.8}$$

which has the solution

$$m_S(z) = m_S(0) + \frac{1}{c/\eta}Dm_L z \tag{3.1.9}$$

for the case in which the Stokes and fundamental modes are co-propagating.

When $m_S \gg 1$, the number of photons in the Stokes mode is large and the equation (3.1.4) becomes

$$\frac{dm_s}{dz} = \frac{1}{c/\eta}Dm_L m_S \tag{3.1.10}$$

which for an undepleted input field has the solution

$$m_S = m_S(0)e^{Gz} \tag{3.1.11}$$

where $m_S(0)$ is the photon occupation number in the Stokes mode at the input to the Raman medium, which is equal to the quantum noise level if no Raman field is injected into the medium. These two limits represent spontaneous Raman scattering, in Eqns.

86

(3.1.8 and 3.1.9), and stimulated Raman scattering, in Eqns. (3.1.10 and 3.1.11). The Raman gain coefficient G in Eqn. (3.1.11) is given by

$$G = \frac{D m_L}{c/\eta} = \frac{8\pi^4 c^2 n}{\omega_S^2 h \omega_L \eta_S^2} \left(\frac{\partial^2 \sigma}{\partial \omega \partial \Omega} \right)_0 I_L \qquad (3.1.12)$$

where n is the number density of Raman active molecules, I_L is the intensity of the laser which is pumping the stimulated Raman scattering, σ is the scattering cross section considered as a function of optical frequency (ω) and scattering solid angle (Ω).

Stimulated Raman scattering can then lead to cascading: multiple higher order Stokes and anti-Stokes waves are present simultaneously. A complete description would require solving Maxwell's equations and a vibration equation containing all the frequencies of interest. To get 1 Stokes, need a pump (fundamental) and a Raman-active medium; getting the second Stokes' requires additionally either a 1 Stokes input wave or a population of molecular vibrators in the $v = 1$ state initially, with third Stokes in turn needs 2 Stoke and vibrators in the $v = 2$ state, etc. Therefore, the next best option to solving for multiple orders is to construct a model using the fundamental wave plus 1 Stokes and eventually 1 anti-Stokes (which is couple to the 1 Stokes' wave, as shall be shown below).

To do this, begin with a collection of n molecular harmonic oscillators per unit volume, which are independent of each other such they collectively won't support any wave with non-vanishing group velocity. Take these vibrators to be 1-dimensional, that is,

87

the internuclear spacing q has $\partial/\partial x = 0$ and $\partial/\partial y = 0$. Then the internuclear spacing will be modified by the molecular vibrations such that

$$\frac{d^2 q(z,t)}{dt^2} + \beta \frac{dq}{dt} + \omega_v^2 q = \frac{F(z,t)}{m} \tag{3.1.13}$$

The polarizability α has already been given in Eqn. (3.1.1b), and the dipole moment (polarization of a single molecule) in Eqn. (3.1.1a). The potential energy W stored in the induced dipole moment is given by

$$W = \frac{1}{2}\epsilon \vec{E} \circ \vec{E} = \frac{1}{2}\langle \vec{p} \circ \vec{E} \rangle = \frac{1}{2}\alpha \langle \tilde{E}^2(z,t) \rangle \tag{3.1.14}$$

Since the force is given by F = dW/dq, this means that the force driving the molecular oscillators is given by

$$\tilde{F} = \frac{1}{2}\left(\frac{d\alpha}{dq}\right)_0 \langle \tilde{E}^2(z,t) \rangle \tag{3.1.14}$$

If the total optical field is from fundamental and 1 Stokes waves, it might be expressed as

$$\tilde{E}(z,t) = A_L e^{i(k_L z - \omega_L t)} + A_S e^{i(k_S z - \omega_S t)} + c.c. \tag{3.1.15}$$

Combining Eqns. (3.1.14) and (3.1.15) yields a time-varying applied force which obeys

$$\tilde{F}(z,t) = \left(\frac{d\alpha}{dq}\right)_0 \left[A_L A_S^* e^{i[(k_L - k_S)z - (\omega_L - \omega_S)t]}\right] \equiv \left(\frac{d\alpha}{dq}\right)_0 \left[A_L A_S^* e^{i(Kz - \Omega t)}\right] \tag{3.1.16}$$

The polarization of a medium is given by the polarization of the molecules in the medium multiplied by the molecular density of the medium, P(z, t) = n p(z, t), so by combining Eqns. (3.1.1a) and (3.1.1b) we obtain the medium's polarization:

$$\tilde{P}(z,t) = n\left[\alpha_0 + \left(\frac{\partial\alpha}{\partial q}\right)_0 \tilde{q}(z,t)\right]\tilde{E}(z,t) \tag{3.1.17}$$

88

This total polarization has nonlinear component

$$\tilde{P}_{NL}(z,t)=n\left(\frac{\partial \alpha}{\partial q}\right)_0\left[q(\omega)e^{i(Kz-\Omega t)}+c.c.\right]\times\left[A_L e^{i(k_L z-\omega_L t)}+A_S e^{i(k_S z-\omega_S t)}+c.c.\right] \qquad (3.1.18)$$

Multiplying the exponentials (including complex conjugate terms) will yield four different frequency components: $\omega_L = \omega_L - \omega_S + \omega_S$, $\omega_S = \omega_S - \omega_L + \omega_L$, $\omega_A = \omega_L + \omega_{L} - \omega_S$, and $\omega_{2S} = \omega_S + \omega_S - \omega_L$. For our purposes, the most important of these is the 1 Stokes components, which comes from:

$$e^{i[(k_L-k_S)z-(\omega_L-\omega_S)t]}\times e^{-i(k_L z-\omega_L t)}=e^{-i(k_S z-\omega_S t)} \qquad (3.1.19a)$$

$$e^{-i[(k_L-k_S)z-(\omega_L-\omega_S)t]}\times e^{i(k_L z-\omega_L t)}=e^{i(k_S z-\omega_S t)} \qquad (3.1.19b)$$

This part of the nonlinear polarization oscillates at the Stokes frequency ω_S, and can therefore be called the Stokes polarization:

$$\tilde{P}_{NL}(z,t;\omega_S)=P(\omega_S)e^{i\omega_S t}+c.c. \qquad (3.1.20a)$$

$$P(\omega_S)=n\left(\frac{\partial \alpha}{\partial q}\right)_0 q^*(\Omega)A_L e^{ik_S z} \qquad (3.1.20b)$$

The term $q^*(\Omega)$ is the amplitude of the molecular vibration and is obtained by solving Eqn. (3.1.13) with the trial solution

$$\tilde{q}=q(\Omega)e^{1(Kz-\Omega t)}+c.c. \qquad (3.1.21a)$$

$$q(\Omega)=\frac{(1/m)[\partial \alpha/\partial q]_0 A_L A_S^*}{\omega_v-\Omega^2-2i\Omega\gamma} \qquad (3.1.21b)$$

The Raman susceptibility $\chi_R(\omega_S)$ can be defined by the equation

$$P(\omega_S)=6\chi_R(\omega_S)|A_L|^2 A_S e^{ik_S z} \qquad (3.1.22)$$

89
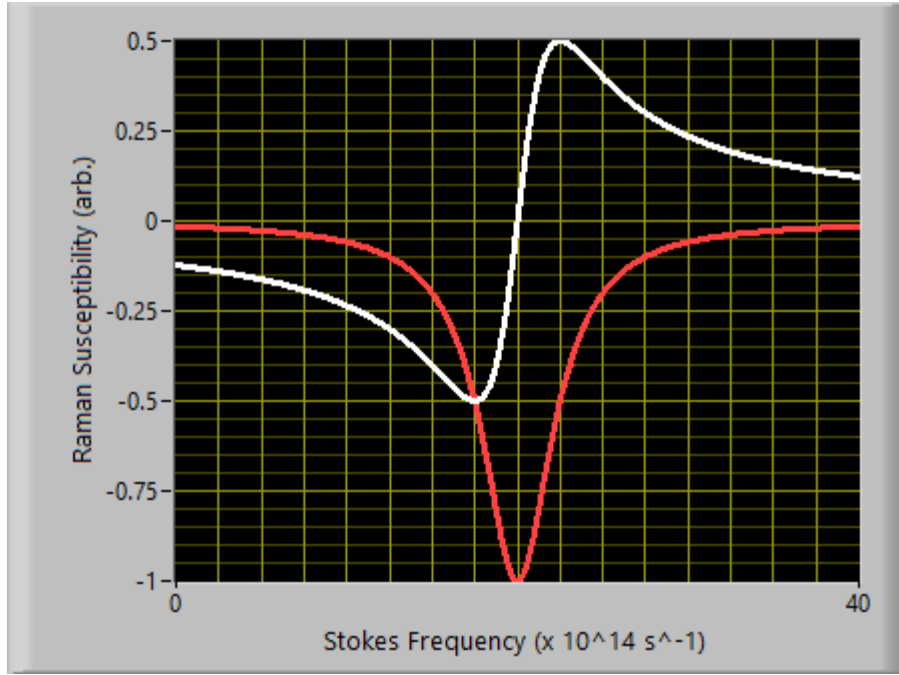
Figure 3.1: Real (white) and imaginary (red) parts of the Raman susceptibility. Both are normalized to the the peak of the imaginary part of the Raman susceptibility. The resonant frequency is $\omega_S = \omega_L - \omega_v = 2\times10^{15}$ s^{-1}, at which the imaginary part is negative and at its maximum value, and at which the real part has a value of 0. The FWHM of the imaginary part is determined by the damping term $\gamma = 5\times10^{14}$ s^{-1}.

which means that an expression for the Raman susceptibility can be found by combining Eqns. (3.1.20), (3.1.21), and (3.1.22):

$$\chi_R(\omega_S) = \frac{(n/6\mathrm{m})(\partial\alpha/\partial q)_0}{\omega_v - \Omega^2 - 2i\Omega\gamma} \tag{3.1.23}$$

The evolution of the field amplitude can now be solved as the wave propagates. Equation (3.1.22) gives the z-dependence of the Stokes polarization, so the Stokes' field's amplitude's evolution can be solved for in the slowly-varying amplitude approximated using:

90

$$\frac{d A_S}{dz} = - \Gamma_S A_S \qquad\qquad (3.1.24a)$$

where

$$\Gamma_S = - 12\pi i \frac{\omega_S}{\eta_S c} \chi_R(\omega_S) |A_L|^2 \qquad\qquad (3.1.24b)$$

is the Stokes absorption coefficient. Note that near the Raman resonance, the imaginary part of the susceptibility term $\chi_R(\omega_S)$ is large and negative, as shown in Fig. 3.1. This means that the real part of the absorption coefficient is also large and negative and that the solution to Eqn. (3.1.24a) is an exponential with a positive argument, that is, the Stokes wave will undergo exponential gain, as per Eqn. (3.1.11). Combining the solution to Eqns. (3.1.24) with Eqn. (3.1.23) yields

$$A_S = A_S(0) e^{G(\omega_S) z} \qquad\qquad (3.1.25)$$

with the gain coefficient $g(\omega_S)$ being the inverse of the real part of the absorption coefficient, so that

$$G(\omega_S) = \frac{k_S \epsilon_0 \left(\frac{\partial \alpha}{\partial q}\right)_0 n \beta |A_L|^2}{32 \eta_S^2 m \omega_v \left([\omega_v - (\omega_L - \omega_S)^2] + \beta^2/4\right)} \qquad\qquad (3.1.26)$$

It is now worth noting a few things about the anti-Stokes signal in passing. First, since the frequencies of first Stokes and first anti-Stokes are related through $\omega_L - \omega_S = - (\omega_L - \omega_A)$. The susceptibility for the anti-Stokes wave is related to the susceptibility of the Stokes wave described by Eqn. (3.1.23) by noting that the sign of the Ω term is reversed.

91

This yields that the susceptibilities of Stokes and anti-Stokes are actually related through $\chi_R(\omega_A) = \chi_R{}^*(\omega_S)$.

Second, the Stokes and anti-Stokes waves can both be generated via four-wave mixing such that the four-wave mixing susceptibilities are also complex-conjugate pairs: $\chi_A(\omega_A) = \chi_F{}^*(\omega_S)$. The total polarization at Stokes' frequency is thus ultimately given by[113]

$$P(\omega_S) = 6\chi_R(\omega_S)|A_L|^2 A_S e^{ik_S z} + 3\chi_F(\omega_S)|A_L|^2 A_a^* e^{i(2k_L - k_a)z} \tag{3.1.27}$$

where the four-wave mixing susceptibility is ultimately twice the Raman susceptibility, $\chi_F(\omega_S) = 2\chi_R(\omega_S)$. A consequence of this is that the Stokes and anti-Stokes waves are coupled, which is to say that their amplitudes obey

$$\frac{dA_S}{dz} = -\Gamma_S A_S + \kappa_S A_a^* e^{i(2\vec{k}_L - \vec{k}_S - \vec{k}_a)\vec{z}} \tag{3.1.28a}$$

$$\frac{dA_a}{dz} = -\Gamma_a A_a + \kappa_a A_S^* e^{i(2\vec{k}_L - \vec{k}_S - \vec{k}_a)\vec{z}} \tag{3.1.28b}$$

where the absorption (or gain) coefficient is defined as in Eqn. (3.1.24b)—keeping in mind that the susceptibility is for either Stokes or anti-Stokes as appropriate—and the coupling coefficients κ are defined by

$$\kappa_j = \frac{6\pi i \omega_j}{\eta_j c} \chi_F(\omega_j) A_L^2, \qquad j = S, a \tag{3.1.29}$$

It should be noted here in closing that the typical refractive index for a material with normal dispersion rises monotonically but not linearly with frequency, which means that the refractive index experienced by the laser will be less than the average of the refractive indices experienced by Stokes and anti-Stokes. As a consequence of this, perfect phase

matching can be achieved if the Stokes and laser waves propagate at some nonzero angle with respect to each other.

Another difference between stimulated Raman scattering and 4-wave mixing processes should be mentioned briefly here. In SRS, the gain is governed by the imaginary part of the third-order susceptibility. In other words,

$$P^{(3)}(\omega_S)=i\,\epsilon_0\,\Im\,[\chi^{(3)}(\omega_S;\omega_S,\omega_L,-\omega_L)]|E_L|^2 E_S \qquad (3.1.30a)$$

This is to be contrasted with the 4-wave mixing process, in which the nonlinear polarization is real:

$$P^{(3)}(\omega_S)=6\,\Re\,[\chi^{(3)}(\omega_4;\omega_3,-\omega_2,\omega_1)]E_1 E_2^* E_3\,e^{i(\vec{k}_1-\vec{k}_2+\vec{k}_3)\cdot\vec{r}-i\omega_4 t} \qquad (3.1.30b)$$

The implication[114] is that SRS is automatically phase-matches and therefore that the spontaneous signal spreads in a solid angle of 4π, and the stimulated signal sees referential gain in the direction determined by the pump laser. However, 4-wave mixing is not automatically phase-matched, and as a result the direction of the anti-Stokes (or amplified Stokes, for that matter) wave is determined by the directions of the other 3 waves used to generate it. Specifically, the phase matching condition for generating 1 anti-Stokes (ω_{AS}; ω_L, -ω_S, ω_L) requires that $\vec{k}_{AS}=\vec{k}_L+\vec{k}_L-\vec{k}_S$.

Some experimental results utilizing Raman scattering are presented and discussed in Chapter 4, since this is the basis for the second color in the two-color laser system.

3.1.2 Raman Scattering in Plasma

93

The mechanism for Raman scattering in a plasma is a plasma wave rather than a molecular vibration. The corresponding frequency shifts are therefore by the plasma's resonant frequency ω_p.

A plasma's resonant frequency must be smaller than the frequency of a laser if the laser is to propagate through it. If the laser frequency is less than the plasma frequency, $\omega_0 < \omega_p$, then the refractive index $\eta = 1 - (\omega_p/\omega_L)^2$ becomes negative, and the electrons "shield" the plasma from the laser's propagation: the incident laser pulse will therefore be reflected. The typical laser-plasma wakefield therefore involves an underdense plasma, with $\omega_L \gg \omega_p$.

Since the resonant frequency of the plasma is smaller than the laser's frequency, plasma waves cannot be driven resonantly by the laser pulse. Instead, the photons in the laser scatter from the electron wave in the plasma such that scattered photons undergo a frequency shift, $\omega_R = \omega_L - \omega_p$. This is Raman scattering, and may be sidescatter, forward Raman scattering (FRS, sometimes also abbreviated SFR or SRF), or backward Raman scattering (BRS, sometimes also SRB). The growth rate of BRS is generally greater than that of FRS; BRS has a growth rate Γ such that the number of e-fold increases of the instability $N_e = \Gamma t$ is given by[115]

$$N_e \simeq \left(a_0^2 k_p k_L / 8 \right)^{1/2} |\zeta|$$
(3.1.31)

where $\zeta = z - ct$. This is in the weakly-coupled regime; in the strongly-coupled regime, higher harmonics of the Raman backscatter may be generated, specifically in the odd harmonics. The stimulated Raman backscatter growth rate is[116]

$$\Gamma_{SHB} = \sqrt{3}\,\omega_L \left(\frac{\omega_p^2 F_l}{4\,\omega_L^2 \sqrt{1+a_0/2}} \right)^{1/3}$$

(3.1.32)

where F_l is the harmonic coupling function

$$F_l = \frac{(2l+1)a_0^2}{4\sqrt{1+a_0/2}} \left[J_l\!\left(\frac{(2l+1)a_0^2}{4\sqrt{1+a_0/2}} \right) - J_{l+1}\!\left(\frac{(2l+1)a_0^2}{4\sqrt{1+a_0/2}} \right) \right]^2$$

(3.1.33)

The photons undergoing FRS will propagate nearly collinearly with the photons of the fundamental laser pulse. Thus, the FRS photons and the fundamental photons will beat together with a beat frequency $\Omega = \omega_0 - \omega_R = \omega_p$. In other words, the frequency of the beat wave is resonant with the plasma electrons, and will therefore resonantly drive the electron wave by stimulating the scattering of the fundamental laser wave into the FRS wave.

If the laser pulse is considerably longer than the plasma wave, $\tau_l \gg \omega_p c$, the pulse will become modulated and eventually breaks up into a series of short pulse-packets. In essence, the refractive index (and thus the group velocity) decreases as electron density increases, so that in the regions where the electron density is at a peak, the group velocity is smaller than in regions where there is an electron density trough. The result is that the laser tends to become modulated in time so that the peaks of laser intensity are 90 degrees out of phase with the peaks of electron density—and this modulation drives the electron density perturbation still harder, resulting in even more scattering, thus setting up a positive feedback loop with increased growth of the instability.

I have so far described a three-wave mixing process for FRS, in which the pump laser field's fundamental frequency and wave vector (ω_L, k_L) depletes into first Stokes' light ($\omega_{1S} = \omega_L - \omega_p$, $k_{1s} = k_L - k_p$) and the plasma wake itself (ω_p, k_p). There also exists four-wave mixing processes from which can be generated first Stokes, plus first anti-Stokes ($\omega_{1A} = \omega_L - \omega_p$, $k_{1A} = k_L + k_p$), and higher-order Raman scattering (called cascading). Indeed, the four-wave FRS process actually exists in two regimes, a resonant one and a nonresonant one, so that there are three total regimes for FRS[116]. The corresponding regimes, temporal growth rates, and number of e-folding increases for these instabilities[115],[117],[118],[119] are shown in Table 3.1.

The resonant 4-wave mixing spatial growth rates for Stokes ($\Gamma_S = \omega_p^2 a_0 / \omega_p^2 8^{1/2}$) and for anti-Stokes ($G_{AS} = w_p^{3/2} a_0$) can be obtained from[120]

$$2 i k_0 \frac{\partial a_{AS}}{\partial z} = \frac{\omega_p^2}{c^2} a_0 \eta_e \frac{1}{1 + \omega_p/\omega_L} \tag{3.1.34a}$$

$$2 i k_0 \frac{\partial a_S}{\partial z} = \frac{\omega_p^2}{c^2} a_0 \eta_e \frac{1}{1 - \omega_p/\omega_L} \tag{3.1.34b}$$

The difference in sign between the two terms in the numerator on the far right-hand side of Eqns. (3.1.32 a and b) means that the Stokes signal will be larger than the anti-Stokes signal.

Type of FRS	Regime	Spatial Growth Rate	Number of e-foldings increase
3-wave mixing	$a_0^2|\zeta|/ct \ll 16\omega_p^5/\omega_L^5$	$\Gamma_3 = \omega_p a_0(\omega_p/\omega_L)^{1/2}$	$N_{e3} \approx 2\Gamma_3(|\zeta|/ct)^{1/2}$
Non-resonant 4-wave mixing	$16\omega_p^5/\omega_L^5 \ll a_0^2|\zeta|/ct \ll 2\omega_p^2/\omega_L^2$	$\Gamma_N = \dfrac{\sqrt{3}\,\omega_p}{2}\left(\dfrac{a_0\,\omega_p^2}{2\,\omega_L^2}\right)^{2/3}$	$N_{eN} \approx 1.5\Gamma_N(|\zeta|/ct)^{1/2}$
Resonant 4-wave mixing	$a_0^2|\zeta|/ct \gg 2\omega_p^2/\omega_L^2$	$\Gamma_R = \omega_p^2 a_0/(8\omega_L^2)^{1/2}$	$N_{eR} \approx 2\Gamma_R(|\zeta|/ct)^{1/2}$

Table 3.1: Regimes and growth of forward Raman scattering instability. Note that these are all obtained from 1D analysis.
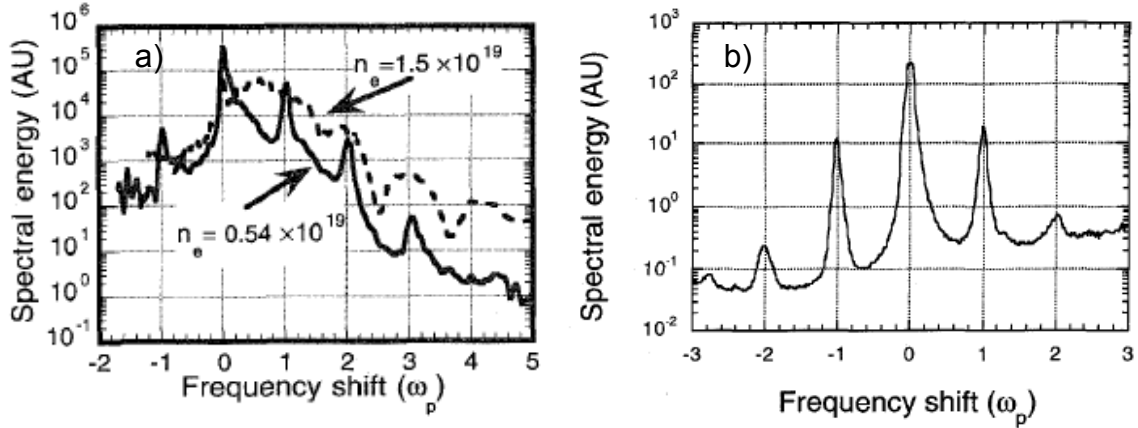
Figure 3.2: Spectral effects of FRS on the pumping laser and on a frequency-doubled co-propagating probe[125]. a) The laser's spectrum for a 1053 nm, 25TW, laser with a spot size of 20 μm FWHM after pumping a helium plasma of density 5.4×10^{18} cm⁻³ (solid) or 1.5×10^{19} cm⁻³ (dashed). The shifts are normalized to the plasma frequency, so the peak at 0 is the fundamental of the laser, the peak at -1 is the first Stokes, and so on. b) Second harmonic probe beam's spectrum after interaction with the plasma wave for a plasma of density 6×10^{18} cm⁻³. The shifts are again normalized to the plasma frequency.

As the FRS instability grows, it can pass through all three of these regimes, beginning with 3-wave mixing and then through nonresonant 4-wave mixing and into

resonant 4-wave mixing. The scaling of BRS has been investigated experimentally[121], though FRS has not as of this time. The growth of the forward Raman scattering instability and the subsequent beating with and depletion of the pump cause an envelope modulation in the laser. This method of driving a wakefield is therefore referred to as self-modulated laser wakefield acceleration (sm-LWFA), and was the basis of many early LWFA experiments prior to the discovery of the bubble regime.

Forward Raman scattering has been observed[122],[123],[124] and temporally characterized[125] experimentally. The primary manifestation of the FRS is the appearance of shifted peaks in the optical spectrum. This can be seen directly in the pump spectrum, or in a co-propagating probe pulse, as shown in Fig. 3.2. The pumping spectrum ultimately gains several anti-Stokes peaks, and also one clear Stokes' peak, each of which is offset by an integer increment of the plasma's frequency. There are more anti-Stokes peaks, and the 1 anti-Stokes peak is stronger than the 1 Stokes peak: this is because the phase-matching conditions favor anti-Stokes in the forward direction of this experiment.

The pump spectrum in Fig. 3.2a is shown for two different plasma densities. At the lower density, n_e=5.4×10^{18}cm^{-3}, each of the Stokes and anti-Stokes peaks are sharp and well-defined, indicating that the plasma is homogenous and has a coherence time on the order of the laser pulse duration (0.7-1.0 ps). At the higher density, $n_e = 1.5×10^{19}$ cm^{-3}, the Stokes and anti-Stokes peaks are still shifted by integer values of the plasma frequency, implying that the coherence time is much shorter than the laser pulse duration, on the order of only a few plasma lengths (~100 fs). Further, the plasma wave itself is distorted, and wavebreaking occurred, which results in a large increase in both the

number and maximum energy of the electrons accelerated by this wave. In both cases, the shifts are normalized to the frequency of the plasma involved, so in both cases the shifts appear in integer numbers even though the plasma frequencies involved differ.

The second harmonic probe (Fig. 3.2b) contains both Stokes and anti-Stokes peaks, also spaced by integer values of the plasma frequency. The probe undergoes Thompson scattering interactions with the oscillations of the plasma waves, from which the amplitude of the plasma wave can be determined. The efficiency of this scattering interaction is given by[126]

$$\frac{P_s}{P_L} = \frac{1}{4} (\delta n_e)^2 r_0^2 \lambda_L^2 L^2 \frac{\sin^2(\Delta k\, L)}{(\Delta k\, L)^2} \qquad\qquad (3.1.35)$$

where r_0 is the classical electron radius, L is the interaction length (e.g. diffraction length), and $\Delta k = k_L - k_S \pm k_p$ is the wave vector mismatch. A co-propagating SHG probe or other co-propagating probe which is spectrally distinct from the pump laser can also be used to characterize the temporal evolution of the FRS instability, as shown in Fig. 3.3.

When the probe leads the pump, there is still of course some overlap between the two (both have some finite duration, in this case of approximately 400 fs). The Thompson-scattered satellites first become visible when the probe leads the pump by 700 fs, at which time their frequency shift is only 3×10^{14} s^{-1}, as compared to the shift of 3.3×10^{14} s^{-1} when there is zero delay between the two or when the pump arrives first. The
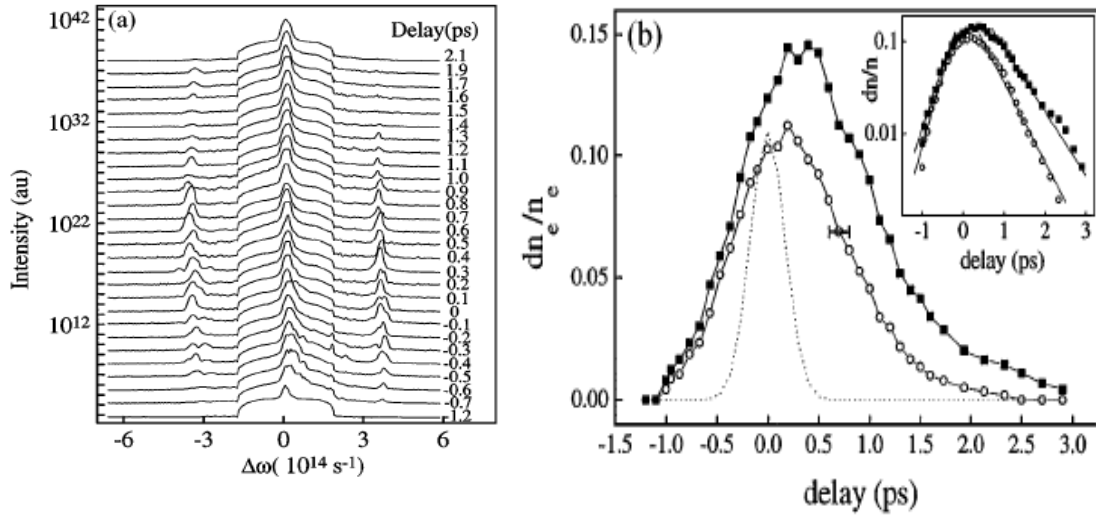
Figure 3.3: Forward Raman scattering and plasma wave amplitude evolution measured by forward-scattered probe[124]. a) The spectrum of the probe after scattering from the plasma wave as a function of the delay between probe and pump lasers. b) Plasma wave amplitude determined by the scattering efficiency of 1 Stokes (closed squares) and 1 anti-Stokes (open circles) in the probe, plotted against delay time between probe and pump pulses. The dotted line is the 400 fs duration of the 600 mJ pump, the horizontal error bar is representative of the error in this experiment, and the inset shows exponential fits to the wakefield growth and decay. The plasma resonant frequency in this case is 3.3×10^{14} s^{-1}, and the probe was 15 mJ of light frequency-doubled from the pump.
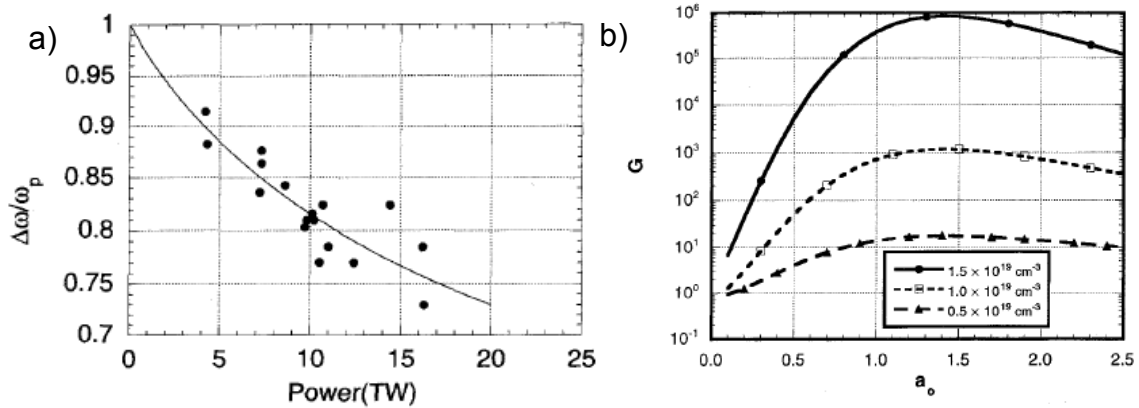
Figure 3.4: Raman shift and gain as functions of the laser intensity[125]. a) Sideband frequency separation normalized to nonrelativistic plasma frequency as a function of laser power for a 20 μm spot. The continuous curve is the fit calculated by $\Delta\omega/\omega_{p0} = (1 + a_0^2/2)^{-1/4}$, where $\omega_{p0} = 1.83 \times 10^{14}$ s^{-1} is the nonrelativistic plasma frequency. b) Raman gain as a function of the laser's normalized vector potential (e.g., the intensity) at three plasma densities.

100

reason for this is that the helium is not all ionized at once, but rather requires some finite amount of time to ionize; the resonant frequency of the fully ionized plasma corresponds to the 3.3×10^{14} s^{-1} shifts in the probe. The field itself also takes some time to grow, and so maximizes ~300 fs after the peak of the pump pulse, and lasts for about 2 ps thereafter.

It should also be noted for the sake of completeness that the Raman frequency and gain are both functions of the laser's intensity (or normalized vector potential a_0). This is on account of the relativistic electron mass effect. The plasma frequency in a non-relativistic plasma is given by

$$\omega_{p0}=\sqrt{(4\pi e^2 n_e)/\epsilon_0 m_e} \tag{3.1.36}$$

When the laser becomes sufficiently intense that it drives the plasma relativistically, the plasma's frequency becomes $\omega_p = \omega_{p0}/\gamma^{1/2}$. The relativistic Lorentz factor is in turn given by $\gamma=\sqrt{1+a_0^2}$ for a linearly polarized pump laser. Therefore, the plasma frequency and hence the Raman shift will decrease as the laser's intensity increases. Furthermore, because the Raman gain is proportional to the plasma frequency, gain will eventually begin to fall off at relativistically high intensities.

3.2   ELECTROMAGNETIC CASCADING AND BEATNOTE GENERATION

Electromagnetic cascading (EMC) in a plasma was first considered by Cohen *et al.* in the context of using the beat between two laser waves to heat a plasma[127].

The process begins with two lasers of frequencies[vi] ω_L and ω_{L-1} and wavenumbers k_L and k_{L-1} incident on a plasma of resonant frequency ω_p. These waves have a beat frequency $\Omega = \omega_L - \omega_{L-1} = \omega_p + \Delta_L$, where $\Delta_L \ll \omega_p$, so their beat is near to but not necessarily equal to the plasma resonance. The result will be that the beat wave will excite linearly-damped longitudinal plasma waves (plasmons) which then interacts with the two laser waves to produce two more electromagnetic waves. The wavevectors of these new waves are $\vec{k}_{L-2} = \vec{k}_{L-1} - \vec{k}_p$ and $\vec{k}_{L+1} = \vec{k}_{L-1} + \vec{k}_p$. These new waves can then also interact with the plasmons to form additional shifted waves $\vec{k}_{L-N} = \vec{k}_{L-1} - (N-1)\vec{k}_p$ and $\vec{k}_{L+N} = \vec{k}_{L-1} + N\vec{k}_p$.

Stimulated Raman scattering and eventually the resulting Raman cascade is similar to by not the same thing as EMC. EMC is a nonresonant phase modulation, which results in the generation of frequency sidebands, and which is caused by the pulses' creation of and propagation through a comoving refractive index grating. The modulation is thus somewhat akin to self-phase and cross-phase modulation as a consequence of passing through a medium (the perturbed plasma) whose refractive index is not constant. FRS on the other hand is a resonant response seeded by the plasma density perturbation from which the pump and Raman modes are scattered.

The cascade rate is given by

$$\Gamma \equiv -c\frac{d\langle l \rangle}{dz} = \frac{1}{4L^3}\frac{\beta\omega_p^2}{\beta^2+\Delta^2}\frac{\alpha^2}{(1+\alpha^2)^2}\frac{W_0}{n_e m_e c^2} \tag{3.2.1}$$

---

vi Note that in Sec. 3.1, the second laser, with frequency ω_{L-1} and wavenumber k_{L-1} corresponds to the 1 Stokes wave.

where β is the damping constant, $W^0 = W_{L-1}{}^0 + W_{L-1}{}^0$ is the input energy, $\alpha = |A_{L+1}|/|A_L|$ is the ratio of the input vector potentials' amplitudes of the two input beams.

It should be added here that EMC occurs primarily in a collinear or nearly collinear geometry. Cohen *et al.* state that this is on account of the large mismatches for the higher orders in the cascade in a highly-nonlinear geometry. There is a second reason why EMC or even the phase-matched Raman cascading would require a collinear geometry, which is that the interaction length would be very short in a non-collinear geometry. This is especially true given that the beams must be focused, typically to small (~10 μm) spot sizes in order to have sufficiently large intensities to undergo EMC into higher order modes.

An analytic solution for the temporal and spatial evolution of the EMC[128] can be obtained by beginning with Maxwell's equations, the fluid equations, and the slowly-varying envelope approximation. The resulting equations of motion are

$$\dot{e}_m + e_m{}' = (\omega_1/\omega_m)(e^* e_{m+1} - e e_{m-1}) \qquad (3.2.2a)$$

$$\dot{e} + \frac{3 v_e^2}{c^2} e' - i \frac{v_e^2 v_1}{c^3} \sqrt{\omega_p/\omega_1} e'' + (\beta + i \Delta |e|^2) = \sum_m e_m e_{m-1}^* \qquad (3.2.2b)$$

where e and e_m are the electric field amplitudes $e = (\omega_1/\omega_p)^{1/2} E/E_L$ and $e_m = (\omega_1 E)/(\omega_p E_L)$, v_e is the electron thermal velocity, and $v_1 = |q_e|E_L/m_e\omega_1$ is the quiver velocity, and β is the normalized damping factor. Since there are initially only two spatially uniform modes (m = 0 and m = 1, or fundamental and 1 Stokes) present, and assuming that $|m| \ll \omega_1/\omega_p$ so that $\omega_1{\sim}\omega_m$, Eqns (3.3.2) reduce to

103

$$\dot{e}_m = (e^* e_{m+1} - e e_{m-1})$$ (3.2.3a)

$$\dot{e} + (\beta + i \Delta |e|^2) = \sum_m e_m e_{m-1}^*$$ (3.2.3b)

The solution to these is then

$$e_m(\tau) = (-1)^m \exp[\vartheta (\psi - \theta) + i\theta][\rho J_m(2W) - \exp(-i\psi) J_{m-1}(2W)]$$ (3.2.4)

where J_m is the Bessel function of the first kind, $\tau = \Omega_g t$ is the time coordinate whose derivative is represented by a dot, and where the transformation

$$w = E \exp(i\psi) = \exp(i\theta) \int_0^\tau e(\tau') d\tau'$$ (3.2.5)

has been used. The initial conditions for Eqns. (3.3.2) are $e_1(0) = 1$, $e_0(0) = \rho \exp[i\theta]$, $e(0) = 0$, and all other $e_m(0) = 0$.

The intensity of the mth mode is therefore given by

$$|e_m|^2 = \rho^2 J_m^2(2W) + J_{m-1}^2(2W) - 2\rho J_m(2W) J_{m-1}(2W) \cos \psi$$ (3.2.6)

The temporal evolution of the electromagnetic modes in the EMC are show in Fig. 3.5. This plot show the relative intensities $|e_m|^2$ which are evolving according to Eqn. (3.2.6). The cascade ultimately generates many higher order side-bands , albeit at a much lower amplitude than the initial two beams' amplitudes. The plot is generated with the parameters $\Delta = 125$ and $\rho = 0.5$, which result in a plasmon-wave amplitude oscillation period of $\tau_0 = 0.486$. For comparison, this means that if the lasers used to pump the EMC are a Ti:Sapph laser centered at 800 nm with an initial initial intensity of 1.1×10^{18} W/cm² and an Nd:glass laser centered at 1054 nm with an initial initial intensity of 1.1×10^{18} W/cm², incident on a plasma of density 6.0×10^{19} cm⁻³, the period t_0 is about 0.953 ps, and so Fig. 3.5d showing a cascade of many orders takes place after ~5.7 mm of plasma.

Electromagnetic cascading has also been suggested as a method for focusing[129] and trapping laser pulses, albeit only at smaller plasma wave amplitudes[130]. When the plasma wave is driven to larger amplitudes, the beams are defocused rapidly instead. The threshold for the cascade self-focusing effect is up to 10 times smaller than for relativistic self-focusing, to which we now turn.
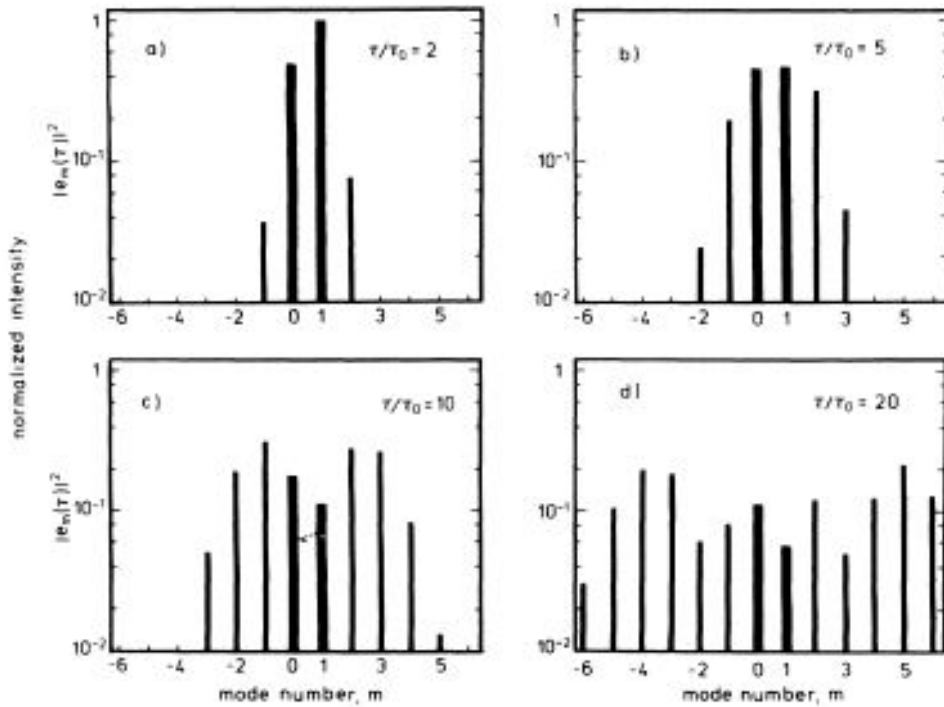
Figure 3.5: Temporal evolution of the electromagnetic cascade's mode spectra. a) At time $\tau = 2\tau_0 \mathord{-}\mathord{-}{>}t = 1.91$ ps, b) $\tau = 5\tau_0 \mathord{-}\mathord{-}{>}t = 4.77$ ps, c) $\tau = 10\tau_0 \mathord{-}\mathord{-}{>}t = 9.53$ ps, and d) $\tau = 20\tau_0 \mathord{-}\mathord{-}{>}t = 19.06$ ps. This is done for $\Delta = 125$, $\rho_2 = 0.5$, and therefore the period of the plasmon-amplitude solution is $\tau_0 = 0.486$. The physical times are calculated assuming that the lasers used to make the beat are centered at 800 nm (e.g., Ti:Sapph) and 1054 nm (e.g. Nd:glass) and have initial intensities of 1.1×10^{18} W/cm²., and with a plasma of density 6.0×10^{19} cm⁻³, meaning $(\omega_0 - \omega_1)/\omega_p \approx 1.29$.

3.3   RELATIVISTIC SELF-FOCUSING (RSF)

A sufficiently powerful laser pulse will undergo self-focusing in an underdense plasma. This is because the refractive index of the plasma will vary transversely with the intensity of the laser and the subsequent relativistic mass corrections (and thus resonant frequency) of the electrons such that the laser experiences the greatest refractive index on-axis. There exists an analogous effect in nonlinear optics: the Kerr effect, which is a $\chi^{(3)}$ effect. Relativistic self-focusing can cause electron cavitation and the subsequent destruction of the wakefield in the linear regime, and on the other hand it can result in the guiding of a laser pulse.

2.3.1 Self-Focusing in Nonlinear Media: Nonlinear Optical Analogue to RSF

The self-focusing of light is a well-known effect in nonlinear optics. The Kerr-effect is a result of the nonlinear polarization of a medium:

$$P^{NL}(\omega) = 3 \chi^{(3)}(\omega = \omega + \omega - \omega)|E(\omega)|^2 E(\omega) \tag{3.3.1}$$

Where $\chi^{(3)}$ is the third-order nonlinear susceptibility (tensor indices have been suppressed for simplicity). The total polarization of the medium is the sum of the linear and nonlinear polarizations:

$$P^{TOT}(\omega) = P^L + P^{NL} = \chi^{(1)} E(\omega) + 3 \chi^{(3)}(\omega = \omega + \omega - \omega)|E(\omega)|^2 E(\omega) \equiv \chi_{eff} E(\omega) \tag{3.3.2}$$

This effective susceptibility χ_{eff} give the total refractive index η of the medium:

$$\eta = \sqrt{1 + 4\pi \chi_{eff}} \equiv \eta_0(\omega) + \eta_2 I \tag{3.3.3a}$$

Where I is the time averaged intensity of the optical field, $I = I(\omega) = \eta_0 c/(2\pi)|E(\omega)|^2$, η_0 is the linear refractive index and η_2 is the nonlinear refractive index, which are given by[131]

$$\eta_0 = \sqrt{1 + 4\pi\chi^{(1)}} = \sqrt{\epsilon\mu} \tag{3.3.3b}$$

$$\eta_2 = \frac{12\pi^2}{\eta_0^2 c}\chi^{(3)} \simeq \frac{0.0395}{\eta_0^2}\chi^{(3)}\,[esu] \tag{3.3.3c}$$

Where ϵ and μ are the permittivity and permeability of the medium, respectively. Table 3.2 shows a few typical order-of-magnitude values of nonlinear refractive index, nonlinear susceptibility (in esu), and responses times for a variety of mechanisms.

The refractive index is therefore intensity-dependent, and since $I = I(r, \omega)$ the refractive index varies with axial distance r. Since a laser is generally most intense-on axis, and the intensity falls off with r, this means that the refractive index seen by an intense laser (or a less-intense probe beam propagating with the laser) will peak on-axis and fall off with r as well. The result is that the medium acts as a positive lens[vii] and focuses the laser (or probe), which is called self-focusing (or cross-focusing, in the case of a probe). This self-focusing effect can overcome or be countered by diffraction. Since $\eta_0 \sim 1\text{-}2$ for most relevant materials, it is worth noting that the nonlinear refractive index is generally small compared to the linear refractive index.

It is possible to calculate the effective focal length of self-focusing. Assuming that the beam is initially collimated and has a characteristic waist w_0 after which the

---

vii This is assuming that $\eta_2 > 0$, which is typically the case with nonlinear media.

Mechanism	η_2 (cm^2/W)	$\chi_{1111}^{(3)}$	Response time (seconds)
Electronic polarization	10^{-16}	10^{-14}	10^{-15}
Molecular orientation	10^{-14}	10^{-12}	10^{-12}
Electrostriction	10^{-14}	10^{-12}	10^{-9}
Saturated atomic absorption	10^{-10}	10^{-8}	10^{-8}
Thermal effects	10^{-6}	10^{-4}	10^{-3}

Table 3.2: Some typical values for the nonlinear refractive index and the nonlinear susceptibility for linearly polarized light [131].

intensity has fallen off significantly[viii], then it is possible to treat a ray which is initially a distance w_0 ("marginal ray") from the laser's center as experiencing a merely linear refractive index (e.g. $\eta_{mar} = \eta_0$). A ray traveling on-axis ("central ray") will experience a refractive index described by Eqn. (3.3.3).

According to Fermat's principle, the optical pathlength $z_{opt} = \int \eta(r) dl$ is constant for all rays traveling from a wavefront at the input of the focusing medium to the focal point. Using Fermat's principle and Eqn. (3.3.3a),

$$(\eta_0 + \eta_2 I) z_{sf} = \eta_0 z_{sf} / \cos\theta_{sf} \qquad (3.3.4)$$

Where z_{sf} is the effective focal length of the self-focusing beam, and θ_{sf} is the "self-focusing" angle subtended by a marginal ray and the central ray. A helpful diagram is shown in Fig. 3.6. Assuming that $z_{sf} \gg w_0$, the angle θ_{sf} will be small and so $\cos\theta_{sf} \approx 1 - (1/2)\theta_{sf}^2$. Therefore, (3.3.4) can be solved for the self-focusing angle:

$$(\eta_0 + \eta_2 I) z_{sf} = \frac{\eta_0 z_{sf}}{(1 - (1/2)\theta_{sf}^2)} \rightarrow \theta_{sf}^2 \approx 2\,\eta_2 I / \eta_0 \qquad (3.3.5)$$

---

viii For example, the waist w_0 for a Gaussian pulse represents the $1/e^2$ intensity radius (a factor of ~7.5 reduction).

so long as $\eta_2 I/\eta_0 \ll 1$, a condition which generally is true. For example, if $\eta_2 \sim 10^{14}$ cm^2/W (as per electrostriction or molecular orientation), an intensity of $\sim 10^{14}$ W/cm^2 would be required to have the nonlinear and linear terms be the same order of magnitude. This intensity exceeds the damage threshold of any solid material and indeed will begin to ionize the outer-shell electrons of high-Z atoms by Coulomb barrier-suppression.

The analysis so far has made two assumptions which can now be addressed. The first is that diffraction is negligible, which is true for very high-powered lasers. The second is that the laser beam is initially collimated. Of course, an initially converging beam will simply focus more quickly, or (if self-focusing is negligible) will pass through a focus and then become a diverging beam.

It is therefore worth stating that the self-focusing angle can be corrected for both diffraction and for an initially divergent beam. To correct for diffraction, the actual propagation angle θ for the beam becomes[132]

$$\theta = \begin{cases} \theta_{conv} = \sqrt{\theta_{sf}^2 - \theta_{dif}^2}, & \theta_{sf}^2/\theta_{dive}^2 > 1 \\ \theta_{dive} = \sqrt{\theta_{dif}^2 - \theta_{sf}^2}, & \theta_{sf}^2/\theta_{dive}^2 < 1 \end{cases} \tag{3.3.6a}$$

Where the subscripts "conv" and "dive" represent a converging (e.g. focusing) beam and a diverging (e.g. defocusing) beam, respectively. The diffraction-corrected convergence angle θ_{conv} is illustrated in Fig. 3.6, and the divergence angle θ_{dive} can be visualize by mirroring θ across the dashed "guide" line. The diffraction angle θ_{dif} is given by

$$\theta_{dif} = 0.61 \lambda_{L0}/\eta_0 d \tag{3.3.6b}$$

Where λ_{L0} is the vacuum wavelength of the laser and d is the laser's beam diameter.
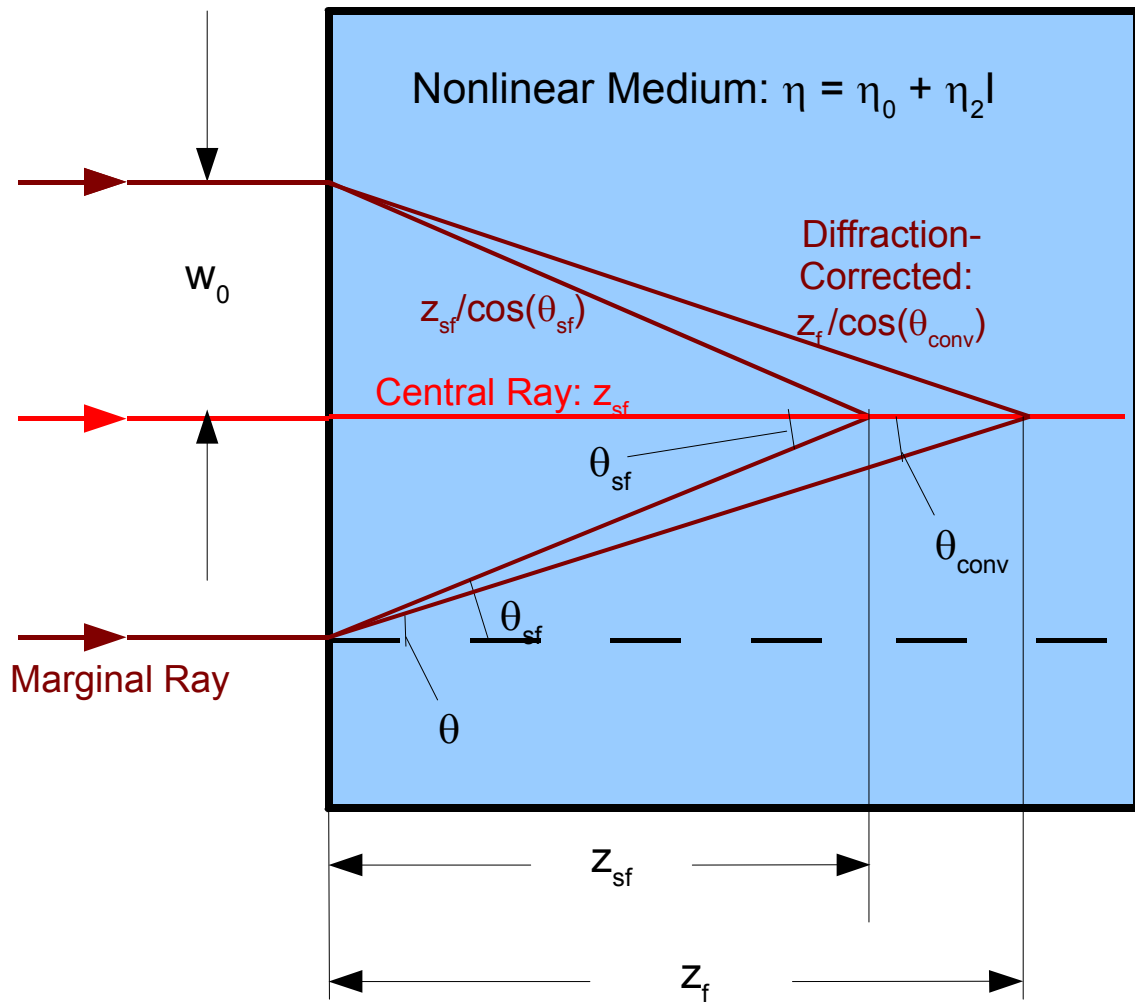
Figure 3.3.1: Illustration of the prediction of the self-focusing distance z_{sf} via Fermat's principle. It should be noted that the real ray trajectories will actually curve within the media because the intensity will increase as the beam focuses. However, these curved trajectories can be approximated as straight lines for $z_{sf} \gg w_0$. The focal length z_{sf} and the corresponding angle θ_{sf} assume no diffraction; including diffraction lengthens the focal length, $z_f > z_{sf}$ on the assumption that self-focusing overcomes diffraction ($\theta = \theta_{conv}$), and so the actual angle of convergence $\theta_{conv} < \theta_{sf}$. If diffraction overcomes self-focusing, then the angle $\theta = \theta_{dive}$, and the beam continues to expand (albeit more slowly than if self-focusing is absent).

The diffraction angle is inversely proportional to beam size: diameter as in Eqn. (3.3.6b) or twice the waist, d = 2w. The self-focusing angle is in turn dependent on intensity, I = P/A where P is the beam's power and A is the laser's spot area, $A = \pi w^2$. According to Eqn. (3.3.6a), whether the laser focuses or defocuses depends on the ratio $(\theta_{sf}/\theta_{dif})^2$. Using Eqns. (3.3.5) and (3.3.6b), this ratio of angles becomes

$$\frac{\theta_{sf}^2}{\theta_{dif}^2} = \frac{2\eta_2 I/\eta_0}{(0.61\lambda_{L0}/\eta_0 d)^2} \equiv \frac{2\eta_2 P/(\eta_0 \pi w^2)}{(0.61\lambda_{L0}/(2\eta_0 w))^2} \tag{3.3.7}$$

The threshold for diffraction to overcome self-focusing is $(\theta_{sf}/\theta_{dif})^2 = 1$. If Eqn. (3.3.7) under this threshold condition is solved for power P, this gives the critical power above which self-focusing will overcome diffraction:

$$P_{cr} = \frac{(0.61)^2 \pi \lambda_{L0}^2}{8\eta_0 \eta_2} \tag{3.3.8}$$

This critical power can be further modified if the beam is initially diverging (e.g. not collimated), which satisfies the second assumption of this analysis. If the beam is initially divergent ($\theta_i < 0$), the critical power becomes[133]

$$P_{cr}[\theta_i < 0] = (1 + \theta_i^2) P_{cr}[\theta_i = 0] \tag{3.3.9}$$

A general expression for the focal length of the the beam for the self-focusing focal length with arbitrary initial spot size w_i at the entrance to the nonlinear medium and arbitrary beam waist position (z_{min}), minimum spot size w_0 at focus without self-focusing, and power is[132]:

$$z_{sf} = \frac{k w_i^2/2}{\sqrt{P/P_{cr} - 1} + 2 z_{min}/(k w_0^2)} \tag{3.3.10}$$

where $k = \eta_0 \omega_L / c$.

This critical power allows us to define several regimes. In the first, $P < P_{cr}$, the beam will not focus at all, but rather will continue to diffract. In the regime $P \simeq P_{cr}$, the beam will focus, but diffraction effects are not negligible: $z_f > z_{sf}$. In a third regime, $P \gg P_{cr}$, diffraction becomes negligible, and the angular and focal length corrections can be ignored: $\theta_{conv} \approx \theta_{sf}$ and $z_f \approx z_{sf}$.

A fourth regime of interest if the self-trapping regime in which $P = P_{cr}$. In this regime, the self-focusing effect and the diffraction effect counter-balance each other so that the beam propagates as a filament of ~ constant diameter[ix]. One explanation[132],[134] of self-trapping (or self-guiding) is to envision it as a case of total-internal reflection at the boundary between two regions in a nonlinear medium. In the first region, the laser is not propagating and the refractive index is $\eta = \eta_0$; in the second region, the laser is propagating, and has the refractive index $\eta = \eta_0 + \eta_2 I > \eta_0$. The laser is guided (or trapped) if it undergoes total internal reflection at the boundary between these two regions.

Self-trapping will also occur in the regime where $P \gg P_{cr}$. However, in this regime, the self-trapping takes the form of filamentation and beam break-up: rather than being guided as a single filament, the beam splits into several filaments, each of which caries power $P \approx P_{cr}$. The actual size (diameter) of the filaments may vary, or it may (under certain circumstances) produce a geometrically regular pattern[135].

---

ix In actuality, a beam undergoing self-focusing can be guided similarly, though it undergoes a sort of "breathing" process in which the beam converges s a result of self-focusing, then begins to diverge as a result of diffraction.

This filamentation ultimately grows out of small perturbations in the laser's wavefront. This in turn means that the threshold for filamentation and the length over which a beam breaks up into separate filaments is not as easy to define as the critical power and focal lengths for self-focusing. For example, a "clear" laser will have a much higher filamentation threshold than a "dirty" laser because the former has fewer (and smaller) wavefront perturbations from which filamentation can grow than the latter. One estimate for the threshold power for filamentation (P_{fil}) is[136]

$$P_{fil}/P_{cr} = 4 G^2 \qquad\qquad (3.3.11a)$$

and the filamentation length (z_{fil}) is similarly estimated to be

$$z_{fil} = \frac{G}{\eta_2 I k_{vac}} = \frac{G}{\eta_2 I \omega_L/c} \qquad\qquad (3.3.11b)$$

where G is a numerical factor typically ~ 3-10 which attempts to account for the presence or absence (and relative strength) of wavefront perturbations: G is larger for a "clear" beam and smaller for a "dirty" beam, for example. Note that $z_{fil} < z_{sf}$, which implies that if filamentation occurs then whole-beam self-focusing will not occur, and that furthermore filamentation can be induced for a sufficiently large laser power.

3.3.2 Relativistic Self-Focusing in Plasma

The refractive index η of a plasma can be obtained in a similar manner as the refractive index in other media. When an electric field is applied to a plasma, it induces a polarization given by the dipole moment per unit volume:

$$\vec{P}=\int dr\,\rho(\vec{r})\,\vec{r}=n_e e\,\vec{r} \qquad (3.3.12)$$

where the rightmost hand side is the dipole moment per unit volume for a uniform plasma with electron density n_e. If the polarization is a linear function of the electric field, e.g.

$\vec{P}=\chi_{eff}\,\vec{E}$, as per Eqn. (3.3.2), then the electric displacement field is given by

$$\vec{D}=\epsilon_0\vec{E}+\vec{P}=\epsilon\vec{E} \qquad (3.3.13a)$$

$$\epsilon=1+4\pi\chi_{eff} \qquad (3.3.13b)$$

If the electric field has the form $E\sim\exp(i\omega_L t)$ + c.c., and if we ignore ion motion (which is very slow compared to electron motion owing to the difference in mass) and collisions, then the equation of motion for an electron is that of a harmonic oscillator,

$$m\ddot{\vec{r}}=e\vec{E}=-m\omega_L^2\vec{r}\to\vec{r}=(-e/m\omega_L^2)\vec{E} \qquad (3.3.14)$$

The polarization can be obtained from combining Eq. (3.3.14) and the expression of the polarization above to yield

$$\vec{P}=(-n_e e^2/m\omega_L^2)\vec{E}\to\chi_{eff}=-n_e e^2/m\omega_L^2 \qquad (3.3.15)$$

Therefore, the refractive index of an unmagnetized plasma $\eta^2=\epsilon$, can be obtained by combined Eqns. (3.3.13b) and (3.3.15):

$$\eta^2=1-\frac{\omega_p^2}{\omega_L^2}=1-\frac{4\pi e^2 n_e}{\gamma\epsilon_0 m_e\omega_L^2} \qquad (3.3.16)$$

where ω_p is the plasma frequency, $\omega_p=\sqrt{(4\pi e^2 n_e)/\gamma\epsilon_0 m_e}$. This analysis so far has paralleled the analysis in Sec. 3.3.1, in particular Eqs. (3.3.1) – (3.3.3). In RSF, the physical mechanism by which the effective nonlinear refractive index changes is the relativistic electron mass change, which is accounted for by γ.

114

For a non-relativistic plasma ($\gamma \approx 1$), this refractive index depends on the density of the electrons in the plasma $n_e(r, z)$. As discussed in Sec. 3.1.2, the z-dependence of the electron density (and thus of the refractive index) can lead to a self-modulated pulse which may ultimately break up into a train of short pulses for pulses longer than the plasma wavelength.

For a relativistically intense laser pulse, there is a second parameter which affects the refractive index: γ. For a linearly polarized lase pulse, the relationship between normalized vector potential and the relativistic term is given by

$$\gamma = \sqrt{1 + a^2} \tag{3.3.17}$$

Where the normalized vector potential a is given by

$$a = \frac{e E}{m_e c \omega_L} = 8.55 \times 10^{-10} \times I^{1/2}[W/cm^2]\lambda[\mu m] \tag{3.3.18}$$

Since the laser has some transverse profile $I = I(r)$, the relativistic correction will also have a transverse profile $\gamma = \gamma(r)$: specifically, the larger the intensity, the larger the relativistic correction, and thus also the larger the refractive index of the plasma. The intensity of a typical laser pulse—Gaussian, Sinc, etc.—is greatest on-axis, and so therefore is the refractive index, meaning that the relativistic electrons in the plasma will act as a positive (focusing) lens for the laser pulse. This is illustrated in Fig. 3.7.

Intensity vs transverse distance from center
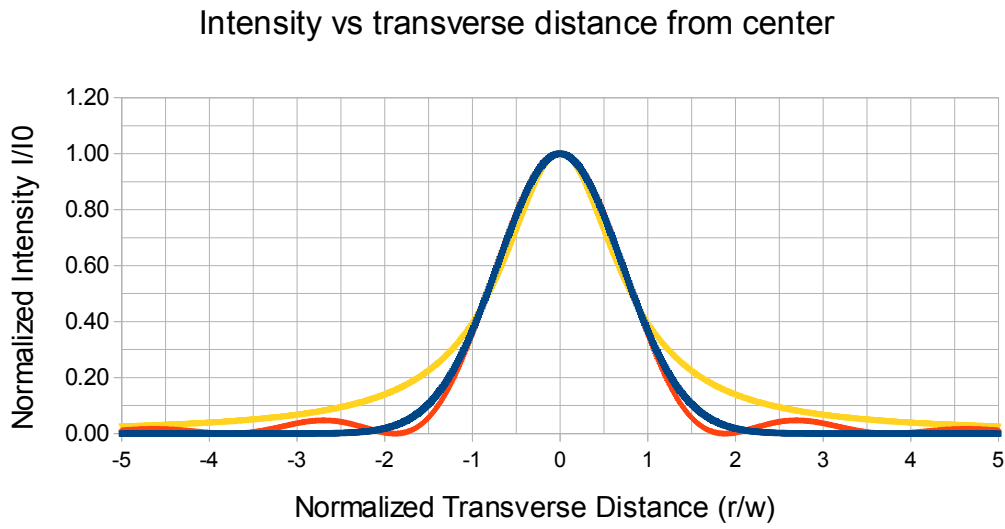
Possible Refractive Index vs Transverse Distance from Beam Center
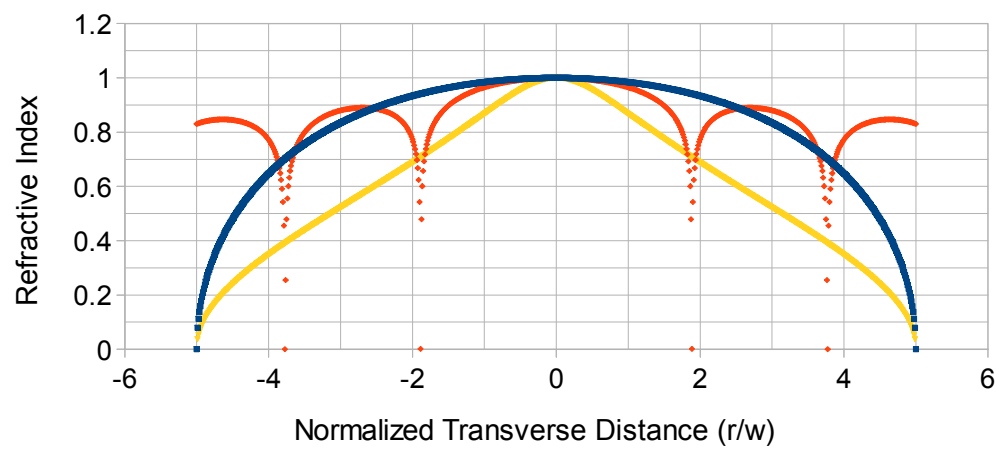
Figure 3.7: Illustrative graphs of intensity profiles and resulting refractive index profiles. The pulse profile types are for a Gaussian (blue), a sinc (red), and a Lorentzian (yellow) transverse profile, and in all cases the intensity has been normalized to the peak intensity and the refractive index to the maximum refractive index value. The transverse distance from pulse peak has also been normalized to the FWHM radius of the pulse in each case.

As in nonlinear media, this focusing effect can be balanced against (or can overcome) diffraction. Diffraction is overcome by RSF in plasma when the laser's power exceeds some critical power (P_{cr}):

$$P_{cr} = 17.4 \times \left(\frac{\omega_L}{\omega_p}\right)^2 [GW] \qquad (3.3.19)$$

When the laser's power exceeds this critical power, the pulse will be focused until the spot size is sufficiently small that diffraction causes defocusing—the spot size will oscillate in the plasma due to the interplay of RSF and diffraction. In this case, the laser's spot size evolves according[137],[138] to

$$\frac{d^2 R}{d z^2} = \frac{1}{Z_{R0}^2 R^3}\left(1 - \frac{P}{P_{cr}}\right) \qquad (3.3.20)$$

where $R = r_s/r_0$ is the normalized spot size, r_0 is the minimum spot size in vacuum, and Z_{R0} is the vacuum Rayleigh length. The first term on the right hand side is the diffraction term, the second is the self-focusing term. This equation has the solution

$$R^2 = 1 + (1 - P/P_{cr})z^2/Z_{R0}^2 \qquad (3.3.21)$$

So far I have ignored charge displacement effects. However, as the laser spot is focused, the resulting laser intensity will increase $I \sim r^{-2}$, and thus the resulting field strength can totally expel all electrons from the region of the pulse (cavitation), creating an ion-channel. When this happens, the self-focusing effect itself can be nullified (the electron medium responsible for RSF has been expelled from the region of the laser pulse), but the laser itself may be guided in this channel somewhat akin to a laser being guided in an a fiber optic—or a filament.

117
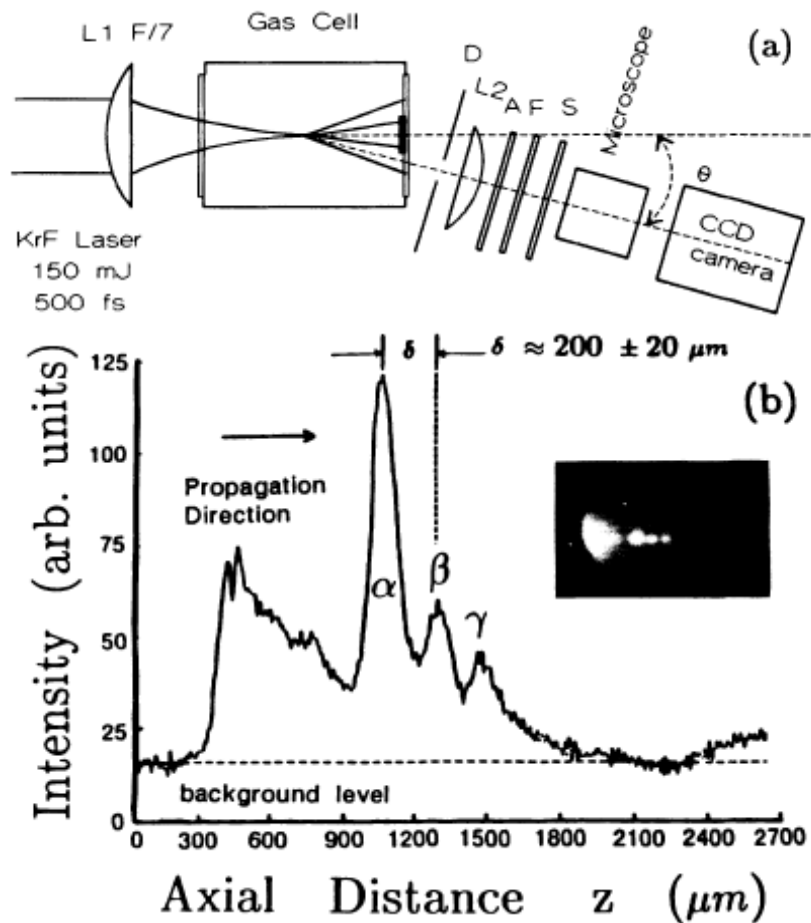
Figure 3.3.3: Results of an early RSF experiment in which self-guiding of a laser pulse through a plasma was observed[142]. a) The set-up of the experiment. The laser is focused into a back-filled gas chamber, with scattered light being observed off-axis to enable single shot observation of the light's scattering (and hence, intensity) as it propagates. The imaging system consists of a diaphragm D which restricts the solid angle collected to ~5° while also increasing the depth of field; a Lens L2 which images the region near the laser's (vacuum) focal plane; an attenuator A to adjust intensity on the fluorescing screen S; a spectral filter which consists of a pair of highly reflecting (>99%) mirrors centered at 248 nm with ~10 nm bandwidth, which are meant to reflect the 248 nm light to the screen but transmit any other scattered light; and then a microscope objective lens to image the screen onto the ccd camera. b) Intensity lineout data as a function of propagation distance, with the raw ccd image as an inset. The resolution in this case was ~10 mm, the gas was N_2 at a density of 1.35×10^{20} cm^{-3}, and the spacing of the intensity maxima is approximately $\delta = 200 \pm 20$ μm. The peaks α, β, and γ are caused by self-focusing followed by diffraction.

118

A second consequence of this electron cavitation effect is that the wakefield itself now operates in the bubble regime. It has been noted that the laser pulse quality (and evolution) plays a very important role[139],[140],[141] in the energy and quality of the accelerated electrons. For example, acceleration length and therefore accelerated electron bunch energy depend on the drive laser's spot size, as noted in Chapter 1. A more complete discussion of scaling laws for the bubble regime can be found in Chapter 1 (Sec. 1.2.3), and in references [139]-[140].

The first known observation of RSF occurred about 20 years ago with an early terawatt-class KrF laser[142]. The laser delivered $\approx 3 \times 10^{11}$ W (≈ 150 mJ in ≈ 500 fs) centered at 248 nm to a focal spot of 3.5 mm for a peak intensity of $I_0 \approx 8.6 \times 10^{17}$ W/cm^2. The target in question was a chamber back-filled to a maximum density of 1.89×10^{20} cm^{-3} of gas, with the gas being any one of He, Ne, Ar, Kr, Xe, N_2, CO_2, or a mixture of Xe (4%) and N_2 (96%). The set-up of the experiment and its key result are shown in Fig. 3.8.

The data shown in Fig. 3.8b is for N_2 gas at a density of 1.35×10^{20} cm^{-3}, and can be explained as follows. First, the laser is focused by lens L1 onto the target—this is the broad peak beginning at 300 mm in the chart of Fig. 3.8b—which it ionizes, thus beginning to defocus somewhat, hence causing the first peak to decay. However, at some point enough nitrogen has been ionized (or enough levels of the nitrogen are ionized) that the plasma's density increases such that the laser's power exceeds the critical power for RSF per Eqns. (3.3.16) and (3.3.19). At this point, the laser begins to focus again thanks to the relativistic effects of the plasma, thus also increasing the laser's intensity and

forming the first RSF peak, which is labeled α in Fig. 3.8b. At some point, the pulse is intense enough to expel all of the electrons from its path, and total cavitation occurs. Once this has occurred, there is no longer a relativistic medium in the laser's path to guide it, and diffraction causes the laser to expand and the intensity to drop[x]. This expansion causes the intensity to drop below the threshold for cavitation, and the beam then focuses again, causes cavitation (even partial cavitation suffices as the power depletes), then repeats a final time before the pulse's power falls below the critical power for RSF. Each RSF peak is less intense than the previous peaks on account of pump depletion, though the peaks are evenly spaced.

It should also be noted here that in these experiments, the self-focusing effect was observed for N_2 and higher-Z gases but not for helium. The reason for this is that nitrogen has more ionizable electrons than helium, meaning in turn that the plasma created from ionizing N_2 will have a greater electron density, ergo a greater plasma frequency and hence a lower critical power for RSF when compared to helium at the same atomic density, as per Eqns. (3.3.16) and (3.3.19). Thus, the laser exceeds the critical power for RSF when N_2 is used as the target, but not when helium is used.

Note that the explanation above explicitly assumes that the multiple focal peaks is due to charge displacement effects. There are actually several possible phenomena which could explain the modification of the refractive index necessary for RSF and for the focusing and refocusing behavior in Fig. 3.8b:

---

x   It is worth noting that diffraction and self-focusing usually have some interplay such that a self-focused pulse can "breath," that is, it can focus from self-focusing and then at some point begins to defocus due to diffraction, then refocus (self focusing), and so on.
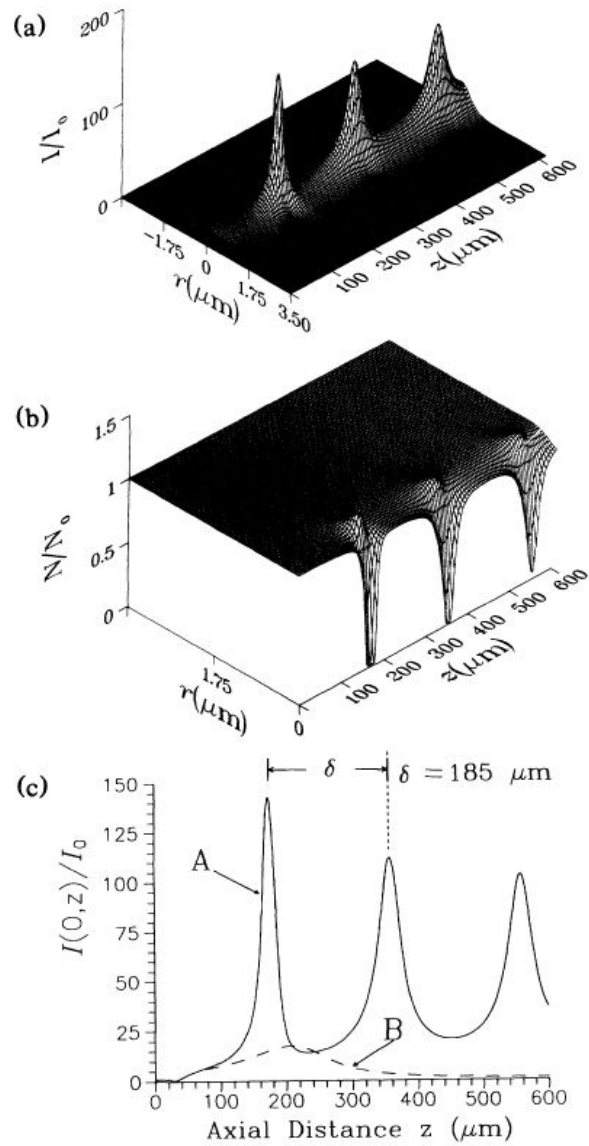
Figure 3.3.4: Calculations of beam intensity, plasma electron density, and the beam intensity profile evolution. This has been done for N_2 at density $n_e = 1.35 \times 10^{21}$ cm^{-3} and with laser power $P = 3 \times 10^{11}$ W and vacuum focus size $r_0 = 3.5$ μm. a) Intensity normalized to initial peak intensity, b) electron density normalized to the background density n_e, and c) normalized axial intensity profiles. The solid curve A includes both RSF and charge displacement and correspond to a lineout from a), whereas the dashed curve B neglects charge-displacement and results in a single focus of lower intensity than obtained with charge displacement included.

121

1. Kerr effect from the ions, which are not fully-ionized.

2. Ion motion, which has been neglected so far.

3. Charge displacement (e.g. cavitation).

4. Relativistic electron motion (RSF).

The Kerr effect may be discounted because the atoms in this experiment have their outer shells fully ionized, leaving only 1s electrons bound (or none at all in the case of helium). The pulse durations are short enough that ion motion can be neglected, and RSF mostly accounts for the first intensity peak α, but not for β or γ.

However, the charge displacement[143] cannot be discounted, as shown in Fig. 3.9. In essence, simulations show that the electrons are expelled from the region of highest laser-focused intensity, and that at this point the laser has begun to defocus. If the laser is undepleted, then it will continue to refocus and then defocus indefinitely, provided that filamentation does not first occur.

The charge displacement term adds a modification to the Eqn. (3.3.20) describing the evolution of the laser's spot size[138]

$$\frac{d^2 R}{d z^2} = \frac{1}{Z_{R0}^2 R^3} \left(1 - \frac{P}{P_{cr}} - \frac{\delta n(0)}{2 \Delta n_{cr}} R^{-2} \right) \tag{3.3.22}$$

The third term on the right hand side of Eqn. (3.3.22) governs the ponderomotive (charge displacement) contribution to the laser's spot size evolution. This term is also intensity-dependent such that the ponderomotive contribution alone will not overcome diffraction, that is $P/P_{cr} < 1$ implies that $\delta n(0) < 2 \, \Delta n_{cr}$, indicating that the ponderomotive channel

alone cannot guide the laser. It does, however, enhance the RSF effect such that the effective critical power required for self-focusing is

$$P_{cr} = 16.2 \times \left(\frac{\omega_L}{\omega_p} \right)^2 [GW] \tag{3.3.23}$$

More recent experiments have used pre-formed plasma channels to guide laser pulses, though RSF is a critical factor in many LWFA experiments. In particular, the modification of the laser's spot size has a significant impact on any LWFA experiments which attempt to access the bubble regime.

3.4   WHY TWO COLORS ARE BETTER THAN ONE

The introduction of a second laser pulse whose frequency ω_s is shifted slightly from the main laser pulse's frequency ω_L can be used to seed or suppress some of these laser-plasma instabilities. Additionally, if this frequency shift is small, $\omega_L - \omega_s \ll \omega_L$, then the group-velocity walk-off between the two pulses will be small, meaning that the second pulse can be used as a low walk-off velocity, co-propagating probe. Alternatively, the second pulse can be counter-propagated to the first pulse to make a slowly propagating colliding-pulse injector. In general, there are three instabilities which the second color laser is meant to control: forward Raman scattering, electromagnetic cascading, and relativistic self-focusing.

3.4.1 Seeded Forward Raman Scattering

Seeded forward Raman scattering (SFRS) works in a similar manner as a plasma beatwave accelerator (PBWA), with a few notable differences. For one, PBWAs use two lasers with similar amplitudes: usually, the weaker pulse intensity is >10% that of the stronger pulse. The second difference is that PBWAs typically use lower-density plasmas (n_e ~10^{16}-10^{17} cm^{-3}), on account of the fact that the two beating frequencies are close together. For example, Clayton *et al*. used two frequencies of a CO_2 laser to produce the beat which drives the plasma oscillations near-resonantly[144].

In the proposed SFRS experiments[145],[146], the plasma density may be $n_e > 10^{19}$ cm^{-3}, and the seed intensity is initially ~1% of the pump intensity. Furthermore, the pump itself may be weaker than in PBWA, requiring as little as 38 mJ in 100 fs as opposed to previous PBWA experiments, which used the CO_2 lines at 10.59 μm and 9.56 μm and delivered pulses at 12 J (10.59 μm) and 4 J (9.65 μm) in 2 ns[144] or 50 J split between the two lines in 1.2 ns[147].

As per the discussion in Sec. 3.1.2 above, the FRS instability undergoes exponential growth before saturation. The form of this growth is dependent upon the regime in which the FRS instability is operating (see Table 3.1.1 in Sec. 3.1.2), but for a sufficiently long interaction length and assuming the instability grows from noise, FRS will pass consecutively from 3-wave mixing to nonresonant 4-wave mixing and into resonant 4-wave mixing. In SFRS, the gain essentially skips the less efficient 3-wave mixing (or more-or-less spontaneous scattering) and nonresonant 4-wave mixing (transient) regimes and begins in the more efficient resonant 4-wave mixing regime.

The growth of the wakefield, $\chi = \delta n/n_0 - a_0^2/4$, is then given by[119]

$$\chi_S = \chi_{S0} \sum_{n=0}^{\infty} \left(\frac{\psi/c}{t - \psi/t} \right)^n I_{2n}(g) \rightarrow \chi_{S0} \frac{\exp(g)}{\sqrt{2\pi g}} \tag{3.4.1}$$

where the number of e-foldings increased $g = \Gamma \tau$ is given by

$$g_{1D1} = \frac{a_0 \omega_p^2}{2 \omega_L} \sqrt{(t - \psi/c)\psi/c} \tag{3.4.2}$$

where ψ is the distance from the head of the pulse and $\delta n/n_0$ is the electron density perturbation normalized to the background plasma density. In the limit where the laser's spot size is small, 3-D effects such as the 3-D envelope self-modulation (ESM) instability become dominant. In this instability, the plasma wave forms a periodic refractive index structure which acts as a series of converging (negative density perturbation) and diverging (positive density perturbation) lenses. The result is that the laser spot is focused along some of its longitudinal positions but defocused along others, which in turn leads to a longitudinal amplitude modulation of the pulse, which in turn caused even stronger wakefield excitation. In this regime, the growth is characterized by the ESM instability, whose gain is given by

$$g_{3D1} = \frac{3\sqrt{3}}{4} (2 k_p \psi)^{1/3} \left(\frac{a_0 ct}{w_L} \right)^{2/3} \tag{3.4.3}$$

where w_L is the laser's transverse spot size. The transition from the 1D to the 3D regime occurs as the gain g_{3D1} becomes larger than the gain g_{1D1}. There are three regimes for the gain to be defined:

1. $g \gg 1$, in which the FRS or ESM instability grows very rapidly and achieves saturation quickly.

2. $g > 1$, in which the instability grows, but depends on the initial perturbation to the plasma density.

3. $g \leq 1$, in which the gain is insufficient for the instability's growth.

As an example, an 800 nm Ti:Sapph laser delivering 1 J on-target in 100 fs (10 TW) with a focused spot size of 10 μm ($I = 3.18 \times 10^{18}$ W/cm^2, $a_0 = 1.21$), whose target is a plasma of density 1×10^{19} cm^{-3} (e.g. $\omega_p/\omega_L = 0.07578$) over a 1 mm interaction length (3.34 ps interaction time; this is comparable to the dephasing length, as per Sec. 1.4) will produce a gain of $g_{1D1} \approx 6.80$ and $g_{3D1} \approx 19.0$. This system would operate between the second and third regimes.

If the laser's energy is much lower than this 1 J on-target parameter, or if a larger spot size is chosen, etc., then this interaction would be in the second regime. In this case, the FRS and ESM instabilities grow but not very rapidly, and wavebreaking will not occur unless a significant plasma density perturbation[xi] is present prior to the laser's interaction with the plasma. Hence, there are two options for a lower-energy laser: seed the plasma density perturbation (e.g. with a second high-power pulse or particle "pre-driver"), or seed the FRS instability by using a second color laser pulse.

This second color pulse can be of low-amplitude: for an undepleted pump, the expected gain is a factor of ~900 in the second color via SFRS. It should co-propagate

---

xi It should be noted that for a laser pulse whose duration is several plasma periods, the back of the pulse actually can experience some significant seeding on account of the perturbation driven by the front of the pulse. A pulse with 10 J in 1 ps will self-seed where a 1 J in 100 fs pulse won't.

with the pump with a frequency offset such that the beat between the two will drive FRS resonantly. The early perturbation used in Eqn. (3.4.1) to calculate later perturbation can be obtained for both the seed (χ_{SS0}) and for the background perturbation (χ_{BS0}), and their relative importance can be compared[145]:

$$\frac{\chi_{BS0}}{\chi_{SS0}} = \frac{1}{\sqrt{2}\pi} \frac{\lambda_p^3}{L^3} \frac{a_0}{a_{0seed}}$$

(3.4.4)

so that the seed becomes significant when

$$\frac{a_{0seed}}{a_0} > \frac{1}{\sqrt{2}\pi} \frac{\lambda_p^3}{L^3}$$

(3.4.5)

A set of 1D particle-in-cell (PIC) simulations have been employed to determine the optimum amplitude of the seed relative to the pump, assuming that the seed frequency is shifted from the pump frequency by the plasma frequency: $\omega_s = \omega_L - \omega_p$. Thus, the seed's intensity is varied relative to the pump intensity, and the peak and total energies of accelerated electrons are plotted against the normalized seed vector potential in Fig. 3.10. Note that the total laser energy is the same in all simulations, meaning that if the seed energy is increased, the pump energy is decreased. This is akin to beginning with a laser operating at a single frequency band and then splitting off a fraction of the energy to generate a second frequency band (e.g. by Raman shifting it). The seed is then the shifted portion of the energy and the pump the unshifted portion. The simulation is then shown for two possible efficiencies of shifting, denoted by the solid (100% efficiency) and dashed (30% efficiency) lines in Fig. 3.10. As Fig. 3.10a shows, the optimum seed under these conditions has an intensity of ~1% of the pump's intensity.

127

a)

b)
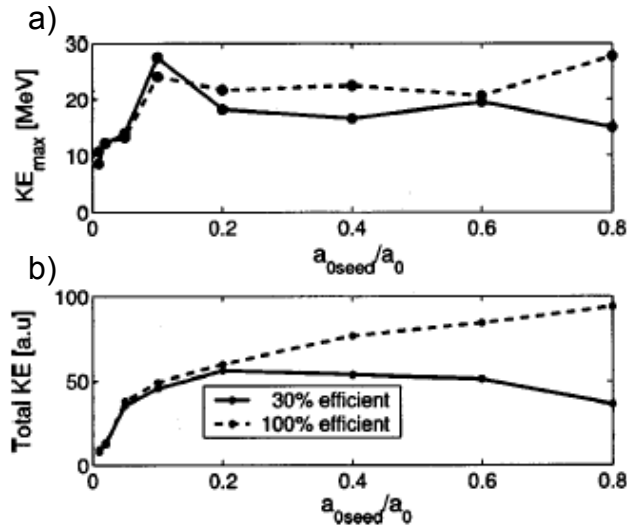
Figure 3.10: Electron energy vs normalized seed vector potential[146]. a) Peak electron kinetic energy and b) total electron energy, assuming either 100% conversion efficiency (solid) or 30% conversion efficiency (dashed) for the seed pulse.

a)   b)
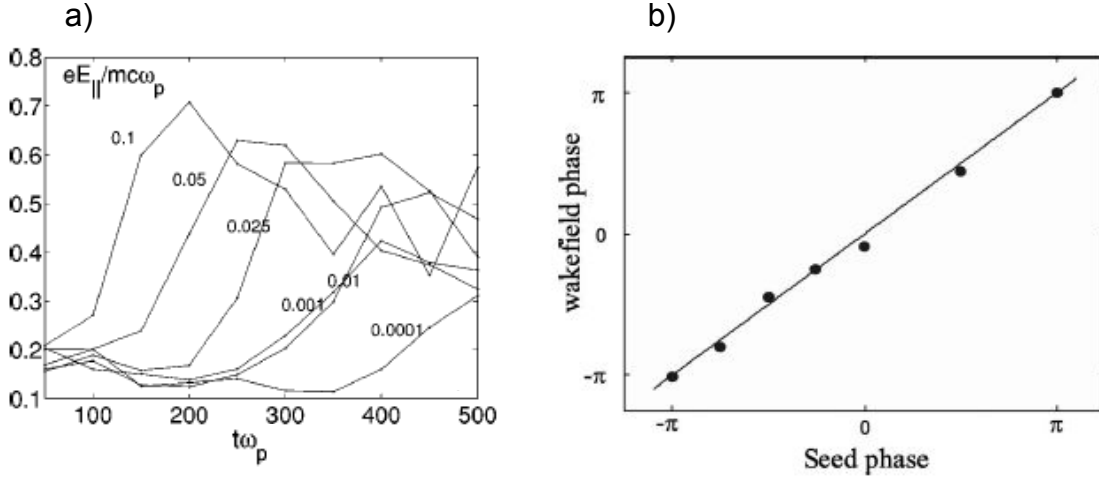
Figure 3.11: The effects on the wakefield of varying the seed's initial amplitude and phase[145]. a) Wakefield amplitude evolution in time for several initial seed amplitudes. b) Wakefield phase vs seed phase w.r.t. pump. In both cases, the pump's normalized vector potential is $a_0 = 0.5$ and the laser-to-plasma ratio is $\omega_L/\omega_p = 6$.

128

Additional 1D PIC codes show that the seed's parameters can be used to control the amplitude and phase of the excited plasma wave. The effects of changing the seed's amplitude and phase are shown in Fig. 3.11. It should be noted that in Fig. 3.11a, the pump's normalized vector potential is 0.5 and the ratio of plasma density to pump density is $\omega_L/\omega_p = 6$. For a Ti:Sapphire laser centered at 800 nm whose focal spot size is 10 μm, this is equivalent to a pump power of 17.5 TW, a Rayleigh time equivalent to 500 on the time scale of Fig. 3.11, and a plasma density approaching 4.8×10^{19} cm^{-3}. Therefore, the SFRS instability grows very rapidly from even a small seed, with the time required to reach a maximum amplitude (e.g. wavebreaking) and the actual amplitude the wakefield reaches being controllable by adjusting the amplitude of the seed. In general, a larger seed amplitude leads to both a larger wakefield amplitude and a faster rise time to that amplitude.

Furthermore, the phase of the seed is shown to control the phase of the wakefield, which is of especial interest for generating a multi-stage accelerator (see Chapter 2, Sec. 2.5.2). This result works under the assumption that two gas jets are used in series to create the multi-stage accelerator, and that each of the stages (e.g. jets) is pumped independently, that is, the pump and seed are both split into two branches, with one branch pumping the first sage and the other pumping the second stage. The phase between the pump and seed itself is random, but the phase difference between the two stages can be controlled, which according to Fig. 3.11b means that the phase of the wakefield in the second stage with respect to that of the first stage can be controlled. This

is crucial for creating a multi-stage accelerator: without the seed, the FRS or ESM instability would grow from random noise, and hence would have random phase—which in turn would mean that the second stage could act to accelerate or decelerate the injected electron bunch at random. Thus, the seed acts in an analogous manner to quasi-phase-matching in nonlinear optics.

Simulations using 2D PIC codes also suggest that seeding the FRS instability leads to improvements in electron energy and charge when compared to the unseeded sm-LWFA. For example, the total charge of "hot" electrons produced with energy > 1MeV is expected to be ~0.62 nC using a 38 mJ pump and 10 μm spot size and a $a_{0seed}/a_0 = 0.1$; this is comparable to the ~1 nC generated in unseeded experiments using a 500 mJ laser pulse[148]. The former energy is attainable today with kHz repetition rates, but the latter is not, so SFRS offers a possible method for generating a kHz source of hot electrons.

3.4.2 EMC Beatnote Generation and Compression

Electromagnetic cascading produces a series of beat-note sidebands which can then be compressed into a train of few-femtosecond pulses. This is done by sending in a laser pulse operating around two frequency bands whose beat frequency $\Omega = \omega_0 - \omega_1 < \omega_p$. These drive an electron plasma wave (EPW) which ultimately creates a refractive index grating which is co-moving with the two pulses. Scattering from the EPW then creates a series of Stokes and anti-Stokes sidebands which are shifted by Ω from the initial pulse frequency bands. If the EPW is driven below resonance $\Omega < \omega_p$, it produces sidebands which are initially positively chirped[149]: the red Stokes sidebands lead the blue anti-

Stokes sidebands (with lower orders being nearer to the center of the train). Since plasma is anomalously dispersive, the GVD of a plasma is such that the blue part of the spectrum can outrun the red part, which in this case results in the compression of the beatnotes.

A similar method of compressing a cascade (albeit, a Raman cascade) at lower intensity in molecular gases has been suggested[150],[151],[152] and observed[153],[154]. In these experiments, the intensity is limited to relatively small values; for example, Shverdin *et*
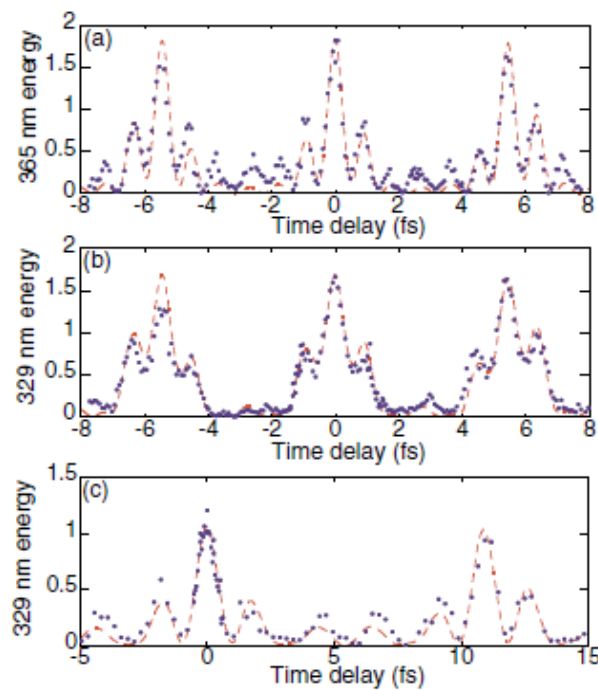
Figure 3.12: Correlations of several single-cycle waveforms generating by coherent control of 4-wave mixing[xi]. The phases of several independent Raman sidebands are controlled using independently using a liquid crystal modulator. The blue dots are measured correlations (50 shots averaged), the red dashes are the theoretical trace. The measurements are done for signals at a) 365 nm, b) 329 nm, and c) delaying a pulse consisting of the three highest frequencies wrt the four lowest frequencies.

al. use ~1 GW/cm^2 to drive the interaction, and produce a 1 MW pulse whose duration is ~1.6 fs. The results of this experiment are shown in Fig. 3.12.

Beatnote generation and compression is meant to operate at higher intensities in a plasma, e.g. with initial intensities of 10^{16} W/cm^2 or higher. The concept is ultimately to use a plasma to first generate a series of sidebands through EMC, and then to use GVD to compress these sidebands into a train of ultrashort pulses[155]. Ideally, this process can be broken into two stages, the conceptual illustration of which is shown in Fig. 3.13. The first stage is a modulator with a low plasma density and low beat frequency: this would result in the generation of many sidebands which are closely spaced in frequency, and in low GVD so that the various sidebands retain a coherent chirp. The second stage is a compressor at higher plasma density (and hence a greater GVD). Additionally, FRS can interfere with the modulation process and with the chirp of the generated pulses, and so should be avoided[149]: this is more easily done in a low-density modulator.

If the two stages are separated as described, then it is possible to obtain analytic scaling laws for the frequency modulation and compression process[149],[156]. The envelope equations become

$$\left[2\mathrm{i}\,\frac{\omega_l}{v_g}\frac{\partial}{\partial z} - \frac{d}{v_g^2}(\omega_l - \omega_0)^2 \right] a_l \approx k_p^2 \left(C_l - R_l^a - R_l^q \right) \tag{3.4.6}$$

where $k_p = \omega_p/c$ and $d = n_0/n_{cr}$ is the normalized electron density of the modulator plasma. This equation takes into account the propagation of sidebands through the plasma with the first term on the left hand side ("LHS"), the GVD of the sidebands (second term on LHS), and sideband coupling via nonlinearities (the rights hand side "RHS"). The three
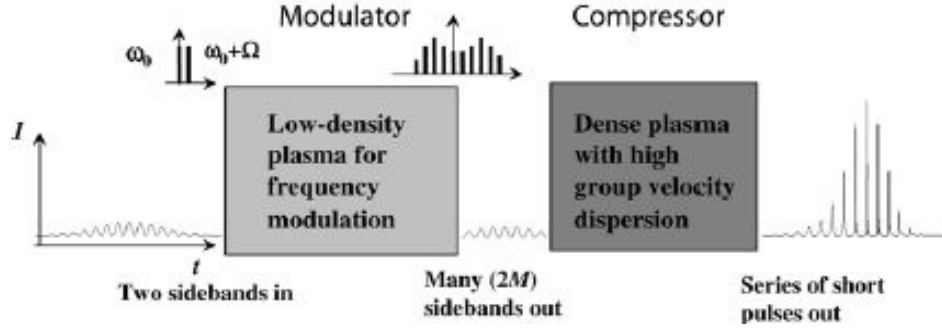
Figure 3.13: A conceptual representation of the two-stage plasma beatnote compressor system[x]. Two frequency sidebands, ω_0 and $\omega_l = \omega_0 + \Omega$ are initially incident on a low-density plasma with $\omega_p > \Omega$. This low-density plasma acts as a frequency modulator by generating many positively-chirped sidebands via electromagnetic cascading, and these sidebands are then incident on a higher density plasma with greater (anomalous) GVD. This second plasma acts as a compressor, which results in a train of shorter compressed pulses out of the system.

nonlinear terms are C_l, which couple neighboring sidebands and describe the near-resonantly-driven harmonics of the EMC and forward Raman cascade; R_l^a and R_l^q, which describe nonlinear frequency shifts due to relativistic mass increases in electrons oscillating in the transverse field and non-resonantly-driven EPW (for R_l^a), and the longitudinal and near-resonantly-driven harmonics of the EPW (for R_l^q) fields of the non-resonantly driven EPW. If $v_g \approx c$, then Eqn. (3.4.6) can be written as

$$\left[\frac{2i}{k_0}\frac{\partial}{\partial z} - d\left(\frac{\omega_l - \omega_0}{\omega_0}\right)^2 \frac{\omega_0}{\omega_l}\right] a_l \approx d\,\frac{C_l - R_l^a - R_l^q}{\omega_l/\omega_0} \qquad (3.4.7)$$

In the compressor, the GVD is large but not resonant with the beat pulses (e.g. the plasma frequency is not near an integer multiple of Ω). Since this plasma is nonresonant, the near-resonant coupling term R_l^q should be negligible, and so it can be ignored.

133
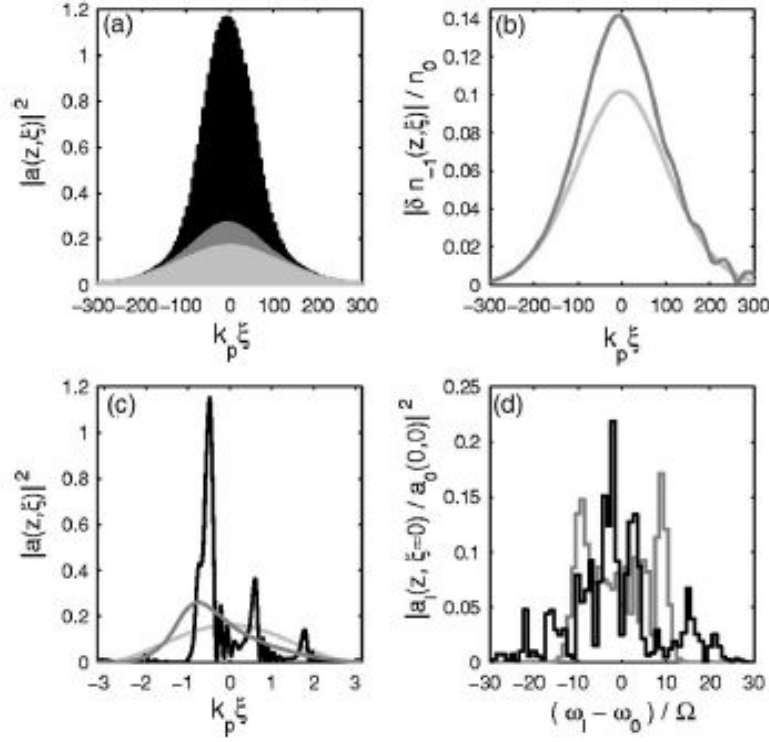
Figure 3.14: Cascade compression in two stages, modulator and then compressor[149]. The quantities are shown at the entrance to the modulator (light gray), at the exit of the modulator which is also the entrance to the compressor (dark gray), and at the exit of the compressor (black). The quantities plotted are a) the laser pulse intensity, where the time window includes 100 beat notes; b) the normalized amplitude of the near-resonant EPW, $\delta n_{-1}/n_0 = N_e/d$; c) the beat note intensity near the pulse center; and d) the laser spectra near $\xi = 0$. These plots include nonlinearities and GVD in both stages.

Therefore, the compression process can be described by an equation which has a similar form to Eqn. (3.4.7):

$$\left[\frac{2i}{k_0} \frac{\partial}{\partial z} - d_C \left(\frac{\omega_l - \omega_0}{\omega_0} \right)^2 \frac{\omega_0}{\omega_l} \right] a_l \approx d_C \frac{C_l^{(C)} - R_l^{a(C)}}{\omega_l/\omega_0} \tag{3.4.8}$$

The solution to Eqn. (3.4.7) in the limit where both R terms are 0 and the GVD is ignored (d~0) are then analytic:

$$a_l(z, \xi) = \sum_{\sigma=0,1} a_\sigma(0, \xi) e^{i(l-\sigma)(\theta+\pi)} J_{l-\sigma}(2W) \tag{3.4.9}$$

where θ, ψ, W have the same definitions as used in Eqn. (3.2.6). This implies that a slab of thickness $z_M = 2M/(N_e k_0)$ will produce M sidebands on each side of the fundamental frequency, with a total bandwidth of $\Delta\omega \sim 2d^{1/2}M\omega_0$. Alternatively, $M \sim r_e z_M l_0 |n_e - n_0|$ where $r_e = e^2/(m_e c^2)$ is the classical electron radius. The peak compression in an unperturbed compressor for which $C_l^{(C)} - R_l^{a(C)} \approx 0$ will occur at a distance

$$z_C = \frac{\pi/3}{k_0 M} \left(\frac{\omega_0^2}{\omega_{p(c)} \Omega} \right)^2 \tag{3.4.10}$$

The results of some simulations using Eqns. (3.4.7) and (3.4.8) with the boundary conditions N_e (z, $\xi = -\infty$) and $a_0(0, \xi) = a_1(0, \xi) = A e^{-\xi^2/(c\tau_L)^2}$ are shown in Fig. 3.14. In general, the laser's peak intensity has increased by a factor of ~7.2 at the exit of the compressor when compared to at the entrance of the modulator, with duration being compressed form 120 fs at the entrance to the modulator and 13 fs at the exit to the compressor. Figure 3.14c shows that the pulses become relativistic in the compressor, and thus compression is taking place in the nonlinear regime. Therefore, the sidebands are further coupled in the compressor and the bandwidth of the laser is further increased, so that the bandwidth at the exit of the compressor is nearly twice that of the bandwidth at the exit of the modulator, as shown in Fig. 3.14d. The parameters in Fig. 3.14 for the two-stage compressor are that the initial laser amplitude is $A = 0.2$, the modulator has density $n_0 = 8.75 \times 10^{17}$ cm^{-3} and $d = 5 \times 10^{-4}$, and the compressor density is $n_{0(c)} = 25 n_0 = 2.19 \times 10^{19}$

cm^{-3}. Note that for a laser of fundamental wavelength $\lambda_0 = 800$ nm, the first Stokes must

be at wavelength $\lambda_1 < 818$ nm to satisfy the condition $\Omega \equiv \omega_0 - \omega_1 < \omega_p$.

The beatnote compressor does not necessarily need occur in two stages. For the one-stage compressor whose results are shown in Fig 3.15, the plasma density is $n_0 = 1.75 \times 10^{18}$ W/cm^2 (d $= 10^{-3}$) and the laser's fundamental is centered at 800 nm with duration 560 fs, the compressed pulses see an almost 10-fold increase in intensity (Fig. 3.15a). Furthermore, the plasma is sufficient to generate 30 total sidebands (15 on each side of the fundamental); however, GVD causes the spectrum to favor the red, as shown in Fig. 3.14b—without dispersion included (green curve), the spectrum is symmetric about the fundamental, but with GVD the spectrum is markedly more red than blue (black bars). The electron density perturbation also grows 7-fold along the laser's path, which is some interest to electron acceleration.
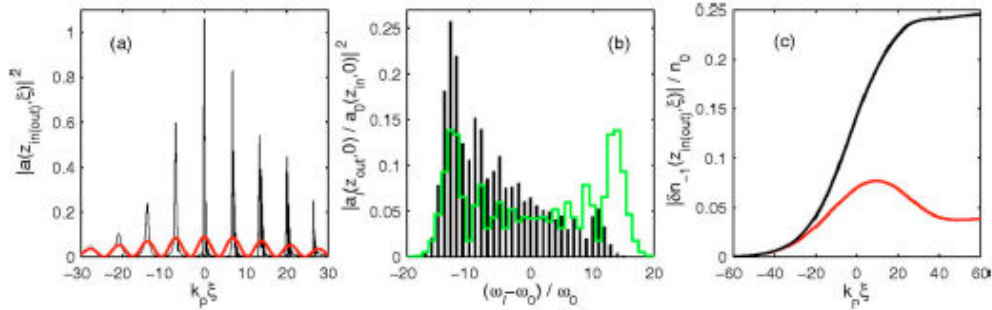
Figure 3.15: Single-stage beatnote compressor with EMC and compression in a single plasma[ix]. a) The laser intensity is show at the entrance (red) and exit (black) of the 3.2 cm long plasma. The time window shows 9 beat notes near the pulse's center. b) Amplitudes (black bars) of the cascade components at the plasma output and the spectrum (green) without dispersion at the position $z = z_{15}$ (e.g. 15 sidebands produced on either side of the fundamental) and the retarded time $\xi = tv_g - z = 0$. c) The normalized amplitude of the near-resonant EPW component, $|\delta n_{-1}|/n_0 = |N_e|/d$, is plotted at the plasma's entrance (red) and exit (black).

The single-stage beatnote compressor is therefore feasible, and the set-up is certainly less complicated, since the plasma can be of uniform density. With that said, there does exist a variety of schemes for producing a plasma of nonuniform density, e.g. of low initial density at the beginning (stage 1 modulator) and then higher density at the end (stage 2 compressor). Some examples of this are discussed in Chapter 1 of this dissertation in the context of plasma density ramping for particle injection purposes (see Sec. 1.3.3).

3.4.3 Enhanced or Suppressed Relativistic Self-Focusing

The relativistic self-focusing instability may be controlled (enhanced or suppressed) by the use of a two-color laser system[157],[158],[159]. The control of the optical guiding (focusing, defocusing, or ~same area propagation) can be managed by shifting the plasma frequency with respect to the lasers' beat frequency. This effect is a transverse analogue to the electromagnetic cascading (EMC) beatnote generation and compression discussed in Secs. 3.2 and 3.4.2, and EMC is predicted to occur in the regime where RSF-enhancement or -suppression is optimized. Therefore, RSF control can be described analytically in early stages, but requires numerical simulations as the pulses propagate and EMC progresses.

The vector potential at the boundary (plasma entrance) should describe a two-color laser:

$$a(\vec{r}_\perp, 0, \xi) = e^{-ik_0\xi}[a_0(\vec{r}_\perp, 0, \xi) + a_1(\vec{r}_\perp, 0, \xi)e^{-ik_\Omega\xi}] \qquad (3.4.11)$$

where $\vec{r}_\perp$ is the transverse direction, $\xi = ct - z$ is the retarded time, $\Omega = \omega_0 - \omega_1 << w_0$ is the difference frequency between the two colors, and $k_\Omega = \Omega/c$ and $k_0 = \omega_0/c$. Inside the plasma, the ponderomotive force form the two-color beat wave will generate a co-moving modulation of the refractive index which will lead to the production of laser sidebands in an EMC as described above. If these sidebands are ignored—they can be for $0 \leq z \leq Z_R/4$, where Z_R is the Rayleigh length—then the lasers and plasma wave obey the set of coupled paraxial equations[vii]

$$\left(2 i k_l \partial / \partial z + \Delta_\perp \right) a_l \approx k_l^2 \left(1 - \eta_l^2 \right) a_l \tag{3.4.12a}$$

$$\eta_l^2(r) - 1 = \left(k_p / 2 k_l^2 \right) \left[|a_l(r)|^2 + 2 C |a_m(r)|^2 \right] \tag{3.4.12b}$$

$$C = 1 - C_N \equiv 1 - \frac{\Omega/(2\omega_p)}{(\Omega/\omega_p)^2 - 1} \tag{3.4.12c}$$

where C is the cross-focusing coefficient, ω_p is the plasma frequency, and the subscripts (l, m) are (1, 0) and (0, 1). The cross-focusing coefficient C is plotted against the normalized beat frequency Ω/ω_p in Fig. 3.16. The vector potentials and hence the refractive index all vary with transverse distance form the laser axis: all three are peaks on-axis and then fall off either monotonically with distance (for a Gaussian profile) or fall off monotonically to some minimum value (e.g. in a sinc profile).

Therefore, in Eqn. (3.4.12b), the first term on the RHS describes relativistic self-focusing whereas the second describes cross-focusing between the two colors. According to Eqn. (3.4.12c) and Fig. 3.16, the cross-focusing effect enhances self-focusing if C>0
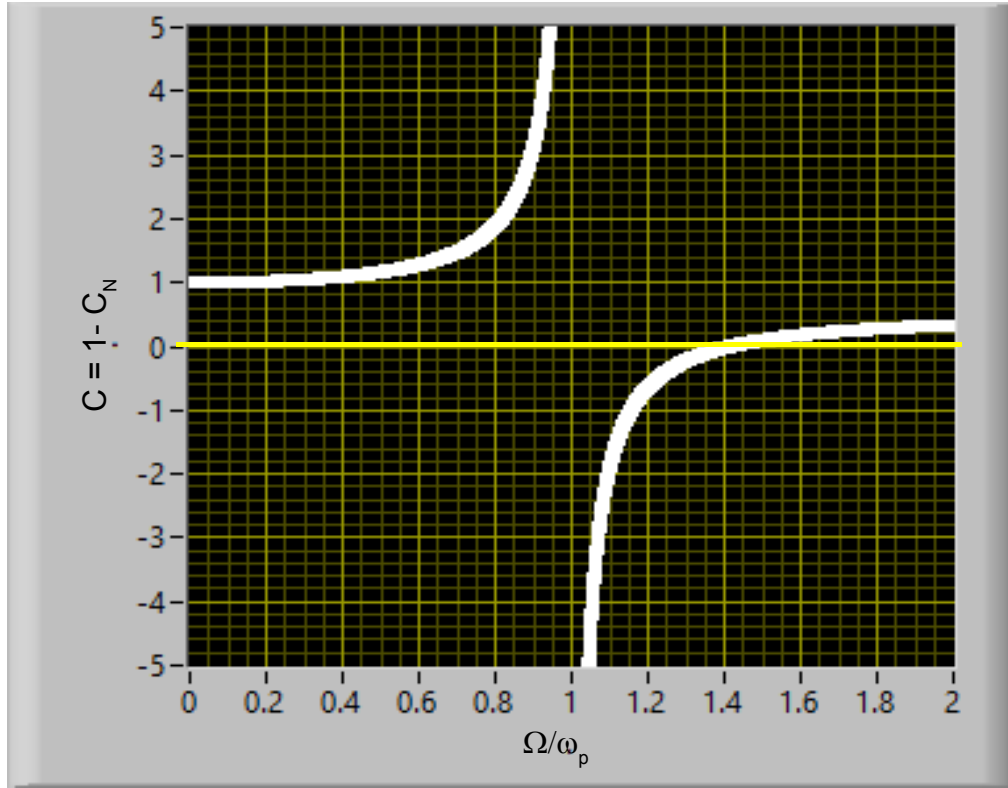
Figure 3.16: The cross-focusing coefficient as a function of normalized beat frequency. When C > 0, the cross-focusing enhances self-focusing, but when C < 0, the cross-focusing suppressed self-focusing. This latter condition is satisfied when the normalized beat frequency is in the range $1 < \Omega/\omega_p < 2^{1/2}$.

(which occurs when $\Omega < \omega_p$), but it suppresses[xii] self-focusing if C<0 (which occurs when $\Omega > \omega_p$). Furthermore, although the value of C is fixed once frequencies of the two colors and of the plasma are determined, it is possible to choose C, a_l, and a_m such that both lasers undergo defocusing or mutual guiding. The lasers' spot sizes evolve according to[vii]

$$\frac{\partial^2 r_l}{\partial z^2} = \frac{4}{k_l^2 r_l^3}\left[1 - (P_l/P_{cr}) - \frac{8C(P_m/P_{cr})r_l^4}{(r_m^2 + r_l^2)^2}\right] \tag{3.4.13}$$

---

xii The reader will note that this is actually a rule of thumb only. Once $\Omega^2 > 2\omega_p^2$, C > 0 again, and cross-focusing again enhances RSF. Similarly, $\Omega < 0$ only implies that the two lasers have switched roles (e.g. $\omega_0 < \omega_1$ instead of $\omega_0 > \omega_1$).

where P_l and P_m are the instant powers of the lth and m^{th} beams, and the normalizing factor P_{cr} is the critical power of a single monochromatic beam. The stationary points of Eqn. (3.4.13) correspond to mutual guiding of both beams, meaning that match propagation is achieved when the power P_l, the cross-focusing coefficient C, and the area ratio $R = (r_{00}/r_{01})^2$ satisfy

$$\frac{P_l}{P_{cr}} = (1+R)^2 \left[\frac{(1+R)^2 - 8CR^{2m}}{(1+R)^4 - 64\,C^2\,R^2} \right] \tag{3.4.14}$$

With the aide of cross-focusing, it therefore becomes possible for the two beams to guide each other through the plasma even when both have less than the critical power for self-focusing. In general, the higher-power beam with larger spot size tends to guide the lower-power beam with smaller spot size.

It should be noted that once EMC gets underway, the two-color approximation is no longer valid because of the presence (and even dominance) of other frequency sidebands. Further, the effect of cascading is in general to focus the beams, and EMC has in fact been proposed as a method for guiding a lower-than-critical power beam through a plasma[129] under certain conditions.

Thus, the EMC further enhances RSF in the regime where C > 0 and hinders RSF suppression in the regime where C < 0. This two-color model is therefore accurate for predicting the initial stages of the pulses' propagation through the plasma, but begins to break down after ~ z = 0.25 Z_R as the EMC begins to occur. After z = Z_R, the EMC begins to saturate and the resonant response FRS will begin to suppress it. The simulation results of laser peak intensity evolution in the plasma is plotted in Fig. 3.4.9.

140
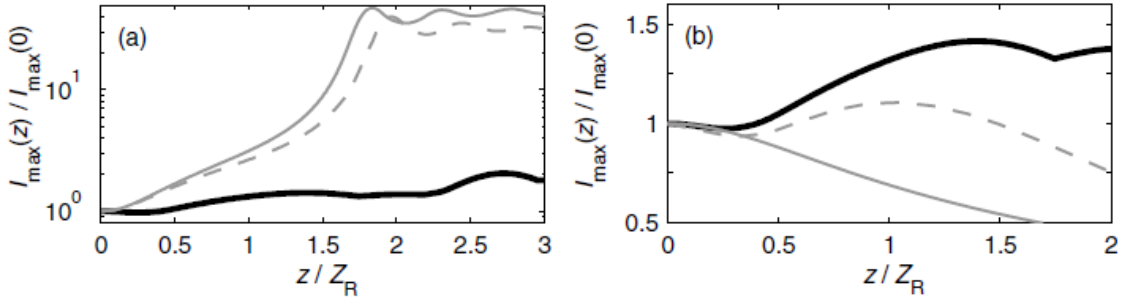
Figure 3.17:   Laser peak intensity evolution as the pulses propagate through the plasma[vii]. a) WAKE simulation results for monochromatic (solid gray), two-color laser with Ω/ω_p = 3.18 (dashed gray), and two-color laser with Ω/ω_p = 1.25 (solid gray). b) Comparison between results of fully relativistic WAKE code (black), the model from Eqns. (3.4.11-14) for two-color laser propagation (solid gray), and a cascade simulation which accounts for local electron response and EMC (dashed gray).

In Fig. 3.4.8, the total power of the two beams always exceeds the critical power for RSF at the plasma entrance: $P_0 + P_1$ = 1.1 P_{cr}, where the power partition is P_0/P_1 = 17/3 for a two-color beam or P_1 = 0 for a monochromatic beam. The simulations show that self-focusing can be suppressed for a two-color beam provided that the two frequencies are near enough to the plasma resonant frequency (that is, provided that the value of C is sufficiently large and negative). Thus, the far-from-resonant case of Ω/ω_p = 3.18 behaves similarly to the monochromatic case—RSF followed by electron cavitation and then a guided beam after $z=2Z_R$—while the near-resonant Ω/ω_p = 1.25 case shows some initial suppression of the RSF and only mild focusing in later stages. Some simulated laser intensity isocontours and axial lineouts are show for these three scenarios in Fig. 3.18.
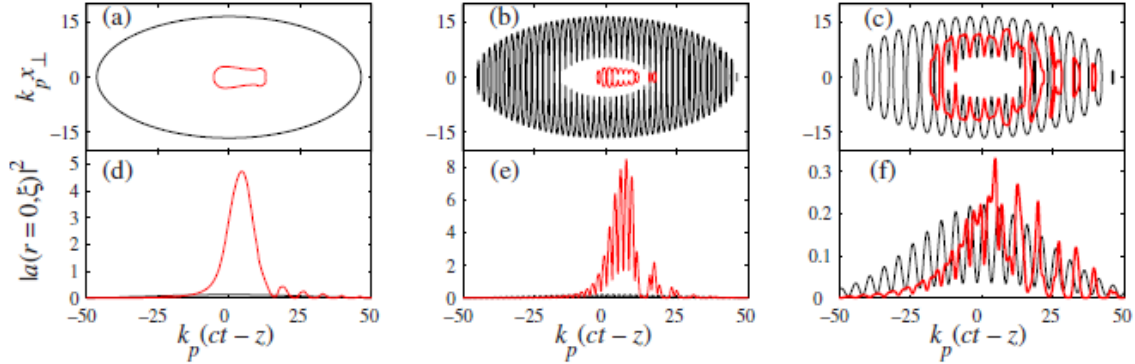
Figure 3.18: Radial and axial profiles of the laser taken at plasma entrance and exit for monochromatic and two-color beams[viii]. In all cases, the entrance (black) is taken to be at z=0 and the exit (red) is at $z = 2Z_R$, with the top three (a-c) showing the $1/e^2$ intensity isocontours and the bottom (d-f) showing the corresponding axial lineouts. The leftmost column (a and d) is for a monochromatic beam with $P = 1.1P_{cr}$. The middle column (b and e) is for two-color beam with $\Omega/\omega_p = 3.18$, $P_0/P_1 = 1.1$, and $P_0 + P_1 = 1.1P_{cr}$. The rightmost column (c and f) is for two-color beam with $\Omega/\omega_p = 1.25$, $P_0/P_1 = 1.1$, and $P_0 + P_1 = 1.1P_{cr}$.

These mostly confirm the results from Fig. 3.17, namely that the beam will focus via RSF unless the two sidebands have a near-resonant beat frequency. There are, however, a few points of interest found in Fig. 3.18 which would be missed in Fig. 3.17. The isocontours in Fig. 3.18 are showing the effective longitudinal axis (via retarded time) along the x-axis, and (for 3.18a-c) the y-axis is actually showing the transverse direction. Hence, the initial elliptical contour shape corresponds to a pulse which is longer in time than its transverse extent. This implies that the output contours are not only smaller in transverse spatial extent (RSF/transverse focusing), but also in longitudinal extent (e.g. compression of the pulse duration).

It also implies that the back part of the two-color near-resonant pulse for which RSF has been suppressed is also eroded. This is in part because of the pulse compression

142

described above, and in larger part due to the fact that as the pulse propagates, it first drives an EMC and a nonresonant plasma response, and then later begins to drive a resonant response as the EMC saturates and FRS begins to dominate.

This is also the explanation for why the two-color envelope model becomes less successful at predicting the behavior of the pulse after a short propagation distance, and why even the code with EMC and local electron response gives a different result from WAKE. All three initially give the same results in Fig. 3.17b, up until the beam has propagated for $z = 0.25Z_R$. Up until this point, the laser consists of two significant sidebands.

However, the EMC generates additional sidebands, whereas the two-color envelope propagation model only makes allowance for two such sidebands: thus, the simple analytic model predicts that the two beams will continue to defocus monotonically as they propagate, whereas more extensive simulations show that they will continue defocusing until $z \approx 0.5Z_R$, after which the beams begin to focus, albeit far less rapidly than in the case of monochromatic RSF. The EMC response begins to saturate after $z \approx Z_R$, and as a result the simulation considering only EMC with local electron response differs somewhat from the WAKE simulation results. The nonresonant plasma density perturbation which causes EMC gradually decays and is replaced by the resonant plasma response causing FRS, so that the laser's output spectra should include some weak Raman features shifted from the fundamental by integer multiples of ω_p.

Finally, because the plasma waves evolve as the pulse propagates, the cross-focusing coefficient is not actually constant during propagation. Rather, it gradually decays as the additional sidebands cause the propagating pulses' beat to become less and less resonant with the plasma. This means that the initial effect of defocusing gradually gives way to mild focusing. Nevertheless, these simulations predict that the two-color pulse will suppress or at least considerably weaken RSF: after $z = 3\ Z_R$ (16 cm, according to the parameters of the simulation), the near-resonant two-color pulse intensity had increased by only a factor of ≈ 2, as opposed to ≈ 40 for the monochromatic or non-resonant two-color pulses—with only a $\approx 5\%$ energy loss. The transverse spot size for the two-color pulse is moreover reduced by a factor of $\approx (1/2)^{1/2}$ as opposed to a factor of ≈ 5 for the monochromatic case. Therefore, adding a second color to the laser system gives a method for suppression RSF in plasmas. It is the generation of that second color that this work turns in the next chapter.

Chapter References

[102] A. Smekal, "Zur Quantentheorie der Dispersion," *Naturwissenchaften*, Vol. **11**, 873-875, 1923.

[103] C.V. Raman, "A new radiation," *Indian J. Phys.,* Vol. **2**, 387-398, 1928.

[104] C.V. Raman and K.S. Krishnan, "A New Type of Secondary Radiation," *Nature,* Vol. **121**, 501-502, 1928.

[105] G. Landsberg and L. Mandelstam, "A new occurrence in the light diffusion of crystals," *Naturwissenchaften*, Vol. **16**, 557-558, 1928.

[106] E.J. Woodbury and W.K. Ng, *Proc. I.R.E.*, Vol. **50**, 2367, 1962.

[107] G. Eckhardt, R.W. Hellwart, F.J. McClung, S.E. Schwartz, D. Weiner, and E.J. Woodbury, "Stimulated Raman Scattering from Organic Liquids," *Phys. Rev. Lett.*, Vol. **9**, 455-457, 1962.

[108] N. Bloembergen, "The stimulated Raman effect," *Am. J. Phys.*, Vol. **35**, 989, 1967.

[109] R.W. Hellwarth, "Theory of stimulated Raman scattering," *Phys. Rev. A*, Vol. **130**, 1850, 1963.

[110] M. Belkin, personal communication, November 3 2011. M. Belkin, "Spontaneous and stimulated Raman scattering" [pdf], November 3, 2011, retrieved from http://blackboard.utexas.edu

[111] Yariv, Amnon (1989), *Quantum Electronic, Third Edition* (pp. 459-464), New York, John Wiley and Sons.

[112] Boyd, R.W. (2003), *Nonlinear Optics, Second Edition* (pp. 452-457), Elsevier, Academic Press.

[113] Boyd, R.W. (2003), *Nonlinear Optics, Second Edition* (pp. 462-465), Elsevier, Academic Press.

[114] M.C. Downer, personal communication, March 12, 2009.

[115] T.M. Antonsen, Jr. and P. Mora, "Self-focusing and Raman scattering of laser pulses in tenuous plasmas," *Phys. Rev. Lett.*, Vol. **69**, pp. 2204-2207 (1992).

[116] E. Esarey, P. Sprangle, J. Krall, and A. Ting, "Overview of Plasma-Based Accelerator Concepts," *IEEE Trans. Plas. Sci.*, Vol. **24**, No. 2, pp. 252-288 (1996).

[117] W.B. Mori, C.D. Decker, D.E. Hinkel, andT. Katsouleas, "Raman forward scattering of short high-intensity lasers," *Phys. Rev. Lett.*, Vol. **72**, pp. 1482-1485 (1994).

[118] J. Krall, A. Ting, E. Esarey, P. Sprangle, and G. Joyce, "Enhanced acceleration in a self-modulated laser wakefield accelerator," *Phys. Rev. Lett.*, Vol. **48**, pp. 2157-2161 (1993).

[119] C.D. Decker, W.B. Mori, T. Katsouleas, and D.E. Hinkel, "Spatial temporal theory of Raman forward scattering," *Phys. Plasmas*, Vol. **3**, No. 4, pp. 1360-1372 (1996).

[120] G. Shvets, personal communication, November 23, 2011.

[121] C.-H. Pai, M.-W. Lin, L.-C. Ha, S.-T. Huang, Y.-C. Tsou, H.-H. Chu, J.-Y. Lin, J. Wang, and S.-Y. Chen, "Backward Raman Amplification in a Plasma Waveguide," *Phys. Rev. Lett.*, Vol. **101**, 065005 (2008).

[122] C.A. Coverdale, C.B. Darrow, C.D. Decker, W.B. Mori, K.-C. Tzeng, K.A. Marsh, C.E. Clayton, and C. Joshi, "Propagation of Intense Subpicosecond Laser Pulses through Underdense Plasmas," *Phys. Rev. Lett.*, Vol. **74**, No 23, pp. 4659-4663 (1995).

[123] D. Umstadter, S.-Y. Chen, A. Maksimchuk, G. Mourou, and R. Wagner, "Nonlinear Optics in Relativistic Plasmas and Laser Wake Field Acceleration of Electrons," *Science*, Vol. **273**, No. 5274, pp. 472-475 (1996).

[125] A. Modena, Z. Najmudin, A.E. Dangor, C.E. Clayton, K.A. Marsh, C. Joshi, V. Malka, C.B. Darrow, and C. Danson "Observation of Raman Forward Scattering an Electron Acceleration in the Relativistic Regime," *IEEE Trans. Plas. Phys.*, Vol. **24**, No. 2, pp. 289-295 (1996).

[124] S.P. LeBlanc, M.C. Downer, R. Wagner, S.-Y. Chen, A. Maksimchuk, G. Morour,and D. Umstadter, "Temporal Characterization of a Self-Modulated Laser Wakefield," *Phys. Rev. Lett.*, Vol. **77**, No. 27, pp. 5381-5384 (1996).

[126] R.E. Slusher and C.M. Surko, "Study of density fluctuations in plasmas by small-angle CO_2 laser scattering," *Phys. Fluids,* Vol. **23**, No. 3, 472 (1980).

[127] B.I. Cohen, A.N. Kaufman, and K.M. Watson, "Beat Heating of a Plasma," *Phys. Rev. Lett.*, Vol. **29**, No. 9, pp. 581-584 (1972).

[128] S.J. Karttunen and R.R.E. Salomaa, "Electromagnetic Field Cascading in the Beat-Wave Generation of Plasma Waves," *Phys. Rev. Lett.*, Vol. **56**, No. 6, pp. 604-607 (1986).

[129] P. Gibbon and A.R. Bell, "Cascade Focusing in the Beat-Wave Accelerator," *Phys. Rev. Lett.*, Vol. **61**, No. 14, pp. 1599-1602 (1988).

[130] P. Gibbon, "The self-trapping of light waves by beat-wave excitation," *Phys. Fluids B*, Vol. **2**, No. 9, pp. 2196-2208 (1990).

[131] Boyd, R.W. (2003), *Nonlinear Optics, Second Edition* (pp. 191-193), Elsevier, Academic Press.

[132] Boyd, R.W. (2003), *Nonlinear Optics, Second Edition* (pp. 311-314), Elsevier, Academic Press.

[133] Yariv, Amnon (1989), *Quantum Electronic, Third Edition* (pp.483-488), New York, John Wiley and Sons.

[134] R.Y. Chiao, E. Garmine, and C.H. Townes, "Self-Trapping of Optical Beams," *Phys. Rev. Lett.*, Vol. **13**, 479, 1964.

[135] R.S. Bennink, V. Wong, A.W. Marino, D.L. Aronstein, R.W. Boyd, C.R. Stroud, Jr., S. Likishova, and D.J. Gauthier, "Honeycomb Pattern Formation by Laser-Beam Filamentation in Atomic Sodium Vapor," *Phys. Rev. Lett.*, Vol. **88**, 113901, 2002.

[136] Boyd, R.W. (2003), *Nonlinear Optics, Second Edition* (pp. 318-323), Elsevier, Academic Press.

[137] P. Sprangle, C.M. Tang, and E. Esarey, "Relativistic Self-Focusing of Short-Pulse Radiation Beams in Plasmas", *IEEE Trans. Plasma Sci.*, Vol. **15**, 145 (1987).

[138] E. Esarey, C.B. Schoeder, and W.P. Leemans, "Physics of laser-driven plasma-based electron accelerators," *Rev. Mod. Phys.*, Vol. **81**, No. 3, pp. 1229-1285 (2009).

[139] S. Gordienko and A Pukhov, "Scalings for ultrarelativistic laser plasmas and quasimonoenergetic electrons", *Phys. Plasmas*, Vol. **12**, 043109, 2005.

[140] M. Geissler, J. Schreiber, and J. Meyer-ter-Vehn, "Bubble acceleration of electrons with few-cycle laser pulses," New J. of Phys., vol. **8**, 186 (2006).

[141] X. Wang, R. Zgadzaj, N. Fazel, S.A. Yi, X. Zhang, W. Henderson, Y.-Y. Change, R. Korzekwa, H.-E. Tsai, C.-H. Pai, Z. Li, H. Quevedo, G. Dyer, E. Gaul, M. Martinez, A. Bernstean, T. Borger, M. Spinks, M. Donovan, S.Y. Kalmykov, V. Khudik, G. Shvets, T. Ditmire, and M.C. Downer, "Petawatt-laser-driven wakefield acceleration of electrons to 2 GeV in 1017 cm-3 plasma," AIP Conf. Proc. **1507**, 341 (2012).

[142] A.B. Borisov, A.V. Borovskiy, V.V. Korobkin, A.M. Prokhorov, O. B. Shiryaev, X.M. Shi, T.S. Luk, A. McPherson, J.C. Solem, K. Boyer, and C.K. Rhodes, "Observation of Relativistic and Charge-Displacement Self-Channeling of Intense Subpicosecond Ultraviolet (248 nm) Radiaton in Plasmas," *Phys. Rev. Lett*., Vol. **68**, No. 15, 2309-2312 (1992).

[143] A.B. Borisov, A.V. Borovskiy, O.B. Shiryaev, V.V. Korobkin, A.M. Prokhorov, J.C. Solem, T.S. Luk, K. Boyer, and C.K. Rhodes, "Relativistic and charge-displacement self-channeling of intense ultrashort laser pulses in plasmas," *Phys. Rev. A*, Vol. **45**, No. 8, pp. 5830-5845 (1992).

[144] C.E. Clayton, C. Joshi, C. Darrow, and D. Umstadter, "Relativistic Plasma-Wave Excitation by Collinear Optical Mixing," *Phys. Rev. Lett.*, Vol. **54**, No. 21, pp. 2343-2346 (1985).

[145] M. Fomyts'kyi, C. Chiu, M. Downer, and F. Grigsby, "Controlled plasma wave generation and particle acceleration through seeding the forward Raman scattering instability," *Phys. Plasmas*, Vol. **12**, No. 2, 023103 (2005).

[146] M. Fomyts'kyi, C. Chiu, M. Downer, and F. Grigsby, "LWFA with Low Energy Raman Seeded Pulses," *CP737, Advanced Accelerator Concepts: 11th Workshop*, Ed. Vitaly Yakimenko, pp. 846-852 (2004).

[147] N. Ebrahim, P. Lavigne, and S. Aithal, "Experiments on the plasma beat-wave accelerator," *IEEE Trans. Nucl. Sci.*, Vol. **32**, No. 5, pp. 3539-3541 (1985).

[148] W. P. Leemans, D. Rodgers, P. E. Catravas, C. G. R. Geddes, G. Fubiani, E. Esarey, B. A. Shadwick, R. Donahue, and A. Smith, "Gamma-neutron activation experiments using laser wakefield accelerators," *Phys. Plasmas*, Vol. **8**, No. 5 2510 (2001).

[149] S. Kalmyov and G. Shvets, "Nonlinear evolution of the plasma beat wave: Compressing the laser beat notes via electromagnetic cascading," *Phys. Rev. E*, Vol. **73**, No. 4, 046403 (2006).

[150] F. L. Kien, J.Q. Liang, M. Katsuragawa, K. Ohtsuki, K. Hakuta, and A.V. Sokolov, "Subfemtosecond pulse generation with molecular coherence control in stimulated Raman scattering," *Phys. Rev. A*, Vol. **60**, No. 2, 1562-1571 (1999).

[151] A.V. Sokolov, D.D. Yavuz, and S.E. Harris, "Subfemtosecond pulse generation by rotational molecular modulation," *Opt. Lett.*, Vol **24**, No. 8, pp. 557-559 (1999).

[152] F. L. Kien, K. Hakuta, and A.V. Sokolov, "Pulse compression by parametric beating with a prepared Raman coherence," *Phys. Rev. A*, Vol. **66**, No. 2 023813 (2002).

[153] A.V. Sokolov, D.R. Walker, D.D. Yavuz, G.Y. Yin, and S.E. Harris, "Raman Generation by Phased and Antiphased Molecular States," *Phys. Rev. Lett.*, Vol. **85**, No. 3, pp. 562-565 (1999).

[154] M.Y. Shverdin, D.R. Walker, D.D. Yavuz, G.Y. Yin, and S.E. Harris, "Generation of a Single-Cycle Optical Pulse," *Phys. Rev. Lett.*, Vol. **94**, No. 3, 033904 (2005).

[155] S. Kalmykov and G. Shvets, "Guiding of Laser Beams in Plasmas by Radiation Cascade Compression," *AIP Conf. Proc. Advanced Accel. Conc. 12*, Vol. **CP877**, pp. 395-401 (2006).

[156] S. Kalmykov and G. Shvets, "Compression of laser radiation in plasmas via electromagnetic cascading," *Phys. Plasmas*, Vol. **13**, No. 5, 056707 (2006).

[157] S. Y. Kalmykov, S. A. Yi, and G. Shvets, "All-optical suppression of relativistic self-focusing of laser beams in plasmas," *Phys. Rev. E* Vol. **78**, No. 4, 057401 (2008).

[158] S. Kalmykov, S. A. Yi, and G. Shvets, "All-optical control of nonlinear focusing of laser beams in plasma beat wave accelerator," *Plasma Phys. Control. Fusion*, Vol. **51**, 024011 (2009).

[159] S.Y. Kalmykov, B.A. Shadwick, and M.C. Downer, "All-optical Control of Nonlinear Self-Focusing in Plasmas Using Non-Resonantly Driven Plasma Wave," *AIP Conf. Proc. Advanced Accel. Conc. 14*, Vol. **CP1299**, pp. 752-757 (2010).

Chapter 4

The Chirped-Pulse Raman-Amplified Terawatt Laser System

4.1   INTRODUCTION

The design, implementation, performance, and limitations of a two-color terawatt laser system are discussed in this chapter. The focus of this chapter is the chirped-pulse Raman amplification (CPRA) laser which is the second color of the UT^3 system: the commercial titanium-doped sapphire (Ti:Sapph) laser which forms the first color is discussed in Appendix A.

Terawatt and even petawatt laser systems are commercially available from a number of laser manufacturers. Durations as short as a few tens of femtoseconds—and bandwidths of a few tens of nanometers--or energies in the kilojoules are commonly available, with Gaussian or top-hat spatial profiles which are often highly focusable. Table 4.1.1 shows a comparison of several of the most important parameters for commercially available terawatt or petawatt laser systems designed by Thales in operation at a variety of laboratories in the US.

All of these commercially available lasers share one important trait in common: they are single-color[xiii]. The experiments which I discussed at the end of the last chapter (Sec. 3.5) require the use of two spectrally distinct, high power laser bands whose

---

xiii Single color here means that the laser's spectrum is centered around a single peak frequency, that is there are no spectrally distinct sidebands present simultaneously with this primary pulse..

frequency difference is nevertheless small ($\Delta\omega \sim 0.1{-}0.2\ \omega_{laser}$). In other words, many of these experiments require the use of a two-color terawatt laser system. Since such a system is not commercially available, one had to be designed and constructed for use in these experiments.

The two-color terawatt was designed around a commercially available single-color terawatt laser system. The laser system used for this purpose is a Thales-manufactured Ti:Sapph laser which is capable of emitting pulses nominally centered at 800 nm with a band-width limited duration of 25 fs and an energy of 1.125 J—yielding a total power of 45 TW—with a repetition rate of 10 Hz.

Laser/Institution	UT³/University of Texas at Austin	Scarlet/Ohio State University	Diocles/ University of Nebraska	BELLA/Lawrence Berkely National Laboratory
Pulse Energy	1.25 J	15 J	3 J	42.2 J
Pulse Duration	25-30 fs	40 fs	30 fs	40 fs
Peak Power	45 TW	400 TW	100 TW	>1 PW
Strehl Ratio	< 0.9	< 0.9	Unknown	Unknown
Repitition Rate	10 Hz	1 shot/minute	10 Hz	1 Hz
Wavelength (nm)	~800 nm ~873 nm	~800 nm	~ 800 nm	Unknown
M^2	< 1.5	<1.5	Unknown	Unknown
Pulse- to-Pulse Energy Stability	>1.3% rms	>1.3% rms	Unkown	Unknown
Contrast Ratio	10^{10}:1	10^{10}:1	10^{10}:1	Unknown

Table 4.1: Specifications of a few Thales lasers around the U.S.A. All specifications taken from Thales website and the websites of the lasers listed or from the nominal parameters as reported.
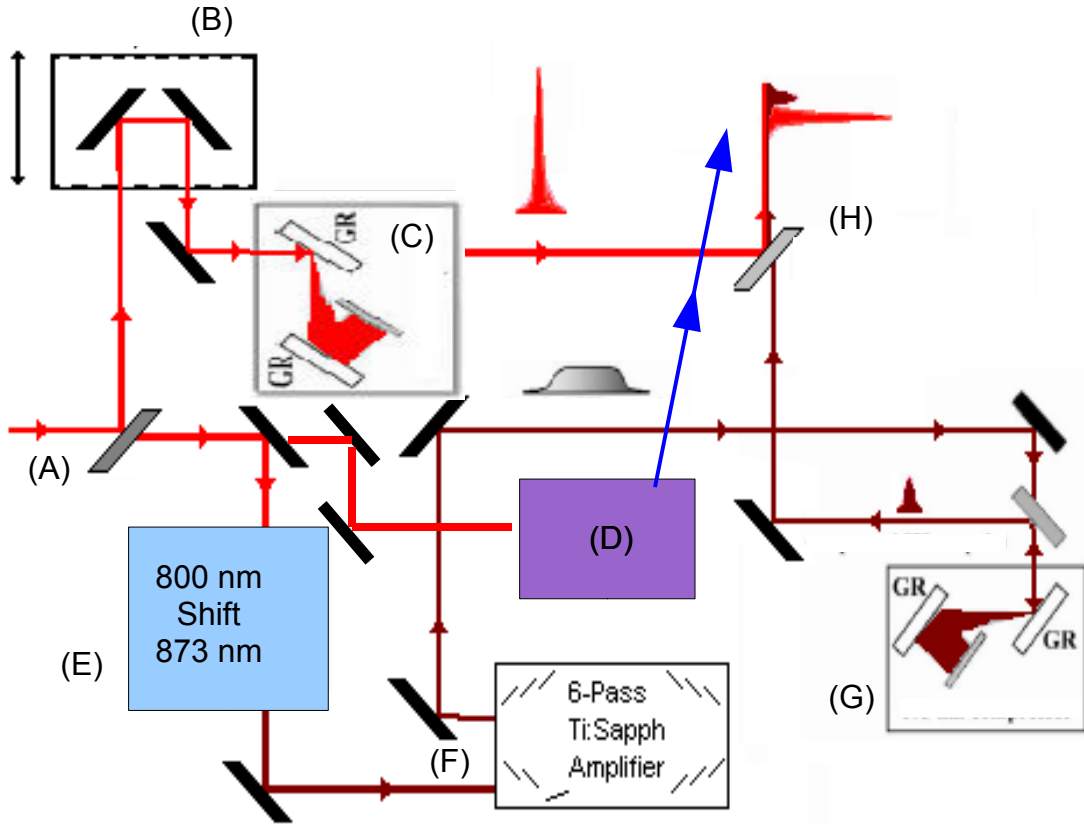
Figure 4.1: Overview of the two-color laser system. The energy of the primary pulse is first amplified to full power. It is then sent to a beam splitter (A) which reflects ~90% of the energy and transmits ~10%. The reflected portion, typically 1.5-1.8 J, is sent to a 20 meter delay line (B), and from there to a grating compressor, where it is typically compressed to ~30-35 fs with 0.9-1.2 J, which yields ~30-40 TW peak power (C). The remaining 10% of the pulse is then further split for use in probe lines (D) and for creating the Raman laser (E). The Raman laser itself consists of a two-stage shifter and amplifier (E), an externally-pumped 6-pass Ti:Sapphire bowtie amplifier which amplifies up to >300 mJ in the first Stokes 873 nm mode (F), and a dedicated grating-pair compressor (G) which compresses the pulse to as short as <100 fs and up to ~150 mJ or 1.5 TW peak power (G). The two pulses are then sent to the target chamber, where they may be combined via a dichroic beam splitter which reflects at 800 nm and transmits at 873 nm (H).

The second color is generated by splitting a fraction of the energy from the pre-compressed 800 nm commercial laser ("primary beam"). This split pulse is then shifted to 873 nm via Raman scattering—this is the first Stokes wave generated with an 800 nm fundamental wave incident on a barium nitrate crystal. The first Stokes wave is then amplified in an externally-pumped Ti:Sapph amplifier, and then it is compressed to a bandwidth-limited, ~Gaussian pulse of duration ~100 fs.

4.2   SYSTEM DESIGN

In this section, I give a basic overview of the system design for the University of Texas Two-Color Terawatt ("UT³")'s Raman laser system (sometimes called the secondary color, secondary pulse, Raman pulse, etc.). The "secondary pulse" Raman system is designed in four stages: seeding, stimulated Raman amplification, Ti:Sapph amplification, and compression. Figure 4.1 shows the set-up of this system.

First, ~10% of the energy is split from the primary pulse after its final amplification but before its compression. Nominally, this is 150 mJ. Much of this 150 mJ is then split off for use in various probe lines, with a portion of this being split and irised and resized before sending it to the Raman system. This 30 mJ, 500 ps pulse is used to generate the secondary pulse. The primary pulse is sent to a delay line, then is compressed to ~25 fs (at bandwidth limit) using a pair of 1480 lines/mm gratings. It is then sent to the target chamber. We generated the secondary pulse in three stages, then compress it and re-combine it with the primary pulse via a dichroic mirror in the wakefield target chamber. Figure 4.2 shows the first two stages of the Raman system in
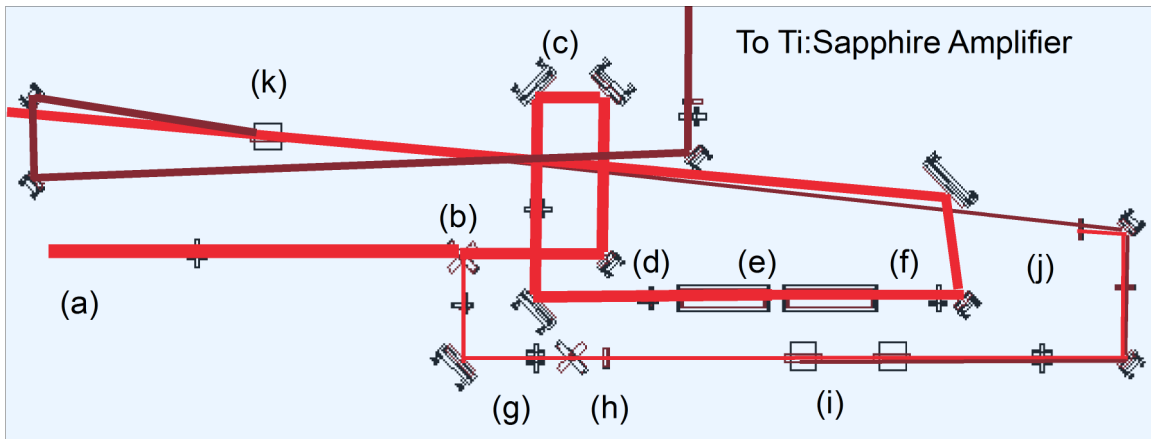
Figure 4.2: Detail of the Raman shifter and amplifier. The system begins with ~30 mJ of 800 nm light which is split off from the main pulse (a). This is then further split into two lines, a pump and a probe (b). The pump line is >90 % of the energy, and is sent to a delay (c) to achieve temporal overlap of the two pulses, and then is sent through a half-wave plate (d) and a pair of thin film polarizers (e) which allows us to control the pump energy. Typically, ~15-20 mJ of 800 nm pump light is sent to the amplifier crystal (k). The seed line begins with ~2.5 mJ of energy, which is sent through a half-wave plate (g) and a polarizing beam splitter (h) so that its energy is also controllable independently of the pump energy. Typically, ~0.2 mJ is used to seed the Raman shifters. This is focused by an f/30 lens into a pair of barium nitrate crystals (i), which produces a series of Stokes and anti-Stokes shifts. The first Stokes is to 873 nm, typically 10-20 uJ, but up to >0.1 mJ is possible. This is then collimated and sent through an 873 nm interference filter (j) to remove the residual 800 nm light and any Stokes' and anti-Stokes orders other than 1st Stokes. This 873 nm seed is then combined with the pump laser in a barium nitrate crystal (k) and amplified up to ~3 mJ in a single pass, and then sent to the Ti:Sapphire crystal for final amplification.

detail: the Raman shifter and the Raman amplifier. The first stage of the Raman system involves splitting <10% of the available secondary pulse energy (~2.5 mJ), irising it, and focusing it via an f/50-f/200 (depending on iris) lens into a pair of barium nitrate crystals.

This first pair of Raman crystals—the "seed" line crystals—are used to generate a small Raman-shifted signal with ~10-20 μJ energy with which to seed the second stage Raman amplifier. The second stage, Raman amplifier is a third barium nitrate crystal, which is used to generate ~1 mJ of first Stokes' light. The goal of the first two stages is

154

low-energy beam with broad bandwidth and ~Gaussian mode to seed the Ti:Sapphire amplifier.

The Raman crystals used are all barium nitrate[160], $Ba(NO_3)_2$. These crystals have a Raman active vibrational mode[161] centered at 1047 cm^{-1}, so that the seed pulse is shifted from 800nm to 873 nm. The use of a pair of crystals in the seed line is something new to our set-up. Grigsby[162],[163],[164] used only a single seed crystal, Zhavoronkov[165] a single stage consisting of only one crystal. Using a pair of crystals enhances the performance of the first and second stages of this system, and will be discusses further in the next section.

The ~1 mJ amplified Raman beam is then sent to a Titanium-doped Sapphire (Ti:Sapph) crystal where is has been amplified to up to 330 mJ, centered at 873 nm. The Ti:Sapph crystal is pumped by a frequency-doubled 1.1 J Nd:YAG laser, with a spot size of ~0.35 cm (FWHM) and ~10 ns pulse duration, with a top-hat spatial transverse mode profile. The Nd:YAG laser is itself split into two beams, one to pump each face of the Ti:Sapph crystal whose small-signal absorption is approximately 90%.

The Raman beam itself passes through the Ti:Sapph amplifier in a 6-pass "Bowtie" geometry. Here it is amplified by 2 orders of magnitude, with some pulses attaining energies of >300 mJ. Figure 4.3 shows the farfield modes of the beam through each of the first three stages of this experiment. The Fundamental beam is nearly Gaussian when it arrives at the amplifier crystal (Fig. 4.3a), and the seed mode (Fig. 4.3b) is cleaned up in the amplifier crystal[166] due to a phase averaging effect (Fig. 4.3c), and

ultimately has a nearly Gaussian profile after final amplification in the Ti:Sapphire crystal (Fig. 4.3d).

After final amplification, the beam is sent to a dedicated pair of compressor gratings and compressed. Compression to the (Gaussian) bandwidth limit is attainable. The third stage fully amplified Raman beam has been compressed to durations as short as <80 fs. It should be noted, however, that not all proposed experiments call for a fully compressed pulse duration. For example, the relativistic self-focusing control experiments[167],[168],[169] require a pulse duration sufficiently long to interact with the plasma over several plasma wavelengths—which is >200 fs.
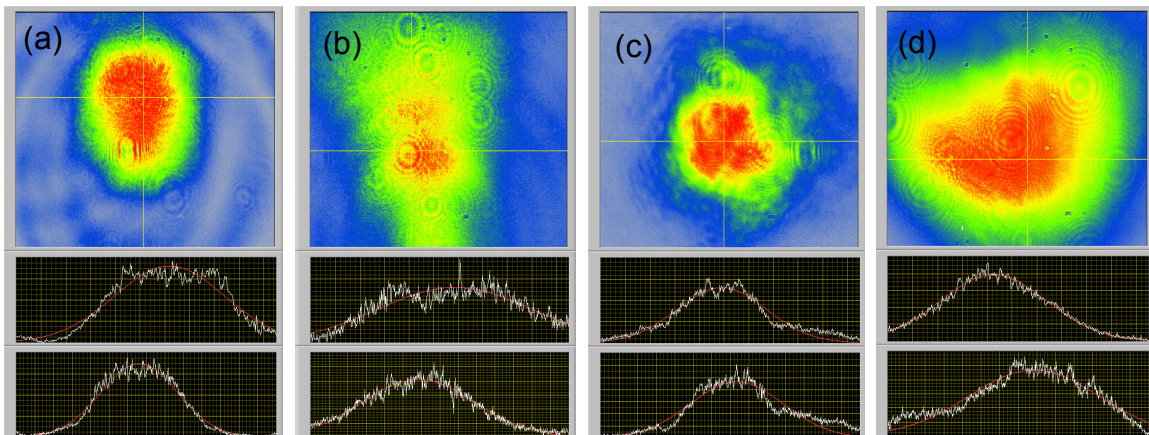
Figure 4.3: Evolution of the farfield mode through the first three stages of the Raman CPA system. From left to right, this is the mode of the 800 nm fundamental beam (a) as used to pump the amplifier crystal in the second stage. The Raman signal used to seed this second stage (e.g. the signal out of the first stage) is somewhat bi-modal (b), but the beam undergoes some cleanup after one pass through the amplifier crystal in the second stage (c), and is further cleaned up (and also shaped) in the Ti:Sapphire crystal after 6 passes (d). The total energy in (d) is 105 mJ. Below each ccd image are the horizontal (upper) and vertical (lower) line-outs (white) along with a Gaussian fit (red).
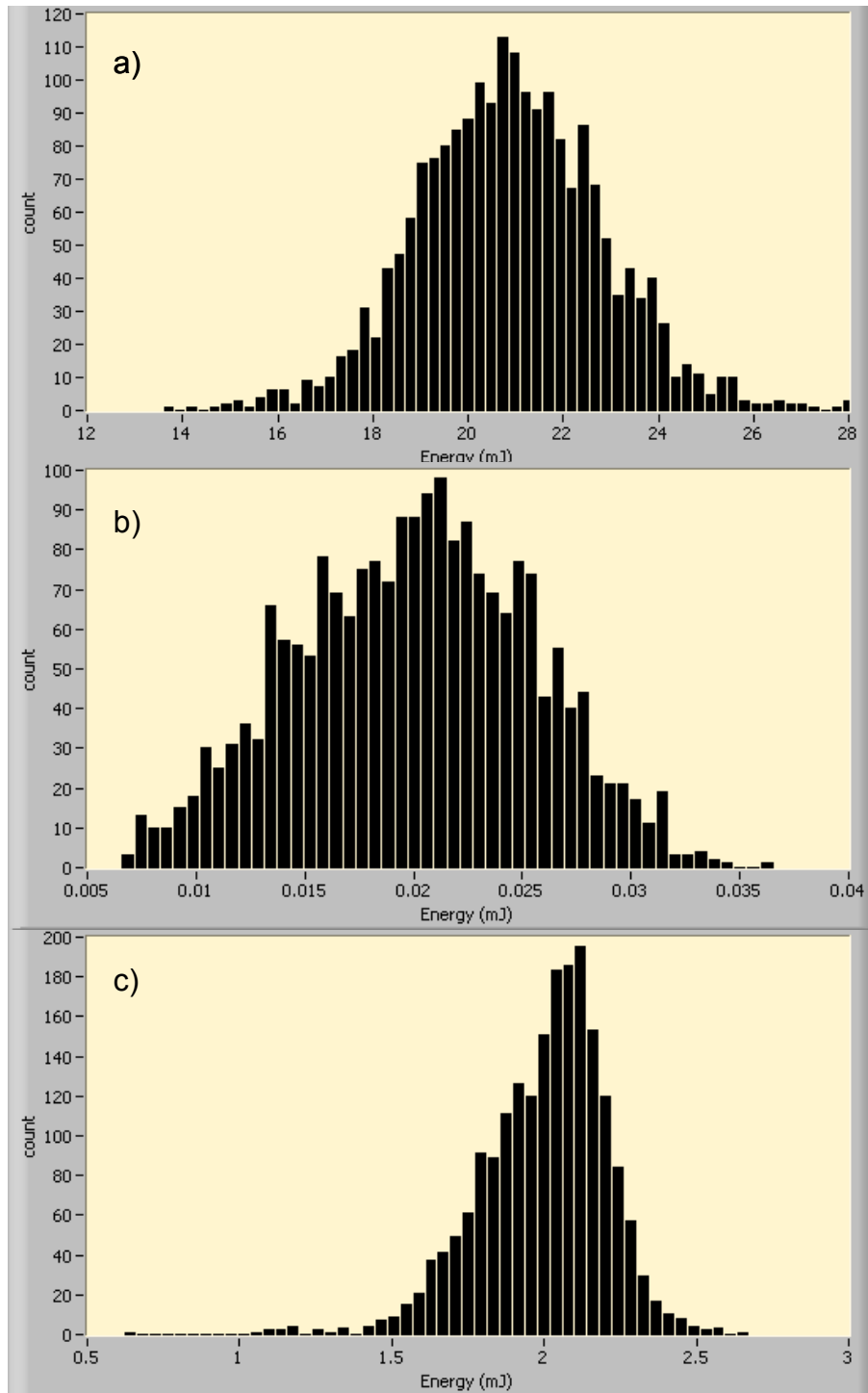
Figure 4.4: Energy histograms in first two stages of the Raman system. a) The 800 nm pump at the position of the amplifier crystal, b) the Raman seed at 873 nm at the position of the amplifier crystal, and c) the amplified 1 Stokes energy.

157

Some energy histograms from the first two stages are shown in Fig. 4.4. The 800 nm pump has been attenuated to ~20 mJ for the second stage[xiv], with ~200 μJ in the seed line after the iris and energy tuner. The manufacturer's specs give a nominal energy variation of $\pm 5\%$ FWHM, though as can be seen in Fig. 4.4a, this variation can actually be closer to $\pm 10\%$.

This in turn translates into a large variation in Raman seed energy, as per Fig. 4.4b, nearly $\pm 50\%$ FWHM. This variation is is part due to the fluctuations in the pump energy, and in part due to fluctuations in mode and even spectrum (both of which are relatively minor shot-to-shot), and in large part due to fluctuations in the background noise level from which stimulated Raman scattering (SRS) grows. The instability of the seed further translates into large fluctuations in the second stage Raman energy. This fluctuation is mitigated somewhat by saturating the gain in the second stage. However, saturating the gain in the second stage can narrow the spectrum of the 1 Stokes mode, and can moreover lead to a less clean transverse mode, both of which will be discussed below. In Fig. 4.4c, the gain of the second stage is below saturation, but the energy spread is still narrowed somewhat to only $\pm 25\%$.

---

xiv The pump energy is generally chosen to optimize the output spectrum and mode of the 1 Stokes in the second stage. The energy and spectrum of the pump itself are generally reasonably stable, though the mode shifts over long timescales (days, weeks, or even months of operation, given occasional re-alignment of the system).

4.3   Considerations in the Raman Shifter

What follows in this section is a discussion of the first two stages of the Raman laser system: the shifter and the amplifier. In these first two stages, a Raman-shifted mode centered at 873 nm is generated and amplified to a typical energy of ~1 mJ with a clean, nearly Gaussian mode profile and a compressible broad bandwidth.

Following the work of Franklin Grigsby[3], I divided the Raman generation process into two stages: Stage 1 (or the first stage) is the Raman shifter and Stage 2 (or the second stage) is the Raman amplifier. The purpose of the first stage is to generate a small signal 1st Stokes wave with which to seed the second stage. The second stage further amplifies the 1st Stokes wave and then uses this amplified beam to seed a Ti:Sapphire amplifier—Stage 3 (or the third stage)—which is discussed in Sec. 4.5 of this chapter. The goals of these first two stages then are to generate a coherent, compressible broadband beam which is spectrally distinct from the primary pulse[xv] and which can then be amplified in the third stage. Therefore, the 1st Stokes beam would ideally have a comparable bandwidth to the fundamental beam (and hence duration), with a similar transverse mode and a final compressed energy of >100 mJ. Thus, the primary considerations are energy, compressed duration, and transverse mode focusability which can match the focused fundamental beam, with bandwidth being an important consideration in that it determines the shortest possible pulse duration according the to Heisenberg uncertainty principle and the Fourier transform limit.

---

xv Spectrally distinct here means that the peak of the secondary pulse is outside of the spectral wings of the primary pulse.

To this end, the first stage needs to generate a small-signal pulse with a reasonably broad bandwidth and a reasonably smooth mode. The transverse mode itself does not need to be perfectly Gaussian nor tophat in profile, but it should ideally remain free of local "hotspots" and other such features. In principle the rule for the seed line is, first choose parameters for the best transverse mode and the broadest spectrum, then ensure that the output energy is >10 µJ in the 1st Stokes mode to adequately seed the second stage. In actual practice, the best set of spectra, mode, and bandwidth is not so obvious, and is typically determined in retrospect by adjusting for the optimum signal out of the second stage or even later stages.

The reason for breaking this process into two stages is documented by Grigsby[3] and is born out by my own observations: namely, breaking the Raman shifting/amplifying process into two stages helps to generate a nicer transverse mode. Specifically, when the intensity of the fundamental beam in the first stage is sufficiently high to generate ~ mJ energies in the 1st Stokes mode, the beam tends to self-focus, which results in filamentation and the formation of hot spots and poor beam focusability. The Raman seed mode for several incident fundamental pulse energies is shown in Figure 4.5. For a low incident energy, the resulting seed mode has a ~ Gaussian profile, though a very low 10-20 µJ energy. As the incident fundamental energy is increased to > 1 mJ, the resulting Raman mode increases in energy, and retains a nice profile, but then this Raman mode begins to filament at higher energy (still <100 µJ).

One significant difference between the set-up of my two-stage system and that of Grigsby's is the addition of a second seed crystal in my set-up. I added this second crystal

because I observed that two seed crystals give a better combination of mode, energy, and spectrum out of the second stage than does one seed crystal. The spectrum and mode is affected by the input parameters of the fundamental beam, by the focusing geometry (mostly, f/#) of the iris-lens pair at the input of the seed line, and by the positions of both seed crystals.

The placement of the two barium nitrate crystals with respect to the focal position of the beam is chosen to optimize the combination of spectrum, mode, and energy out of the second stage. Other parameters of importance are size of the beams in both lines, the energy of both the 800 nm pulse in the seed line and the 800 nm pulse in the second stage pump line, the temporal overlap of the two pulses, the angle between both pulses in the
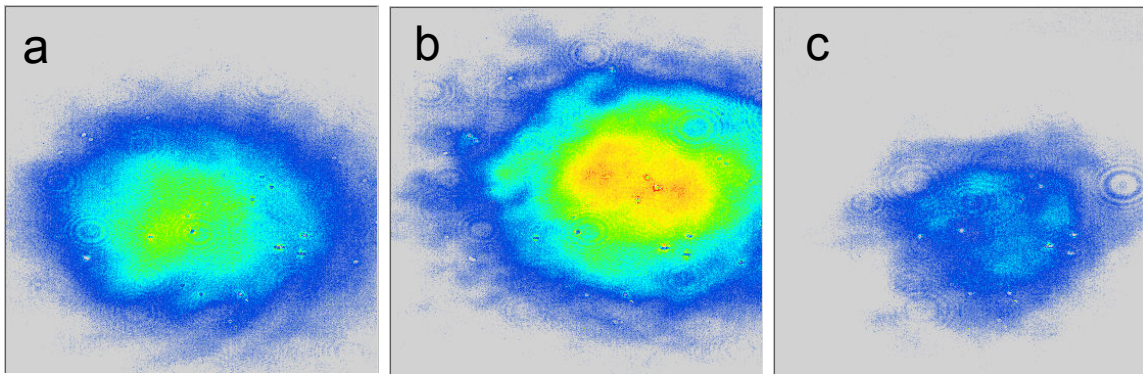
Figure 4.5: The mode of the Raman seed generated by an 800 nm laser beam focused by an f/167 lens into a a 5 cm-long barium nitrate crystal. The crystal is placed so that the focus of the pulse is in the center of the crystal. The pulse energy is then adjusted by rotating a half-waveplate so that the 800 nm has a) 50 μJ, b) 200 μJ, and c) 320 μJ incident on the crystal.

second stage. As a rough guideline, I try to get a ~Gaussian mode with >1 mJ and >15 nm FWHM bandwidth in the spectrum from this stage. Another parameter of importance is the position of the seed crystal(s) relative to the seed line's focal plane.

4.4   Effects of Seed Crystal Position on Mode, Energy, and Spectrum

In this section I will discuss how seed crystal's position relative to the seed line's focal plane affects the Raman beam's energy, mode, and spectrum.

The Raman seed's energy, spectrum, and mode all depend on the intensity of the fundamental beam's pulse intensity within the seed crystal. Based on the way that the seed line is designed (see the bottom portion of Fig. 4.2), there are ultimately four things which can be readily and independently controlled within the seed line, four "knobs to turn" as it were. These are: the fundamental beam's energy (controlled by the half-waveplate in conjunction with the polarizing beam splitter); the effective f/# of the focusing lens (controlled by opening or closing the iris at the entrance to the seed line); and the positions of the two crystal relative to the focal plane of the seed line (controlled by moving each of the two crystals along a track).

Naively, one would expect to see the maximum energy output when the seed crystal is centered around the focal plane of the seed line (for one crystal). The Raman process involved is initially spontaneous Raman scattering.

The spontaneous scattering is not especially dependent on intensity but rather on total number of photons (energy), and thus happens as efficiently at low-intensity (away from focus) as at high-intensity (at focus) beam[170]:

162

$$\frac{dm_s}{dz} = \frac{D}{c/n} m_L,$$

(4.3.1)

where m_S is the number of photons in the Stokes' mode, m_L is the number of photons in the laser (fundamental) mode, n is the refractive index of the medium, and D is a proportionality constant. However, once some photons have been scattered into the 1 Stokes' mode, stimulated Raman scattering might begin, and this process is dependent on the fundamental pulse's intensity:

$$I_s(z) = I_s(0) e^{g I_L z}$$

(4.3.2)

Where I_S is the 1 Stokes intensity, I_L is the laser (fundamental) intensity, and g is a gain coefficient.

A beam which focuses earlier in the crystal will begin with a smaller value of $I_S(0)$, whereas the laser is in this case not depleted and thus $I_L \sim$ constant save that the spot size is changing (the beam goes through a focus). Thus, the beam is mostly expanding and thus I_L is mostly decreasing as the beam propagates in this case. On the other hand, if the focus is later in the crystal, more photons will have scattered into the Raman mode, so $I_S(0)$ will be larger in the high-intensity portion of the crystal during which the bulk of the stimulated Raman scattering is occurring. Since the highest intensity of the pulse is at and around the focal plane—where the pulse occupies the least area—it therefore follows that the crystal should be centered on the focal plane to contain the greatest beam intensity throughout. If the focus is too early or too late in the crystal, then this high-intensity portion of the crystal will have a shorter length z inside the crystal.

163
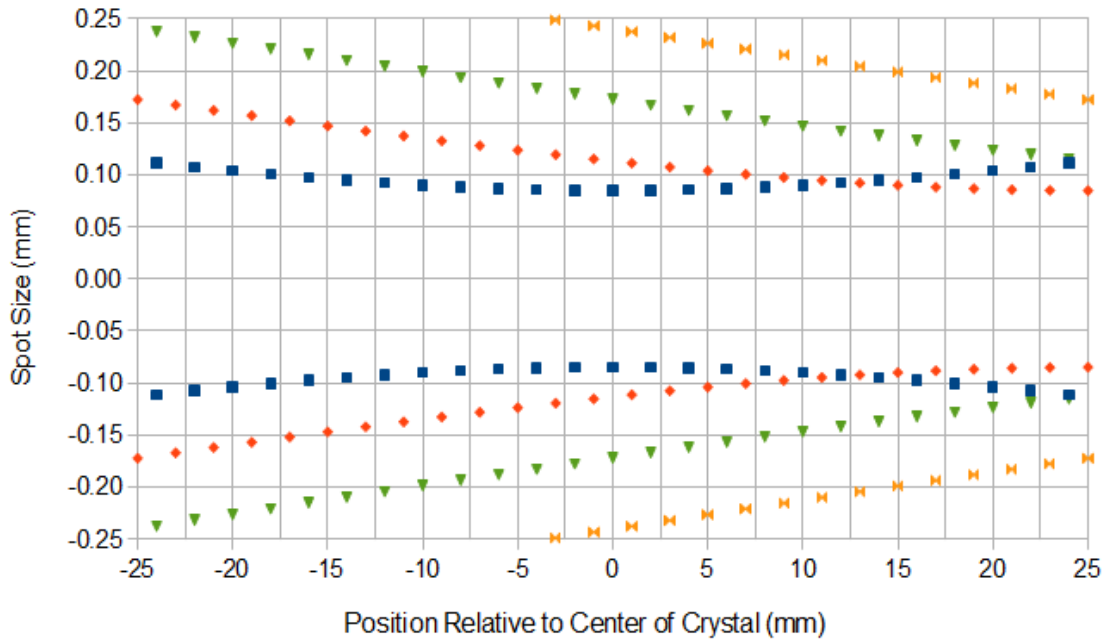
Figure 4.6: Evolution of mode size in the barium nitrate crystal as a function of focal position with respect to the crystal's center. Positive number means the position is towards the exit face of the crystal, negative towards its entrance face.

Figure 4.6 shows the 800 nm beam's transverse mode size evolution inside of the crystal for several crystal positions. In all three cases, the beam is focused by an f/167 lens, but the crystal position relative to the focal plane is changed in each case. The blue squares represent a crystal which is placed with its center at the focal plane of the beam, and thus also represents the crystal which will have the highest intensity at its center. The spot size in this case ranges from 85 µm to 110 µm, so the intensity is reduced by a factor of ~40% at the entrance and exit of the crystal relative to the center. The beam represented by the red triangles has the crystal placed so that its center is 25 mm from the focal plane—which is equivalent here to placing the focal plane on the exiting face of the crystal. The beam is in other words continuing to focus through the crystal, and thus is

164

becoming more intense as it propagates through the crystal, but also has an average intensity lower than the case of the blue-squares beam. The remaining two beams both centered on the focal spot of the fundamental pulse in the seed line. Naively, the optimum position for the seed crystal would therefore be centered at the focus of the pumping beam.

However, as shown in Fig. 4.7, this naïve estimate is not always the case. Rather, the optimum position for the placement of the seed crystal relative to the fundamental pulse's focus actually depends on the fundamental pulse's energy. This placement of the seed crystal determines not only the energy of the seed pulse (Fig. 4.7a), but also the energy of the 1 Stokes pulse after amplification in the second stage (Fig. 4.7b), which mostly follows the shape of the seed's energy-delay curve. At lower energies, both curves more-or-less follow the "naive" model, peaking when the crystal is centered near the focal spot. The slight difference in the the peak and the focal position is most likely due to the resolution of this particular experiment, in particular the fact that the seed pulses tend to be unstable in energy from shot-to-shot and thus the points plotted represent average energies over hundreds of shots at each position; the error bars themselves are ~10% of these averages.
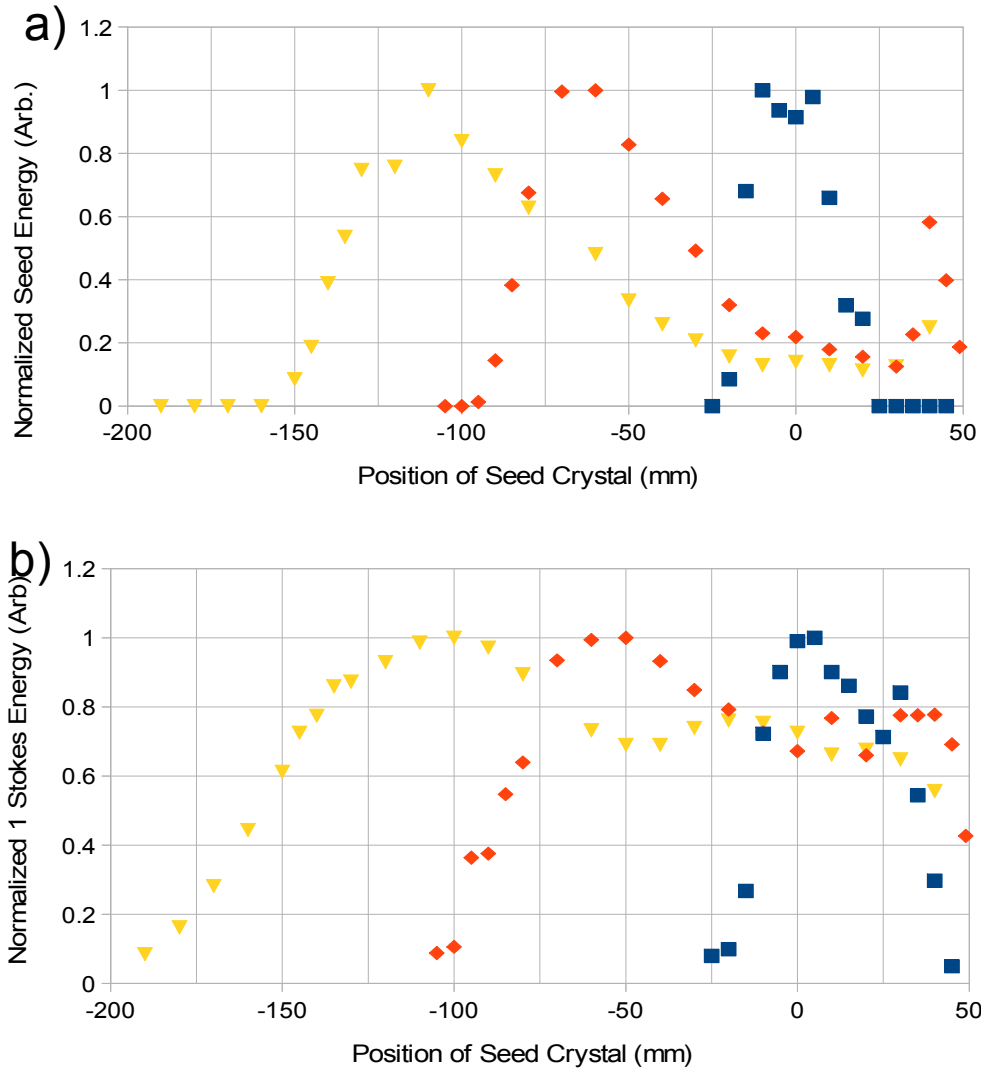
Figure 4.7: The effects of seed crystal position on Raman energy. Seed crystal position has an effect on a) the seed line's output energy and on b) the amplified 1 Stokes energy out of the second stage. This has been measured for several seed line input energies: 320 μJ (blue), 1.31 mJ (red), and 2.07 mJ (yellow). In the case of the amplified 1 Stokes energy, a pumping energy of ~12 mJ centered at 800 nm was used. The seed crystal's position is always specified as distance from the crystal's center to the focal plane of the laser, with negative number meaning that the laser passes through the crystal's center before the beam's focal plane. Each data point is the average energy over 200 shots.

As the energy of the fundamental beam in the seed line is increased, the optimum position for crystal placement moves away from the focal plane and towards the input mirror. The curve itself actually exhibits a second peak, but is not symmetric about the focal plane, with a preference given to placing the crystal before and not after the focus. Moreover, the amplified energy curve in Fig. 4.7b continues to follow the seed energy curve in Fig. 4.7a, but with less emphasis on the post-peak dip (the dip between the first and second peaks).

The shifting of the energy peak—and the existence of the second energy peak—can be explained as follows. At the lower seed line fundamental energy, the pulse does not obtain sufficient energy to undergo catastrophic self-focusing inside the barium nitrate crystal, and thus does not suffer filamentation. Under this set of conditions, the output energy is determined primarily by the intensity of the pulse during spontaneous Raman scattering, and secondarily (very weakly) by the number of Raman photons generated via spontaneous scattering. Therefore, the optimum position for the crystal is that position in which the fundamental pulse has the greatest intensity inside of the crystal, which is our naive solution in which the crystal is centered on the fundamental beam's focus.

On the other hand, at higher incident energies, the fundamental pulse undergoes self-focusing, which becomes strong enough to cause filamentation when the crystal is near the beam's focus. The result of this self-focusing is not only a poor mode, but also a less-efficient mode-match between the fundamental pulse and the Raman pulse. This in

167

turn would result in a less-efficient driving of the stimulated Raman scattering process, and hence ultimately in a lower-energy Raman beam. A possible reason for the optimal position's shifting to before the focus as opposed to merely away from the focus is that the beam may undergo some self-cleaning as it passes through the focus.

This also provides a plausible explanation for the existence of the second peak position for the seed crystal. At some point, the crystal moves far enough away from the focal plane in the other direction (crystal is after focus) that the intensity drops below the filamentation threshold in this direction, too.
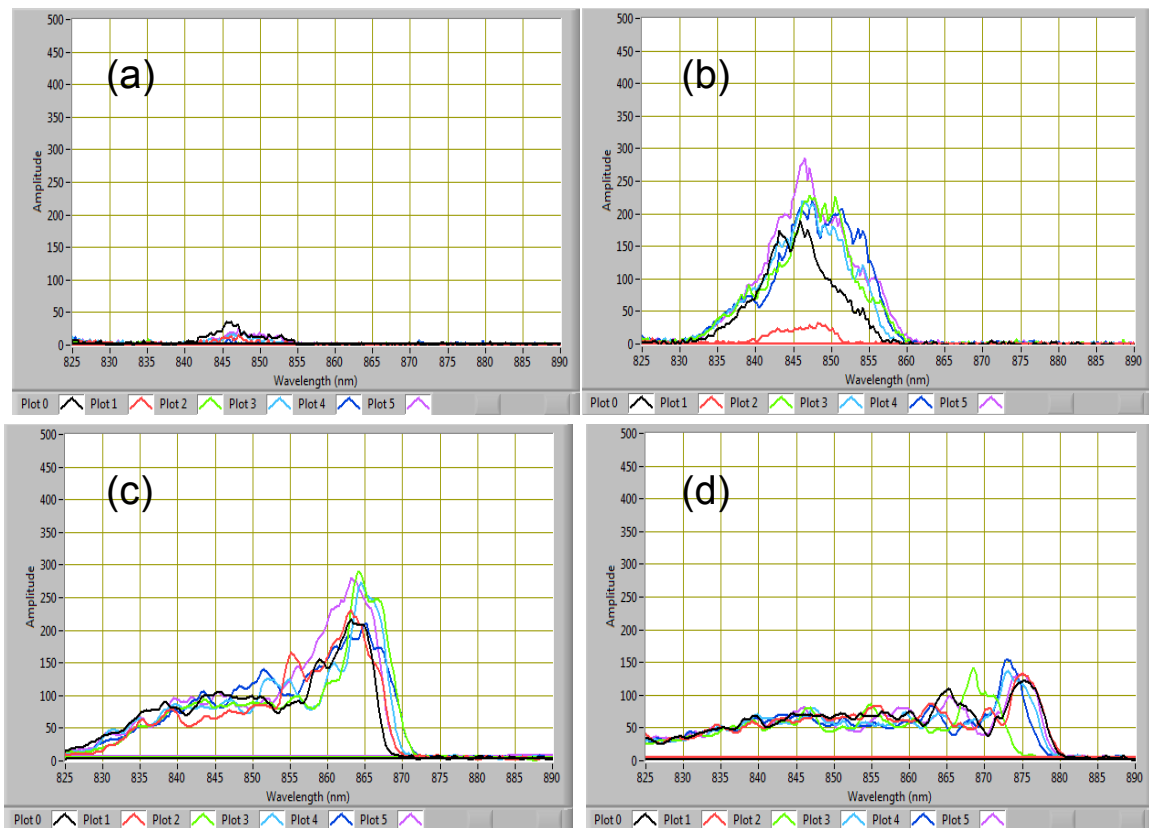
Figure 4.8: The spectra of the amplified 1 Stokes as a function of crystal position. These are second stage spectra, and depend on the first stage crystal's position. The seed crystal's position is the position of the crystal's center relative to the focal plane of the laser in the seed line, and is a) 7.5 cm before focus, b) 5.0 cm before focus, c) 2.5 cm before focus, d) and at focus.

Moreover, the position of the crystal in the seed line effects the spectrum, as shown in Figs. 4.8(a-d). Essentially, the crystal's position determines the spot size of the 800 nm pulse as it passes through the Raman medium. If the spot size is small, then the intensity will be larger and will drive the Raman shifting medium more strongly, whereas if the spot size is large, the intensity will be smaller and will therefore drive the Raman shifting medium less strongly. The result is that if the pulse focus occurs well outside of the seed crystal, very little light will be scattered into any of the Raman modes, and so the Raman seed signal will be barely detectable and certainly insufficient to seed to the second stage (Fig. 4.8a). As the seed crystal is moved nearer to the focal plane, the seed line intensity is increased, and so the Raman signal becomes sufficient to seed the second stage, thus also broadening the second stage Stokes' spectral bandwidth (Fig. 4.8b). However, as the intensity increases in the seed crystal, the leading edge of the primary pulse pumps the Raman gain medium sufficiently to saturate the signal early, meaning that the 1st Stokes spectrum exhibits a red-shifted spike after the second stage (Fig. 4.8c). This spike persists even as the intensity is increased enough to undergo self-phase modulation and white-light generation (Fig. 4.8d).

Suffice it to say that this effect is more difficult to characterize with a second seed crystal. However, I have observed with some consistency that although the alignment process using two crystals takes slightly longer, the end result is often a slightly broader second-stage bandwidth with similar energy and mode structure when compared with just one crystal. The second-stage energy stability is also improved by adding a second seed
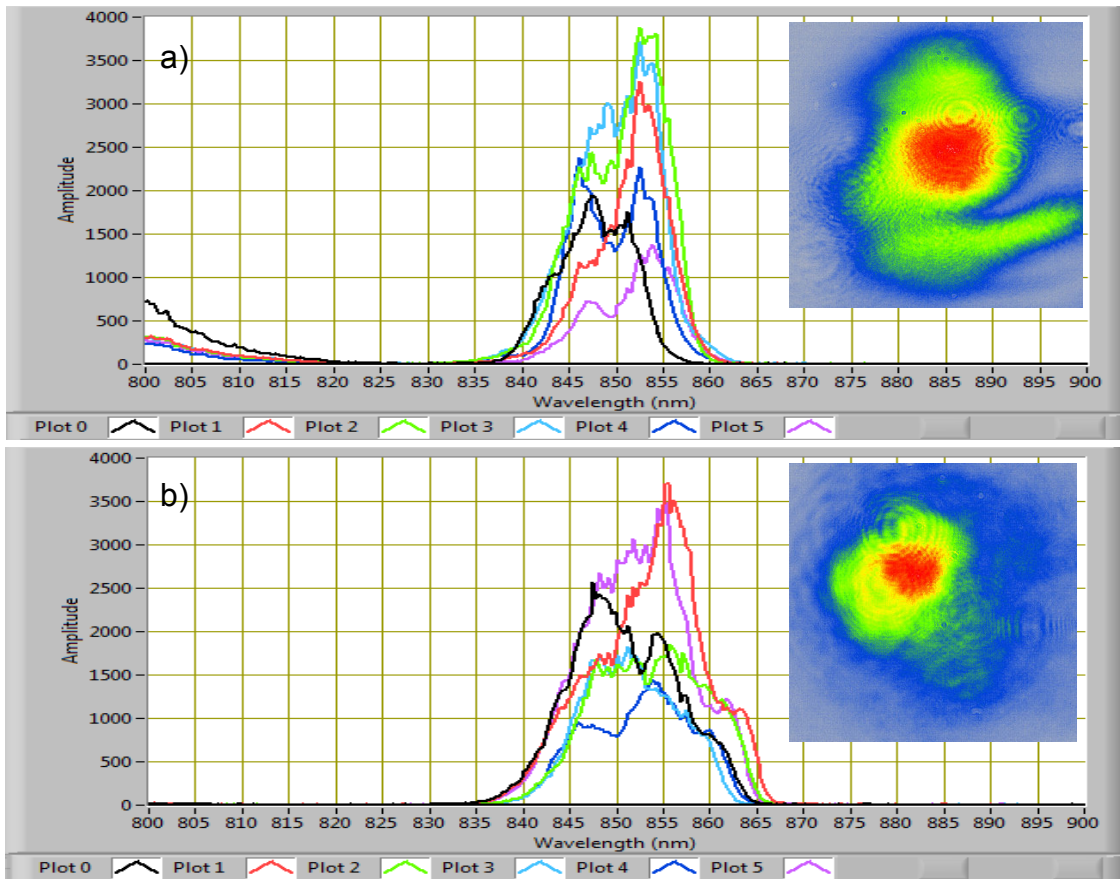
Figure 4.9: Comparison for second stage output between one seed line crystal and two seed line crystals. With one seed crystal present a) the spectrum had a bandwidth of 10-15 nm FWHM, but with two crystals present in the seed line this spectrum broadens to 15-20 nm FWHM. The insets show the 1 Stokes beam's transverse mode after amplification in the second stage to the energies at which these spectra are taken: 1.1 +/- 0.4 mJ (one crystal) or 1.0 +/- 0.2 mJ (two crystals).

crystal. Adding a third crystal is a bit more cumbersome, and does not seem to offer sufficient (if any) enhancement of the system to warrant the extra time spent aligning a third crystal.

The first seed crystal is placed well before the focus of the seed line beam, the second crystal is placed with back surface nearly at the focal plane for optimal

performance. The second-stage Raman spectrum is also somewhat broader for two crystals as compared to the case where only one is used, as shown in Fig. 4.9.

4.5 OTHER CONSIDERATIONS IN THE RAMAN AMPLIFIER

There are several other considerations for the second stage of this system, including the optimum angle between pump and seed (or whether it's best to use a collinear as opposed to non-collinear geometry); the effects of the pump delay on the Raman beam; and balancing between energy, mode, and spectrum.

In the second stage, the Raman beam undergoes both stimulated Raman scattering and other higher-order four-wave mixing processes. These processes are pumped by the remainder of the 800 nm pulse, which has typically been attenuated to ~15 mJ. The result is a Raman cascade from which we take the First-Stokes' wave, which has now been amplified to ~1.5 mJ. Actually, higher energies can be achieved, but the mode quality and spectrum both suffer when this is attempted. Stokes energies of as much as 3 mJ are attainable from the amplifier crystal (single pass), but the result is often filamentations and beam fragmentation (Fig. 4.10). This is due to the fact that once the secondary beam energy exceeds ~0.5 mJ, the intensity is sufficient to generate higher order Stokes and anti-Stokes waves:

$$\omega_{1s} = \omega_{1s} + \omega_f - \omega_f \tag{4.5.1a}$$

$$\omega_{1as} = \omega_f + \omega_f - \omega_{1s} \tag{4.5.1b}$$

$$\omega_{2s} = \omega_{1s} + \omega_f - \omega_{1as} \tag{4.5.1c}$$

171

$$\omega_{2s} = \omega_{1s} + \omega_{2s} - \omega_{1s} \qquad\qquad\qquad\qquad (4.5.1d)$$

Where the subscripts stand for fundamental (f), n^{th} Stokes order (ns) or n^{th} anti-Stokes order (nas). Note that the first and last of these expressions are both automatically phase-matched, but that the second and third expressions are not. The first equation of the set is Raman scattering from fundamental to first Stokes, the second involves the generation of first anti-Stokes from the fundamental and first-Stokes; the third equation describes how this first anti-Stokes can then be used to generate second Stokes, which can then mix with first Stokes to generate more second Stokes light. Since this last process is also automatically phase-matched, the first Stokes wave begins to pump stimulated second Stokes scattering (that is to say, the 873 nm light begins to undergo an additional Stokes-shift into second Stokes), thus depleting the first Stokes beam.

The spectrum of part of the Raman cascade after one pass through the second stage crystal is shown in Fig. 4.11. Each mode order of the cascade (e.g. fundamental, 1st Stokes, 2nd Stokes, 1st anti-Stokes, 2nd anti-Stokes) is spatially separated according to the phase-matching conditions imposed by four-wave mixing. The spectra are obtained via a fiber spectrometer, which is is moved to collect data from each mode individually; these are then added together to produce the "cascade spectrum" in the figure. Therefore, the spectrum shown is not for one single shot, but rather for several shots averaged together. It is also notable that not all orders have the same spectral bandwidth, nor do they each have the same energy: some of the orders will be more preferentially amplified than others due to phase-matching considerations, and furthermore the lower orders will achieve higher energies before the higher orders. This cascade could be used to create an

enhanced FDH probe[171], in which each higher order Stokes sideband provides an additional probe.
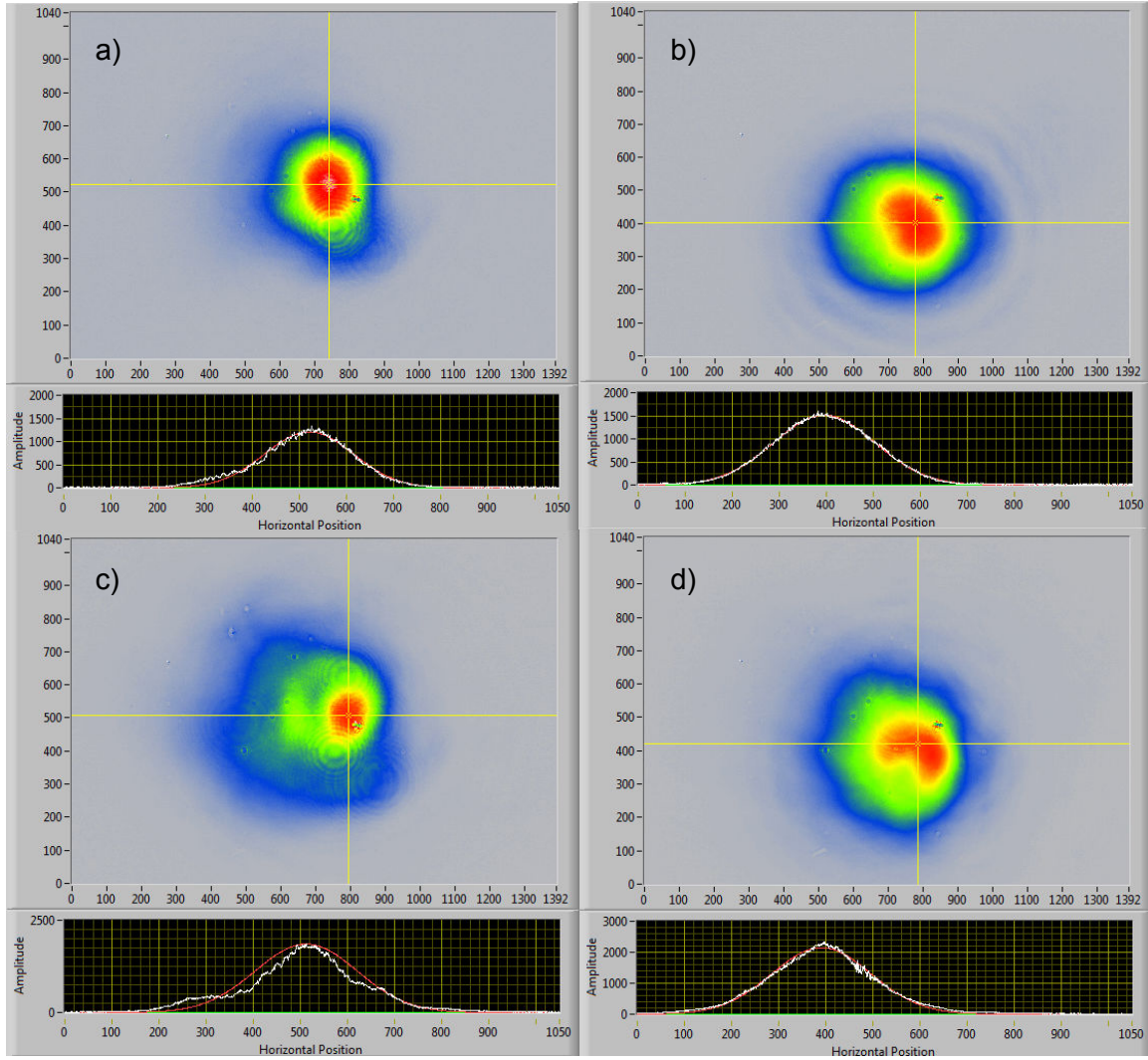
Figure 4.10: The 1 Stokes Raman's transverse mode in farfield after one pass in the amplifier. The Raman wave is amplified to a variety of energies by increasing the 800nm pump beam's energy. The Raman beam's energy is 1.04 mJ (a), 1.42 mJ (b), 1.88 mJ (c), and 2.17 mJ (d). The mode quality deteriorates as the energy increases from 1-2 mJ and beyond. The energy of the 1st Stokes mode is increased by increasing the 800 nm pump energy via tuning the wave plate in the pump line. The seed is therefore unaffected, and the pump's mode and spectrum are also unaffected by this process.
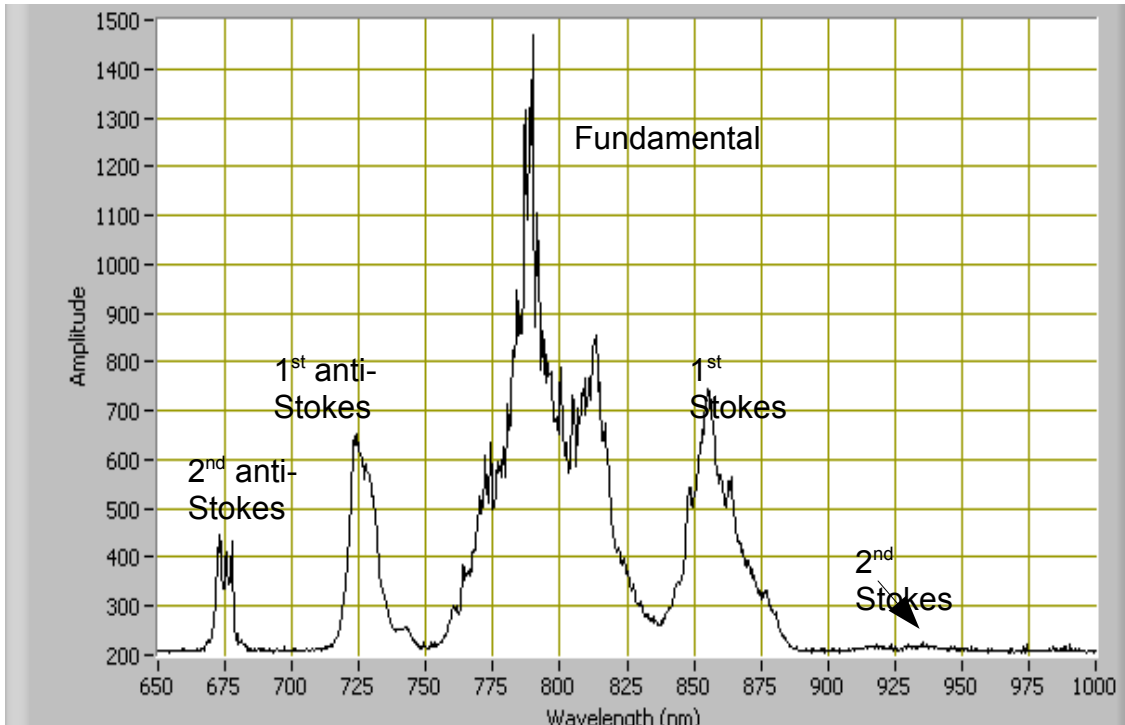
Figure 4.11: The spectrum of the lower order modes in the Raman cascade, from the 2nd anti-Stokes to the 2nd Stokes. The fundamental beam was initially centered at 790 nm and hence all wavelengths are shifted by ~10 nm to the blue from their expected positions, so that 1st Stokes is centered at 860 nm rather than 873 nm.
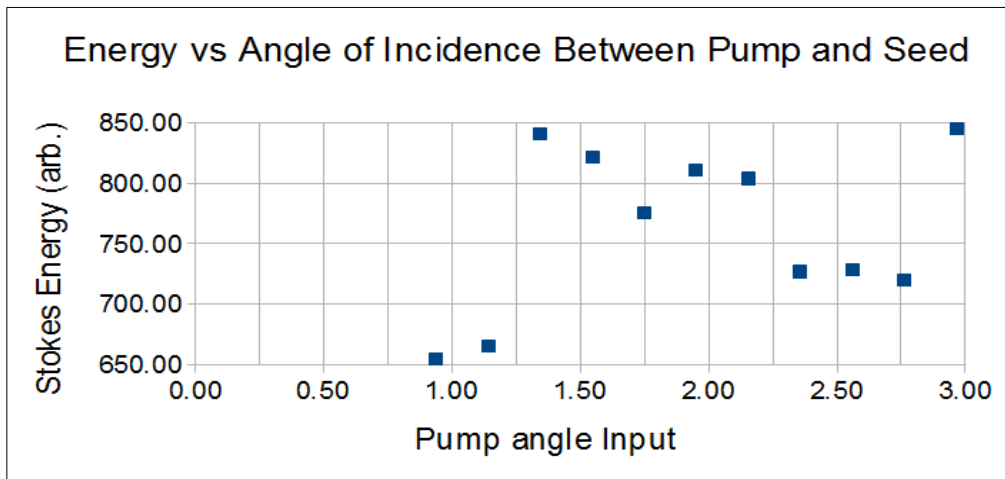
Figure 4.12: Amplified 1st Stokes energy from the second stage plotted against angle of incidence of the pump beam. The seed beam is passing through the crystal at a zero degree angle of incidence, so the angle of incidence for the pump beam is also the relative angel between pump and seed.

174

In a collinear pump-seed geometry, the automatically phase-matched processes will dominate, meaning that the 1st Stokes will eventually deplete into 2nd Stokes and so on. However, in a non-collinear geometry, it is possible to phase-match one or another of these Stokes processes; thus, for example, it is possible to generate 1st Stokes via four-wave mixing from fundamental, 1st anti-Stokes, and 2nd Stokes:

$$\omega_{1s} = \omega_{1as} + \omega_{2s} - \omega_{f} \tag{4.5.2}$$

Thus, the angle between pump and seed beams in the of the non-collinear geometry is chosen to phase-match this process, thereby helping to mitigate depletion of 1st Stokes into 2nd Stokes. This condition is met for an angle of 3 degrees between the 800nm pump and the 873 nm seed. Figure 4.12 shows the second-stage energy plotted as a function of angle between the pump and seed in the Raman amplifier crystal. There are additional angles which can be chosen to phase- match other combinations of Stokes and anti-Stokes modes to generate 1st Stokes from four-wave mixing processes—thus, for example, a peak of sorts appears around an angle of 1.3 degrees.

Another consideration in building this Raman system is bandwidth narrowing. The bandwidth of our main laser pulse is typically 35-45 nm FWHM, which is more than twice the bandwidth of the system used by Grigsby[3]. Thus, in Grigsby's Raman laser, the bandwidth narrowing was a relatively minor effect. It is a more drastic effect in the UT³ laser system, presenting a major design challenge.
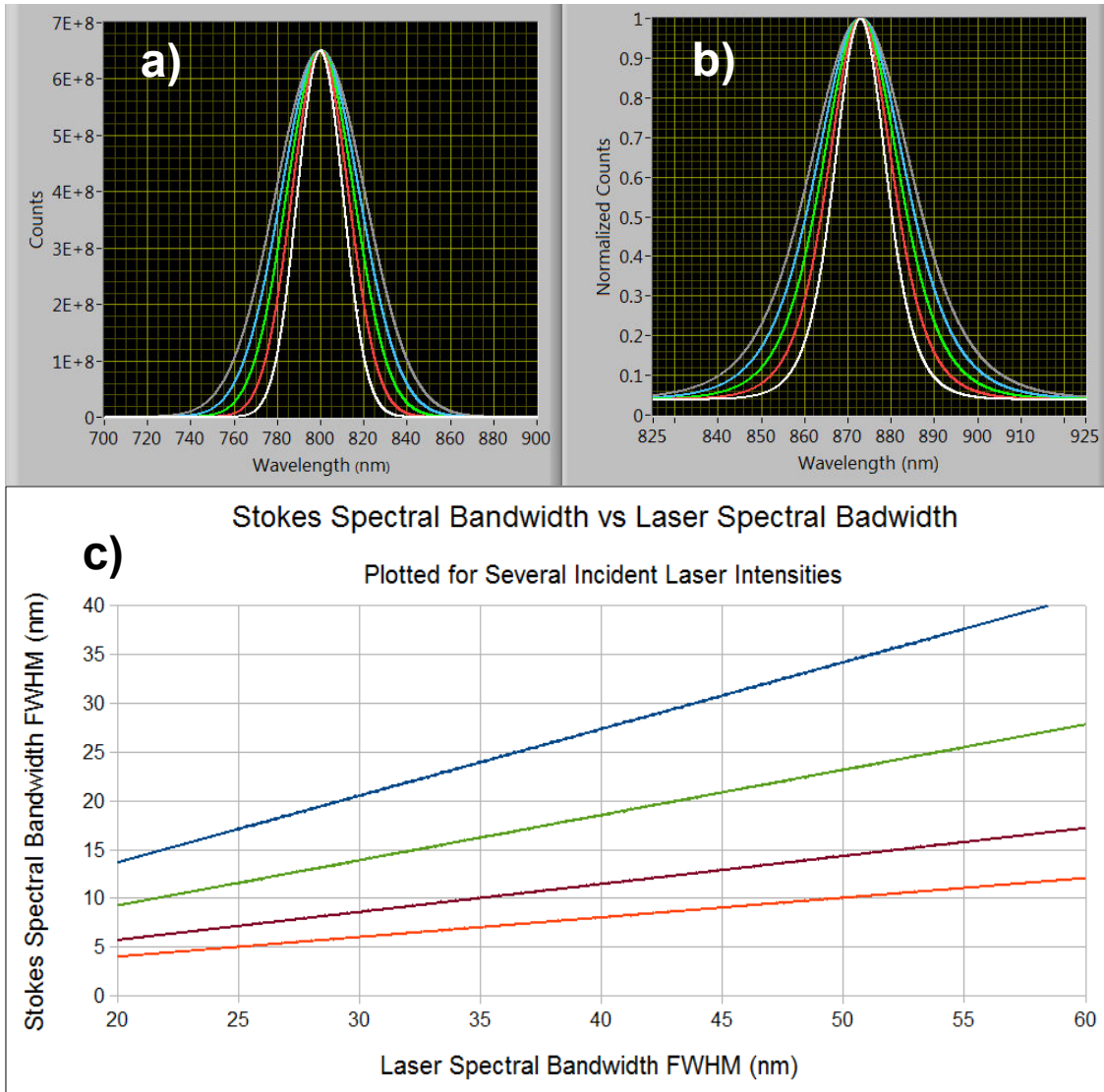
Figure 4.13: Simulated effects of laser spectral bandwidth on the Stokes' spectra. (a)The simulated laser had a Gaussian spectrum centered at 800 nm, similar to the UT3 Ti:Sapph Main Laser, and had FWHM bandwidths of 25 nm (white), 30 nm (red), 35 nm (green), 40 nm (blue), and 45 nm (gray). (b) The resulting 1 Stokes' bandwidths were all narrowed by ~ a factor of two, though all the lasers simulated here were at the same intensity. (c) The relationship between laser bandwidth and stimulated Raman scattering bandwidth is linear for any given intensity: 0.5 GW/cm² (blue), 1.0 GW/cm² (green), 2.5 GW/cm²(maroon), and 5.0 GW/cm² (orange), though the intensity better determine by how much the bandwidth will be narrowed.

The bandwidth typically ranges from 10-20 nm (FWHM), and the peak wavelength between 870-880. This actually represents a slight redshift in the first Stokes spectrum from the expected value—our laser is nominally centered at 800 nm, corresponding to a first Stokes of ~873 nm, but often is centered around 790 nm (and thus corresponds to a 1 Stokes spectrum centered around ~863 nm). This redshift is due to the leading edge of our pulse depleting the Raman gain in the system. Our pulses are positively chirped, so the leading edge of the pulse is red compared to the trailing edge.

It should be noted here that the bandwidth from the Raman system is generally narrower than the bandwidth of the 800 nm laser from which the Raman beam is generated. The main laser typically has a bandwidth of 35-45 nm FWHM, so it is narrowed by a factor of 2-3, as shown in Fig. 4.13. The reason for this narrowing is two-fold. First, the Raman laser experiences gain narrowing during stimulated Raman scattering because the output Stokes intensity is dependent[172],[173],[174] on the input pump intensity, as per the discussion in Chapter 3 (Sec. 3.1.1) of this dissertation:

$$I_s(z) = I_s(0)e^{G_R z} \tag{4.5.3a}$$

$$G_R = g I_L(\omega, r) \tag{4.5.3b}$$

$$I_L(\omega) \approx I_L(\omega_0) e^{\frac{-(\omega - \omega_0)^2}{2\Delta\omega^2}} \tag{4.5.3c}$$

where G_R is the gain for stimulated Raman scattering, $\Delta\omega$ is the Gaussian bandwidth, and ω_0 is the laser's peak frequency mode, and the laser is assumed to have an approximately Gaussian spectral distribution about its central frequency. Thus, the bandwidth will narrow for anything other than a perfect flat-top spectrum because the laser intensity and

hence the stimulated Raman scattering's gain will decrease for frequencies other than the peak frequency (Fig. 4.13).

The second reason is because the seed pulse gain gets saturated. Essentially, some gain saturation is needed to combat the effect of the gain narrowing: if the wings of the pulse are to be amplified sufficiently to keep the spectrum broad, then these wings must themselves be at sufficiently high intensity to saturate the Raman gain. However, because the pulse is chirped, the leading (red) wing arrives in the seed crystal first, and then is Stokes-shifted by the $Ba(NO_3)_2$ crystal. However, when this wing is at or near saturation, the gain gets depleted for the trailing (blue) wing of the pulse, and the result is a Stokes beam which is further red-shifted in spectrum due to this gain depletion.

Furthermore, because the Stokes wave and the fundamental wave interacting in the second stage Raman amplifier are both chirped, a small delay in the pump's (fundamental's) timing with respect to the seed's (1st Stokes') timing results in the interaction of different frequency modes in the Raman crystal. The result is that by changing the delay of the pump with respect to the seed, we observe both a difference in output 1st Stokes' energy (coarse-scan) and in output 1st Stokes' spectrum (fine-scan).

The changes in output energy (Fig. 4.14) have been previously reported, e.g. by Grigsby *et al.*[3] However, Grigsby postulated that the delayed "spikes" in the energy were due to pre- and post-pulses. Thus, the central peak is caused by the interaction between the 800 nm pump arriving simultaneously with the 873 nm seed and stimulating Raman scattering to amplify the first Stokes' energy, whereas the earlier energy peaks were due to SRS with a post-pulse and the later peaks to the SRS-interaction of the seed with a pre-

178

pulse. However, the UT³ Laser employs an XPW[175],[176] ("cross-polarized wave") pulse cleaner to remove pre- and post-pulses. The measured contrast ratio between the main pulse and any pre- and post-pulses is ~10^{10}:1, meaning that pre-pulses and post-pulses would have a miniscule amount of energy in the amplifier crystal—perhaps tens of nanojoules. It may be possible for such a small amount of energy to nevertheless play a part in the four-wave mixing process, since these pre-pulses and post-pulses may be at a slight frequency offset form the main pulse due to the chirp in each.
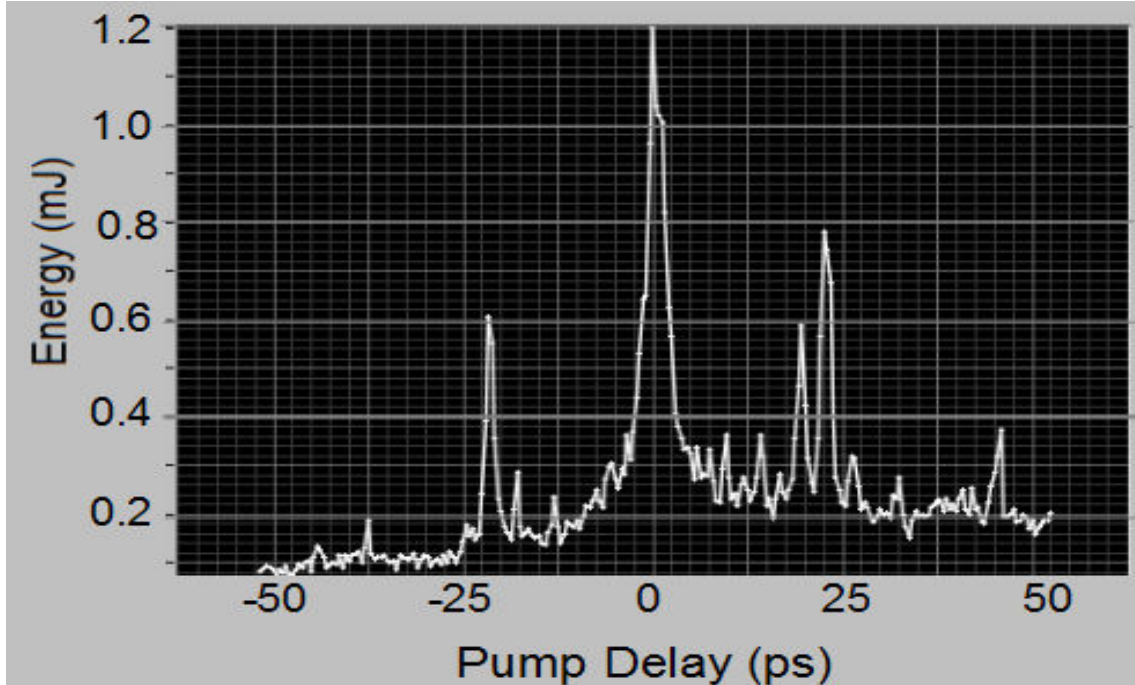
Figure 4.14: The energy of the amplified 1 Stokes beam is dependent on the delay between the 800 nm pump beam and the 873 nm seed beam in the second stage amplifier crystal. A negative delay means the pump is arriving earlier than the seed, and a positive delay means that the pump is arriving later than the seed. The FWHM of the peak centered around 0 delay is ~5 ps here.
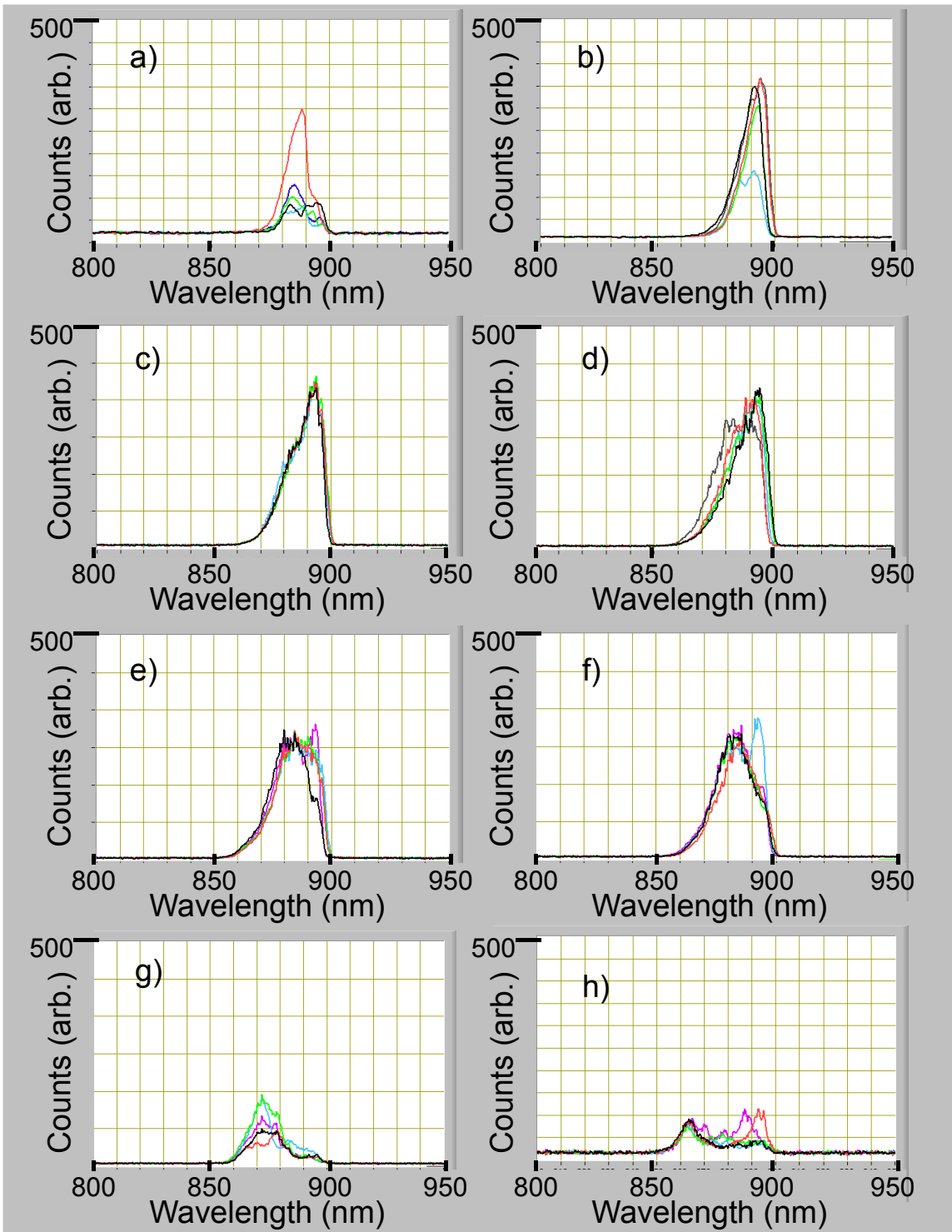
Figure 4.15: First Stokes spectra for various pump line delays.

The Stokes' energy is not the only thing which is dependent on the relative delay between pump and seed. The amplified first Stokes spectrum also changes with somewhat with the delay between pump and seed. This is to be somewhat expected, since a delay between pump and seed means a change in the frequency difference between the two pulses: this is due to the fact that both are positively chirped. However, the duration of each pulse is ~500 ps (FWHM), and the pulses are ~ linearly chirped, with the bandwidths being $\Delta\lambda_{LBand}$ ~40 nm → $\Delta\nu_{LBand}$ = 18.7 THz for the pump and $\Delta\lambda_{RBand}$ ~ 20 nm → $\Delta\nu_{RBand}$ = 7.86 THz for the seed: in other words, each picosecond of delay is equivalent to a change in frequency of $\Delta\nu_L$ = 37.5 GHz → $\Delta\lambda_L$~0.01 nm and $\Delta\nu_R$ = 15.7 GHz → $\Delta\lambda_R$~0.0068 nm, respectively. This means that the anticipated shifts in the spectrum of the amplified 1st Stokes wave should be negligible—practically unobservable—for small picosecond-scale delays between the pump and the seed.

However, the actual second stage Raman spectra experience observable shifts in their peak wavelength when the pump is delayed with respect to the seed. These shifts occur for small changes in the delay between the two pulses, specifically the spectra center shifts by >10 nm as the delay between pump and seed is scanned across the main peak in Fig. 4.14. This represents a total change in delay of <5 ps, which should result in a change in peak bandwidth of ~0.5 nm for our chirped pulses. Figure 4.15 shows the spectra of the 1 Stokes signal for different time delays between pump and seed in the second stage amplifier crystal. All of these spectra are taken for the case in which the two pulses arrive within 5 ps of each other: in other words, the chirp factor should be

181

insignificant. The spectra correspond to the pump's arriving before the seed by 2.00 ps (Fig. 4.15a), by 1.33 ps, (Fig. 4.15b), by 0.67 ps, and by 0.33 ps (Fig. 4.15d); the pump's arriving at the same time as the seed (Fig. 4.15e); and the pump's arriving after the seed by by 0.33 ps, (Fig. 4.15f), by 0.67 ps (Fig. 4.15g), and by 1.00 ps (Fig. 4.15h).

The amplified Raman pulse is then resized and compressed using a pair of 1200 lines/mm grating. Although the shot-to-shot fluctuations in the fundamental pulse's spectrum was minimal, there was still some fluctuation in the spectrum of the Raman beam. Fig. 4.16a shows the spectrum of the fundamental beam at input to the seed simultaneous to the amplified spectrum of the Raman beam. There is little change in shot-to-shot spectra for the fundamental beam, but the changes in the spectra—profile, bandwidth, and center—for the Raman beam are much more pronounced. This is in part because the Raman pulse spectrum depends on the fundamental beam's spectrum and its intensity (depends on energy, size, size at focus in the seed line, and mode quality). While the fundamental spectrum is nearly constant, the mode and energy fluctuate somewhat from shot to shot: the fundamental beam's energy is stable within 5% of the average energy, but the mode fluctuations are more difficult to characterize, since it is the shape as much as the size which changes, albeit slightly.

Because the pulse duration is dependent on bandwidth and also the center wavelength, these fluctuations in the Raman spectra result in some fluctuations in the compressed pulse's duration. We therefore observed some pulses as sort as 60 fs, though a typical duration was closer to 75-80 fs (Fig. 4.16b). The bandwidth limit duration for a pulse centered at 873 nm with a FWHM bandwidth of 15 nm is 74.3 fs, so these pulses
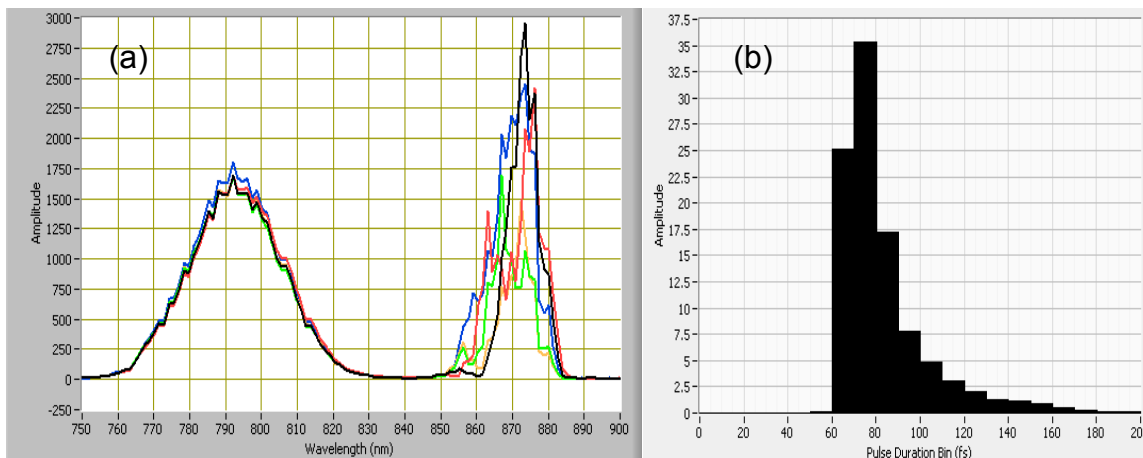
Figure 4.16: (a) The spectra of the main laser (left, centered at ~793 nm) and the Raman laser (right, centered at ~873 nm) for 5 different shots. Each fundamental-Raman pair was taken simultaneously via a two-channel spectrometer. Very small variations in the spectra of the fundamental spectra do not correspond to similarly small changes in the Raman spectra. Furthermore, the Stokes spectra are actually red-shifted relative to the expected center of ~866 nm. (b) These fluctuations in Raman spectra in turn lead to fluctuations in pulse duration, giving some shots as short as 60 fs, and some shots exceed 120 fs. Note that this compression data was taken without amplifying in the Ti:Sapphire amplifier.

are compressed to near the bandwidth limit for a Gaussian pulse. This minimum pulse duration of 55 fs is half the shortest length observed in Grigsby's CPRA system, and with comparable energy. The compressor's energy transmission efficiency was measured to be ~50% at this time.

4.6   THE RAMAN LASER'S TI:SAPPH AMPLIFIER AND COMPRESSOR

The Ti:Sapph amplifier was pumped by a Spectra Physics Quanta-Ray Pro-350 Q-switched, frequency-doubled Nd:YAG laser. The pump laser's nominal parameters are 9

ns pulse duration, 1.20 J pulses centered at 532 nm, with a spot size of 0.35 cm and ~tophat transverse profile at the position of the crystal. Typical performance delivered about 1.0-1.1 J, nominally split by a 50/50 beam splitter to pump both sides: in practice, ~45% of the energy pumped one side and 55% the other. The crystal itself had a small-signal absorption of ~90%.

A relatively simple energy-gain simulation was run for the Ti:Sapph system to determine the number of passes to optimize energy output. Some sample simulation results are shown in Fig. 4.17. The simulations are run for 8 passes at a variety of input Stokes' energies, assuming a perfect match between the Raman mode and the pump mode (0.35 nm waist). A loss from scattering of 3% per pass is assumed, and the simulations are run for different pump energies (1.2 J, 1.1 J, 1.05 J, and 1.00 J). It is clear from these simulations that the amplifier begins to saturate after the 6th pass, with very little difference in energy for different input energies in the 8th pass for a given pump energy. Using a seed with input energy 1.5 J (as per Fig. 4.10 and discussion), the expected output energy is 541 mJ after 6 passes, 581 mJ after 7 passes, and 580 mJ after 8 passes. Since each pass adds some delay to the system, and since it furthermore adds some daily alignment time, the amplifier was set up in 6 passes.

The total path length of the Ti:Sapphire amplifier exceeds 12 m (it has 6 passes, each measuring approximately 2 meters on average). However, because the spot size is fairly large at the input to the system, changes to the spot size due to diffraction should be negligible if the beam is well-collimated. For a 0.35 cm initial waist, the Rayleigh range is ~48 m and the spot size at the exit should be approximately 0.39 cm.
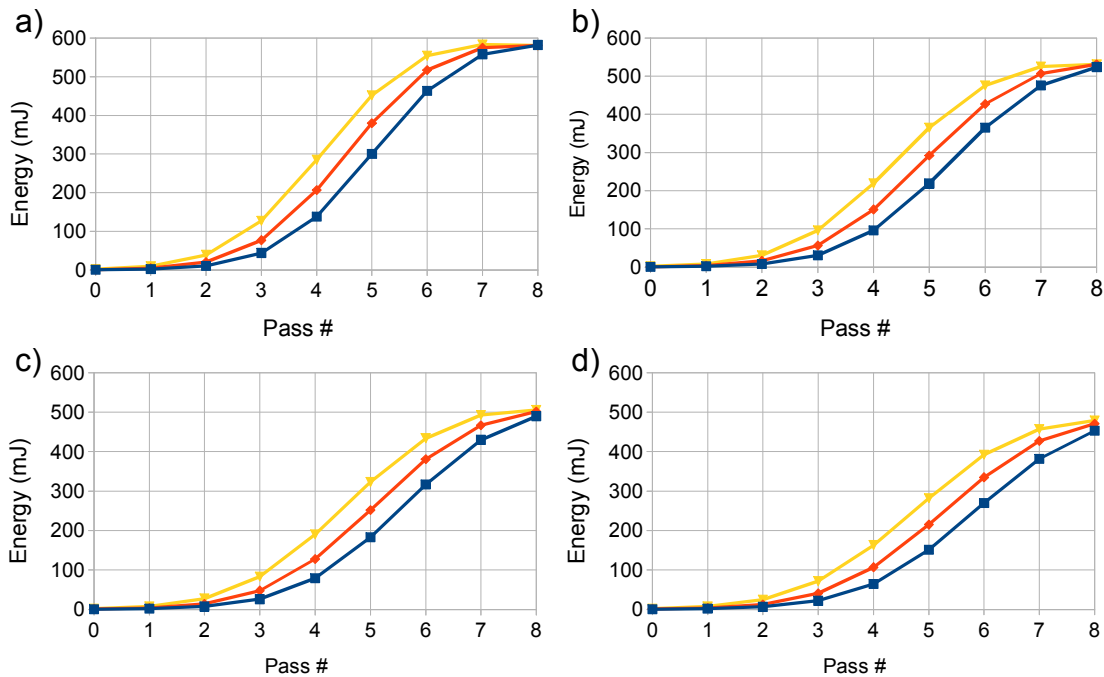
Figure 4.17: Simulated energy per pass for 8 passes in a mode-matched Ti:Sapph amplifier. The mode size of both seed and pump is 0.35 cm waist, and the seed beam is a Raman pulse centered at 873 nm with an 18 nm FWHM bandwidth and 0.5 mJ (blue squares), 1.0 mJ (red diamonds) or 2.0 mJ (yellow triangles) initial energy. The pump laser is a 9 ns frequency-doubled Nd:YAG laser centered at 532 nm, with a total energy of a) 1.20 J, b) 1.10 J, c) 1.05 J, or d) 1.00 J. The per-pass loss due to scattering is assumed to be 3%, and the small signal absorption of the Ti:Sapph is 90%.

Three other effects should be noted here. First, the 1 Stokes energy is not always stable. This has already been mentioned, and and example of the fluctuations in the energy of the 1 Stokes used to seed the Ti:Sapph amplifier is shown in Fig. 4.4c. The second is that although the different Stokes and Anti-Stokes orders are spatially separated (at least in the non-collinear geometry), there is often some fundamental signal mixed with each order. In order to ensure that only the 1 Stokes mode is amplified by the Ti:Sapph, an interference filter which transmits at 880 nm (80 nm FWHM bandwidth) is

185

placed after the second stage amplifier crystal but before the input to the Ti:Sapphire amplifier. This filter effectively has an optical density > 3.0[xvi] outside of this specified range, and transmits ~70% of the intensity the light at the peak of that range. In practice, this means that a 1 Stokes mode whose energy measures 1.5 mJ after the second-stage amplifier crystal will seed the Ti:Sapph amplifier with approximately 1.0 mJ.

The third consideration is that the mode shape, quality, and size all matter. The simulations behind Fig. 4.17 assume that the pump has an ideal tophat mode and that the seed mode is a perfect Gaussian. A representative sample of the typical seed mode profile is in Fig. 4.10 (Sec. 4.5).

The Quanta-Ray's mode is nearly top-hat in profile. However, there is of course some ramp at the mode's edge and the mode is only smooth to within a few percent r.m.s. at the top, and this only under full power. Figure 4.18 shows some examples of this pump mode at the position of the Ti:Sapph crystal. The mode has been relay-imaged from a position within the pump cavity, approximately 70 cm from the pump's output; these images were taken by removing the Ti:Sapph crystal and placing a ccd in the same location. The pump mode changes profile as the current is changed, in large part because the phase-matching condition of the frequency-doubler crystal is sensitive to temperature,

xvi Optical density (O.D.) is on a logarithmic scale, so O.D. 1 removes 1 order of magnitude of the intensity of the light being filtered and transmits 10%, O.D. 2 transmits 1%, O.D. 3 transmits 0.1%, etc.
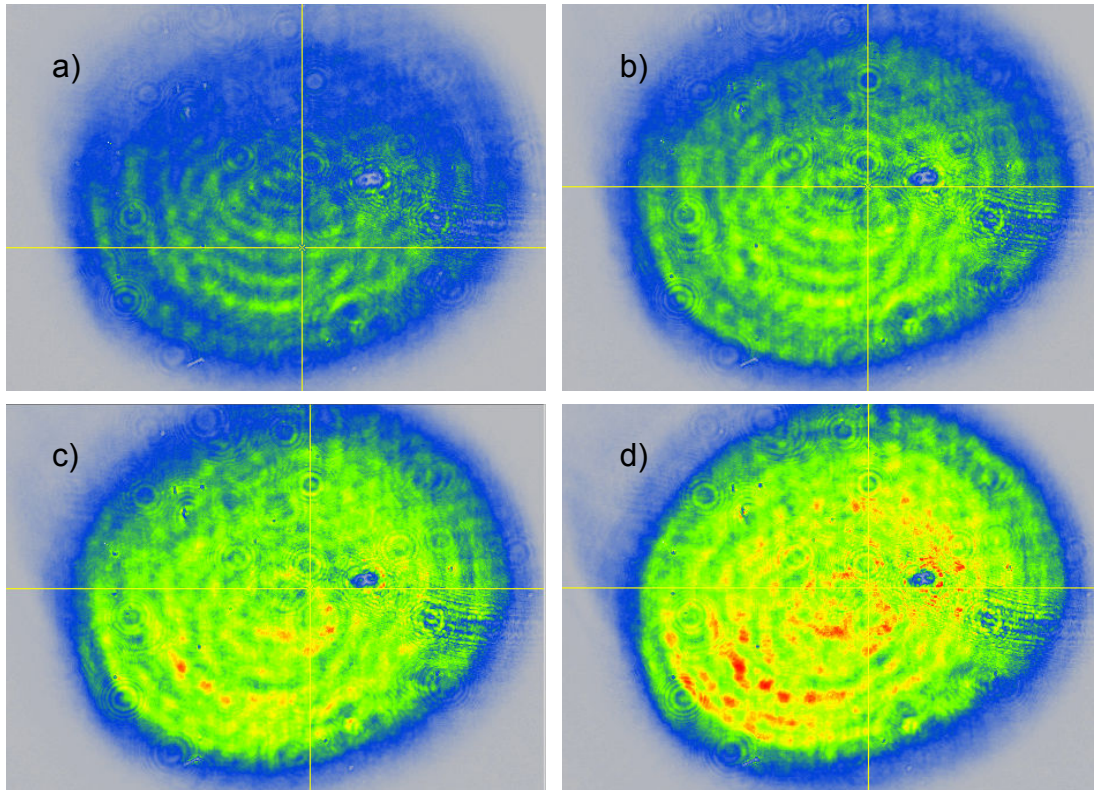
Figure 4.18: The Quanta-Ray Pro-350 mode used to pump the Ti:Sapph crystal in the third stage "Final Amplifier" of the Raman laser system. These are taken at the position of the crystal itself, with the cursor being placed at the line-average maximum for each mode. The modes are taken for different amplifier current levels (10 is full power): a) 7, b) 8, c) 9, and d) 10. The color scale represent intensity, with the difference between red (maximum) and blue being ~5% r.m.s.

which is in turn dependent on the power-flux of the Nd:YAG laser at 1064 nm. This latter is directly controlled by changing the flashlamp current.

A histogram of 10,000 shots of the amplified Raman energy after the 6-pass Ti:Sapph amplifier is shown in Fig. 4.19. The average energy observed was 248 mJ, with a FWHM distribution of $\pm 25\,\text{mJ}$, with a pumping energy of ~ 1.10 J. The input energy of the seed was approximately 1 mJ, with a mode similar to that of Fig. 4.10b and an energy distribution of $\pm 0.25\,\text{mJ}$, similar to that of Fig. 4.4c.
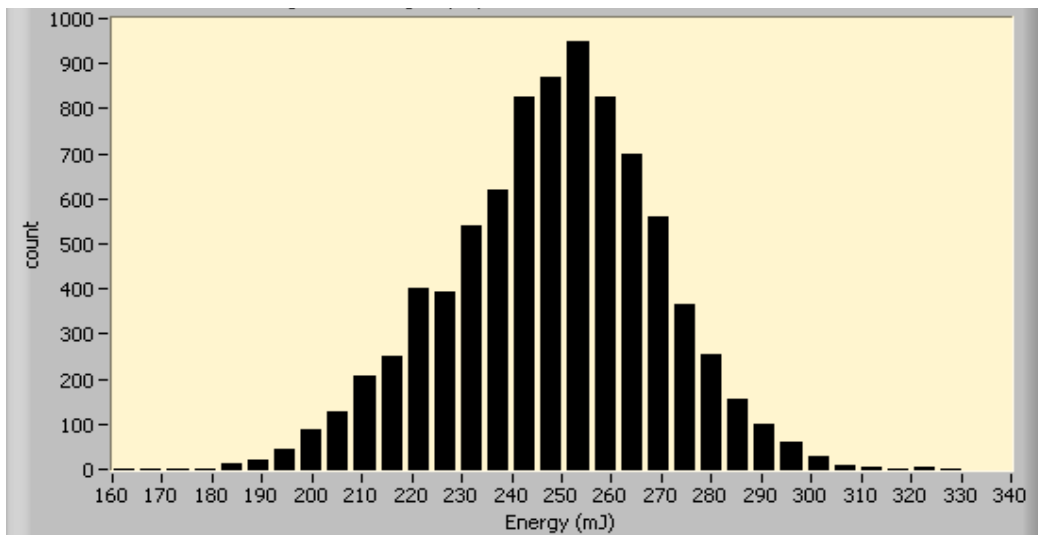
Figure 4.19: Histogram of the Raman pulse energy after amplification in the 6-pass Ti:Sapphire Final Amplifier. The average energy was measured at 248 mJ, with energies as large as 330 mJ observed. The energy spread here is now only ~10% FWHM.

This energy is less than that predicted by the simple simulation, an effect which might be explained in part by the ~425 mJ predicted in Fig. 4.17b, a result which might be explained by a combination of three causes: pointing stability, mode asymmetry, and mode size mis-match.

First, there is some slight pointing instability after the second stage, which nevertheless makes consistent overlap of the pulse through all 6 passes of the third stage difficult. Alignment of the 6-pass Ti:Sapp amplifier is accomplished by replacing the crystal with an iris an aligning the seed beam pass-y pass through this iris using a ccd. Additionally, there is a pair of irises at the input to the Ti:Sapp amplifier through which the beam is first aligned. This procedure allows for an optimum alignment on average of the beam pointing, but any given shot can deviate somewhat from this average position

by as much as 0.1 mm on the first pass, with additional deviation per pass thereafter. Recall that the beam mode is initially optimized at 3.5 mm in waist ($1/e^2$ intensity radius). The beam is then shifted very slightly when the crystal is replaced, and so some slight additional tweaking the pass mirrors is done to optimize energy output.

The second and third explanations for a decreased spot energy are related to each other. Because the mode is slightly asymmetric, merely matching mode size is not sufficient to optimize energy: in the ideal case, mode size and symmetry would be matched. Because the Raman mode is not symmetric—and because the Raman mode shape actually fluctuates shot-to-shot as per Figs. 4.4 and 4.10 (energy fluctuates, and mode changes with energy)—a perfect mode-match cannot be achieved between the seed and the pump. Additionally, the mode sizes can only be approximately matched by the two-lens-telescope used to resize the beam from its ~2 mm FWHM size (average) from the second stage to the needed 3.5 mm waist for the third stage.

In the collinear geometry, the average amplified energy form the second stage was 100 mJ with a similar spread in energies; this lower amplified energy is due to a poorer mode in the collinear geometry, which lacks the mode cleaning effects of phase-averaging between pump and seed in the second stage crystal.

The output mode under maximum amplification was typically clean with a nearly-Gaussian profile. However, this system occasionally generated a self-focused mode with a hotspot whose estimated fluence was ~30 J/cm^2: well above the damage threshold for most coatings (not to mention the crystal itself). This self-focused mode was

the effect of a combination of thermal lensing and of a small hot-spot which developed randomly in the Raman mode itself: the effect occurred approximately once every 10-100 shots, depending on alignment and the parameters of the seed and the pump. The hot spot was not necessarily correlated with a higher shot energy, but rather with small changes in the mode out of the second stage amplifier crystal. The fluence in the hot spot is estimated to exceed 25 J/cm^2 and is sufficient to instantly damage the coating of the mirror at the output of the amplifier. More problematic still is that it risks causing damage to the Ti:Sapphire crystal.

In order to mitigate this problem, an expanding air of lenses were placed on the fourth pass of the Ti:Sapph amplifier. These expand the beam slightly (-150 mm focal length followed by a +200 mm focal length) and allow it to propagate with a slight defocus through the last two passes of the amplifier. Additionally, reducing the energy output (and hence increasing the mode quality) of the second stage amplifier also reduces the chance of generating hot-spots in the Ti:Sapph amplified Raman beam. Images of a "normal" mode, a hot-spot focused mode, the mitigated geometry of the Ti:Sapph amplifier, and the resulting energy histogram can be seen in Fig. 4.20.

The observed output energy of this "safer" set-up is significantly lower than the energy previously obtained. As the histogram in Fig. 4.20d shows, the safer amplifier operates with only ~150-160 mJ average energy, and up to 205 mJ in the histogram's tail. It also has a slightly larger σ, due in part to operating further from saturation.
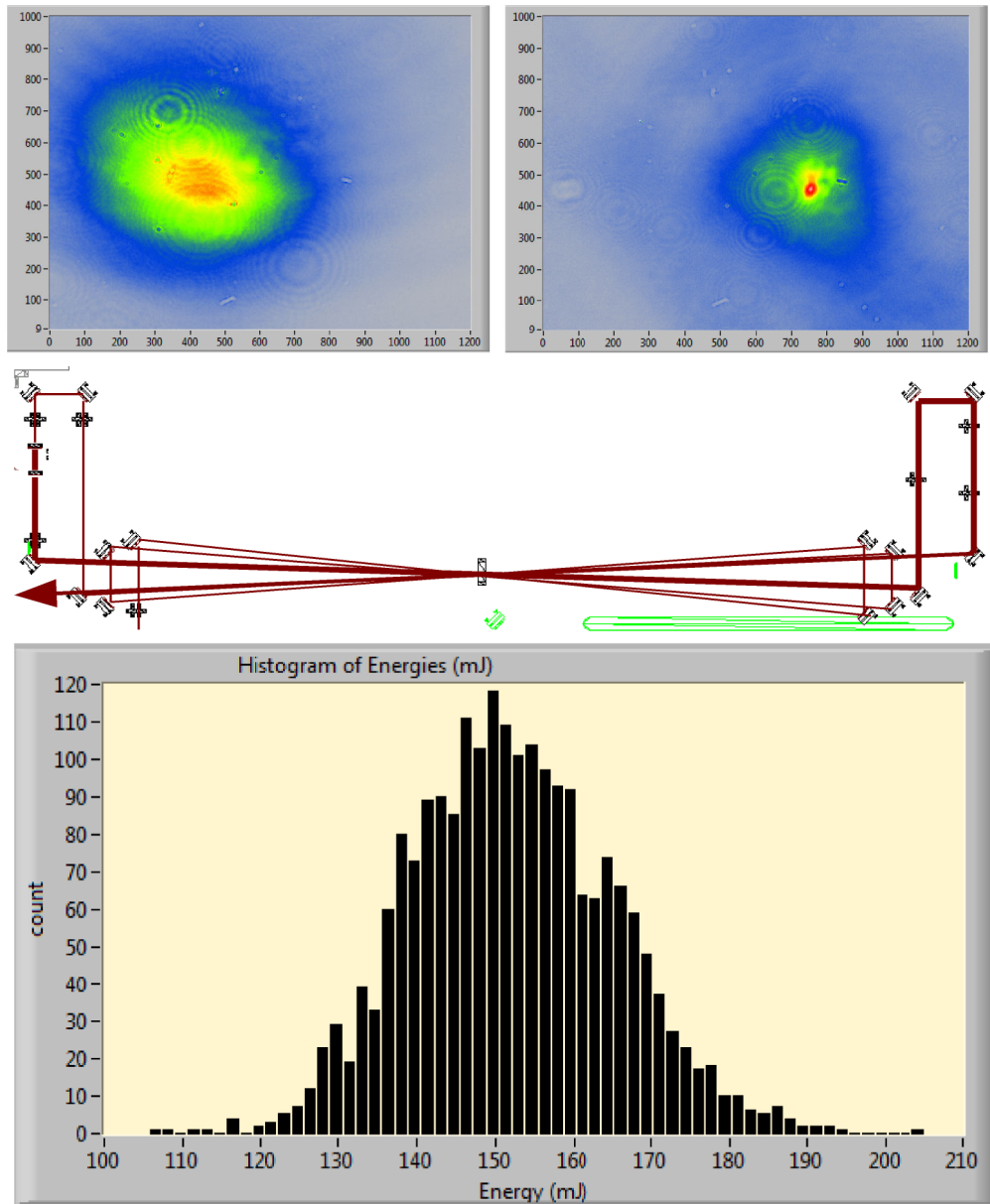
Figure 4.20: Focused hot spots and their mitigation. a) A typical mode after 6 passes has a smooth, nearly Gaussian profile, but b) every few shots focused into a hot spot whose peak intensity is >30x higher than that of the typical mode, causing instant damage to the optics at the output of the amplifier. c) To remedy this problem, the 6-pass amplifier was redesigned with telescope pair (-150 mm f.l. then +200 mm f.l.) placed in a side arm to the amplifier on the 4th pass. This increases the beam's size and leaves it slightly defocusing, which helps to mitigate the focusing problem, but also results in a lower output energy, as shown by d) a histogram of >5,000 shots, the average of which was 155 mJ.

191
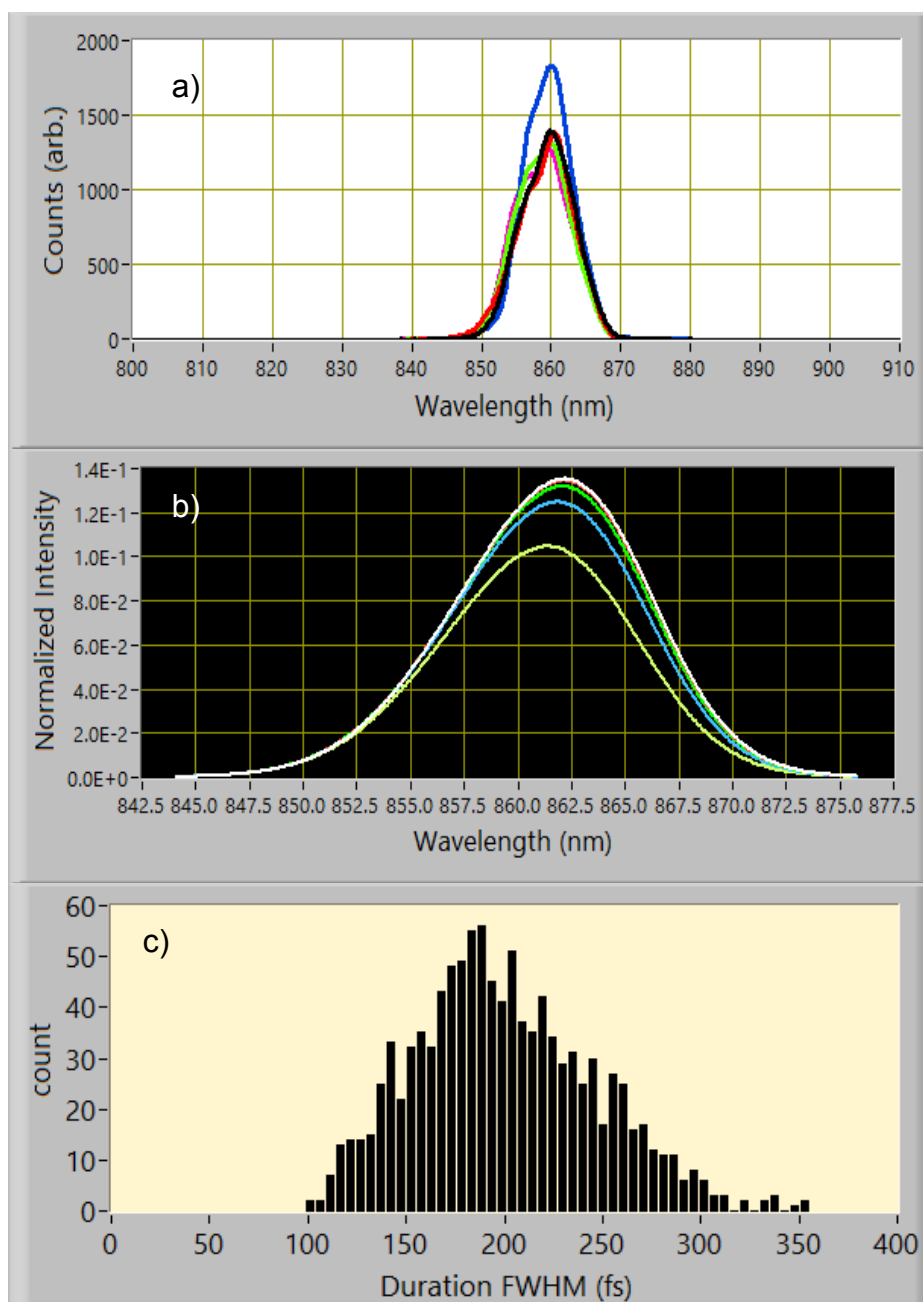
Figure 4.21: Amplified beam spectrum and compression. a) Spectrum of the Raman laser when amplified to ~135 mJ (average): the spectrum has narrowed from ~15 nm FWHM before amplification to ~10 nm FWHM after amplification. This is due to gain narrowing in the Ti:Sapph amplifier. b) A simulation of the effects of gain narrowing predicts a bandwidth decrease from 15 nm FWHM to ~10 nm FWHM. c) A histogram of >1000 shots shows that this pulse can be compressed to 100 fs, though its average compression is nearer to 190 fs with a long tail to 350 fs.

192

The Raman laser undergoes some bandwidth narrowing in the Ti:Sapphire amplifier, which also results in a longer pulse duration after compression, as shown in Fig. 4.21. The pulses after the Ti:Sapph amplifier typically have an average bandwidth of 10 nm FHHM, which can be very stable as shown in Fig 4.21a. However, the bandwidth fluctuates more than this typically, with most shots having between 10-15 m FWHM.

A series of simulations were run to determine whether this bandwidth narrowing is accounted for by gain narrowing only. The spectra in Fig. 4.21b is the output of the simulation given an input pulse with wavelength between 860 nm and 865 nm peak with a consistent 15 nm FWHM bandwidth and Gaussian spectrum; there are six resulting spectra because there were 6 input pulses, each with a slight shift in center wavelength and pointing. The resulting spectra have been consistently narrowed to 10 nm FWHM. An input spectrum of 20 nm FWHM is expected to narrow to 14-15 nm FWHM, which is consistent with the range of measured bandwidths.

The histogram in Fig. 4.21c is taken with the same set of shots which produced the spectra in 4.21a. The average duration in this case was 190 fs, but shots as short as 100 fs and as long as 350 fs were observed. Given the consistency of the spectra bandwidth and central position in Fig. 4.21a, this suggests that the fluctuations in duration are not only due to fluctuations in spectra as was previously thought.

One possible reason for this is the existence of pre- or post-pulses which are sometimes amplified sufficiently to register in the autocorrelator used to measure pulse duration, which is a second-order autocorrelator. If these are sufficiently strong and

sufficiently close to the primary pulse, the fitting function of the autocorrelator will then overestimate the duration of the pulses. Figure 4.22 shows a representative set of shots with (4.22a and c) and without (4.22b and d) the pre- or post-pulses present. These pre- and post- pulses have a random amplitude, perhaps due to fluctuations in the first and second stage of the system: they are then further amplified in the Ti:Sapph amplifier stage, so that their peak intensity is less than though comparable to that of the peak Raman pulse. The primary source of these side pulses is the TFP energy tuner in the second-stage pump line, which produces back-reflections when not at full transmission.
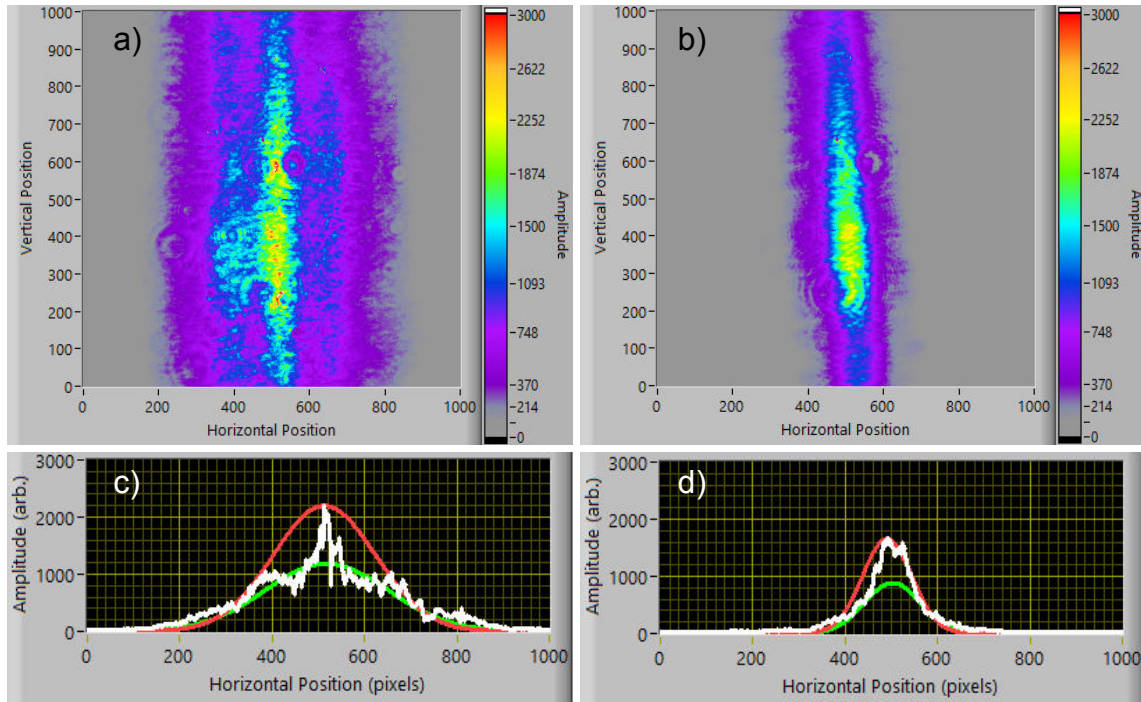
Figure 4.22: Raman laser autocorrelations with and without pre- and post-pulse side peaks. Single shot background-free autocorrelator image of the Raman pulse a) with side pulses, and b) without the side pulses, along with the lineouts of the autocorrelations c) with and d) without the side peaks. The lineouts show sample vertical lineout from the center of the pulse (white), a Gaussian fit for that lineout (red), and the Gaussian fit to the averaged lineouts (green), the last of which is used to compute the approximate pulse duration.

4.7   TARGET CHAMBER CONSIDERATIONS: FOCAL PROFILES AND SYNCHRONIZATION

The two lasers are combined through a dichroic mirror which reflects at 800 nm and transmits at 873 nm. They are then temporally synchronized and focused on-target together by a 60 cm focal-length f/12 15º off-axis parabola mirror, which is gold-coated and therefore reflects ~96% of both beams. The transverse mode of the Raman laser—and of the Main laser, for that matter—can be imaged either directly (at low energy) or indirectly via relay imaging. Both methods produce similar results, though the current relay-imaging system has a lower resolution.

4.7.1 Raman Beam Focus

In the direct imaging system, a 20x microscope objective lens is placed so that it images the focal plane of the laser, and then a ccd camera is placed after this. However, the beam must be attenuated by > 3 orders of magnitude to prevent damage to the objective lens.

Alternatively, the focal lane can be relay imaged, which has the advantage of being done *in situ*. A wedge can be used to reflect 4% of the beam after focus, which is then collimated by a lens and sent out of the chamber through a window. The reason for using only 4% of the beam is to reduce the B-integral through the lens and the output window, which is sufficiently high to cause nonlinear effects such as self-focusing (and for that matter self-phase modulation). The beam is then sent through a focus by a lens which is identical to the collimating lens, with a 20x microscope objective lens imaging

the focal plane from this last lens to a ccd. The objective lens is also on a translation stage so that other planes can be imaged if desired.

The size of the mode can then be determined by one of two methods. The first is to use a USAF test pattern target, which is placed at the laser's focus: the size of the patterns is known, and gives a sense of scale to which the mode can be compared. An alternative method is to place a razor edge on the gas jet stage—which is itself mounted on a 3-d motorized translation stage with a 0.1 µm step size. The razor edge can then be translated into the beam's focal plane until it blocks or unblocks the beam, and then the size estimated from the number of steps to fully block the beam from fully unblocking it.
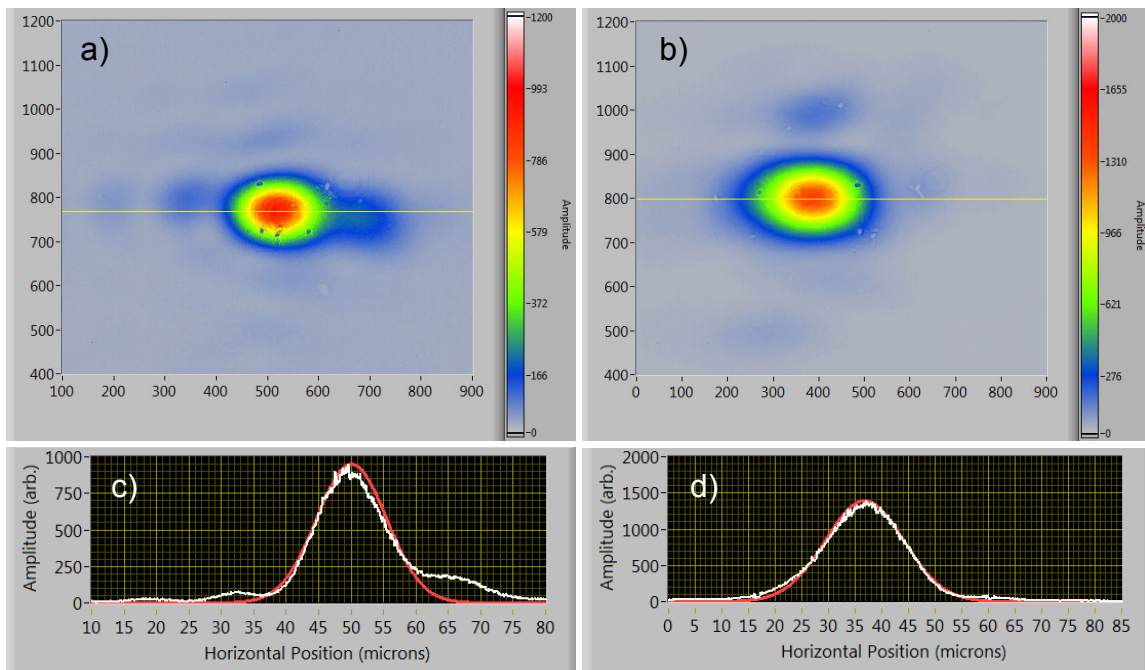
Figure 4.23: Focused modes and lineouts of primary (fundamental) and secondary (Raman) beams. The transverse mode image of a) the primary beam and b) the Raman beam when focused by the OAP onto the front of the gas jet, captured under vacuum via relay-imaging system. The gas jet is not fired in these images, so there is no defocusing or self-focusing present. The yellow line is the axis along which the lineouts of c) the primary and d) the Raman beams are taken. These lineouts include the actual lineout profile (white) and a best-fit Gaussian (red).

196

The Raman beam at focus is slightly elliptical. The FWHM spot size for 100 shots was $10.6\pm0.2\,\mu$m by $16.2\pm0.7\,\mu$m. This is slightly larger than the primary beam, whose mode is also slightly astygmatic and elliptical, with a 100-shot averaged FWHM size of $8.8\pm0.2\,\mu$m by $11.1\pm0.9\,\mu$m. It should be noted here that the difference in size between the two beams is in part due to the fact that the Raman beam's farfield (pre-focus) size is limited by the Raman compressor gratings, which are 4" high: this imposes

Geometry	Optic Size	Transmitted Power P/P_0
Circular	$d = \sqrt{2}\,w$	65.86%
Circular	$d = 2\,w$	86.44%
Circular	$d = \pi\,w$	99.35%
Circular	$d = 4.6\,w$	>99.99%
Square	x = y = 1.5w	70.84%
Square	x = y = 2w	91.85%
Square	x = y = 3w	99.42%
Square	x = y = 4w	99.98%
Square	x = y = 8w	100.00%
Rectangular	x = inf, y = 1.5w	84.16%
Rectangular	x = inf, y = 2w	95.84%
Rectangular	x = inf, y = 3w	99.71%
Rectangular	x = inf, y = 4w	99.99%

Table 4.2: Throughput power and intensity ripple vs normalized optic size obtained via ray-tracing using ZEMAX. The sizes in all cases are specified by the relevant dimensions of the optic--diameter d for a circle, base x and height y for a square or rectangle--normalized to the beam's waist. The transmitted power is taken as the power after the optic (e.g. reflected from a mirror or transmitted through an aperture or lens) normalized to the incident beam power. The results for the circular cross-section compare well to those given by Siegman[177].

a maximum $1/e^2$ waist size of w = 1" to avoid clipping.

Table 4.7.1 gives the expected power throughput from a mirror or other aperture or an optic. This is assuming an ideal mirror (e.g. 100% reflectivity) or lens (100% transmittance) and a Gaussian beam with $1/e^2$ intensity waist w. The Raman compressor's diffraction gratings are essentially rectangular with a base of 8" and a height of 4", which for a w = 1" beam corresponds to x = 8 (x >> w on the first grating and x ~ 4w on the second grating) and y = 2w, since the beam makes two passes which are vertically separated on each grating.

The primary beam's compressor gratings are ~6" high and thus can support a larger beam spot size than the Raman gratings. Essentially, the Raman beam vertical waist is limited to w < 2" at input to the compressor, for which the power transmission is $P/P_0 < 96\%$ (excluding the expected 40% throughput for the grating pair itself) and the intensity ripple $\Delta I/I_0$ in the near-field is ~1%. Additionally, the pickoff mirror is an x = y = 2" square mirror, for which the expected throughput is $P/P_0 < 92\%$.

4.7.2 Time Overlap: Synchronizing the Primary and Secondary Pulses

The time overlap (synchronization) between the two pulses is achieved in steps. The first step is to overlap the two using a fast photodiode, which allows for a relative delay between the two pulses of ~0.2 ns. However, since the two pulses have FWHM durations ~100 fs for the Raman pulse and ~30 fs for the primary pulse when compressed, the primary pulse has a 100 fs window during which it must arrive on-target if it is to be

overlapped in time with the Raman pulse[xvii]. Therefore, a more precise method for overlapping the two pulses is needed.

One possible method is to use sum-frequency generation (SFG) between the two pulses in a second-harmonic crystal. The crystal is placed at (or near) the focus of the two pulses, which results in the generation of frequency doubled light (SHG) along the path of each beam, and then also the generation of SFG which is phase-matched between the two beams. In theory, this is a very precise way of overlapping the two pulses, but it suffers from a few drawbacks in practice. The biggest drawback is that the two pulses are collinear, which means that the primary 800 nm and the secondary (Raman) 873 nm light are propagating along the same axis. Therefore, the 400 nm and 436.5 nm SHG signal will also be collinear with the 417.5 nm SFG signal. Thanks to the small separation in wavelengths for these three signals, filtering them form each other is problematic, especially given that the central wavelength of the primary and hence also of the Raman laser can drift by ± 10 nm on any given day, and that the Raman laser can then have additional drift from this central wavelength as discussed in above (see Sec. 4.5). In other words, spectral filtering (e.g. via interference or bandpass filter) is not a viable solution.

Therefore, a different method of synchronizing the two pulses is used. Both pulses are intense enough to ionize air or even helium; this ionization causes the pulse to defocus, and it also defocuses any pulse trailing the ionizing pulse (within the ionization recombination time). Therefore, the primary pulse can be used as a "pump" and the

---

xvii I am here defining "overlapped" to mean that at least ½ of the shorter pulse is contained within the FWHM duration of the longer pulse. For many of the two-color experiments, a greater overlap may be desired.

Raman pulse as a "probe" such that the Raman pulse energy (and hence, intensity) is reduced to an extent that it does not ionize the target gas. The two pulses are then focused on the target gas, with a pair of ccd cameras monitoring the modes of each via relay imaging as discussed above. The pulses are sent to a pair of ccds using a beamsplitter, and then are spectrally resolved using a pair of bandpass interference filters.

The Raman beam line includes a pair of mirrors mounted on a translation stage with a micrometer screw whose marked resolution is 0.001 inches. This corresponds to a roundtrip delay of 169.5 fs; however, the screw can be turned by less than a full increment: approximately 0.0002 inches, or a roundtrip delay of 33.9 fs. This corresponds to approximately the compressed pulse duration of the primary pulse and is approximately 2-3 times shorter than the shortest compressed Raman pulses observed, so the delay time resolution is short enough to overlap the two pulses. An example of the
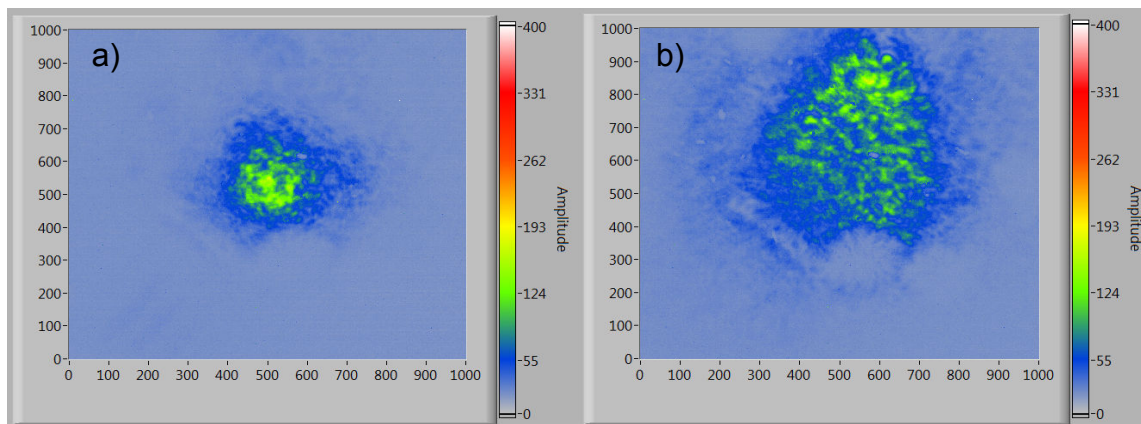
Figure 4.24: Transverse modes of Raman beam used as a probe for ionizaton defocusing. The Raman probe pulse either arrives a) before the primary pump pulse, and hence is not defocused, or b) arrives after the Main pump mode and hence is defocused.

Raman mode when the Raman beam arrives before and after the primary beam is shown in Fig. 4.24.

The method for obtaining time overlap is thus to scan this delay line until the point at which defocusing first occurs. Then the energy of the pump line is lowered and the delay scan repeated (meaning, the Raman line is further delayed) until this point is found again. Ideally, the location at which ionization defocusing begins is found at the lowest possible pump intensity which still ionizes, because at higher intensities the leading edge of the pump may cause ionization and as a result the overlap will be between the Raman probe and the leading edge of the pump, rather than an overlapping of the two peaks (ideal) or even an overlap of the peak of one with the half-maximum of the other (minimum acceptable).

The roles of the two lasers—Raman and Fundamental—can then be reversed and this process repeated from the other direction. This ultimately defines a range of delay positions over which the two pulses are overlapped, typically <0.002 inches on the stage (<340 fs), within which range a quick delay scan can be easily accomplished *in situ* (that is, the delays can be changed within this range to optimize any effects from the two-color laser-plasma interactions in question).

The reason why this range needs to be defined is that the ionization defocusing effect becomes weak and difficult to perceive at lower intensities. Recall from Chapter 2 that ionization may occur via tunneling, for example (this point will be further discussed in Chapter 5). This effect can certainly therefore take place in the wings of a very intense

201

pulse, e.g. a pulse which ionizes via Coulomb barrier suppression. Furthermore, a sufficiently intense pulse will begin barrier-suppression ionization in its own wings.

As an example, consider a pulse whose duration is 100 fs, whose energy is 30 mJ, and whose focus is ~Gaussian with a $1/e^2$ intensity waist of 15 μm. This beam is incident on a helium gas target, the barrier suppression intensities of which can be estimated by[178]

$$I_{BS}[W/cm^2] \approx 4 \times 10^9 \frac{E_{bound}^4[eV]}{q_i^2}$$ (4.7.1)

For helium, this gives a barrier suppression intensity of 1.46×10^{15} W/cm^2 for first ionization and 8.77×10^{15} W/cm^2 for second ionization, which are in reasonably good agreement with experimentally obtained parameters, e.g. $1\text{-}2 \times 10^{15}$ W/cm^2 for singly ionized helium and $0.8\text{-}2 \times 10^{16}$ W/cm^2 for doubly ionized helium[xvi][179]. The laser's peak intensity is thus

$$I_{peak} = \frac{2E}{\pi \tau_{laser} w_0^2}$$ (4.7.2)

which yields a peak intensity of $I_{peak} = 8.49 \times 10^{16}$ W/cm^2. This will easily doubly ionize helium. In fact, assuming that the pulse is also Gaussian in time, the pulse is still strong enough to (singly) ionize helium within 200 fs of the peak intensity; if the energy is reduced to 3 mJ (and thus the peak intensity to 8.49×10^{15} W/cm^2), the pulse is intense enough to singly ionize helium 85 fs before the peak.

The spatial overlap of the two beams is also critical. This is done by using the relay image system and translating the microscope objective to image two different planes which are ~20 mm apart. Since the actual target nozzle has a length of 3 mm, the

overlap obtained via aligning the two beams to the same location in two plane should be more than adequate. In practice, the positions of the two beams are stable to within ~10% of the beams' FWHM diameter, and can be moved in increments of approximately this size. As a double-check, the ionization defocusing should be approximately symmetric about the peak of the pump pulse, so that if the probe beam appears to be defocusing symmetrically about its own center, the two beams are well-overlapped throughout the target region.

Chapter References

[160] P.G. Zverev, T.T. Basiev, V.V. Osiko, A.M. Kulkov, V.N. Voitsekhovskii, V.E. Yakobson, "Physical, chemical and optical properties of barium nitrate Raman crystal," Optical Materials, Vol. 11, 315-334 (1999).

[161] P. G. Zverev, W. Jia, H. Liu, and T. T. Basiev, "Vibrational dynamic of the Raman-active mode in barium nitrate crystal," Optics Letters, Vol. 20, No. 23, 2378-2380 (1995).

[162] F. Grigsby, P. Dong, and M.C. Downer, "Chirped-pulse Raman amplification for two-color, high-intensity laser experiments," *J. Opt. Soc. Am.* B/Vol. **25**, No. 3, 346-350 (2008).

[163] F. Grigsby, P. Deng, and M.C. Downer, "Stimulated Raman Scattering and Compression of Chirped TW Laser Pulses for Two-Color High Intensity Experiments," *QELS Conf. Proc.*, JthD2, 1546-1548 (2005).

[164] F. Grigsby, P. Deng, and M.C. Downer, "Development of 873 nm Raman Seed Pulse for Raman-seeded Laser Wakefield Acceleration," Conf. Proc. AAC 11, 559-563 (2004).

[165] N. Zhavoronkov, F. Noack, V. Petrov, V. P. Kalosha, and J. Herrmann, *Opt. Let.* **26**, 47–49 (2001).

[166] J.T. Murray, W.L. Austin, and R.C. Powell, "Intracavity Raman conversion and Raman beam cleanup," *Opt. Mat.*, Vol. **11**, 353-371 (1999).

[167] S. Kalmykov, S. Yi, and G. Shvets, "All-optical control of nonlnear focusing of laser beams in plasma beatwave accelerator" *Plasma Phys. Control. Fusion* **51,** 024011 (2009).

[168] S. Kalmykov, S. Yi, and G. Shvets, "All-optical suppression of relativistic self-focusing of laser beams in plasmas," *Phys. Rev. E*, Vol. **78**, 057401 (2008).

[169] S. Kalmykov, B. Shadwick, and M. Downer, *CP1299 AAC 14th Workshop, AIP Conference Proceedings*, 752-757 (2010).

[170] R.W. Hellwarth, "Theory of Stimulated Raman Scattering," *Phys. Rev.*, Vol. **130**, No. 5, pp. 1850-1852 (1963).

[171] Z. Li, R. Zgadzaj, X. Wang, P. Dong, and M.C. Downer, "Frequency-domain streak camera for ultrafast imaging of evolving light-velocity objects," *Opt. Lett.*, Vol. **35**, No. 24, 4087-4089 (2010).

[172] Boyd, R.W. (2003), *Nonlinear Optics, Second Edition* (pp. 311-314), Elsevier, Academic Press.

[173] Yariv, Amnon (1989), *Quantum Electronics, Third Edition* (pp.483-488), New York, John Wiley and Sons.

[174] Y. R. Shen (1984), *The Principles of Nonlinear Optics*, New York, Wiley Press.

[175] G.I. Petrov, O. Albert, N. Minkovski, J. Etcepare, and S.M. Saltiel, "Experimental and theoretical investigation of generation of a cross-polarized wave by cascading of two different second-order processes," *J. Opt. Soc. Am. B*, Vol. **19**, No. 2, pp. 268-279 (2002).

[176] N. Minkovski, S. M. Saltiel, G. I. Petrov, O. Albert and J. Etchepare, "Polarization rotation induced by cascaded third-order processes," *Opt. Lett.* Vol. **27**, No. 2, pp. 2025-2027 (2002).

[177] A.E. Siegman (1986), *Lasers*, Mill Valley, CA, University Science Books, pp. 667.

[178] S. Augst, D.D. Meyerhofer, D. Strickland, and S.L. Chin, "Laser ionization of noble gases by Coulomb-barrier suppression," *J. Opt. Soc. Am. B*, Vol. **8**, No. 4, 858-867, (1991).

[179] N. B. Delone and V. P. Krainov, "Tunneling and barrier-suppression ionization of atoms and ions in a laser radiation field," *Physics-Uspekhi*, Vol. **41**, No. 5, 469-485 (1998).

Chapter 5

Measuring the Raman Laser's Intensity

The laser intensity and the related parameter, vector potential (a_0), is of crucial importance for determining the regime of experiments accessible to the laser system. The Main laser's intensity is given nominally as 3×10^{19} W/cm^2, as determined by the manufacturer (Thales): the laser's peak power is 45 TW and it is focused by an f/12 of-axis Parabola (OAP) to a waist of ~10 μm. The Raman beam's intensity has also been characterized.

5.1 CALCULATING INTENSITY FROM RELAY-IMAGE

The simplest method of measuring a laser pulse's intensity is to calculate it from other measurable parameters: energy, duration, and spot size. The peak intensity I_{peak} of a Gaussian laser of spot waist w_0, duration τ_L, and pulse energy W is

$$I_{peak} \simeq \frac{2\,W}{\pi\,\tau_{L^*}\,w_0^2} \tag{5.1.1}$$

Therefore, to calculate the intensity of the laser, one must measure first the laser energy, second the laser pulse duration, and third the spot size. Energy can be measured by a power meter, but it is also possible to calibrate a ccd to accurately measure shot energy because of the linear response of the device to shot intensity.

206

This can be done *in situ* by using mirror leak-throughs, e.g. by placing a power meter on each side of a mirror: after it (to measure reflected energy) and behind it (to measure leaked or transmitted energy) and then calibrating accordingly. Alternatively, a ccd camera has a linear response to intensity, and thus can be used to measure simultaneously both the beam's mode and energy (after calibrating with a more conventional power meter).

The durations of picosecond[180],[181] and femtosecond[182],[183] length pulses can be measured using an autocorrelator[184],[185],[186]. Alternatively, a FROG [9][187] or SPIDER [10][188] may be utilized. The UT³ laser utilizes a single-shot[189] second-order background-free[xviii] autocorrelator, the basic set-up of which is shown in Fig. 5.1, along with an example of a single-shot autocorrelation measurement. A laser pulse passes through a beam-splitter (BS), one branch of the split pulse is sent to a delay stage and then the two branches are combined through a lens in a nonlinear crystal (N.C.) with a $\chi^{(2)}$ susceptibility such as KDP, BBO, etc. The second harmonic generation from each branch is blocked (e.g. by iris, by spatial filtering, etc.) and the sum-frequency generation of the two pulses interacting is passed to a detector. The autocorrelation intensity of the signal is given by

$$I_{ac}(\tau) = \int_{-\infty}^{+\infty} |E(t)E(t-\tau)|^2 dt \qquad (5.1.2)$$

where τ is the delay between the two pulses and E is the complex electric field.

---

xviiiThe name "back-ground free" is because the signal of seen by the detector vanishes for sufficiently large delays between the two branches: the detector only sees the SFG, since all other sources are blocked (or spatially filtered) from reaching the detector.
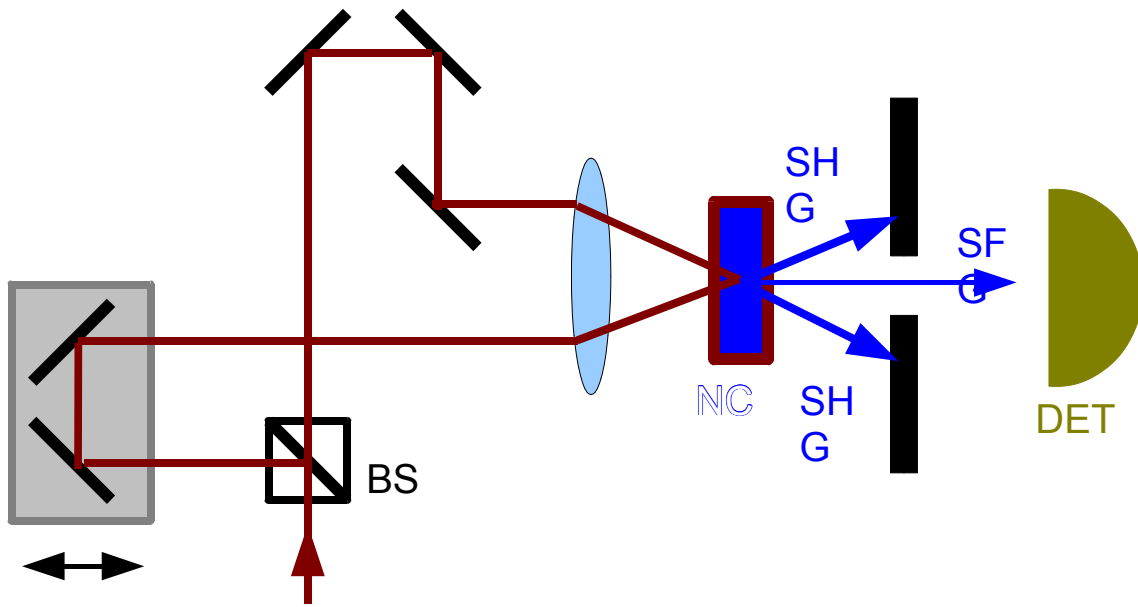
Figure 5.1: Basic set-up of a background-free (intensity) autocorrelator. The chief components include a beam-splitter (BS), a delay stage in one branch after the beamsplitter, a lens (unlabeled), a nonlinear crystal (NC), and a detector (DET). The nonlinear crystal emits both second-harmonic generation (SHG) along each branch and when correctly align also sum-frequency generation (SFG) according to phase-matched conditions.

A simple autcorrelation involves recording this signal intensity at each point of delay and then determining the pulse duration from the width of the $I_{ac}(\tau)$ curve. In a single-shot autocorrelator, the lens is cylindrical rather than spherical, and the detector is a ccd. The ccd can be calibrated with a pixel-to-time conversion factor by translating the delay stage, which effect is manifested by the movement of the signal across the ccd. By comparing the delay through which the stage is moved with the distance (in pixels) across the ccd screen that the autocorrelation streak moves, one can obtain a conversion factor from the width of the autocorrelation streak (in pixels) to pulse duration (e.g. in femtoseconds). One must also take into account some geometric effects pertaining to

pulse-shape, e.g. for a sec² type pulse the calibration factor will be off by a factor of $\approx$ 0.65.

This autocorrelator has been placed on a breadboard inside of the turning box of the laser system, after the dichroic combining mirror. A single pickoff mirror is mounted on a motorized translation stage and moved into position to measure the pulse durations, and then removed to allow the pulses to pass into the target chamber. The disadvantage of this set-up is that it does not allow in-situ measurements of the shot duration: either the pickoff mirror is in place and therefore sends light to the autocorrelator to measure duration, or the mirror is removed in which case light reaches the target chamber but not the autocorrelator. Therefore, pulse durations must be averaged, and so an exact duration is seldom known. An example of pulse duration measured in this manner is shown in Fig. 5.2.

As an alternative to using pulse averaging, the leak-through of any of the mirrors after the compressor may be used. These are all coated to reflect >99% of incident light, but the transmitted light is sufficient to generate a weak autocorrelation signal. However, the pulse measured by the autocorrelator will be stretched in duration due to group velocity dispersion (GVD) from propagation through the mirror (typical substrate is fused silica a.k.a. fused quartz). The approximate duration can be back-calculated under the assumption that the pulses are compressed prior to propagation through the mirror:

$$\tau_{out} = \tau_{in} \sqrt{1 + 4\,\phi_2^2/\tau_{in}^4} \qquad\qquad (5.1.3)$$
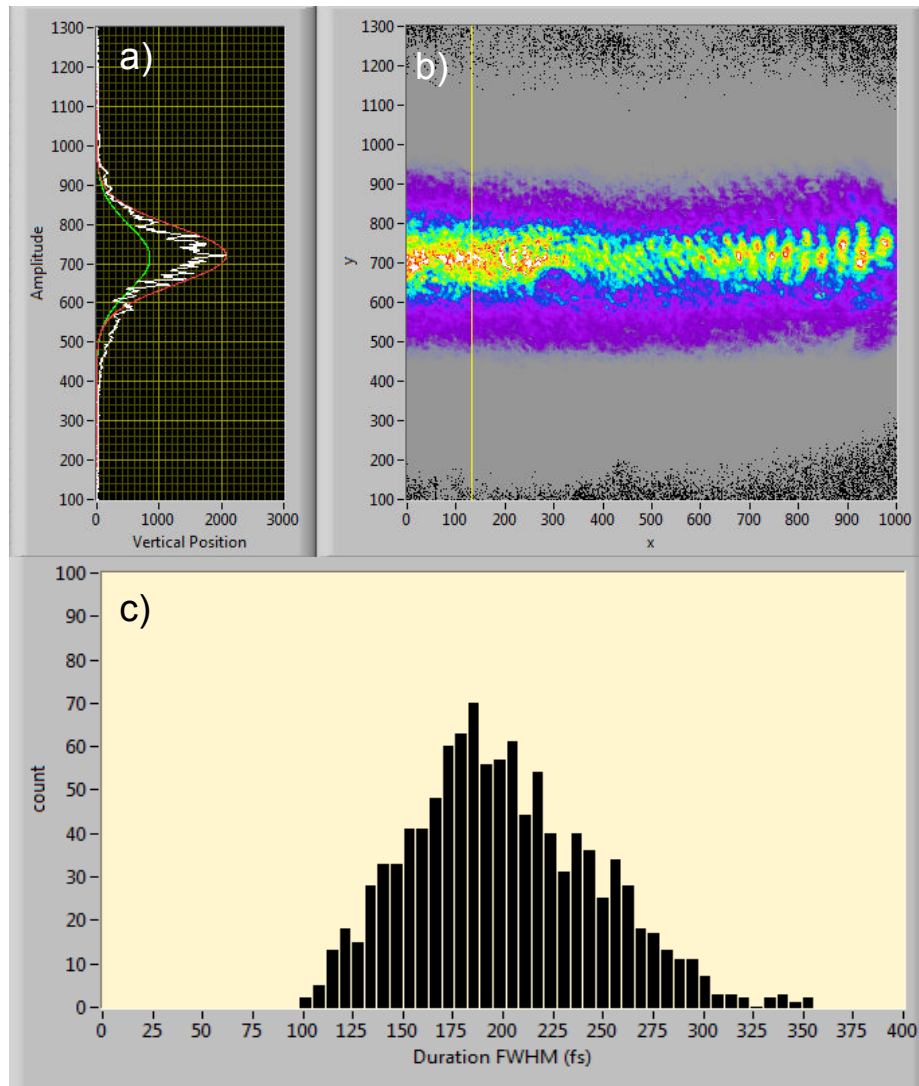
Figure 5.2: Example of a single-shot autocorrelation measurement and a histogram of many such shots. The single-shot measurement consists of the lineout (a) of a ccd streak of SFG light (b). The CCD image can be calibrated to convert pixels width to pulse duration, assuming some fit to the lineout itself. In (a), the white curve is the actual lineout along the yellow vertical line in (b), the red is a Gaussian fit to that lineout, and the green is an averaged Gaussian fit along all the possible vertical lineouts; the duration is determined largely from the green curve. (c) shows a possible histogram consisting of ~1000 shots through the autocorrelator.

where τ_{in} is the pulse duration before passing through the dispersive medium (e.g. the mirror substrate) and τ_{out} is the pulse duration after having passed through the dispersive medium, and the phase term ϕ_2 is the second-order term in the Taylor expansion of the phase $\phi(\omega)$:

$$\phi(\omega) = \phi_0 + \phi_1(\omega - \omega_0) + \phi_2(\omega - \omega_0)^2 + \phi_3(\omega - \omega_0)^3 \dots \qquad (5.1.4)$$

The term ϕ_2 describes the group-velocity (or group-delay) dispersion, and is given by

$$\phi_2 = \frac{1}{2} \frac{\partial^2 \phi(\omega)}{\partial \omega^2}\Big|_{\omega=\omega_0} = \frac{\lambda_0^3}{4\pi c^2} \frac{\partial^2 \eta}{\partial \lambda^2}\Big|_{\lambda_0} z \qquad (5.1.4)$$

The rightmost hand side of (A.1.4) is obtained using the material dispersion equation

$$\phi(\omega) = \frac{2\pi}{\lambda} \eta(\lambda) z = \frac{\omega}{c} \eta(\lambda) z \qquad (5.1.5)$$

and the Sellmeier equation

$$\eta^2 - 1 = \frac{B_1 \lambda^2}{\lambda^2 - C_1^2} + \frac{B_2 \lambda^2}{\lambda^2 - C_2^2} + \frac{B_3 \lambda}{\lambda^2 - C_3^2} \qquad (5.1.6)$$

In fused silica, these B and C coefficients are B_1 = 0.691663, B_1 = 0.4079426, B_1 = 0.8974794; C_1 = 0.0684043 μm, C_1 = 0.11624140 μm, and C_1 = 9.896161 μm[190],[191],[192],[193].

A ccd can also be used to measure the laser's transverse mode via relay-imaging. Two examples of relay-imaging are shown in Fig. 5.3. The laser itself typically is focused on-target, so it is often desirable to image the laser's focal plane. Furthermore, the focal spot size is often small compared to the CCD's resolution: typical spot sizes in the

211

experiments described in this work range from ~10 μm to ~50 μm FWHM, whereas the ccds used have typical pixel sizes of 4.65 μm or 6.45 μm to a side, and the device resolution limit is larger than a pixel. Therefore, it is advantageous to magnify the image in the relay, e.g. by using a microscope objective lens. The actual spot size can be determined by placing an object of known dimensions in the imaged plane: typically, a USAF resolution test pattern target is used for this purpose.

This method for measuring intensity has the advantageous of being relatively easy and straightforward to set up. It uses equipment which any ultrafast/high-intensity lab will already have on-hand (e.g. ccds, an autocorrelator, and a power meter). However, it comes with a few drawbacks as well. For one, if the laser pulse characteristics fluctuate at all, then these measurements will correspondingly fluctuate, and unless the autocorrelation and energy measurements are done *in situ* one can only calculate general ranges of intensities rather than shot-to-shot intensities.

The fluctuations in energy and size tend to follow a nearly Gaussian distribution, and in duration the distribution at least approximately Gaussian, so a general uncertainty in intensity measured might be approximated as[xix]

$$\Delta I \simeq \frac{2\,\Delta W}{\pi\,\tau_{L^\star}\,w_{0x}{^\star}\,w_{0y}} + \frac{2\,W\,\Delta\tau_L}{\pi\,\tau_{L^\star}^2\,w_{0x}{^\star}\,w_{0y}} + \frac{2W\,\Delta w_{0x}}{\pi\,\tau_{L^\star}\,w_{0x}^2{^\star}\,w_{0y}} + \frac{2W\,\Delta w_{0y}}{\pi\,\tau_{L^\star}\,w_{0x}{^\star}\,w_{0y}^2} \qquad (5.1.7)$$

[xix] If the transverse mode is circular rather than elliptical and astygmatic, Eqn. (5.1.7) simplifies to

$$\Delta I \simeq \frac{2\,\Delta W}{\pi\,\tau_{L^\star}\,w_0^2} + \frac{2\,W\,\Delta\tau_L}{\pi\,\tau_{L^\star}^2\,w_0^2} + \frac{W\,\Delta w_0}{\pi\,\tau_{L^\star}\,w_0^3}$$
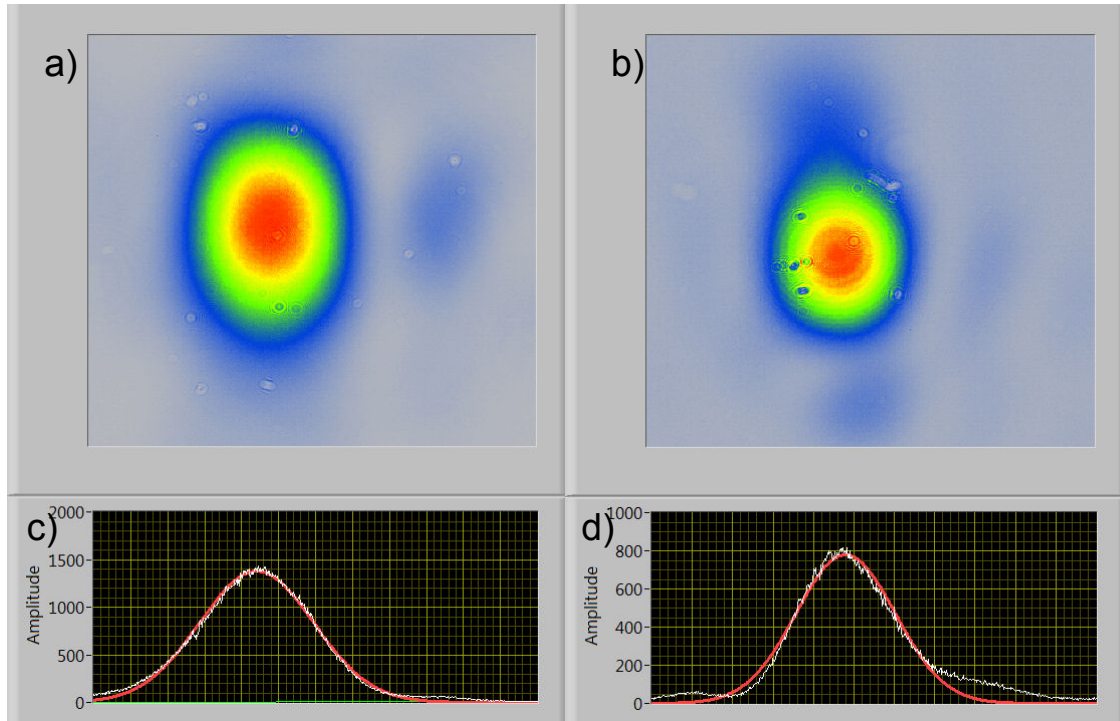
Figure 5.3: Modes imaged via relay imaging. The modes are imaged at the focal plane of the OAP which focuses them on-target. (a) shows the Raman mode in its focal plane, (b) shows the Main beam in the same plane, and (c) and (d) show vertical lineouts from the center of modes (a) and (b) respectively. The target chamber was under vacuum with no gas jet present when these modes were taken.

where ΔW is the uncertainty (standard deviation) in pulse energy, $\Delta\tau_L$ is the uncertainty in pulse duration, and Δw_0 is the uncertainty pulse size. The pulse intensity results would then be give by $I_{peak} = \bar{I} \pm \Delta I$, where the average intensity is obtained by using the average values of pulse duration, pulse length, and spot size. Doing this requires many shots, and can be time-consuming even on a 10 Hz repetition rate system, let alone larger single-shot systems like the Texas Petawatt. The same is true of using leak-through to

obtain *in situ* measurements, since the leaked-through measurements must be calibrated to the actual on-shot parameters (again, using averaging) prior to experiments.

There is another disadvantage to this method of measuring intensity, which is that the relay-imaged laser spot may not be a true representation of the actual on-target shot. The on-target spot may be distorted due to ionization defocusing (or for that matter ion-channel guiding/focusing in the case of a two-color system), and (once a plasma channel is actually formed) due to self-focusing effects. A relay-imaging system which uses the leak-through of a mirror to form the image cannot account for either of these effect, and will only convey the effective vacuum-focus of the laser pulse based on the pulse phase at the leaked-through optic. It cannot convey any phase information obtained from later optics (e.g. deformable mirrors, the actual OAP used to focus the pulse, the phase effects of the target itself, etc). On the other hand, the relay-image can be taken after the target itself, but this is only valid for imaging planes after the target exit. Additionally, phase information might be added by passing through optics after the target itself. This can have the effect of stretching the pulse duration, but also of changing the pulse's phasefront. Any problems involving phase modifications to the mode due to the target itself might be mitigated by simply imaging in vacuum, though this is again not truly *in situ* as a measurement. The additional modifications to phase from the post-target imaging optics cannot be fully corrected, but they may be mitigated somewhat by attenuating the beam.

5.2 Ionization Level Detection

A second method for measuring laser intensity is by detecting the ionization levels in a gas[194]. A sufficiently intense laser pulse can ionize an atom by lowering the Coulomb barrier sufficiently for electron to tunnel out of their orbits of an atomic nucleus[195]; an even more intense pulse can suppress the Coulombic barrier entirely.
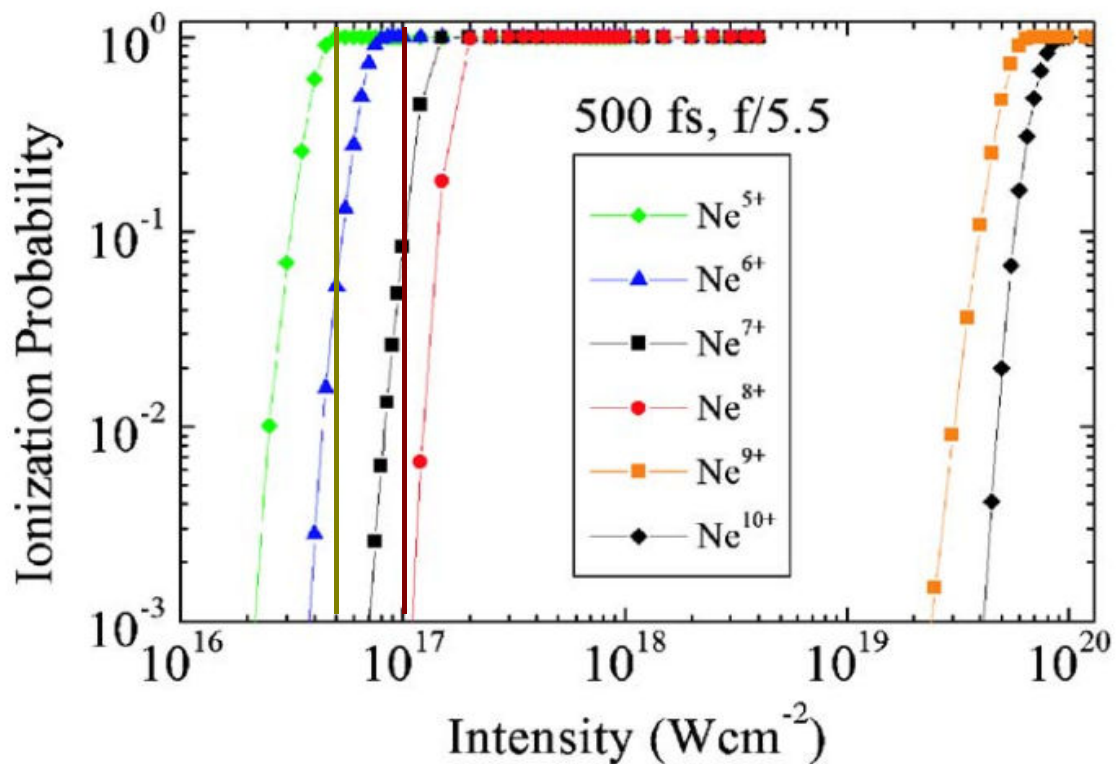
Figure 5.4: Tunneling ionization probabilities for neon using a 500 fs, f/5.5 focus laser pulse centered at 1.05 μm[xviii]. The brown and red vertical lines have been added to better visualize intensities of 10^{17} W/cm² (red) and 5 x 10^{16} W/cm² (brown) for illustrative purposes.

Therefore the ionization level can be used to determine the intensity of a laser. Moreover, an ionization level may be reached for a portion of the atoms in the laser's spot via tunneling ionization, so that some atoms will be ionized beyond the barrier-suppression ionization state (typically by one level). Ionization level can be detected using a time-of-flight detector. Figure 5.4 shows the expected neon tunnel ionization probability as a function of beam intensity.

The total population of ionized atoms can be estimated as follows. The laser spot will encounter a volume contained within an isointensity curve defined by (for example) the half-peak intensity: the number of atoms to be ionized is expected to be contained. For a beam whose focal spot size is 10 μm, the half-peak intensity isocontour includes a volume of ~2000 μm^3, in which there would be present ~10^8 atoms of neon in a gas jet using a 1% neon/99% helium mixture if the gas jet's resultant plasma density is 10^{19} cm^{-3}.

This is too many atoms to accurately measure intensity using tunneling ionization, though it can be used to determine the intensity via barrier suppression ionization. For example, at a peak intensity of 10^{17} W/cm^2 under these conditions (~10^8 atoms in the half-peak volume), nearly all the neon atoms inside this volume should be ionized to at least Ne^{5+}. However, ~5 x 10^6 atoms would be ionized to Ne^{6+} due to tunneling ionization in this volume (and in a smaller volume still, barrier suppression ionization for Ne^{6+} is attained), as well as some (~10^5) Ne^{7+} and even some (~10^2) Ne^{8+} ions would also be detectable depending on the TOF's dynamic range, particularly in the portions of the volume which approached peak intensity.

For this reason, this method is best employed with a far lower concentration of "intensity-detectable" ions. For example, Link *et al.*[xviii] suggest a gas at pressure 10^{-4} Torr, which could be achieved by back-filling the target chamber after pumping down. Back-filling to this pressure with neon would yield ~8000 neon atoms in the same iso-intensity contour-bounded volume; thus, at the same 10^{17} W/cm^2 peak intensity, one would expect to observe Ne^{6+} and Ne^{5+} in abundance, with fewer Ne^{7+} and no Ne^{8+}. The TOF device would likely detect ~95% Ne^{5+} and ~ 5% Ne^{6+}. There are, of course, more lower ionization levels created by the laser outside of this volume (e.g. farther from focus, farther from axis).

Alternatively, the detection of one ionization level and non-detection of the level above imposes an upper and lower bound to the laser intensity. The intensity measurement can then be further refined by choosing a different species of ion (e.g. nitrogen, or argon, etc.) which have different barrier suppression levels and different ionization probability levels.

5.3 Ionization Path Length

A third method for measuring peak intensity is to measure the ionization path length and then compare the (vacuum) spot size size at focus with the (vacuum) spot size at the position where ionization begins. This method has two parts: first, the laser mode evolution must be characterized under vacuum as it propagates through its focus; and

217

second, the distance from focus at which the laser begins to ionize a gas must be determined.

The first part of this method is relatively straightforward, and involves measuring (via relay-imaging or directly) the beam's mode at and near focus. This may be done using a ccd and (if magnification is desired) a microscope objective lens. The distance over which this imaging of the mode must be done is at a minimum the distance from the focus at which the laser is able to ionize the detection medium (helium, air, etc), but must be done under vacuum do as not to introduce ionization defocusing or self-focusing and other mode-modifying nonlinearities and instabilities. Ultimately, the spot size (area) must be known at focus and at the point at which ionization begins to occur.

The intensity required to ionize an atom via barrier suppression (I_{BS}) is given by[196]

$$I_{BS}[W/cm^2] \approx 4 \times 10^9 \frac{E_{bound}^4 [eV]}{q_i^2}$$ (5.3.1)

where q_i is the ionization state of the atom and E_{bound} is the binding energy of that ionization state. Thus, if ionization is detected for a spot of area A_{ion} and the focus spot has an area of A_{focus}, the focus intensity can be estimated as

$$I_{focus} \approx \frac{A_{ion}}{A_{focus}} I_{BS}$$ (5.3.2)

Note that this method does not necessarily distinguish between ionization levels, but rather assumes that ionization is first detected when the intensity is sufficient to reach the first ionization state of the atom (e.g. He^{1+}) via barrier suppression.

Thus, the second part of this method is determining the distance from the focal plane to the onset of ionization. There are several methods for doing this: the ionization track can be observed via the spark it makes in a gas or via recombination luminescence; the ion channel can be detected via transverse interferometry; ionization be be observed optically by the onset of the spark in a gas jet translated away from the focal plane of the laser; and it can be observed by ionization blue-shifting in the laser's spectrum.

5.3.1 Visual Detection of the Ion Channel

An ion channel may be visible to the eye (as a spark) and certainly to a ccd or camera. For example, a high-quality digital camera can photograph the ion channel in air, or for that matter in a chamber back-filled with any other target gas. A Canon Digital Rebel xti SLR camera was used to obtain the image of an ion channel shown in Fig. 5.5.

The method for determining the spot size at which ionization begins is illustrated in Fig. 5.6. The green horizontal line represents the point at which the ionization channel begins, at a distance $z_{ion} \gg Z_R$ from the focal plane of the beam. The beam waist here can then be approximated as

$$w_{ion} \approx \frac{z_{ion}}{f} w_f \tag{5.3.3}$$

where w_f is the waist of the beam prior to focusing. Since in experiments the laser actually propagates through vacuum to its focus (typically on the front of the gas jet), the beam's waist is not significantly defocused by ionization nor self-focused prior to the focal plane (the same is not necessarily true of the beam propagating in air or a back-

filled target chamber). Therefore, the intensity I_0 of the laser at focus can be approximated by

$$I_0 \approx \frac{w_{ion}^2}{w_0^2} I_{BS} \approx \left(\frac{z_{ion} w_f}{f w_0} \right)^2 I_{BS} \tag{5.3.4}$$

where I_{BS} is the barrier suppression ionization of the medium in which the ionization channel is created. In other words, the focal intensity is given by the ratio of areas of the point at which ionization onsets and the focal area, multiplied by the intensity needed for ionization to occur.
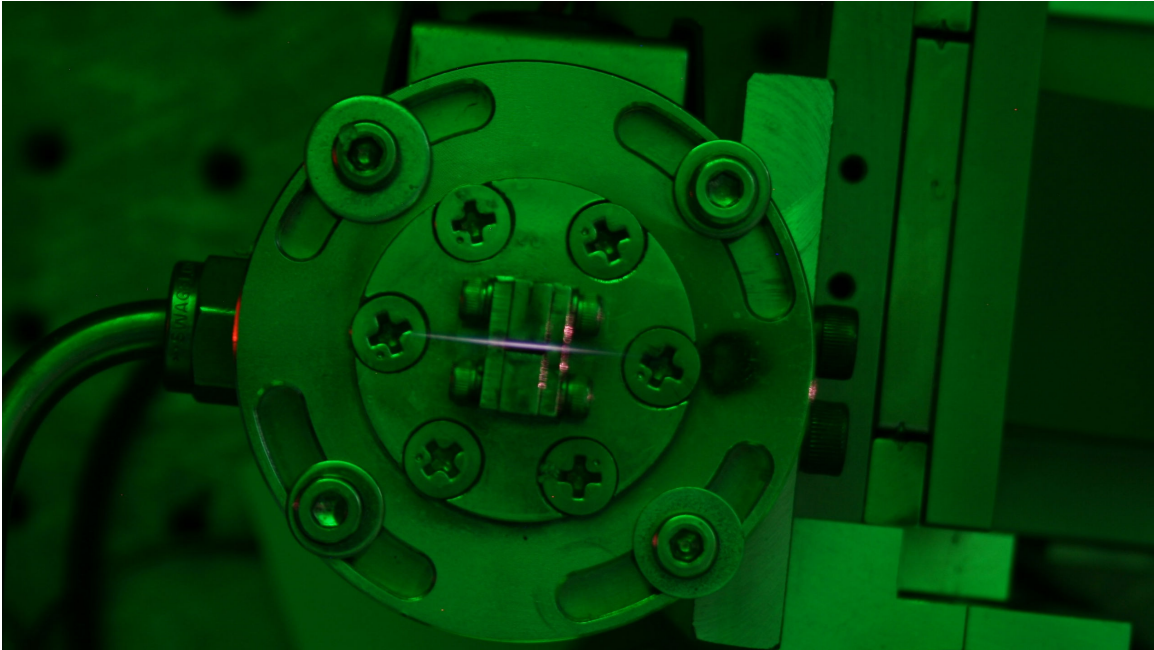
Figure 5.5: Ionization of air by Raman laser. The gas-jet nozzle is shown in the background for scale and orientation, and measures 1 mm by 3mm.
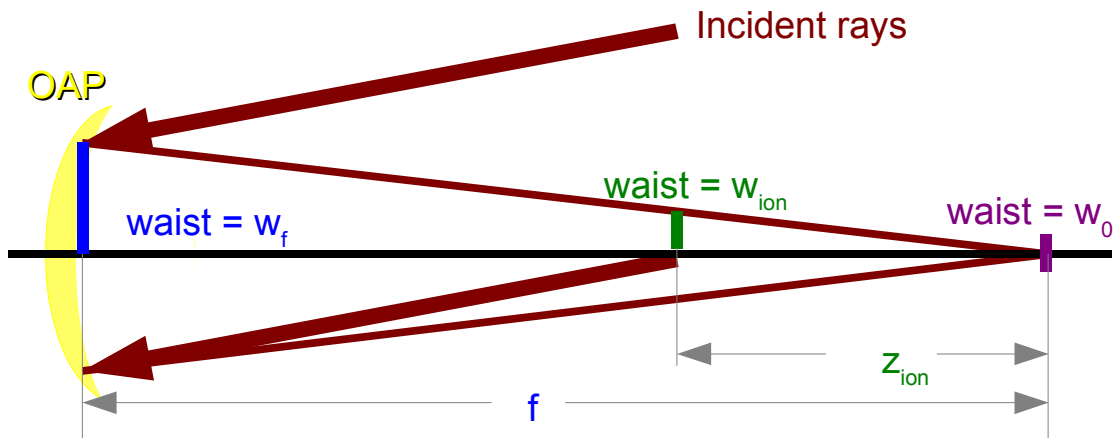
Figure 5.6: Conceptual diagram of how to use the ionization channel to determine beam spot size. The black line is the optical xis after the focusing optic (an off-axis parabola, yellow). Assuming that the point at which the channel (and hence, ionization) begins is a distance $z_{ion} >> Z_R$, the waist of the beam at the point where ionization begins (green) may be estimated from geometry using the focal length (f) and the initial waist of the beam (w_f) before focusing (blue).

A similar approach can be used with recombination luminescence[197]. At a sufficiently low gas-density, many of the nonlinearities and instabilities which can distort the beam's wavefront are effectively removed (their effects become small enough to be neglected); however, the resulting luminescence will also be correspondingly dimmer.

There are a few disadvantages to this method generally. The biggest (and most difficult to overcome) is determining where the onset of barrier suppression ionization occurs. It is difficult to pinpoint the exact location at which the ionization track becomes visible; furthermore, ionization due to tunneling will occur before the barrier-suppression intensity is attained, meaning that there is not necessarily a sharply-defined ionization onset plane. This imposes an uncertainty about the laser spot size at which the intensity is sufficient to ionize the target gas via barrier suppression. Additionally, ionization may

occur for multiple levels in a high-Z gas: therefore, helium and hydrogen present the best targets for this method.

As a first approximation, the ionization spark (and recombination luminescence) becomes detectable at approximately the same position at which the intensity is sufficient for barrier suppression to occur. As Fig 5.4 shows, tunneling probability falls off dramatically as the intensity is decreased away from the barrier suppression threshold: this probability scales approximately with I^5. Therefore a change in intensity of ~50% leads to a reduction by a factor of ~30 in probability of tunneling ionization. For example, the probability[xx] for ionizing Ne^{6+} falls from unity at 8×10^{16} W/cm² to ~3% at 4×10^{16} W/cm².

As for determining the uncertainty imposed by estimating the point at which ionization due to barrier suppression occurs, a simple example should suffice. In this experiment's geometry, the off-axis parabola (OAP) has a focal length of ~60 cm, and the ion channel is first visible ~9 mm from the focal plane. Therefore, the spot size (r_s) scales with the distance from the focal plane (x) as $r_s = r_f x/f$, where r_f is the farfield spot size (e.g. the size of the laser spot at the position of the focusing optic for an initially collimated beam) and f is the focal length of the OAP. This means that the area of the spot scales as $A_s = \pi r_s^2 = \pi(r_f x/f,)^2$. The intensity scales as $1/A$. The relative uncertainty in the spot area is

$$\frac{u_A}{A_s} \approx \frac{2 u_x}{x} \tag{5.3.5}$$

---

xx According to Eqn. (5.3.1), the barrier suppression ionization for Ne^{6+} is approximately 6.9×10^{16} W/cm², which is in reasonably good agreement with the estimates from Fig. 5.2.1.

where u_A is the uncertainty in spot area and u_x is the uncertainty in the barrier suppression ionization onset location. Assuming a generous 1 mm uncertainty in determining this exact location, and given that this is many Rayleigh-lengths away from the focal plane, this gives a relative uncertainty of ~20% in area, and hence in intensity.

5.3.2 Detection of Ionization via Phase-Shift: Interferograms and Shadograms

One possible method for mitigating this uncertainty in ionization onset is to use a transverse interferogram or shadogram to probe the ion channel. The laser ionizes the gas through which it propagates, which in turn modifies the refractive index. For example, the refractive index of air under STP is ~1.00, whereas in a plasma the refractive index is given by

$$\eta^2 = 1 - \left(\frac{\omega_{pe}}{\omega_0}\right)^2 = 1 - \frac{n_e e^2}{\epsilon_0 m_e \omega_0} \tag{5.3.6}$$

where ω_0 is the probe laser's frequency. A simple transverse interferogram can be used to determine the plasma density (and hence the onset of ionization).

The interferogram in this case consists of a weak probe (energy ~30 mJ, duration ~100 fs, waist ~1 cm) which propagates through the gas jet transversely to the ionizing laser pulse. The interferometer's two arms are flipped vertically with respect to each other so that the "bottom" portion of the pulse in arm 2 corresponds to the "top" part of the pulse in arm 1. The amount of phase shift acquired by the probe passing through the portion of the gas jet which has been ionized to form a plasma is dependent on the path-

integrated refractive index, which in this case means the path integrated plasma electron density.

Assuming that the ionization phase shifts are occurring in helium gas, and assuming that the peak intensity is sufficient to fully ionize helium by barrier suppression, there are essentially five regions which might be encountered by a probe beam:

1. The central region in which the pumping laser's intensity is large enough to completely ionize all of the helium atoms to He^{2+} via barrier suppression. The approximate intensity needed for this is $I_{BS}(He^{2+}) = 8.8 \times 10^{15}$ W/cm^2.

2. Thin region in which the laser is sufficiently intense to ionize all the atoms to at least He^{+1} via barrier suppression ionization, and in which some fraction of atoms will be ionized to He^{2+} via tunneling ionization.

3. A region in which most atoms are ionized to He^{1+}, and a negligible number are ionized beyond this by collisions, etc. The barrier suppression ionization ionization intensity for He^{1+} is approximately $I_{BS}(He^{1+}) = 1.5 \times 10^{15}$ W/cm^2.

4. A thin region in which the pump laser intensity is not sufficient for barrier suppression ionization, but is sufficient for tunneling ionization to occur for He^{1+}.

5. A region which is essentially outside of the pump laser or in which the pump laser is too weak for significant ionization of any to occur.

Since the tunneling ionization probability scales with I^5 per Fig. 5.4 and reference [194], the second and fourth regions are effectively negligible for our purposes. If the ionized gas used is of higher Z than helium, there will be additional regions encountered

depending on laser intensity, due to the availability of more electrons to ionize from the atoms used.

There are two major disadvantages to this method of determining beam intensity. The first is that the phase shift is dependent on the density of electrons in the generated plasma, which on the one hand is determined by the laser intensity, but which on the other hand is more strongly determined by the density of the atoms being ionized (a function of gas pressure or gas jet backing pressure). Figure 5.7 shows some interferograms obtained using a gas jet with several backing pressures of helium, along with the expected helium density (in the central region of the pump laser) as a function of backing pressure. In all cases, the intensity used was roughly constant: the pump laser is the primary laser beam of the UT^3 laser, in this case 300 mJ energy before compression (50% efficiency) to 200 fs with a focal spot size of ~12 μm x 16 μm FWHM.

The second disadvantage should also be apparent from Fig. 5.7: the phase shifts become more difficult to detect at lower densities. The 30 PSI case (Fig. 5.7a) in which the shifts are very small corresponds to a density of nearly 1.6×10^{19} cm^{-3}, while the 50 PSI case in which some fringes shift by the equivalent of nearly 2π in phase corresponds to 1.8×10^{19} cm^{-3}. At such high plasma densities, other nonlinearities (including self-focusing or strong ionization defocusing) become large enough to significantly alter the laser profile (and hence, intensity). On the other hand, a sufficiently large phase shift ($>2\pi$) becomes unresolvable as well.
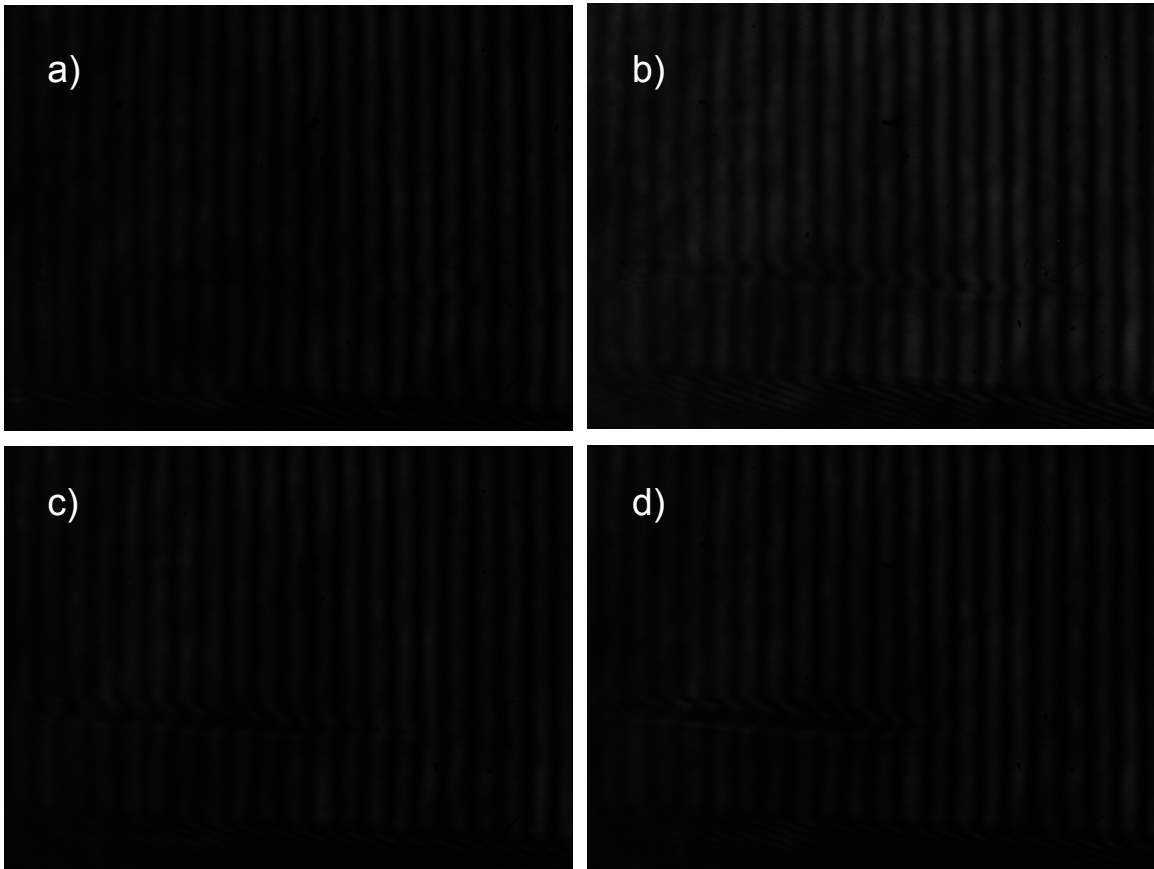
Figure 5.7: Interferogram showing fringe shifts due to the ionization of a helium gas jet by the main laser. Gas jet backing pressure is a) 30 PSI, b) 50 PSI, c) 100 PSI, and d) 150 PSI. The laser is delivering 150 mJ compressed to 200 fs on-target, with a focal spot of 12 mm x 16 mm FWHM, and its propagation axis is 0.5 mm above the gas jet (visible as a shadow at the bottom of each interferogram).

5.3.3 Detection of Ionization via Sparks: Scanning Gas Jet Position under Vacuum

A third method for measuring intensity via ionization is to use the fact that the gas jet can be translated longitudinally with respect to the laser focus. Therefore, it can be moved towards the focusing optic (OAP) until ionization is no longer detected, and then moved

in the opposite direction until full-jet ionization is observed, and then gradually ionization is no longer observed.

Since this is done under vacuum, no nonlinearities can develop in the beam prior to entering the gas jet. The spot size of the beam at the onset of ionization can be compared to the focal spot size to determine the actual peak intensity. This can be done visibly (e.g. by looking for a spark in the gas jet, or by taking a snapshot of the spark) and marking the point at which the spark first disappears/reappears.

As an alternative to visually looking for the spark, ionization can be detected using a spectrometer: a portion of the spectrum blue-shifts when ionization occurs. Therefore, the point at which the blueshift is first detectable in the spectrum is also the point at which ionization first occurs. Figure 5.8 shows some samples of spectral blueshift which indicate that ionization has occurred. At lower backing pressures (and hence lower plasma densities), the spectral shift measurement is at least as sensitive (and often more sensitive) than the interferograms.

Having determined where ionization first occurs and where it last occurs, and knowing the focal plane (it should be roughly the middle between these two extrema), the focus intensity can be determined as described in Sec. 5.3.1. That is, the spot size at both focus and position at which intensity is sufficient to ionize the gas must be known. The ratio of the spot sizes (areas) gives the inverse ratio of the intensities, so that $I_{focus} = (A_{ion}/A_{focus})I_{BS}$ as in Eqn. (5.3.2).
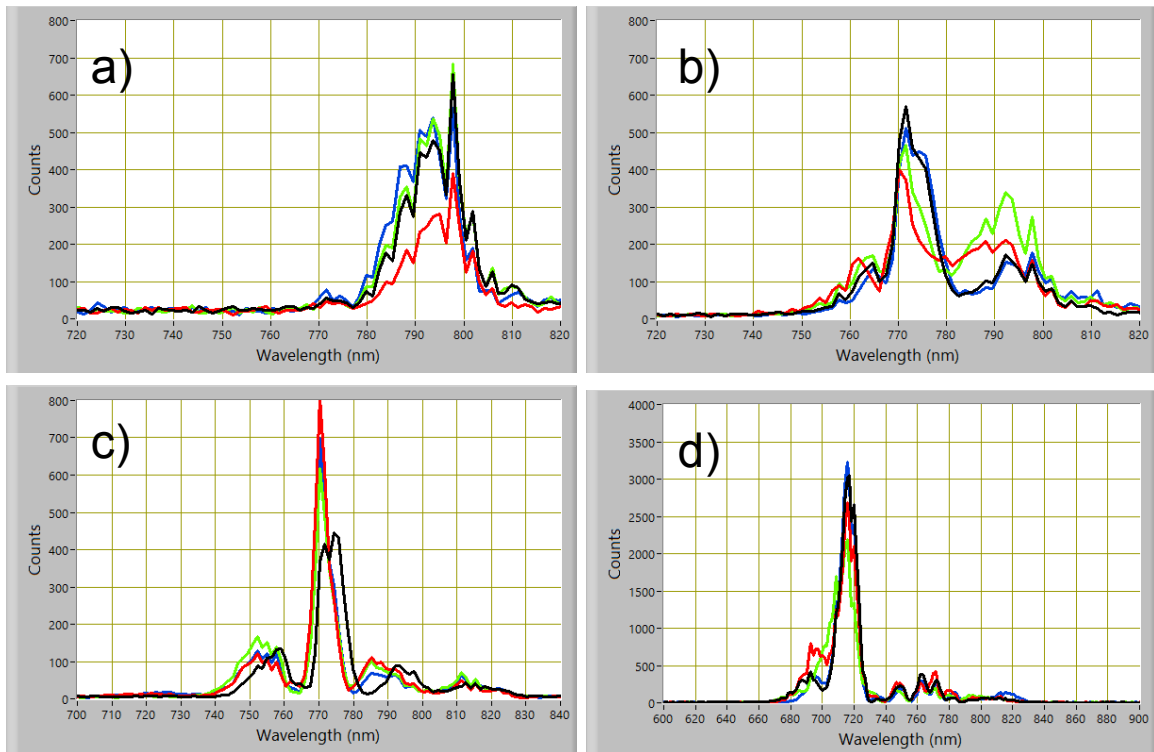
Figure 5.8: Spectrum of primary beam after passing through helium gas. a) The beam's energy is 5.5 mJ, and intensity is not sufficient to ionize the gas; b) energy is 16 mJ, and the intensity is sufficient to ionize helium once but not twice; c) the energy is 37 mJ, and the intensity is sufficient to ionize helium twice; and d) the energy was 145 mJ, and the intensity is sufficient to cause some self-phase modulation. The backing pressure of the gas jet in all cases was ~50 PSI.

However, as shown in Fig. 5.8, the spectral method of this cannot be used at focus to determine the focal intensity, because the laser will undergo self-phase modulation at sufficiently high intensity. At the threshold gas jet position—that is, the gas jet is placed so that ionization occurs only at its edge, as a single small spark—the spectral effects become sufficiently weak that the exact point at which ionization occurs become difficult to determine; similarly, there is some uncertainty as to which point ionization occurs when the spark is visually detected. In practice, the range of possibilities is on the order of tens of microns, perhaps 100 microns at most. Thus, if ionization occurs ~10 mm

before the focal plane, this uncertainty is <1% of the measured propagation length. The motorized translation stages used to position the gas jet move in steps of 0.1 μm, so their contribution to the uncertainty of these measurements is negligible.

5.4   DETERMINATION OF THE RAMAN BEAM'S PEAK INTENSITY

Having discussed these various methods for determining the intensity of the Raman beam, I can now apply some of them to determine the Raman beam's intensity. I did not have access to a time-of-flight spectrometer, so intensity could not be determined via ionization level. Furthermore, interferogram (and shadogram) probes tended to not pick up ionization in air until it was clearly visible to the naked eye as a long ionized channel (or "spark"). However, intensity could be measured using the other methods described above.
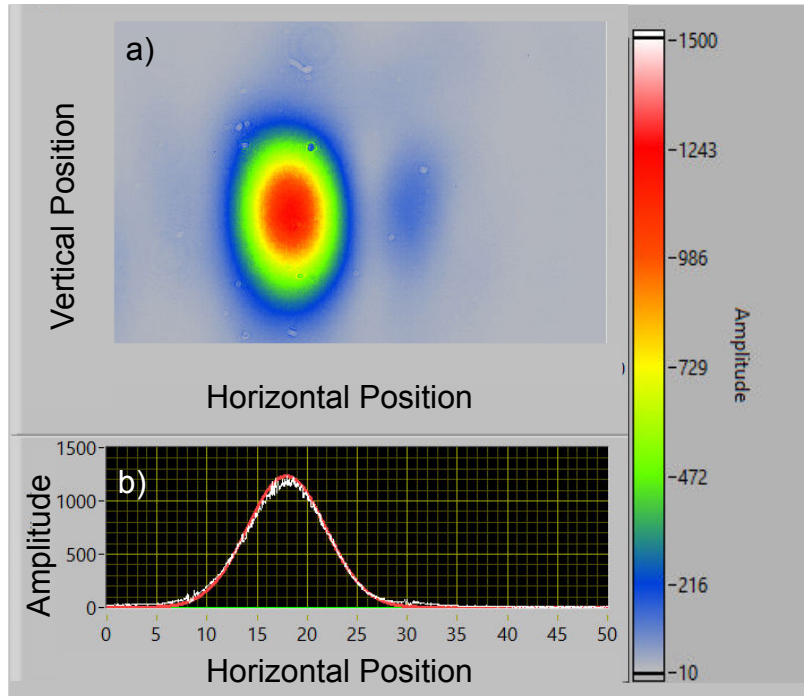
Figure 5.9: Determining the Raman mode size at focus. a) Image of the Raman mode at focus on a ccd, and b) a horizontal lineout of the mode (white) and a Gaussian fit to that lineout (red).The horizontal scale is in microns, so the pulse in this shot has a FWHM horizontal size of ~9.5 μm, and the corresponding vertical size here is ~15.0 μm.
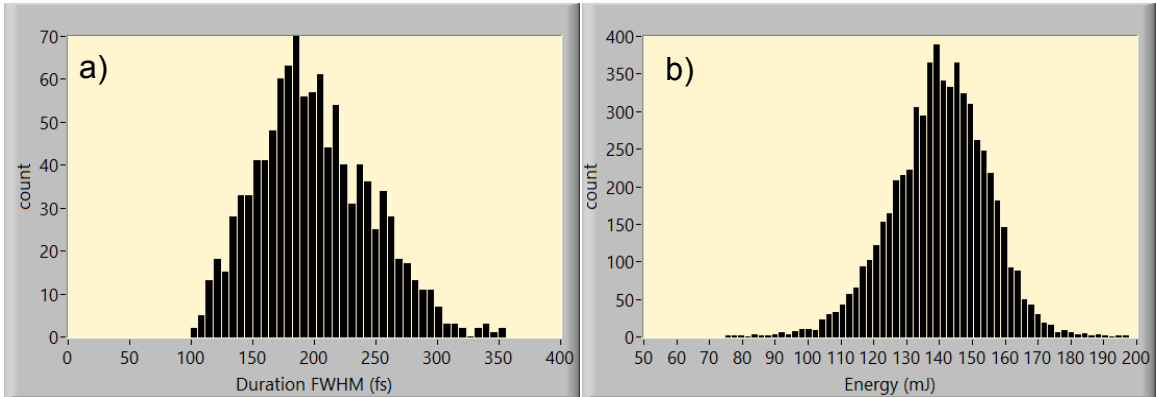
Figure 5.10: Duration and energy stability of the Raman beam. a) Histogram (1,000 shots) of pulse duration during intensity measuring experiments. b) Histogram (10,000 shots) of energy measured at output of the 6-pass Ti:Sapph amplifier on the same day.

5.4.1 Calculation of Intensity from Measured Energy, Duration, and Mode

The duration, spot size, and energy were all measured for this pulse (see Sec. 5.1): a sample of the mode at focus with a horizontal lineout is shown in Fig 5.10. The size was determined by direct imaging of the focus at low energy in air and by relay imaging of the focus at high energy under vacuum. Both spot sizes were comparable; using 100 shots to average and obtaining the FWHM size in x and y axis, the spot size was determined to be $10.6\pm0.2\mu m$ by $16.2\pm0.7\mu m$ under relay image, and with direct imaging it is $9.7\pm0.7\mu m$ by $16.8\pm1.0\mu m$, where the size is specified by average$\pm\sigma$.

The pulse duration fluctuated considerably form shot-to-shot; a histogram of 1000 shots' worth of autocorrelated durations is shown in Fig. 5.10a. The average pulse duration was ~200 fs, though shots as short as 100 fs and as long as 350 fs were recorded, with 180 fs being most nearly the "typical" pulse duration. The estimated uncertainty in pulse duration is 60 fs.

The energy efficiency throughput of the system was determined by measuring energies at output of the 6-pass amplifier and after the final optic (a mirror) before focusing. Both energies were measured over 200 shots using a Coherent FieldMax II TOP Power Meter, with a Coherent J-50MB-HE head (nominal dynamic range: 1 mJ to 2 J). At the output of the 6-pass amplifier, the measured energy was on average 140 mJ, with ~35% of the energy arriving on target. This was also tested at two lower energy levels (obtained by mis-timing the pump laser in the Ti:Sapph amplifier with respect to the Raman beam): with 40.3 mJ out of the 6-pass amplifier, 16.0 mJ (32.4%) arrived on-

target, and with 10.5 mJ out of the 6-pass, 4.01 mJ (36.4%) arrives on target. The energy loss is primarily form the compressor, with some marginal loss on the dichroic mirror and on the 4-lens expanding telescope prior to the compressor chamber; the best-observed performance of the compressor is 45% throughput, though this has decreased somewhat over time.

A histogram of shot energies immediately after the 6-pass amplifier is shown in Fig. 5.10b, in which the average energy is 140 mJ with ~10% energy fluctuation. It should be reiterated here that the day-to-day performance of the Ti:Sapph system fluctuates somewhat depending on the performance of the front-end of the system (meaning, both the main laser and the first two stages of the Raman system). It can reliably be aligned to achieve ~120-130 mJ, though on some days an average of 160 mJ has been observed.

The average peak intensity of the focused laser can be calculated using the average energy, the average pulse duration, and the average spot size. The average pulse energy is 140 mJ out of amplifier, which corresponds to 49 mJ on-target; the average pulse duration is 200 fs, so that the typical power of the laser is 0.25 TW. The average focused-spot size is 10.6 by 16.2 microns FWHM, which corresponds to 9.0 by 13.8 microns $1/e^2$ waist (the focus is very well approximated by a Gaussian fit, as shown in Fig. 5.9), which means an area of 389 mm^2 encloses ~95% of the beam's energy.

As per Eqn. (5.1.7), but accounting for the elliptical shape of the focal spot, the uncertainty in the laser intensity is given by

$$\Delta I \simeq \frac{2\,\Delta W}{\pi\,\tau_L\,w_{0x}\,w_{0y}} + \frac{2\,W\,\Delta\tau_L}{\pi\,\tau_L^2\,w_{0x}\,w_{0y}} + \frac{W\,\Delta w_{0x}}{\pi\,\tau_L\,w_{0x}^2\,w_{0y}} + \frac{W\,\Delta w_{0y}}{\pi\,\tau_L\,w_{0x}\,w_{0y}^2} \qquad (5.4.1)$$

where w_{0x} and w_{0y} are the beam's waists in the x (parallel the laser's polarization, which is P) and y (perpendicular to the laser's polarization) directions, respectively. This yields a peak Raman pulse intensity of $1.40\times10^{17}\pm6.96\times10^{16}$ W/cm^2. The large (~50%) uncertainty is mostly the result of inconsistency in pulse duration. This gives an average normalized vector potential of $a_0 = 0.28$.

5.4.2 Intensity Measured by Visual Detection of the Ion Channel in Air

A Canon EOS Digital Rebel xti SLR camera was used to obtain the image shown in Fig. 5.10. This image is of the ion channel generated by the Raman beam in air at 1 atm pressure. The ion-channel's length form focus is measured, and in this case ionization begins approximately 9 mm from the focal plane and ceases 7-3/8 mm after the focal plane; the asymmetry is to be expected, since ionization defocuses the beam, and also depletes a portion of its energy, which in this case shift the channel towards the beam's entrance (e.g. towards the off-axis parabola mirror used to focus the beam).

At the focus (in vacuum), the spot's area is ~2100 times smaller than at the onset of ionization. Since the barrier-suppression ionization of nitrogen to first level is ~1.8×10^{14} W/cm^2, the corresponding peak intensity at focus of the laser is ~3.8×10^{17} W/cm^2. This gives a corresponding normalized vector potential of $a_0 = 0.46$.
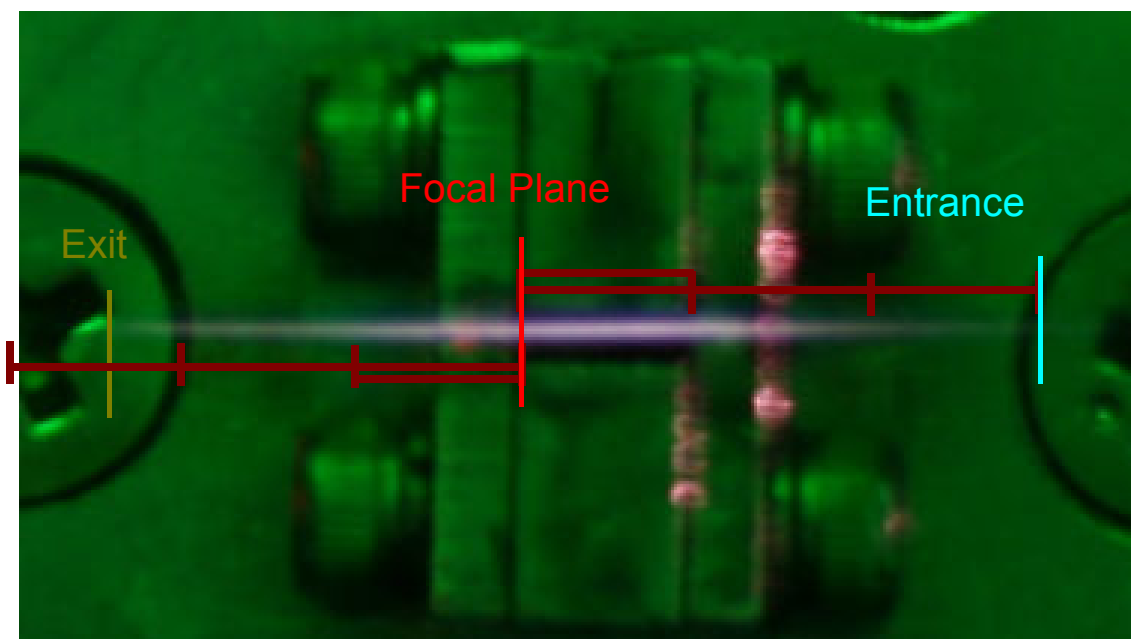
Figure 5.11: Ionization of air by Raman laser. The gas-jet nozzle is shown in the background for scale,and measure 1 mm by 3mm. The vertical lines mark the onset of ionization (teal), the focal plane of the laser (light red), and the plane at which ionization ceases to occur (brown).The dark-red horizontal lines are scales (each tick mark is 3mm).

5.4.3 Intensity Measured by Determining Ionization Onset in Helium Gas Jet

The Raman beam is sufficiently intense to ionize helium to He^{2+}. In order to obtain a third independent measurement of its intensity, the helium gas jet was moved along the propagation axis of the laser (which propagates 0.5 mm above the jet). The jet was moved in increments of 5000 steps (0.5 mm) until the ionization spark was no longer detectable to the eye (looking through a dorsal window).

The spark disappears at motor setting 153,500. At setting 183,000 the ionization spark spans approximately half of the 3 mm gas jet length, and at setting 203, 000 the

ionization spark spans the whole length of the gas jet, and continues to do so until the jet is moved to 233,000. At 253,000 the spark again spans half the channel's length, and at approximately 283,000 the spark disappears. This last number is approximate, because the motor-actuator reaches the end of its motion at approximately this position, and has a tendency to slip slightly at the end of its motion.

These numbers essentially mean that the focal plane of the beam is at approximately 218,000 on the motor setting; since the spark first appears 65,000 steps before this (and disappears roughly 65,000 steps after this), the beam is sufficiently intense to ionize helium 6.5 mm before it reaches its focus. The intensity at focus is therefore determinable by setting up a ratio of the areas of the beam at focus and at the ionization onset position. Since the uncertainty in spot position is 0.25 mm, this gives a focused-spot intensity of 1.12×10^{17} W/cm^2 $\pm$ 4×10^{15} W/cm^2 and an averaged normalized vector potential of $a_0 = 0.25$.

Chapter References

[180] J. A. Armstrong, "Measurement of picosecond laser pulse widths", *Appl. Phys. Lett.*, Vol. **10** No. 1, 16 (1967).

[181] K. Sala, G. Kenney-Wallace, and G. Hall, "CW autocorrelation measurements of picosecond laser pulses", *IEEE J. Quantum Electron.*, Vol. **16** No. 9, 990 (1980).

[182] W. Rudolph, M. Sheik-Bahae, A. Bernstein, and L. F. Lester, "Femtosecond autocorrelation measurements based on two-photon photoconductivity in ZnSe," *Optics Letters*, Vol. **22**, No. 5, pp. 313-315 (1997).

[183] D. Panaenko and Y. Fainman, "Interferometric Correlation of Infrared Femtosecond Pulses with Two-Photon Conductivity in a Silicon CCD," *Applied Optics*, Vol. **41**, No. 18, pp. 3748-3752 (2002).

[184] G. Xinan, . Lambsdorff, J. Kuhl, and W. Biachang "Fast-scanning autocorrelator with 1-ns scanning range for characterization of mode-locked ion lasers", *Rev. Sci. Instrum.*, Vol. **59** No. 9, 2088 (1988).

[185] D. M. Riffe and A. J. Sabbah, "A compact rotating-mirror autocorrelator design for femtosecond and picosecond laser pulses", *Rev. Sci. Instrum.*, Vol. **69** No. 9, 3099 (1998).

[186] J. Collier, C. Hernandez-Gomez, R. Allot, C. Danson, and A. Hall, "A single-shot third-order autocorrelator for pulse contrast and pulse shape measurements," *Laser and Particle Beams,* Vol. **19**, No. 02, pp 231-235 (2001).

[187] D. J. Kane and R. Trebino, "Characterization of arbitrary femtosecond pulses using frequency-resolved optical gating", *IEEE J. Quantum Electron.*, Vol. **29** No. 2, 571 (1993).

[188] C. Iaconis and I. A. Walmsley, "Spectral phase interferometry for direct electric-field reconstruction of ultrashort optical pulses", *Opt. Lett.*, Vol. **23** No. 10, 792 (1998).

[189] F.Salin, P. Georges, G. Roger, and A. Brun, "Single-shot measurement of a 52-fs pulse," *Applied Optics*, Vol. **26**, No. 21, pp. 4528-4531 (1987).

[190] Polyanskiy, Mikhail. "Refractive Index Database," Web. 10 February 2014. http://refractiveindex.info/

[191] I. H. Malitson, "Interspecimen Comparison of the Refractive Index of Fused Silica," *J. Opt. Soc. Am.* Vol. **55**, 1205-1208 (1965).

[192] Anonymous, Handbook of Optics, 3rd edition, Vol. 4. McGraw-Hill 2009.

[193] Anonymous, "Optical Glass Data Sheets," Schott Glass, 19 April 2010, pdf available   at http://www.schott.com/advanced_optics/us/abbe_datasheets/schott_datasheet_all_us.pdf

[194] Anthony Link, Enam A. Chowdhury, John T. Morrison, Vladimir M. Ovchinnikov, Dustin Offermann, Linn Van Woerkom, and Richard R. Freeman, John Pasley, Erik Shipton, Farhat Beg, Patrick Rambo, Jens Schwarz, Matthias Geissel, Aaron Edens, and John L. Porter, "Development of an in situ peak intensity measurement method for ultraintense single shot laser-plasma experiments at the Sandia Z petawatt facility," *Rev. Sci. Instr.*, Vol. **77**, No. 10, 10E723 (2006).

[195] M. Amosov and N. Delone, "Tunnel Ionization of complex atoms and atomic ions in electromagnetic field," SPIE Vol. **664**, 138-140, High Intensity Laser Processes (1986).

[196] S. Augst, D.D. Meyerhofer, D. Strickland, and S.L. Chin, "Laser ionization of noble gases by Coulomb-barrier suppression," *J. Opt. Soc. Am. B*, Vol. **8**, No. 4, pp. 858-867, 1991.

[197] M. Suzuki, "Recombination luminescence from ionization tracks produced by alpha particles in high pressure argon, krypton and xenon gases," *Nucl. Instr. and Methods in Phys. Research*, Vol. **215**, No. 1–2, pp. 345–356 (1983).

Chapter 6

Experimental Capabilities and Future Work

The ramifications of the Raman laser's achievable intensity for future two-color experiments will be discussed. Some of the experiments are feasible with the current "secondary" Raman system (and primary laser) performance, whereas others will require greater Raman energy, power, and/or intensity. In general, the Raman beam is sufficient to act as a seed for many two-color experiments or as a probe, but not as the pump itself. Possible experimental configurations of the Laser Wakefield Target Chamber (LWTC) are presented in Appendix E, a method for further boosting the secondary pulse's power is discussed in Appendix F.

6.1   Seeded Forward Raman Scattering

The theory behind most the the two-color experiment is discussed in Chapter 3 (Sec. 3.4). Here, I discuss the recommended experimental parameters and whether the Raman system in particular is sufficient in its present configuration to meet those parameters. The experiments I will consider here include seeded forward Raman scattering (SFRS) and the Raman-seeded self-modulated laser wakefield accelerator (RS-LFWA), electromagnetic cascading (EMC) with beatnote generation and compression, controlled relativistic self-focusing (RSF), and two-color colliding-pulse injection.

238

6.1.1 Preliminary Discussion

The ideal regime for FRS experiments leading to sm-LWFA is a laser pulse which interacts with the plasma over several plasma wavelengths. The pulse durations should therefore be $c\tau_L \gg \lambda_p$. Furthermore, in order to seed efficiently the pulse durations of the Raman and Main pulse should be approximately matched, and should resonant with the plasma electron frequency. Since the primary pulse is centered at $\omega_L = 2.354\times10^{15}$ s^{-1} (800 nm) and the Raman pulse at $\omega_R = 2.157\times10^{15}$ s^{-1} (873 nm), the plasma frequency should be $\omega_p = 1.97\times10^{14}$ s^{-1}, which corresponds to a density of $n_e = 1.22\times10^{19}$ cm^{-3}.

The experimental set-up is shown in Appendix E (see Sec. E.1 and Fig. E.1). The diagnostics include a pair of ccd cameras—one for each of the primary (fundamental) and secondary (Raman) beams—which relay image a plane near the OAP's focus. The plasma's density is determined by the gas jet's backing pressure: the pressure needed to produce a plasma of the right density in helium 0.5 mm above the nozzle is ~12-15 PSI.

According to the PIC simulations[198] discussed in Chapter 3 (Sec. 3.4.1), the SFRS should be achievable for $W_L \sim 38$ mJ, $\tau =125$ fs ($P \approx P_{cr}$), $\lambda_L = 800$ nm, $a_{0L} = 0.5$, spot size $w_{0L} = 6$ μm, and $\omega_L/\omega_p = 6$, and $a_{0seed} = 0.1\ a_{0L}$. Note that this ratio of laser to plasma frequency implies a plasma of density $n_e \approx 4.84\times10^{19}$ cm^{-3}, and thus a resonant seed centered at 960 nm. This roughly corresponds to the second Stokes light from barium nitrate (938 nm). Furthermore, the low (38 mJ) laser energy used in the simulations comes with a correspondingly small spot size. In the current UT^3 laser

239

system, the spot size at focus is twice as big, thus requiring 4 times more energy to achieve the same intensity as these simulation parameters. If the seed is to be resonant when beating with the pump, either the plasma density must be decreased by a factor of 4 to $n_e \approx 1.22 \times 10^{19}$ cm^{-3}, or the second Stokes shift can be used.

However, earlier sm-LWFA experiments have operated (with single color) in the density regime[199] 2.82×10^{19} cm^{-3} < n_e < 3.82×10^{19} cm^{-3}. LeBlanc *et al.*[200] were able to observe some signal with 140 mJ in 400 fs on target in an 8.5 μm spot size with n_e=2.3$\times 10^{19}$ cm^{-3}. These experiments did have a somewhat greater pumping intensity (and energy) than proposed for SFRS, but were not seeding the FRS instability.

Simulations by Fomyts'kyi *et al.* examined the sensitivity of the SFRS process to frequency mismatch. These simulations obtain the maximum longitudinal electron momentum from 1D PIC simulations for both SFRS and PBWA. The parameters used for SFRS are a_{0L}=0.5 and a_{0S}=0.05 and for PBWA they are a_0' = a_0'' = 0.35, with an interaction time of 500 $\omega_p^{-1} \approx 1.28$ ps, which corresponds to an interaction length of 0.38 mm, well under the 3 mm maximum length of the gas jet in the UT^3 wakefield chamber. A plot of the maximum electron momentum against the frequency mismatch parameter $\zeta = (\omega_{0L} - \omega_S - \omega_p)/\omega_{0L}$ is shown in Fig. 6.1, for both the SFRS accelerator and for the PBWA.
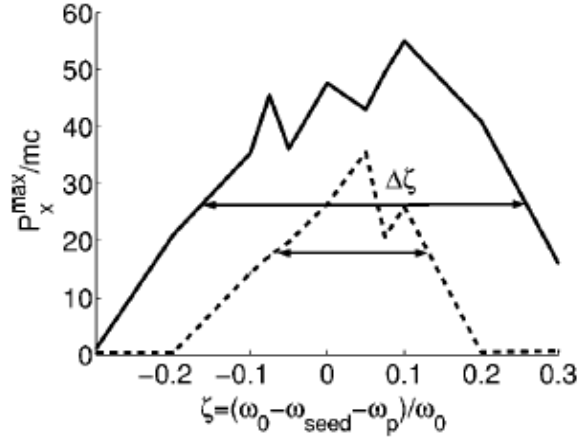
Figure 6.1: Effects of frequency mismatch on maximum electron longitudinal momentum[198]. The frequency mismatch is given for either a SFRS accelerator with $a_{0L} = 10a_{0S} = 0.5$ (solid), or for a PBWA with $a_0' = a_0'' = 0.35$ (dotted line).

According to Fig. 6.1, the maximum accelerated electron momentum falls off by a factor of ½ when $\zeta = (\omega_{0L} - \omega_S - \omega_p)/\omega_{0L} \approx$ -0.15 or +0.25. Since the primary and secondary laser frequencies are under-detuned compared to the plasma resonance frequencies corresponding to the densities at which sm-LWFA and FRS have been observed, it is the first of these numbers, $\zeta = (\omega_{0L} - \omega_S - \omega_p)/\omega_{0L} \approx$ -0.15, which is of more immediate interest. Using λ_L = 800 nm and λ_S = 873 nm, the mismatch parameter for a plasma of density n_e = 2.3×10^{19} cm^{-3} is $\zeta \approx$ -0.034; for a plasma of density n_e = 4.84×10^{19} cm^{-3} it is $\zeta \approx$ -0.086. Therefore, according to Fig. 6.1, the proposed parameter $W_L \approx$ 38 mJ, τ =125 fs ($P \approx P_{cr}$), λ_L = 800 nm, a_{0L} = 0.5, spot size w_{0L} = 6 μm, and ω_L/ω_p = 6, and a_{0seed} = 0.1 a_{0L} should be sufficient to see significant effects from SFRS. Since the spot size is a factor of 2 larger, and since it cannot easily be made smaller with the current set-up, the pump energy can be increased to $W_L \approx$ 150-160 mJ and the seed energy to $W_S \approx$

1.5 mJ in order to maintain the simulated intensities. This allows a proof-of-principle demonstration using the existing wakefield target chamber set-up. Note that this pump energy is equivalent to the lowest energy at which FRS was reported by either LeBlanc *et al.* or Umstadter *et al.*, and that the simulated effect is wavebreaking.

6.1.2 Initial Experimental Results from SFRS

Preliminary results have been obtained using the primary pulse as pump and attempting to use the secondary pulse as seed. First, the 800 nm primary beam was sent alone into the gas jet target. Under the duration of the pulse, the backing pressure of the jet, and the focal plane position within the 3-mm-long gas jet were are varied. As a general rule, the spectral signal from the FRS instability was best observed at higher laser intensity and relatively high backing pressure—both expected results. For example, the signal becomes difficult to discern below a backing pressure of 300 PSI, which corresponds to a plasma of density $n_e = 3.5 \times 10^{19}$ cm^{-3}, or for pulse powers of less than 500 GW.

Both of these parameters are near the lower end of the respective density and energy ranges previously reported[200]. The lowest density at which FRS signal could be discerned was $n_e \approx 2.25 \times 10^{19}$ cm^{-3} (125 PSI), for which the required power was 5.3 TW (270 mJ in 51 fs). The optimum position of the focus at high pump power is the entrance to the gas jet: the pulse power exceeds the critical power for RSF and is therefore guided through the plasma. Some sample spectra are show in Fig. 6.2, in which the duration of the 270 mJ primary pulse is changed. It should be noted here that in contrast to the work of LeBlanc *et al.* and Umstadter *et al.*, there is no frequency-doubled probe pulse present.

Instead, the FRS signal is the Stokes' scattering of the pump pulse itself. Because this pump pulse also undergoes ionization blueshifting and self-phase modulation into the blue part of the spectrum, the anti-Stokes signals are lost in the pump's shifted tail.

At higher backing pressures (>300 PSI) and for durations of ≈140 fs, electrons were observed on the LANEX. Longer pulses tended not to produce electrons, likely on account of having too small of a power; the energy deliver on-target was limited to <300 mJ by laser performance in the primary beam line. Shorter pulses also tended not to produce electrons at higher densities; the likely explanation for this is that the pulses were too weak to access the bubble regime, and therefore produced electrons most efficiently in the sm-LWFA regime. However, this regime requires a pulse whose duration spans several plasma wavelengths to be properly modulated, so that pulses with durations <100 fs were insufficiently long for the modulation to effectively occur.
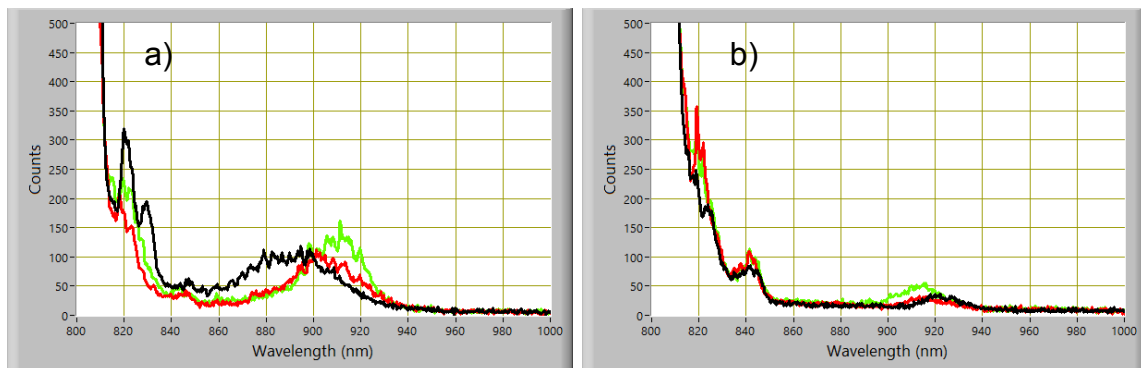
Figure 6.2: Forward Raman scattering spectra from a plasma generated using a helium gas jet with 300 PSI backing pressure. The 270 mJ primary pulse's duration is a) 90 fs and b) 140 fs.
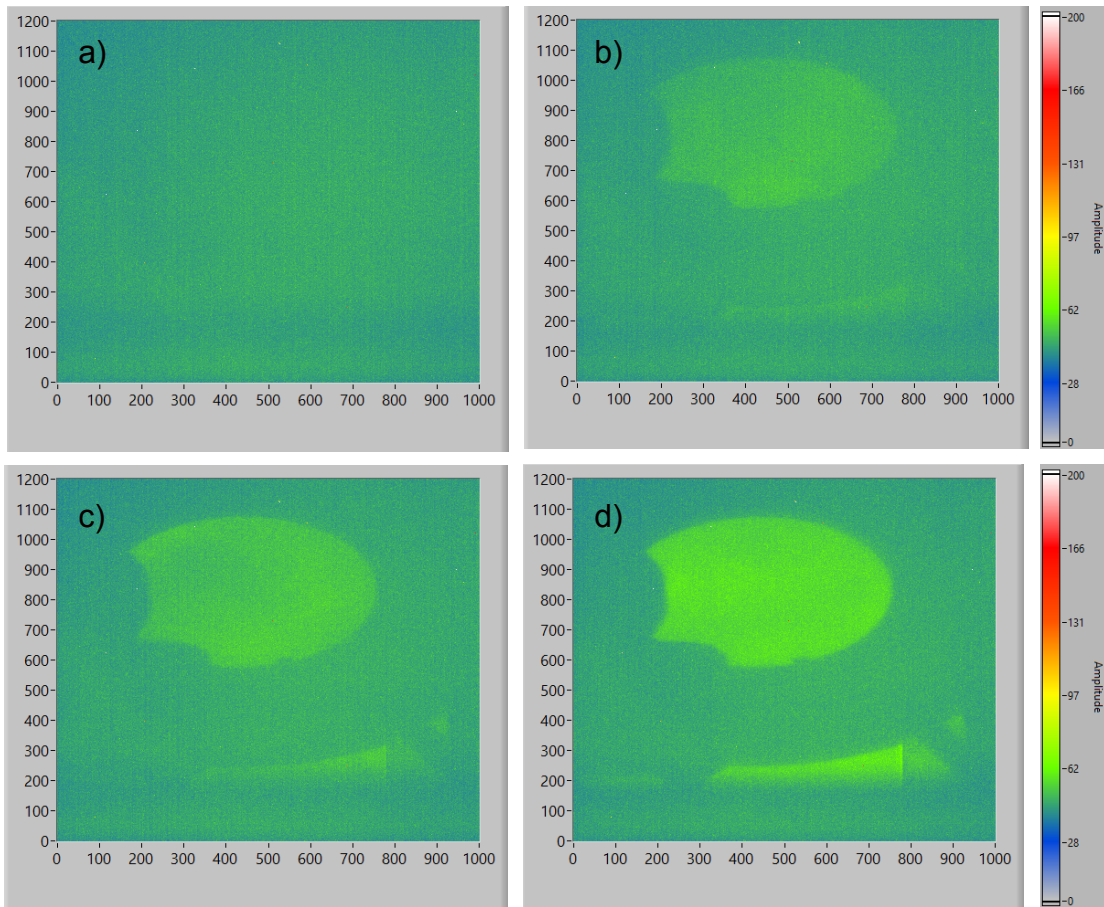
Figure 6.3: CCD images of LANEX screen fluorescing from collisions with accelerated electrons. The laser duration is 140 fs and its energy is 270 mJ, whereas the backing pressure is a) 75 PSI, b) 300 PSI, c) 400 PSI, and d) 450 PSI.

Some images of electrons colliding with a fluorescing screen are shown in Fig. 6.3. However, the magnet has been removed and thus the screen fluorescence brightness only measures relative number of electrons and not their energy spread. The secondary beam at 873 nm appears to have negligible effects on either the FRS spectrum or the electron production. The spectra with and without Raman seed are plotted in Fig. 6.4. There is a marginal increase in the spectral intensity of the FRS signal from the unseeded case in Fig. 6.4a (and Fig. 6.2b) to the seeded case of Fig. 6.4b.

244
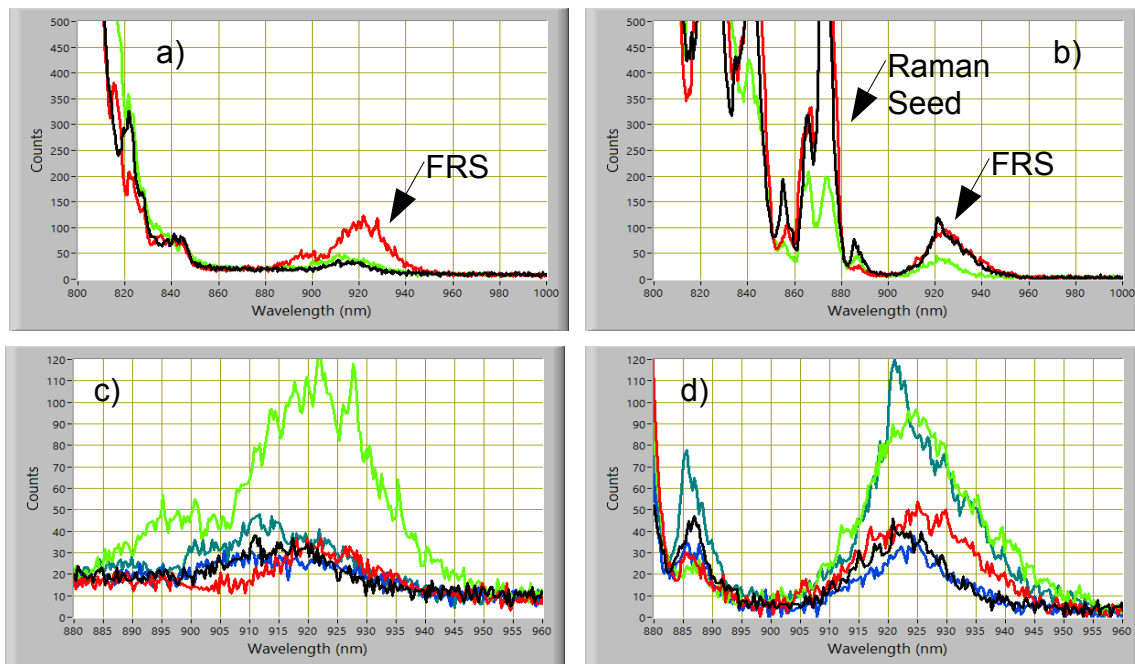
Figure 6.4: Forward Raman scattering in an unseeded and in a seeded 3 mm gas jet. The backing pressure in both cases is 300 PSI, and the pump energy on-target is 270 mJ in 140 fs. The secondary beam centered at 873 nm which is used to seed FRS is a) not present or b) present with an energy of 25 mJ in 300 fs and synchronized with the 800 nm pump pulse; c) a closeup of the FRS spectrum without the seed, and d) a closeup of the FRS spectrum with the synchronized secondary beam acting as seed. The different colors represent different shots captured by the spectrometer.

In the typical shot without the secondary seed pulse, Figs. 6.4 a and c, the FRS signal registers a peak count of 30-40 and are centered around 920 nm with long tails in the blue. For the typical shot with the second pulse present as seed, Figs 6.4b and d, the peak registers 40-50 counts, is centered at 925 nm, and the blue tail is suppressed. The blue tail is a persistent feature in shots without the secondary laser, and it is persistently suppressed in shots with the secondary laser, but is nevertheless most likely noise, since

the suppression continues even when a large delay (~ps) is introduced between the two pulses. The seed pulse has no apparent effect on electron production.

The secondary pulse experiences some relativistic cross-phase modulation[201] (RXPM), as evidenced in Fig. 6.4b. However, because it is so near to the primary pulse in spectra—the two bands very nearly overlap—the extent to which the secondary pulse spectrum is broadened is lost in the primary pulse's spectrum.

6.1.3 Discussion and Future Work Concerning SFRS

There are a few possible reasons for the secondary seed's apparent lack of effect:

1. poor overlap in time (bad synchronization) or space (bad alignment)

2. the seed is too weak to be effective

3. early ionization blueshift of the pump such that the effective pump is "bluer" than the seed

4. the beat frequency is too far from resonance

5. the Raman pulse is reshaped during this interaction, i.e. by ionization defocusing, such that it does not adequately overlap with the pump pulse and hence does not seed the interaction

Each of these can now be considered in turn.

The temporal synchronization was discussed in Chapter 4 (Sec. 4.7), as was the relay-imaging system for the target chamber and its use in achieving spatial overlap. The relay-imaging system has an effective imaging range of ≈20 mm, the approximate center of which is imaging the pulses' focal plane at the entrance to the gas jet. The two pulses

can be overlapped on the relay-imaging ccd for two planes at the opposite ends of the relay's range. This means that the two pulses are ≈collinear over the entire length of the gas jet and several millimeters to its entrance and exit. For good measure, the overlap is checked in a third plane, which is the focal plane. The pulses both have a slight shot-to-shot wobble of ±1 μm in the focal plane (FWHM > 10 μm each), but the average center position of both is within < 1 μm of each other over 100 shots, and even far from the focal plane the centers remain within ≈3 μm of each other shot-to-shot. Therefore the pulses are spatially overlapped within the limits of control for this system.

The synchronization is achieved via cross-defocusing. Essentially, one beam ionizes the target and the other beam, whose intensity is insufficient to cause ionization, is defocused provided that it arrives after the first beam. The secondary beam line was limited to $\tau_S > 250$ fs durations and $W_S < 35$ mJ on-target, which is $I_S \approx 6\times10^{16}$ W/cm^2: enough in principle to doubly-ionize helium near its focus. However, the ionization defocusing effects are very weak on account of only having a very short propagation distance over which ionization occurs, and on account of the fact that the cross defocusing effect is in practice smaller than the self-defocusing effect. Nevertheless, there was some small defocusing effect such that the overlap window could be established within a range of $\Delta\tau_{window} < 400$ fs. To be safe, the synchronization between the to pulses was scanned to within $\Delta\tau_{scan} \approx 5$ ps of either side of this window, in increments of $\Delta\tau_{step} \approx 100$ fs: there was no observed enhancement of the FRS signal within this range.

The next possibility is that the seed is too weak to be effective. However, this possibility can be dismissed because without the seed, the FRS instability grows from background oscillations (noise) in the plasma. The seed's energy is up to 35 mJ distributed over 250 fs, which includes up to 20 mJ in the 140 fs which overlaps with the primary pump pulse. This is many orders of magnitude larger than the background from which FRS normally grows, and it is fully an order of magnitude larger than the most efficient seed pulse considered by Fomyts'kyi (albeit in a 4× larger spot area). Therefore, the secondary pulse should be sufficiently strong to seed FRS.

It is possible that the ionization blueshift plays some effect on the pump's and seed's combined beat wave and its ability to effectively drive the plasma wave. However, the amount of light blueshifted from ionization is dependent on the density of the plasma. Even at the highest densities (450 PSI backing pressure, $n_e \approx 4.75 \times 10^{19}$ cm^{-3}) some amount of light at 800 nm exits the gas jet. This implies that a significant portion of the laser is unshifted in the early stages of propagation when the seeding is most critical. Furthermore, as compared to the original primary pulse center at 800 nm, at this higher density the first blueshifted peak at 720 nm beating with the seed at 873 nm is actually more nearly resonant (albeit slightly overdetuned as compared to the undertuned case at 800 nm).

The third possibility is that the seed pulse frequency is too close to that of the pump pulse such that the beat frequency between the two is too far from the plasma's resonance. The best results for electron production (Fig. 6.3) are obtained at high densities: 400 PSI backing pressure which gives a plasma density of $n_e \approx 4.5 \times 10^{19}$ cm^{-3}.

However, the FRS signal is clearly detectable at lower densities: Figs. 6.2 and 6.4 are both at 300 PSI which gives a density of $n_e \approx 3.5\times10^{19}$ cm^{-3}, and the FRS spectral feature is detectable (albeit barely) at densities as low as $n_e \approx 2.25\times10^{19}$ cm^{-3}. These three densities correspond respectively to $\zeta \approx -0.077$, $\zeta \approx -0.058$, and $\zeta \approx -0.030$ in Fig. 6.1. Thus, according to the 1D PIC simulations, wavebreaking should be occurring in all three cases, with peak electron energies approaching the peak energy obtained for the case of resonantly seeded FRS with $\zeta \approx 0$, $\Omega = \omega_p$.

It is, however, possible that the SFRS process is more sensitive to beat frequency mismatch ζ than is predicted by the PIC simulations. However, the FRS interaction has been observed with a larger initial pump power, 1.2 J before compression and 120 fs compressed duration. Under these conditions, FRS is observable at lower densities. Recall from chapter 3 (Table 3.1.1) that the growth rate for FRS is given by $\Gamma_R = \omega_p^2 a_0/(8\omega_L^2)^{1/2}$ for the resonant 4-wave FRS process. Since the plasma frequency is related to the electron density by $\omega_p = (n_e e^2/\varepsilon_0 m_e)^{1/2}$, it is to be expected that an increase in energy (and hence intensity) by a factor of 2 results in an equal gain for a plasma whose density has been decreased by a factor of $1/\sqrt{2}$, the expected result is that that the FRS signal should be detectable at a density of about 1.47×10^{19} cm^{-3}.

In fact, the FRS signal becomes detectable at a sightly lower density, as shown in Fig. 6.5. The FRS signal becomes detectable at a density of approximately 1.3×10^{19} cm^{-3}, although it fluctuates in both intensity and wavelength from shot-to-shot, with most shots

being undetectable. As the density is increased, the FRS signal both becomes more consistent and redshifts on account of the increase in plasma frequency.
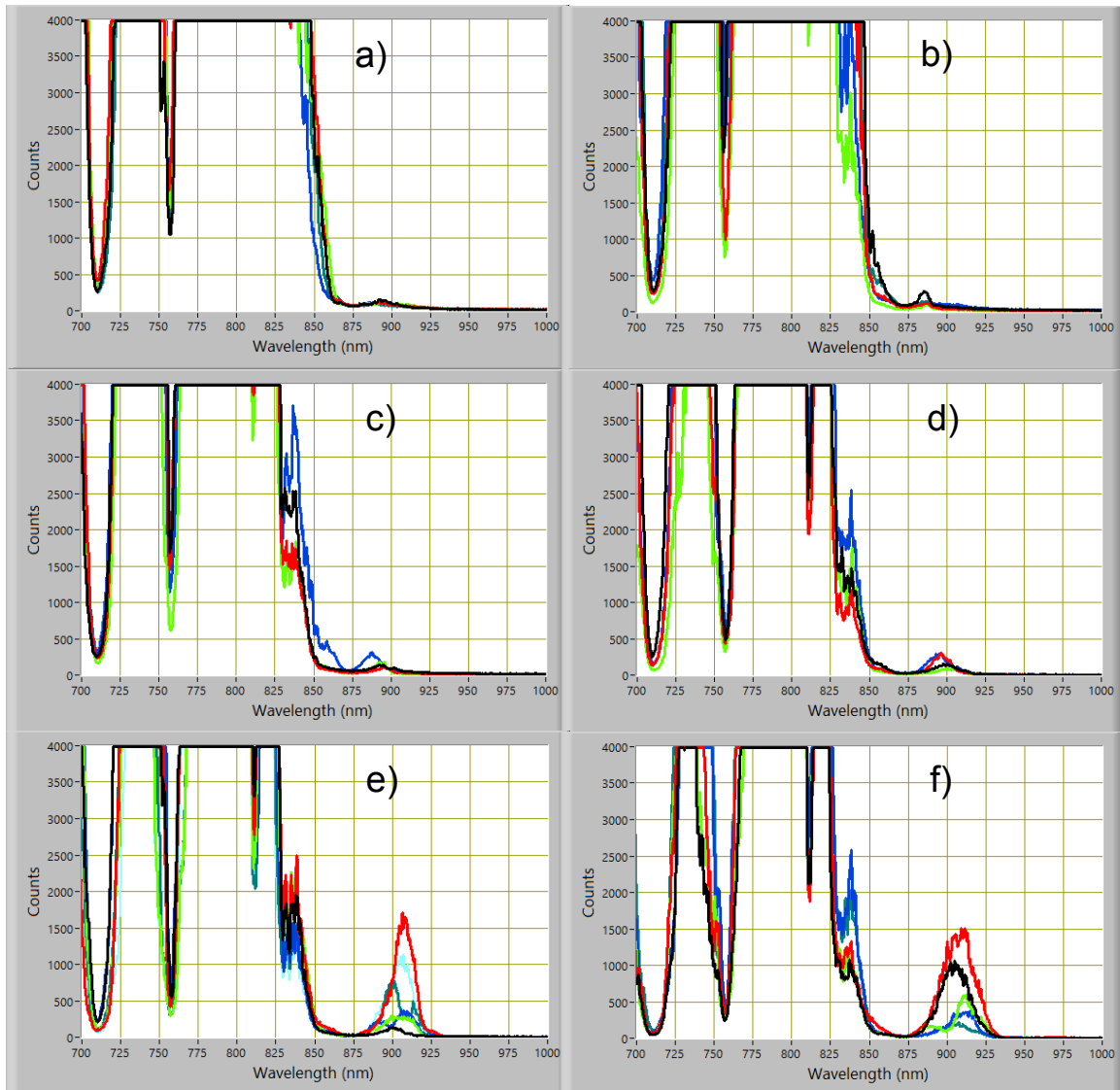
Figure 6.5: Forward Raman Scattering for a monochromatic laser with 540 mJ on target in 120 fs for several plasma densities. The FRS signal is for plasma densities of a) 1.4×10^{19} cm^{-3}, b)1.6×10^{19} cm^{-3}, c) 1.8×10^{19} cm^{-3}, d) 1.9×10^{19} cm^{-3}, e) 2.20×10^{19} cm^{-3}, f) 2.4×10^{19} cm^{-3}.

At the lowest densities, the FRS signal overlaps with the second color laser's spectrum, although there is a small difference in the peak wavelengths. There is no observed effect from the seeding even under these conditions where $\zeta \approx 0$. The seeding also has little to no observed effect on electron injection and acceleration, which is nevertheless observed at lower electron densities ($n_e \approx 2.2 \times 10^{19}$ cm^{-3}) with the higher pump power.

This is almost certainly on account of the final factor, which is the reshaping of the seed mode. There are two causes of this: damage to the final steering mirror before the target, which also decreases the on-target intensity of both pulses; and the primary pump pulse is sufficiently intense such that the ionization channel which it creates defocuses the secondary (Raman seed) pulse before it can adequately seed the interaction. It is therefore necessary to counteract this ionization defocusing e.g. by relativistic cross-focusing/mutual guiding as discussed in Secs. 3.4.3 and 6.3.

6.2 BEATNOTE COMPRESSION

In the EMC beatnote generation and compression experiment, it is important for the resonant Raman scattering and envelope modulation instabilities to be suppressed, since these can come to dominate the EMC. One way of doing this is to ensure that the beat frequency between primary and secondary pulses is far from resonance with the plasma.

With that said, simulations[202] with a near-resonant beat frequency ($\Omega = 0.95\omega_p$)

using ultrafast pulses ($\tau_L \approx 90$ fs) can result in a compressed cascade. The parameters

used in the simulation are $\omega_0 = 2.356 \times 10^{15}$ s^{-1} ($\lambda_0 = 800$ nm) with $a_0 \approx 0.3$ for the primary

pulse, and $\omega_1 = 2.159 \times 10^{15}$ s^{-1} ($\lambda_1 = 873$ nm) with $a_1 \approx 0.048$, both with initial durations of

90 fs. Based on this information, the laser pulse energy needed should be $W_0 = 57$mJ and

$W_1 = 1.23$ mJ, assuming a spotsize of 12 μm FWHM (10.2 μm for $1/e^2$ waist) at focus as

per normal operation of the OAP. For the plasma, the density is $n_0 = 1.35 \times 10^{19}$ cm^{-3} ($\omega_p = $

2.0736×10^{14} s^{-1}, $\Omega = 0.95\omega_p$) which means that $d = 7.725 \times 10^{-3}$. The plasma length is

chosen to be 1.8 mm, for which $M = 5$ sidebands should be generated and compressed.

The simulation results for the EMC beatnote generation and compression of this two-

color laser are shown in Fig. 6.6.
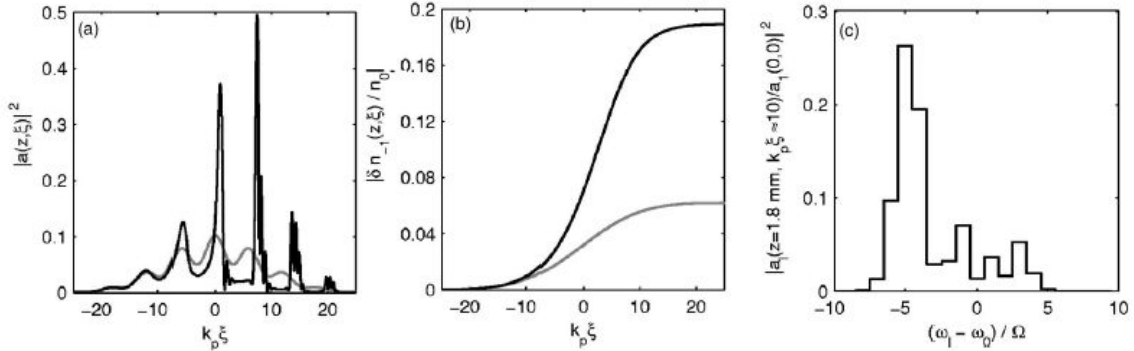
Figure 6.6: Simulation results for the cascade compression experiment with 2-color short pulse laser in dense plasma[202]. These plot show a) laser pulse intensity as a function of retarded time, b) normalized amplitude of near-resonant EPW vs retarded time, and c) the laser spectrum near ξ = 0. The gray curves show these quantities at the plasma entrance (z = 0 mm), and the black curves show these quantities at the plasma exit (z = 1.8 mm).

252

The simulation results shown in Fig. 6.6 suggest that this experiment can be successfully carried out using parameters which are currently available to the UT^3 system. The pulses at the tail of the compressed train are compressed to ~1/4 plasma period, or $\approx$7-8 fs. The 90 fs pulse duration requirement is obtainable for the fully amplified Raman beam, but it is more readily obtainable using a partially amplified pulse, e.g. removing passes for the Ti:Sapph amplifier. However, reducing the pulse duration should actually enhance the SFRS effects which it is desirable to be rid of: therefore, operating with longer pulse durations is beneficial to the EMC compression experiment.

Furthermore, many of these simulations assume a larger spot size, 25-30 μm instead of 12 μm. This spot size requirement can be achieved by making the pre-focused beam's waist smaller, e.g. reduce the waist of the beam incident on the OAP by a factor of 2-3.

Even at longer pulse durations with larger spot sizes, the intensity parameters favorable to this experiment are within the current capabilities of the primary and Raman systems of the UT^3 laser. For example, if the intensity described above with $a_0 \approx 0.3$ and $a_1 \approx 0.048$ is to maintained for a longer pulse (240 fs) and a larger spot size (25 μm), then the energy requirement becomes $W_0 \approx 650$ mJ on-target for the primary beam and $W_1 \approx 14$ mJ for the secondary beam. The latter is easily within the established capability of the Raman line, though the former is at the upper end of typical performance from the primary beam line, which nominally delivers up to 1 J on target but typically delivers 0.9-1.2 J before compression.

Additionally, the diagnostics for this experiment should ideally be capable of resolving pulse duration and spectrum after the plasma modulator/compressor. A singe-shot (2nd order) autocorrelator could be used to measure pulse durations if the pulses in the compressed train are sufficiently separated in time. However, it could not distinguish the order in which the pulses arrive, e.g. to verify whether pulses at the back of the pulse train are more compressed than those at the front per Fig. 6.6a. Furthermore, the pulses are unlikely to be sufficiently separated temporally to appear as individual peaks in the autocorrelator. A 3rd order autocorrelator[203] could be used to determine the order of the pulses. Better still, the output pulse duration would be measured using a FROG[204] (or some variant thereof).

Furthermore, a two-stage modulator-compressor experiment can be made feasible with access to either two gas jets. This would also be beneficial to the two-stage SFRS-LWFA experiments discussed in Sec. 3.4.1. Alternatively, a specially made nozzle which emits a long low-density gas jet followed by a short high-density jet could be used for this purpose.

6.3 CONTROLLING RELATIVISTIC SELF-FOCUSING

The parameters for the suppressed RSF experiment are more exacting than with other experiments. A process for determining the required parameters might be as follows.

- The first requirement is that the total power P_{tot} of both pulses combined must exceed the critical power for RSF: $P_{tot} > P_{cr}$. If this condition is not met, then there is no RSF to suppress.

- The pulses must be over-detuned, but reasonably near to resonance, since only in the range $1 < \Omega/\omega_p < 2^{1/2}$ is the cross-focusing coefficient negative so as to suppress RSF. This places a limit on the range of plasma densities, since the pulse frequency bands are determined: the primary is centered at $\omega_0 = 2.356 \times 10^{15}$ s^{-1} or $\lambda_0 = 800$ nm, and the secondary at $\omega_1 = 2.159 \times 10^{15}$ s^{-1} or $\lambda_1 = 873$ nm.

- In order to interact over many plasma cycles—a requirement for effective RSF suppression—the pulse duration must be $\tau \gg \omega_p^{-1}$. Since the plasma density and hence frequency is already determined by the beat frequency of the two laser pulses, this new requirement set a (lower) limit on the pulse duration.

- The intensity should be chosen so as to not cause electron cavitation. Since the lasers' power and the electron density are both previously determined, this requirement effectively places a restriction on the lower limit of the lasers' spot size.

- The power partition P_1/P_0, where $P_1 + P_0 = P_{tot}$, is determined by the spot size for mutual guiding[205],[206], as show in Fig. 6.7.

All of these parameters must be chosen carefully to allow for the guiding of the laser at ~ constant spot size through the plasma.
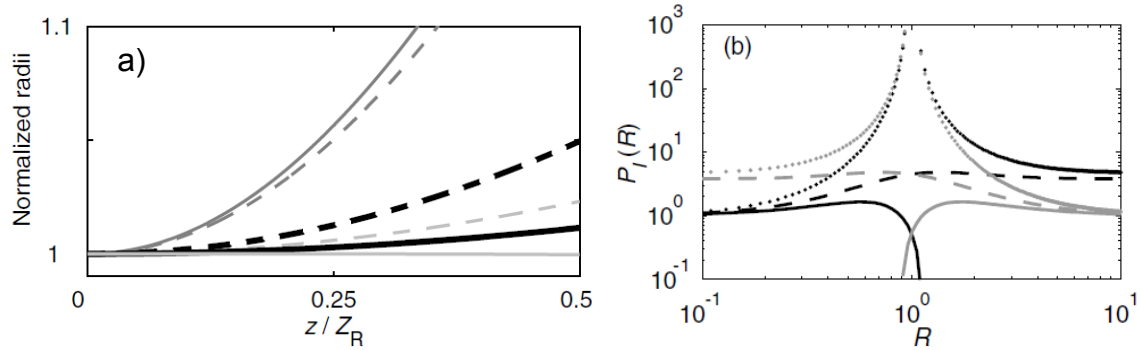
Figure 6.7: Power and spot size considerations for RSF suppression and mutual guiding[206]. a) Evolution of normalized spot sizes r_0/r_{00} (light gray), r_1/r_{00} (dark gray) and mean-squared radius $<r^2/r_{00}^2>^{1/2}$ for power partitions $P_1/P_0 = 0.054$ (solid) and $P_1/P_0 = 3/17$ (dashed). The two-color laser's total power exceeds the critical power for RSF ($P_{tot} = 1.1\ P_{cr}$) and both spots are initially the same size, $r_{00} = r_{01}$. b) Normalized power required for mutual guiding as a function of area ratio $R = (r_{00}/r_{01})^2$ when lasers are over-detuned: $\Omega/\omega_p = (3/2)^{1/2}$ (C<0, dotted), $\Omega/\omega_p = 1.25$ (C<0, dashed) and $\Omega/\omega_p = 3.18$ (C>0, solid). The black curves are for P_0, that is, the primary pulse with shorter wavelength, and the gray curves are for the P_1, that is, the secondary pulse with longer wavelength.

The recommended parameters for doing this are[207] duration $\tau_0 = \tau_1 \approx 210$ fs, normalized powers (power ÷ critical power) $P_0 \approx 1.11$ ($W_0 \approx 0.9$ J at $\lambda_0 = 800$ nm) and $P_1 \approx 0.1234$ ($W_0 \approx 0.1$ J at $\lambda_0 = 873$ nm), pulse duration plasma density $n_e \approx 7.8 \times 10^{18}$ cm^{-3} ($\Omega = 1.25\ \omega_p$), and $w_0 = w_1 = 25\ \mu$m FWHM at focus.

Both of these laser energies exceed the current typical (or even "best") performance of their respective lines in the UT^3 system, since both of these are "on-target" energies. The 0.9 J required of the primary laser system is only slightly less than the nominal 1 J delivered on-target at full power; on a good day (see Appendices A and D) the laser only delivers <800 mJ on-target. Furthermore, the 0.1J requirement for the secondary line is also larger than typically delivered on-target. In both cases, the lower

laser energy is on account of enlarging the spot sizes in the beam lines respective final amplifiers to avoid damaging the amplifier crystals.

RSF enhancement, however, is a less exacting experiment and would serve as a good proof-of-principle test. For this experiment, both powers (combined) should be less than the critical power, and the cross-focusing coefficient should be $C > 0$, meaning that the lasers should be under-detuned or strongly over-detuned. Mutual guiding occurs when the normalized instant power P_1/P_{cr} satisfies
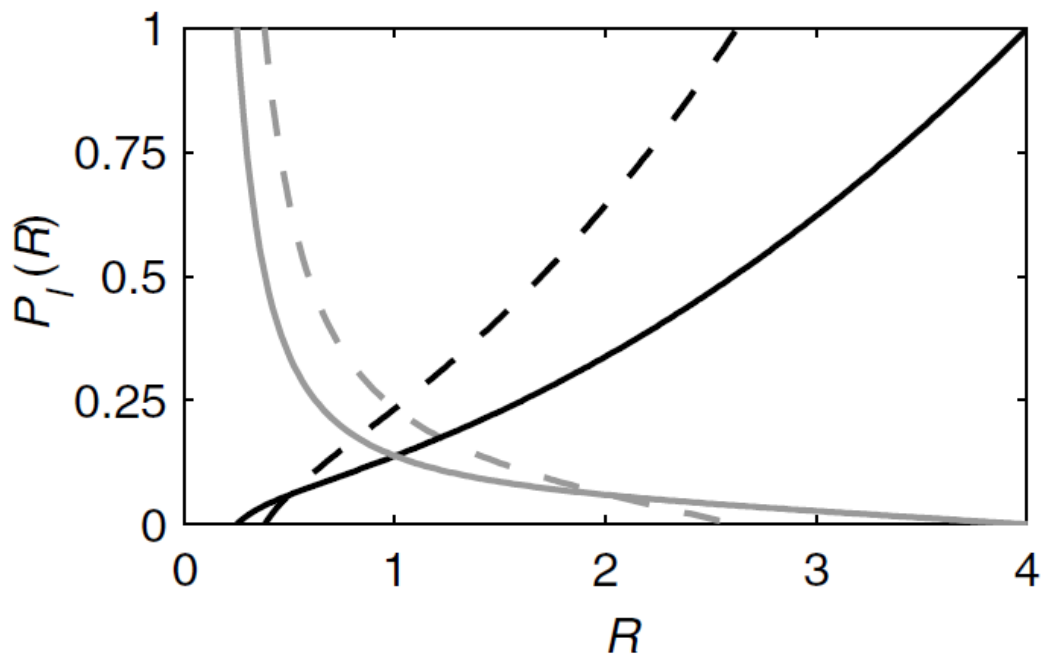
Figure 6.8: Normalized power required for mutual guiding of under-detuned two-color laser[206]. The powers are normalized to the critical power for RSF, with black being the power of the primary pulse P_0 and gray being the power of the secondary pulse P_1. The dashed lines represent the case where $\Omega/\omega_p = 0.75$, and the solid lines represent the case where $\Omega/\omega_p = 0.9$.

$$\frac{P_l}{P_{cr}} = (1+R)^2 \frac{(1+R)^2 - 8CR^{2m}}{(1+R)^4 - 64C^2 R^2} \qquad (6.3.1)$$

where R is the pulses' initial area ratio $R = (r_{00}/r_{01})^2$ and C is the cross-focusing coefficient. Solutions for mutual guiding with two different under-detuned frequencies are plotted in Fig. 6.8.

Near-resonance under-detuned beams in particular should see a strong cross-focusing effect. If the plasma density is chosen to be $n_e = 2.166 \times 10^{19}$ cm^{-3} so that $\Omega/\omega_p \approx$ 0.75, and both pulses initially have the same spot size $w_0 = w_1 = 25$ μm FWHM at focus and duration $\tau_0 = \tau_1 \approx 210$ fs[xxi], then both will require an initial power of $P_0 = P_1 \approx 0.25$ P_{cr} ≈ 325.6 GW for mutual guiding to occur. This corresponds to a pulse energy of $W_0 = W_1$ ≈ 68.4 mJ, which is easily obtainable for the primary laser and readily attainable for the secondary laser.

6.4   TWO-COLOR COLLIDING-PULSE INJECTION

The Raman laser's intensity at focus is approximately equal to the intensity suggested by Esarey *et al.*[208] via simulation, and the higher end of the measured intensities is equivalent to the $a_{0,inj} = 0.4$ used by Faure *et al.*[209] in their colliding pulse experiment. Therefore, the Raman seed's intensity is sufficient to use it as the injector pulse in a two-color colliding pulse experiment. Furthermore, other UT[3] LWTC users are preparing to

---

xxi N.B. This duration involves an interaction over more plasma lengths than in the case of RSF suppression because the plasma density is now greater.

put a colliding pulse line in place for their own experiments, and there is a LANEX which can be used for electron diagnostics in place in the chamber.

However, there is one major drawback to attempting this experiment as a practical matter, which is that the Raman pulse duration is too long. The Raman pulse is sufficient for a proof-of-principle experiment, but the pulse duration should be further shortened, ideally to match the primary beam duration (~30 fs, and even shorter it better). The reason is that the colliding pulse injector produces an electron beam whose energy spread is determined mostly by the injection time, which is also the time over which the pump and injector pulses—in this case a 30 fs primary pulse and a 100 fs Raman pulse— collide. Thus, the 100 fs Raman pulse is a poor choice for producing a monoenergetic beam as compared to a 30 fs pulse which has been split off from the primary pulse and counterpropagated to collide with it.

An alternative option, albeit one requiring an extensive re-configuring of the LWTC and/or a second chamber, would be to combine the colliding-pulse injection experiment with the EMC beatnote compression experiment. The Raman laser and a portion of the primary pulse are first sent to a gas jet target which act as modulator and compressor, thereby generating a train of high-intensity few-cycle pulses. The remainder of the primary laser would be used as the colliding pulse, and this single pulse and the train can counter-propagate and collide in a second gas jet. Such a method could potentially be used to create a high-repetition rate of monoenergetic electron beams.

6.5 CONCLUSION

A secondary laser has been added to the primary commercial TW laser system, to form a two-color terawatt laser system. This secondary line is generated via Raman shifting and amplification—a two-stage process—inside a barium nitrate crystal, and has been amplified to up to > 300 mJ centered at 873 nm. This secondary line is spectrally distinct from the primary and has delivered up to 100 mJ compressed to 100 fs on-target, making it a terawatt laser in its own right. This second terawatt laser is shifted by < 10% from the primary pulse central wavelength, has a bandwdith of 10-20 nm FWHM which fall just outside of the primary pulses' spectrum, and has been successfully synchronized with the primary pulse in a gas jet target.

The pre-compressed secondary (Raman) beam's central wavelength can be fine-tuned over a range of ±15 nm by adjusting the delay between pump and seed pulses in the Raman amplifier crystal. This is in addition to the possibility of further adjusting the center of this wavelength range by intentionally red-shifting the seed pulse's peak value, which can be accomplished by adjusting the intensity of the 800 nm fundamental pulse in the seed line. The redshifting can move the peak wavelength form 873 nm to ~890 nm, meaning the total range over which this peak can be adjusted in principle is from 860 nm up to 905 nm with an 800 nm fundamental. However, this shifting reduces the bandwidth of the beam and increases its duration, as well as decreasing the overall output energy form the 6-pass Ti:Sapphire Final amplifier.

The intensity has been characterized using three methods. All three—ionization in air, ionization in helium, and a simple calculation from the beam's focal parameters

(energy, duration,and transverse spot size)—suggest that the pulse is sufficiently intense to be used as a control for a variety of high-intensity two-color laser-plasma interactions. The peak intensity of the secondary beam when focused by an f/12 off-axis parabola is 1.12×10^{17} W/cm^2 < I_{2peak} < 3.8×10^{17} W/cm^2, which is approximately 1% of the primary pulse' peak intensity, $I_{1peak} \approx 3\times10^{19}$ W/cm^2.

This two-color laser system's parameters are sufficient for enhancing relativistic self-focusing and for beatnote generation and compression to a train of few-cycle pulses. The second pulse can also be used as a low group-velocity walkoff probe for the primary pump, and is sufficiently intense to act as a seed for forward Raman scattering in plasma, though it suffers from being drastically defocused by the primary pumping beam. The secondary pulse is also sufficiently intense to act as a colliding-pulse injector, though ideally it would have a shorter duration (and hence shorter injection length) for this experiment. The secondary color's energy falls somewhat short of the desired parameters for relativistic self-focusing suppression, though this can likely be improved by the addition of a retroreflected Ti:Sapphire booster amplifier.

Chapter References

[198] M. Fomyts'kyi, C. Chiu, M. Downer, and F. Grigsby, "Controlled plasma wave generation and particle acceleration through seeding the forward Raman scattering instability," *Phys. Plasmas*, Vol. **12**, No. 2, 023103 (2005).

[199] S.P. LeBlanc, M.C. Downer, R. Wagner, S.-Y. Chen, A. Maksimchuk, G. Morour, and D. Umstadter, "Temporal Characterization of a Self-Modulated Laser Wakefield," *Phys. Rev. Lett.*, Vol. **77**, No. 27, pp. 5381-5384 (1996).

[200] D. Umstadter, S.-Y. Chen, A. Maksimchuk, G. Mourou, and R. Wagner, "Nonlinear Optics in Relativistic Plasmas and Laser Wake Field Acceleration of Electrons," *Science*, Vol. **273**, No. 5274, pp. 472-475 (1996).

[201] S. Chen, M. Rever, P. Zhang, W. Theobald, and D. Umstadter, "Observation of relativistic cross-phase modulation in high-intensity laser-plasma interactions," *Phys. Rev. E*, Vol. **74**, No. 4, 046406 (2006).

[202] S. Y. Kalmykov, S. A. Yi, and G. Shvets, "All-optical suppression of relativistic self-focusing of laser beams in plasmas," *Phys. Rev. E* Vol. **78**, No. 4, 057401 (2008).

[203] J. Collier, C. Hernandez-Gomez, R. Allot, C. Danson, and A. Hall, "A single-shot third-order autocorrelator for pulse contrast and pulse shape measurements," *Laser and Particle Beams,* Vol. **19**, No. 02, pp 231-235 (2001).

[204] D. J. Kane and R. Trebino, "Characterization of arbitrary femtosecond pulses using frequency-resolved optical gating", *IEEE J. Quantum Electron.*, Vol. **29** No. 2, 571 (1993).

[205] S. Y. Kalmykov, S. A. Yi, and G. Shvets, "All-optical suppression of relativistic self-focusing of laser beams in plasmas," *Phys. Rev. E* Vol. **78**, No. 4, 057401 (2008).

[206] S. Kalmykov, S. A. Yi, and G. Shvets, "All-optical control of nonlinear focusing of laser beams in plasma beat wave accelerator," *Plasma Phys. Control. Fusion*, Vol. **51**, 024011 (2009).

[207] S.Y. Kalmykov, B.A. Shadwick, and M.C. Downer, "All-optical Control of Nonlinear Self-Focusing in Plasmas Using Non-Resonantly Driven Plasma

Wave," *AIP Conf. Proc. Advanced Accel. Conc. 14*, Vol. **CP1299**, pp. 752-757 (2010).

[208] E. Esarey, R.F. Hubbard, W.P. Leemans, A. Ting, and P. Sprangle, "Electron Injection into Plasma Wake Fields by Colliding Laser Pulses," *Phys. Rev. Lett.* Vol. **79**, No. 14, 2682-2685 (1997).

[209] J. Faure, C. Rechatin, A. Norlin, A. Lifschitz, Y. Glinec, and V. Malka, "Controlled injection and acceleration of electrons in plasma wakefields by colliding laser pulses," *Nature*, Vol. **444**, 737-739 (2006).

Appendix A

The UT³ Laser: The Front End and Primary Laser

In this appendix, I discuss the UT³ laser system, in particular the primary system at 800 nm, part of which also serves as the pump to generate the Raman Laser System.
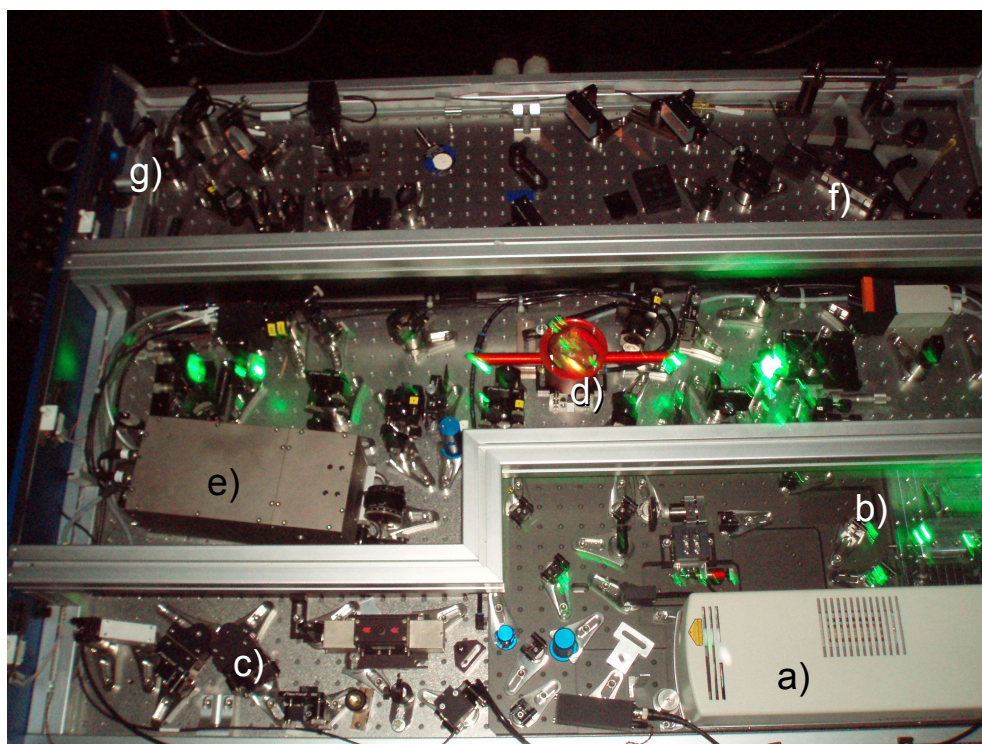
Figure A.1: The Femtolaser front-end system. This is where the laser "begins," with a) the Millenium Pro laser which pumps b) the Ti:Sapph oscillator. This system is amplified to ~400 mW average power and mode-locked before being stretched by c) the glass stretcher to picosecond durations. After being stretched, it is sent to d) the 9-pass Ti:Sapphire oscillator, which is pumped by ~7.5W at 1 kHz from a Jade laser (green light, but laser head not shown). After the first 4 passes in the 9-pass, the laser is sent to e) a Pockels cell pulse selector which reduces it to 1 kHz repetition rate, after which it is further amplified in the 9-pass to up to 1 W average power. It is ten sent to f) the prism compressor, and compressed to ~25fs, and from there g) exits the Femtolaser box.

The front end of the UT³ Laser system is a Femtolasers Femtopower Compact Pro amplifier box, the heart of which is the oscillator. The Femtolaser Amplifier system is show in Fig. A.1, and its oscillator consists of a Ti:Sapphire crystal pumped by a Newport/Spectra Physics Millenium laser, which delivers up to 5 W CW centered at 532 nm. Under normal operation, this laser ultimately pumps with 4.15 W at 532 nm. The Ti:Sapphire crystal lases over a broad bandwidth and uses the Kerr effect to achieve mode-locking. The result is a train of pulses whose output energy is ~300 mW CW and ~400 mW at 76 MHz repetition when mode-locked. The bandwidth of these pulses is ~100 nm FWHM and centered at 800 nm. The duration of these pulses is ~20 fs.
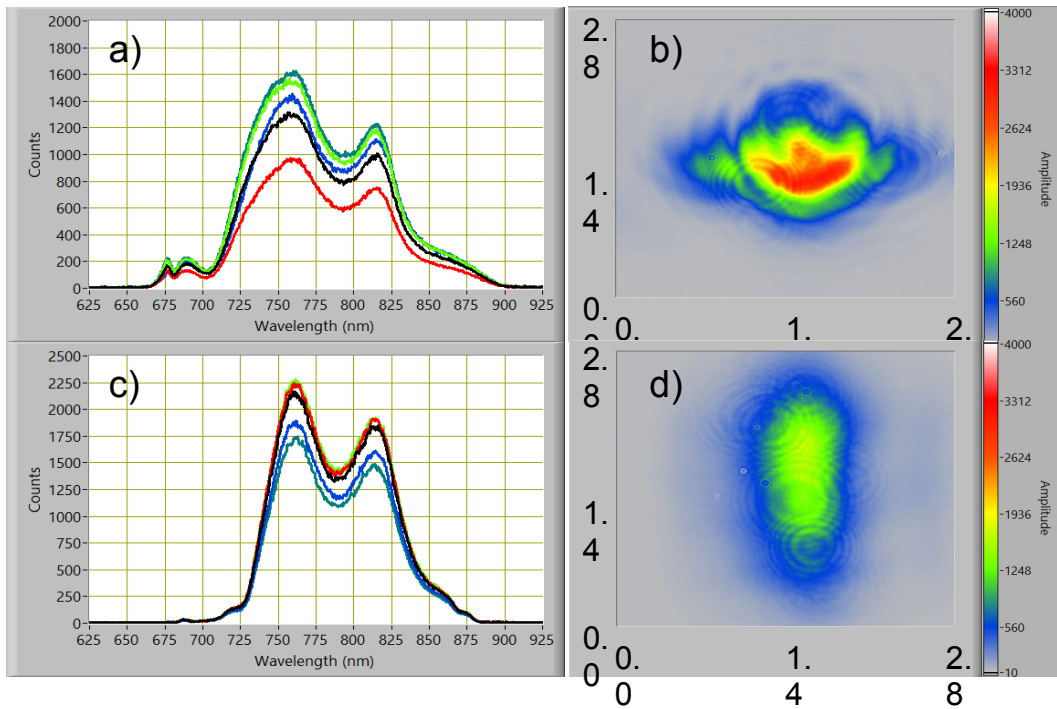
Figure A.2: Modes and spectra of the Femtolaser oscillator front-end. a) Spectrum and b) transverse spatial mode of the mode-locked oscillator prior to stretching. The typical spectral bandwidth is ~100 nm FWHM, and the scale for the mode's diameter given in millimeters. c) The spectrum and d) the transverse spatial mode after stretching in the glass stretcher.
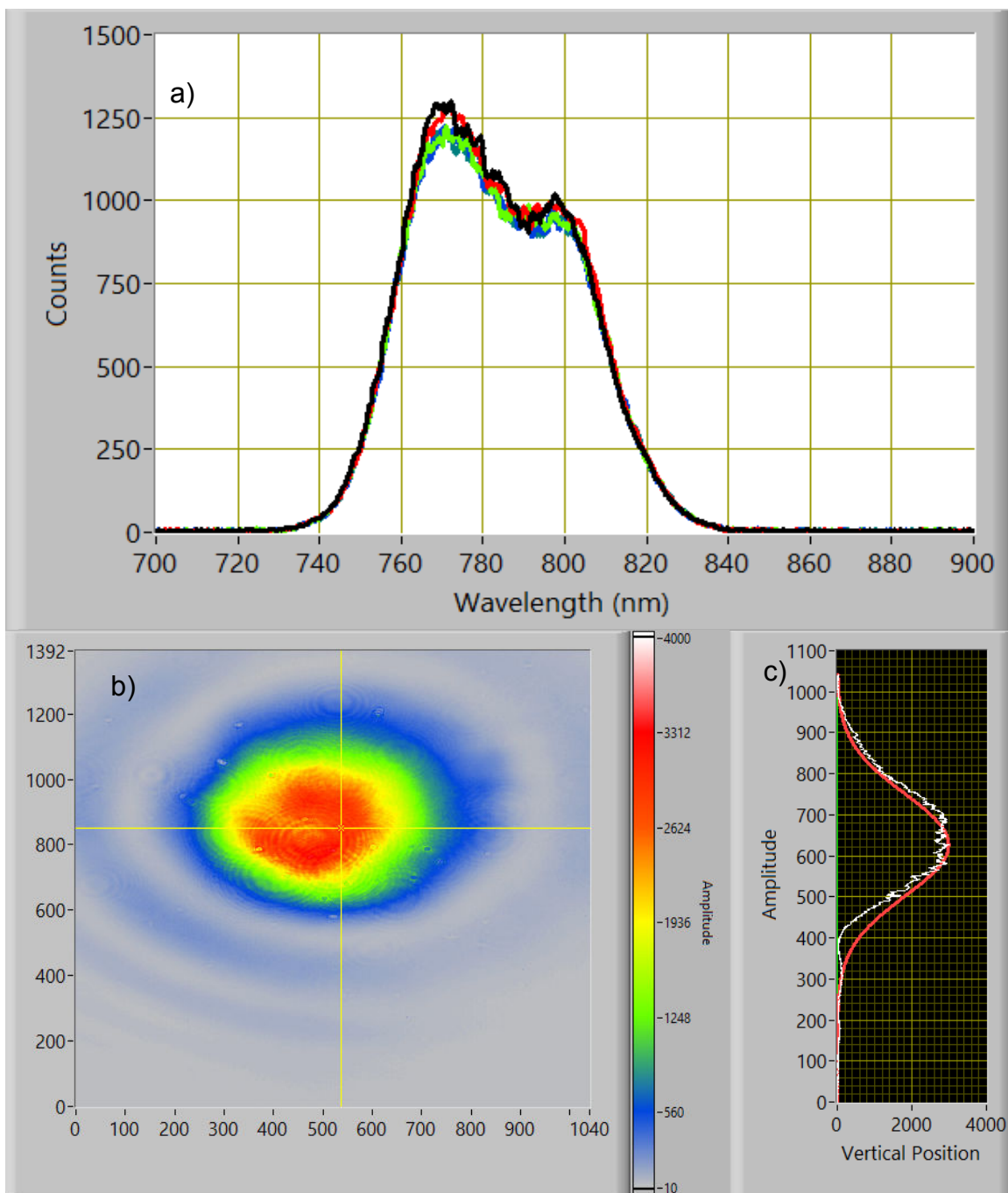
Figure A.3: Spectrum and mode out of the prism compressor. a) Spectra after the compressor has a FWHM of 60 nm, b) the mode is typically round, though there are sometimes fine-features such as the "hole" near its center, c) the mode's lineout is more-or-less Gaussian.

These pulses are sent into a glass stretcher prior to further amplification, which stretches pulse durations to ~ps duration. The mode-locked laser's transverse mode and its spectrum before and after stretching are shown in Fig. A.2. The stretched pulses are then amplified in a 9-pass Ti:Sapph amplifier which is pumped at 527 nm by a Thales Jade laser (frequency-double Nd:YLF). The typical pump power here is 7.5 W average power, delivered at a kHz repetition rate to the Ti:Sapph crystal.

After the first four passes in this 9-pass amplifier, the Ti:Sapph laser is sent through a Pockels cell which reduces the repetition rate to 1 kHz. This signal makes 5 further passes and is nominally amplified to 1 W average power. In actual practice, the typical yield from this system is ~300-450 mW average power, a point which is discussed further in Appendix D. These pulses are then compressed to ~25 fs using a prism-compressor, whose output efficiency is ~66%: the output is reduced from 300-450 mW to 200-300 mW average power. This corresponds to an individual pulse energy of 200-300 μJ. The bandwidth at this point is ~60 nm FWHM. The transverse mode and laser spectra after this compressor are shown in Fig. A.3.

This oscillator-stretcher-amplifier-compressor system generates a number of back-reflections which when compressed can become pre- and post- pulses. In order to clean up the contrast ratio, the pulses are passed through an XPW[210].

267
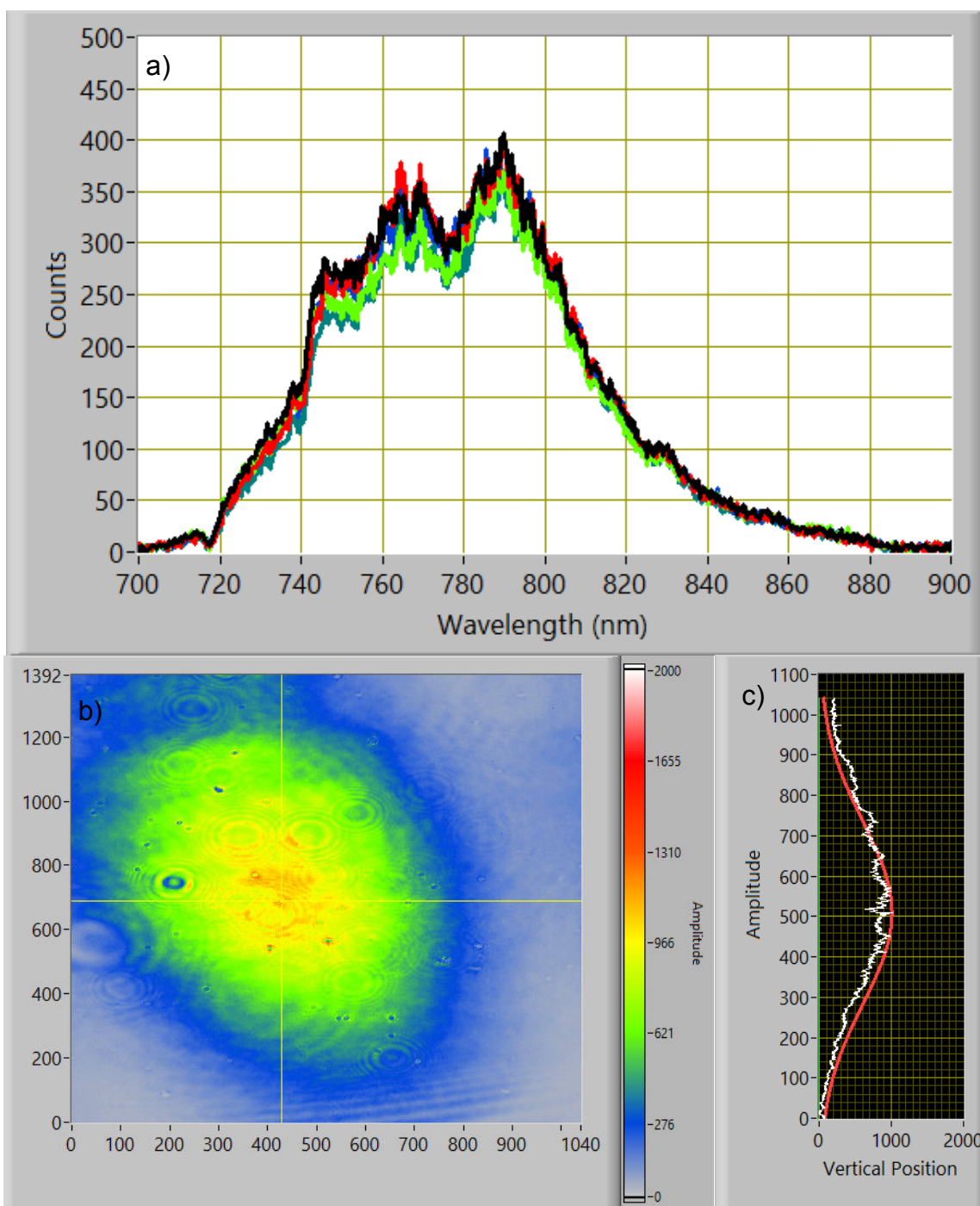
Figure A.4: Spectrum and mode out of the XPW pulse cleaner. a) Spectra after the XPW still has a FWHM of 60-70 nm, and may be broadened slightly by self-phase modulation in the BaF crystals. b) The central mode is typically round and even can be cleaned up somewhat after passing through the pair of BaF crystals and crossed polarizers, which collectively can act as a spatial filter. c) The mode's lineout is more-or-less Gaussian.

The XPW consists of two BaF crystals placed between two crossed polarizers. The laser polarization is linearized by the first polarizers (e.g. It now has p-polarization), and then the laser is focused through the pair of crystals. A third-order nonlinear effect of the crystals is that they rotate the polarization of the laser; and then the laser proceeds through a second polarizer (which transmits s-polarization but reflects p-polarization). Therefore, only the rotated portion of the polarization will pass through the XPW system. This polarization rotation effect is proportional to I^3, so the contrast ratio of the output is improved by the cube of the initial contrast ratio, e.g. an improvement from 10^3 to 10^9.
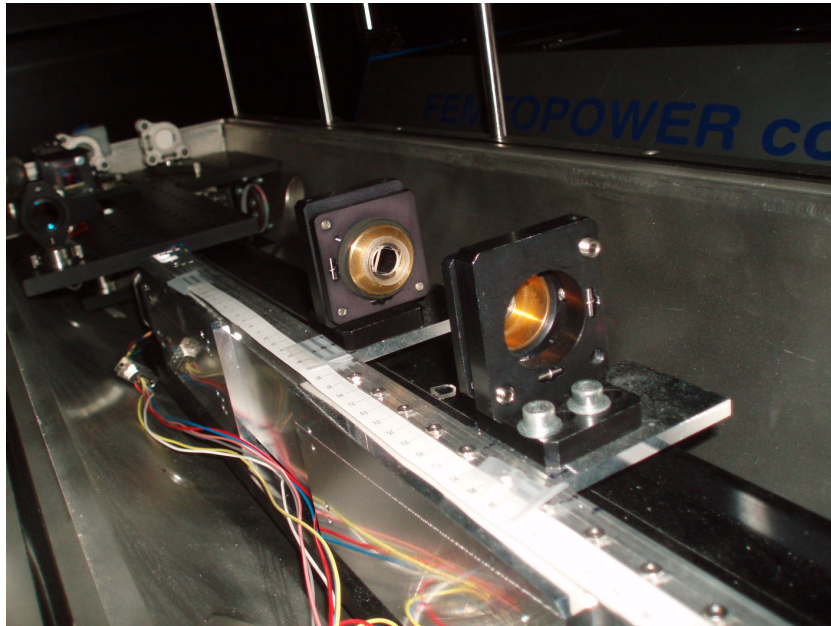
Figure A.5: The XPW nonlinear crystals. The crystals are barium fluoride; in the background is the second polarizing beam splitter, which is crossed with respect to the first polarizing beam splitter.

In the original design plan, this XPW was housed in a vacuum chamber and required ~600 mW input from the prism compressor to generate ~15 mW of cleaned up pulses at the output. However, a re-sizing telescope consisting of a negative and then a positive lens, the latter on an adjustable translation stage, was inserted prior to the XPW along with a polarization-rotating half-wave plate. The result of this is that the XPW's output remains stable at ~10-15 mW, but the input may be reduced to ~200 mW. The current system operates in air at ~STP.

After these pulses are cleaned up by the XPW, they are stretched in duration to 500 ps by a grating stretcher. They are then amplified in a Booster amplifier consisting of two passes (retroreflected) through a Ti:Sapph crystal which is pumped by an identical source to the 9-pass amplifier pump; the pumping power here is 10.0 W, and the output power is 100-200 mW (average) at kHz. A second Pockels cell placed after the Booster amplifier limits repetition rate to 10 Hz. The typical bandwidth here is ~45-50 nm FWHM centered at 800 nm, with 100-150 μJ energy per pulse, as shown in Fig. A.6.

This signal is then sent to the pre-amplifier stage, a 5-pass Ti:Sapphire amplifier in a bowtie configuration. The crystal is pumped by 300 mJ of frequency-doubled Nd:YAG pulses of 9 ns duration and 10 Hz repetition rates. The Ti:Sapph laser is amplified in this configuration to ~40 mJ and then expanded and sent to the Power Amplifier.
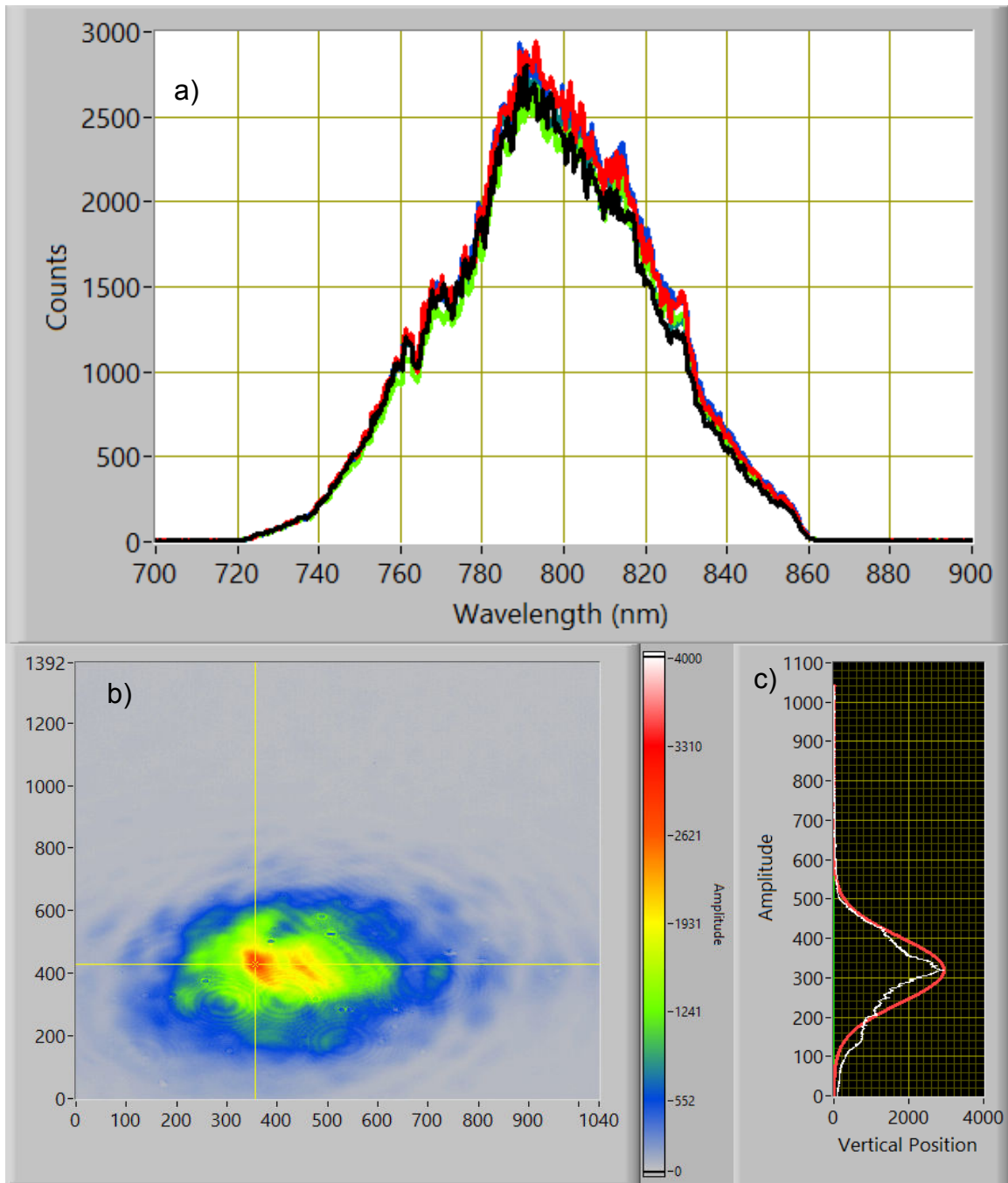
Figure A.6: Spectrum and mode out of the Booster amplifier. a) Spectra after the Booster amplifier should be at least 35 nm FWHM and ma be as great as 55-60 nm FWHM. Typically if it is not this broad, the prism compressor separation should be adjusted to broaden the spectrum. b) The mode should and c) the mode's lineout should ideally be Gaussian, it often isn't. Nevertheless, this mode was amplified to ~45 mJ after the pre-amplifier and had a nearly Gaussian profile after this additional amplification.
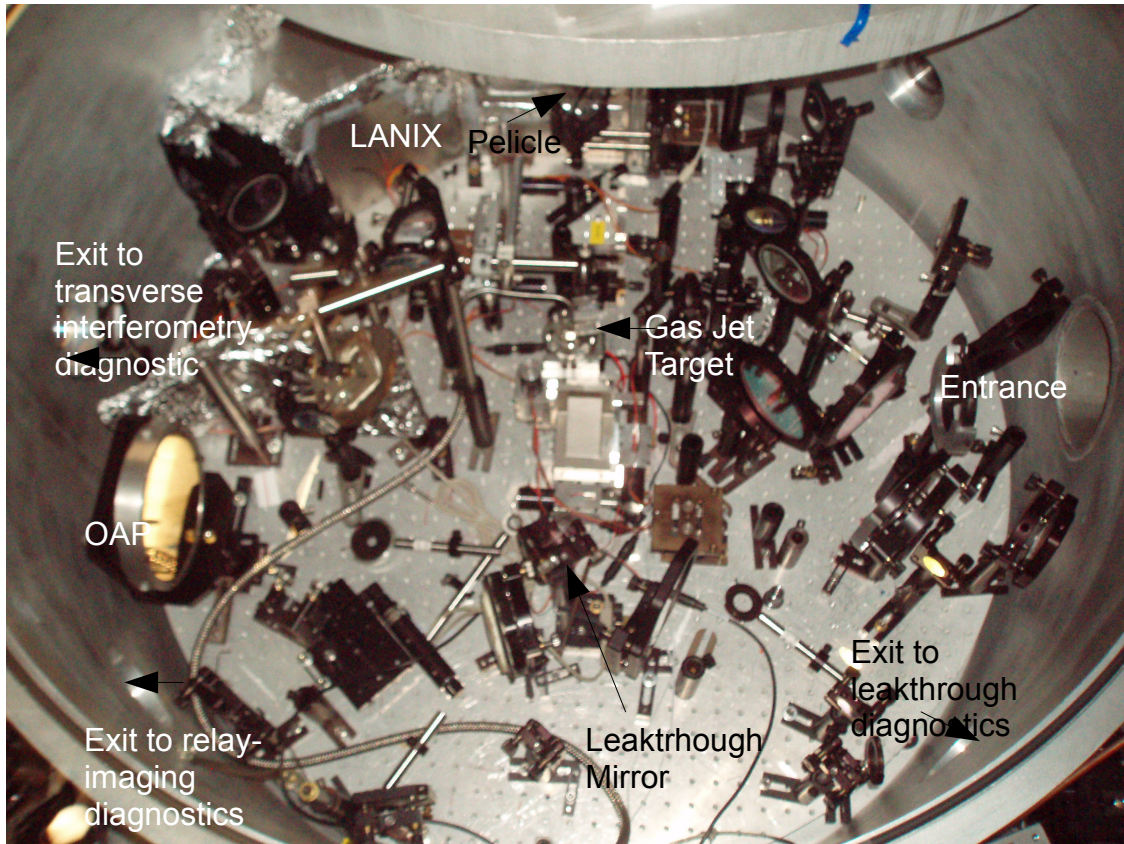
Figure A.7: Picture of the LWFA target chamber with points of interest labeled.

The Power Amplifier is a three-pass bowtie Ti:Sapph crystal pumped by 3.5 J of frequency-doubled Nd:YAG pulses of 9 ns duration and 10 Hz repetition rates. The pulse in nominally amplified to ~1.8 J here, but the mode has since been re-sized to prevent damage to the Ti:Sapph crystals. As a result, the pulse is typically amplified here to 1 J, with a final bandwdith of 35-40 nm FWHM centered at 800 nm. The laser is then split by a 90/10 beam-splitter. The smaller portion (10% of the beam's energy) is further split between a probe line (for transverse interferometry or shadowgraphy, FDH/FDT probing, etc.) and the Raman line. The main beam (90% of the pre-split energy) is passed through an energy tuner consisting of a half-wave plate and a thin-film polarizer, and then sent

through a delay line to synchronize it with the Raman beam when the two are re-combined in the target chamber.

After the delay line, the primary beam is further expanded by a 4-lens telescope (final FWHM diameter is 4 cm in the farfield). It is then compressed to as short as 30 fs[xxii] by a grating-pair compressor (1480 lines/mm), whose efficiency is ~55%. The primary pulse at 800 nm is then re-combined with the Raman pulse via a 800/873 dichroice mirror which reflects at 800 nm but transmits at 873 nm. Both the Raman and the priary beam suffer ~5% energy loss on this dichroic mirror.

The two-color pulse is then focused using a 60 cm focal-length 15º off-axis parabola mirror (OAP). This mirror typically produces an f/12.5 focus, with measured focal spot sizes as small as 11 μm by 13 μm (the beam is slightly astygmatic) at focus. The measured farfield parameters of the laser are thus 450 mJ at 30 fs (30 TW peak) centered at 800 nm and 52.5 mJ at 180 fs (0.58 TW peak) centered at 873 nm.

The target for both beams is a gas jet[211] of dimension 3 mm by 1 mm which is rotatable (i.e. the lasers experience either a 3 mm gas jet or a 1 mm gas jet).

There are several diagnostics which can be used either in-situ or prior to/after any experiment in the wakefield chamber. The in-situ target chamber diagnostics include a probe line which can be changed (prior to the experiment but not in *situ*) to either transverse or longitudinal/small angle probing; a relay-imaging system for both the beam

---

xxii However, the actual duration is sometimes longer than this in experiments. For example, the RSF-suppression experiment recommends a pulse duration of ~200 fs.
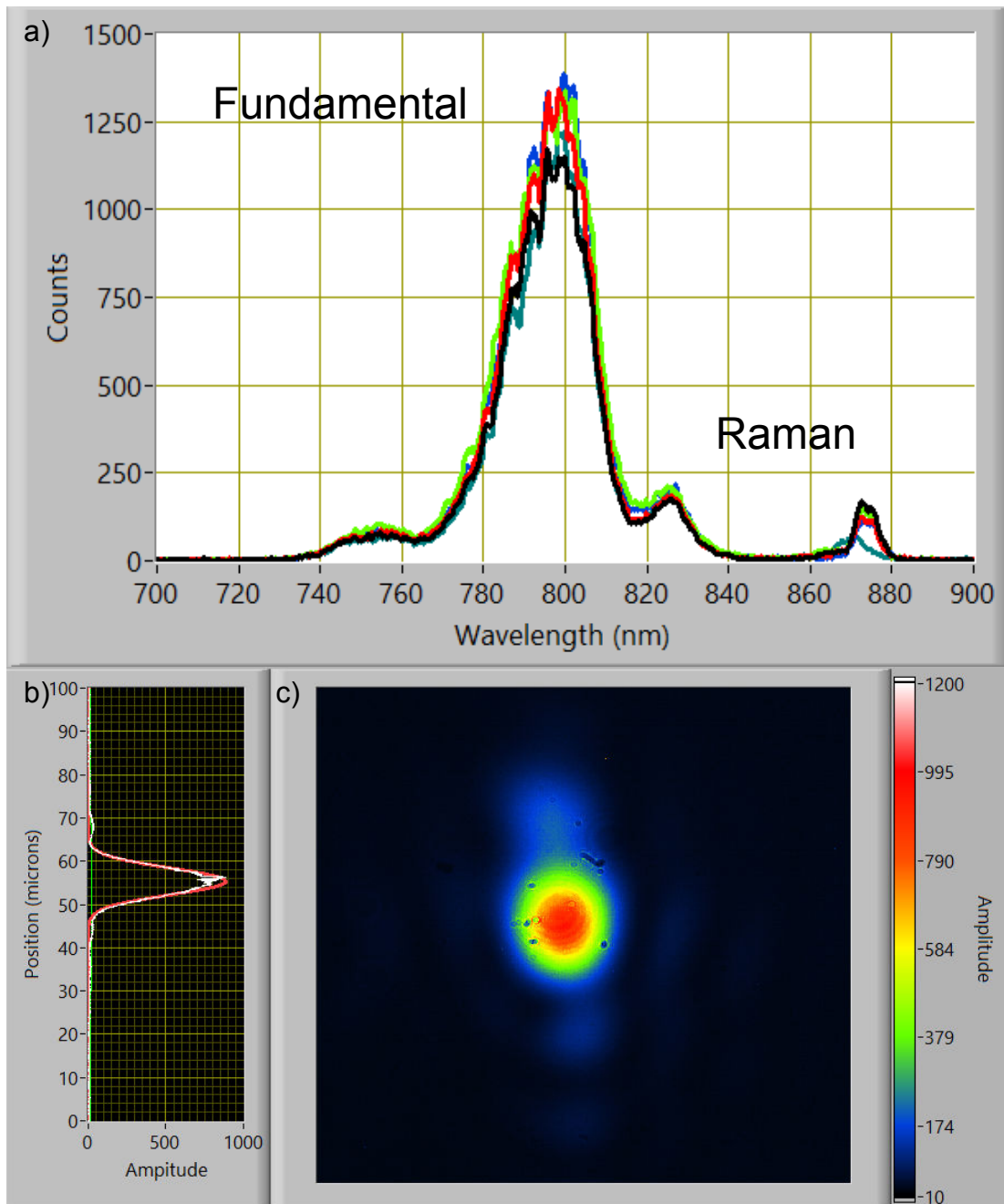
Figure A.8: Spectrum of the two-color laser under vacuum and Primary laser mode at focus. a) The spectrum under vacuum showing the Primary ("Fundamental") spectrum and the Raman 1-Stokes sideband. The Primary laser's spectrum has been narrowed somewhat here, an indication of less-than ideal compression. b) The mode lineout and c) the transverse mode of the Primary laser after being focused by the OAP, which has been optimized. The FWHM is ~10 μm.

274

at both input and output of the target gas jet; a fiber spectrometer at each of the exit and the entrance (via leakthrough) of the gas jet.

Additionally, there is a background free single shot autocorrelator set up in the turning box just prior to the wakefield target chamber, which can be accessed by translating a motorized mirror to alter the laser's path from the wakefield chamber to the autocorrelator. This is not an *in-situ* diagnostic (because it completely re-routes the beam), but it can be used while the chamber is under vacuum and so is worth mentioning because the process of pumping the compressor and target chamber down requires about 3 hours' time.
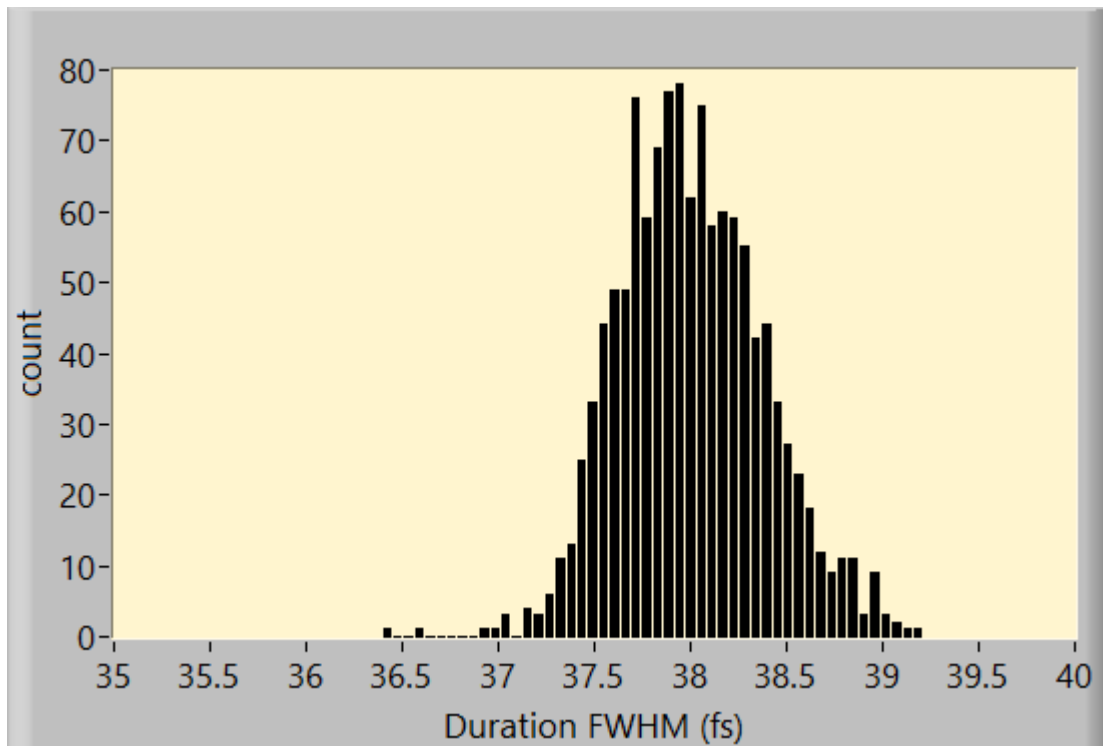
Figure A.9: Histogram of autocorrelation measurements for the primary pulse after final amplification and compression. This is not an optimized compression, but it corresponds to the spectrum shown in Fig. A.8a.

275

A histogram of 1000 shots of autocorrelation measurements for the Primary beam after final amplification and compression is shown in Fig. A.9. The durations in this histogram correspond to the spectrum shown in Fig. A.8a, meaning a non-optimized compression. Nominally the pulses can be compressed to as short as 25 fs, however a typical optimization yield pulses of 30-35 fs. These pulses have been compressed to 38 fs with a FWHM spread of 1 fs, the duration is stable shot-to-shot.

Appendix References

[210] N. Minkovski, S. M. Saltiel, G. I. Petrov, O. Albert and J. Etchepare, "Polarization rotation induced by cascaded third-order processes," *Opt. Lett.* Vol. **27**, No. 2, pp. 2025-2027 (2002).

[211] T. Hosokai, K Kinoshita, T. Wanatabe, K. Yoshii, T. Ueda, A. Zhidokov, M. Uesaka, K. Nakajima, M. Kando, H. Kotaki, "Supersonic gas jet target for generation of relativistic electrons with 12TW-50fs laser pulse," *Proceedings of EPAC*, Paris, France, pp. 981-983 (2002).

Appendix B

Comparison of Results of Collinear and Non-Collinear Second Stage Geometries

In this appendix, I compare and contrast the results of mode, energy, spectrum, and compression between collinear and non-collinear geometry. I also discuss why I ultimately went with the non-collinear geometry between pump and seed in the second stage.

There is no difference between the two geometries in the first stage (that is, the seed line). The difference in geometry occurs in the second stage, in which the 873 nm Raman seed and the 800 nm laser pump are either collinear inside the Raman-amplifier crystal, or non-collinear at a small angle which satisfies the phase-matching conditions discussed in Chapter 4 (see Sec. 4.5).

The schematic difference between the collinear and non-collinear geometries is shown in Fig. B.1. The biggest difference is implied in the name, that is, there is a zero degree angle between pump and probe in collinear geometry but a small angle otherwise. As a result, there is no control of the phase-matching conditions for four-wave mixing processes (see Chapter 3, Sec. 3.1.1) in the collinear geometry. On the other hand, there are two amplifier crystals used in the collinear geometry as opposed to only one in the non-collinear geometry. The second crystal is not possible in non-collinear geometry,

278

though the two beams can be retroreflected for a second pass in the one amplifier first

crystal, provided that care is taken to prevent the retroreflected beams from propagating

back through the laser system and thus causing damage to the front end.
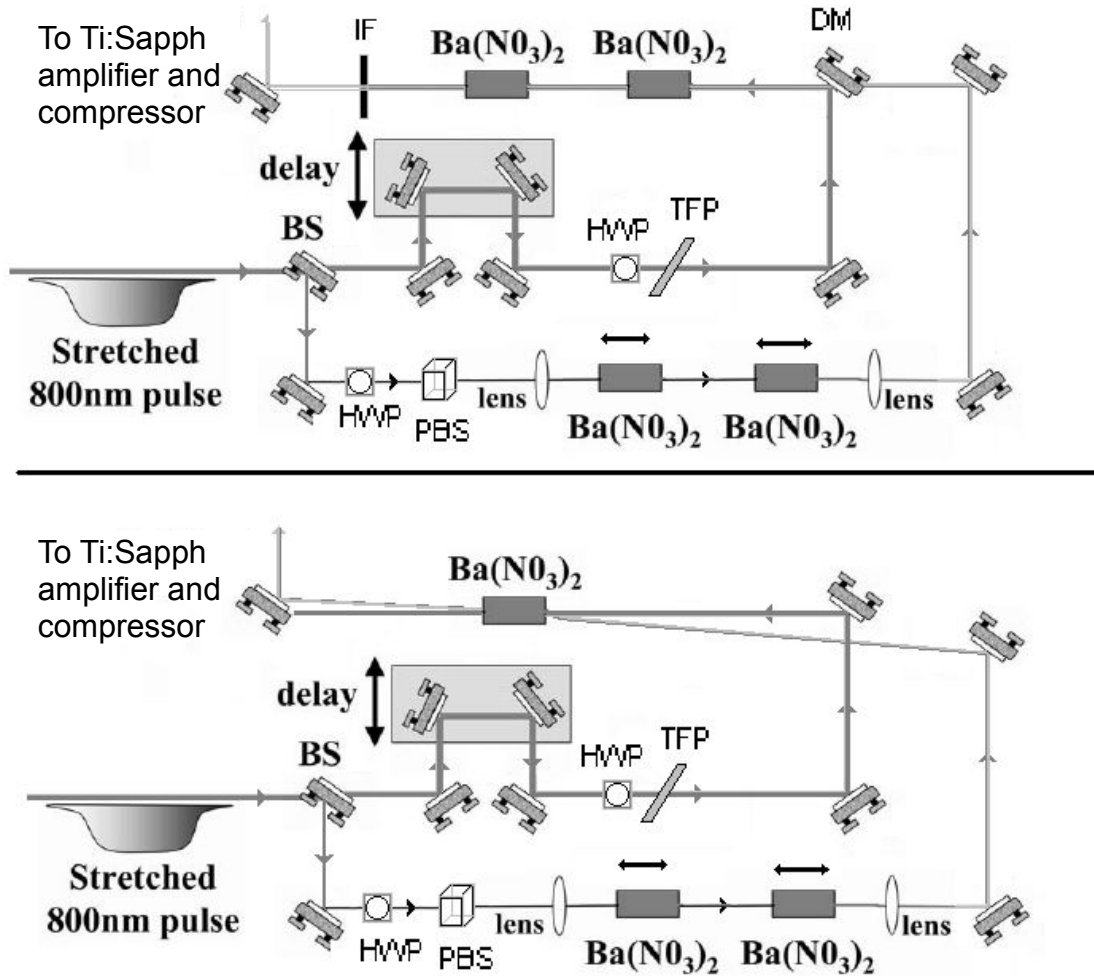
Figure B.1: Details of the Raman shifter and SRS amplifier, in (top) collinear and (bottom) non-collinear configurations. The second barium nitrate crystal is removed from the SRS amplifier arm in non-collinear operation. BS = beam splitter, DM = dichroice mirror, HWP = half wave plate, TFP = thin film polarizer, PBS = polarizing beam splitter, IF = interference filter

279
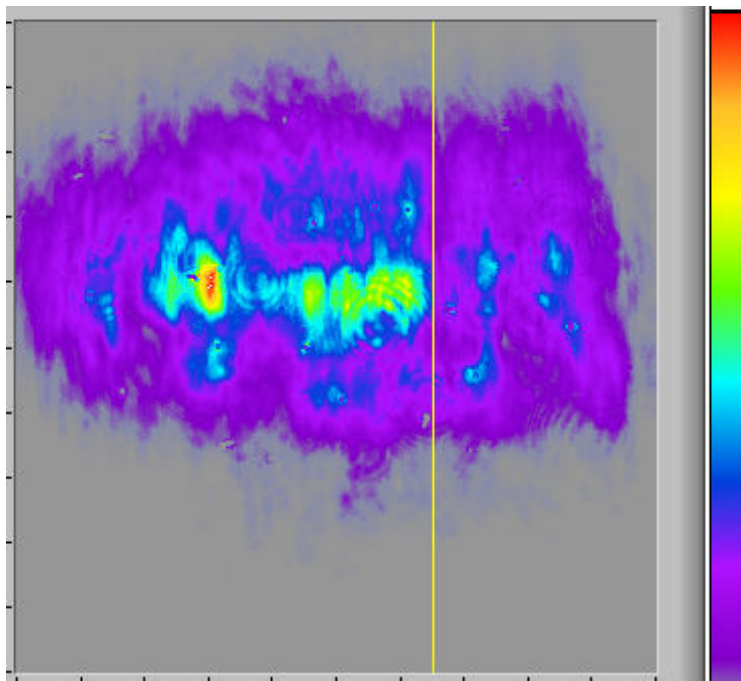
Figure B.2: A mode in the second stage generated by collinear geometry. The color scale represents intensity: there are a series of hot spots spread across the mode, which would risk damaging optics (including the Ti:Sapph crystal) when amplified in the third stage.

Additionally, an interference filter becomes a necessity in the collinear geometry, because there is not separation between the (Raman-amplified) first Stokes pulse and the fundamental pump pulse. Without the interference filter, the fundamental light would propagate along with the Raman light into the Ti:Sapph amplifier, and would then be preferentially amplified instead of the Raman light.

Up to 2.5-3.0 mJ of 1 Stokes light has been observed out of the second stage in the collinear geometry (using two amplifier crystals), which is comparable to the highest observed in the non-collinear geometry (single pass).

However, in the collinear geometry, the mode structure out of the second stage crystal tended to be much worse than in the non-collinear geometry at a comparable energy. This is because in collinear geometry, there is no mode clean-up in the second stage, because there is no phase averaging between the pump and the seed as in non-collinear geometry. Therefore, the output of the second stage crystal may have equal energy and spectrum to that of the non-collinear geometry, but it does so at the expense of having a messier mode with numerous hot-spots, as shown in Fig. B.2.

These hot spots would likely case damage to the optics in the third stage Ti:Sapph amplifier, including the crystal itself, if amplified and not cleaned up. An iris can be used to improve the beams mode-quality producing a clean diffraction pattern, which is safer to amplify. However, this is done at the expense of throwing away >90% of the mode's energy. When this is done, the resulting output energy of the Ti:Sapph amplifier drops to a maximum average of 100 mJ, with a good, nearly Gaussian output mode.

The hot spots discussed in Chapter 4 (Sec. 4.6) were never really an issue for the collinear geometry, largely because of the irising for mode cleanup. In fact, when the non-collinear beam is irised at input to the Ti:Saph amplifier, the hotspots go away there, too, and the resulting output beam energy is ~130 mJ typically. Without irising the non-collinear beam to such an extreme, and energy of 160 mJ (average) has been safely obtained.

In many experiments the higher energy is more important than the shortest pulse duration for the Raman pulse. Since the non-collinear beam is compressible to ~100 fs—

well within the experimentally desirable duration—and since it yields approximately 50% more energy after final amplification, the non-collinear geometry is the better choice.
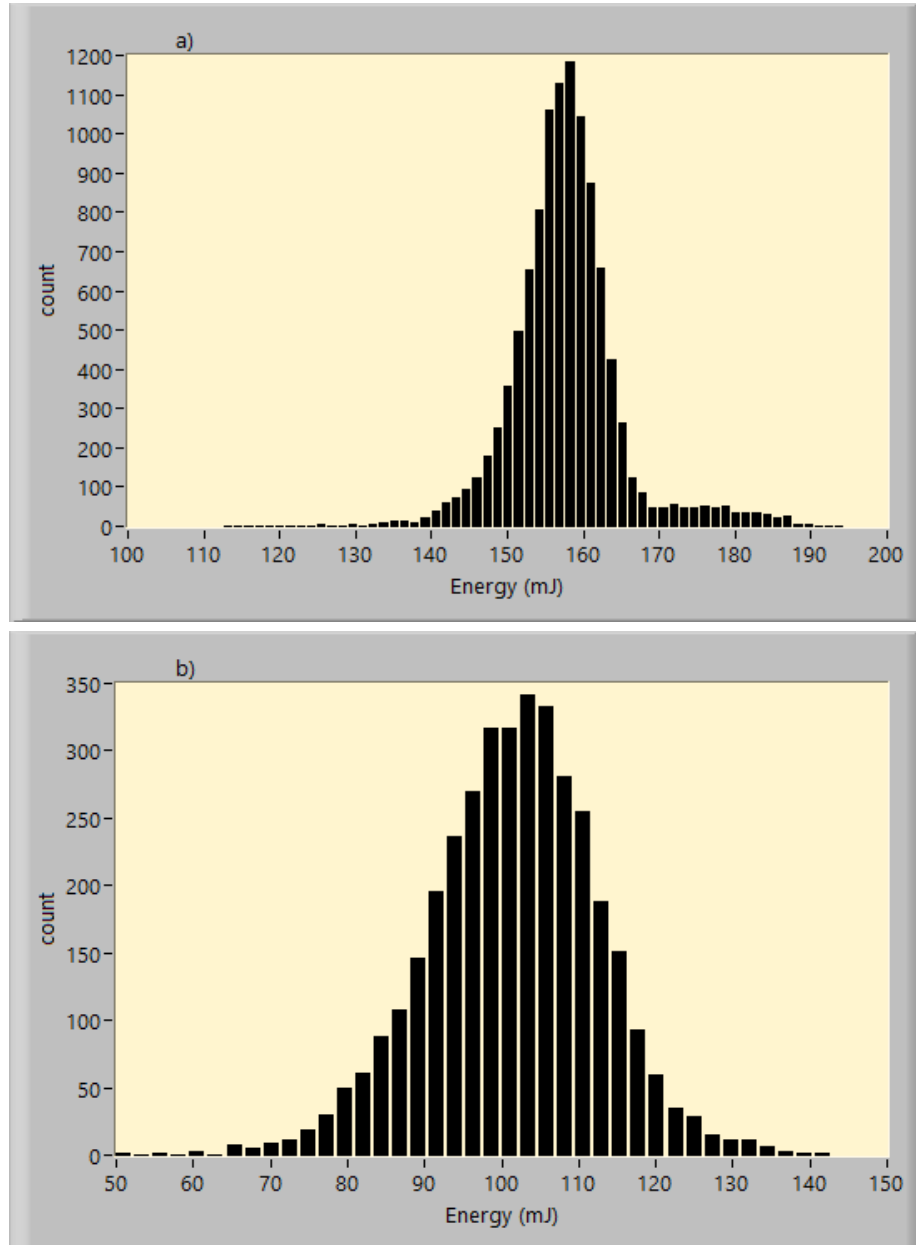
Figure B.3: Energy histograms after Ti:Sapph Final Amplifier for both second stage geometries. a) The collinear geometry averages approximately 100 per shot as compared to b) the non-collinear geometry's 155 mJ per shot average. Both histograms are taken after the final amplifier.

It should be noted in closing that although the non-collinear geometry ultimately outperforms the collinear geometry, the fact that the collinear geometry was amplified and compressed at all is a bit of an achievement. In previous work[212] with a two-stage CPRA system, collinear geometry was observed to produce a Raman cascade at relatively low 1 Stokes energy.

The four-wave mixing process itself becomes significant—and results in the depletion of the 1 Stokes into other Stokes' modes—when the intensity of the 1 Stokes wave becomes comparable to that of the fundamental wave. Since the peak of the 1 Stokes wave is preferentially amplified (prior to depletion), the two beams can have comparable peak intensities when the 1 Stokes Raman pulse energy is still much smaller than the fundamental pulse's energy. The end result is that the central peak of the Raman wave begins to deplete as a pump for the cascading process more rapidly than it is amplified by the fundamental pump, and that moreover it will eventually began to deplete this fundamental pump more rapidly in the "peak" position than elsewhere. The result is a Raman cascade with concentric rings of higher order Stokes and anti-Stokes modes, and a 1 Stokes mode which has a donut-shaped transverse mode.

This donut-mode might be contrasted with the mode in Fig. B.2, which contains ~2.5 mJ of 1 Stokes energy, and which has filamented though not formed a donut. It is possible that the collinear Raman mode might be improved by spatially filtering both the fundamental (pump) mode and the 1 Stokes (seed) mode between the two amplifier crystals.

283

Appendix References

[212] F.B. Grigsby, "Chirped Pulse Raman Amplifier," Doctoral Dissertation, University of Texas at Austin (2009).

Appendix C

The Raman System Compressor: Theory and Alignment

In this appendix, I shall discuss the theory and alignment of the Raman system's compressor. The compressor itself consists of a pair of parallel gratings using 1280 lines/mm groove density, which have a separation of 61.6 cm and a diffraction angle of 37.9°, as shown in figure C.1 below.

C.1 THEORY OF GRATING COMPRESSOR (AND STRETCHER)

The theory of pulse compression via grating pair is first discussed by Treacy[213] and is further discussed by Siders[214]. Compression of a laser pulse is achieved by making the phase of each frequency mode within the pulse zero with with respect to every other frequency mode: the different frequency components then add constructively for a very narrow range of times, and destructively elsewhere, producing a single pulse of short duration, as illustrated in Fig. C.2.

Pulse compression consists essentially in causing all of the frequency modes (Fig. C.2a) to be in phase with each other, so that they interfere constructively for a short duration and destructively elsewhere, as illustrated by Fig. C.2b. Therefore, the duration of the pulse is limited by the frequency bandwidth and by the pulse shape, e.g.

$\Delta t \Delta \omega \approx 0.44$ for a Gaussian pulse or $\Delta t \Delta \omega \approx 0.315$ for a sech^2 pulse. This means

that the desired effect is that $\phi(\omega_1) = \phi(\omega_2)$ for all frequency modes ω_1 and ω_2 in the pulse.
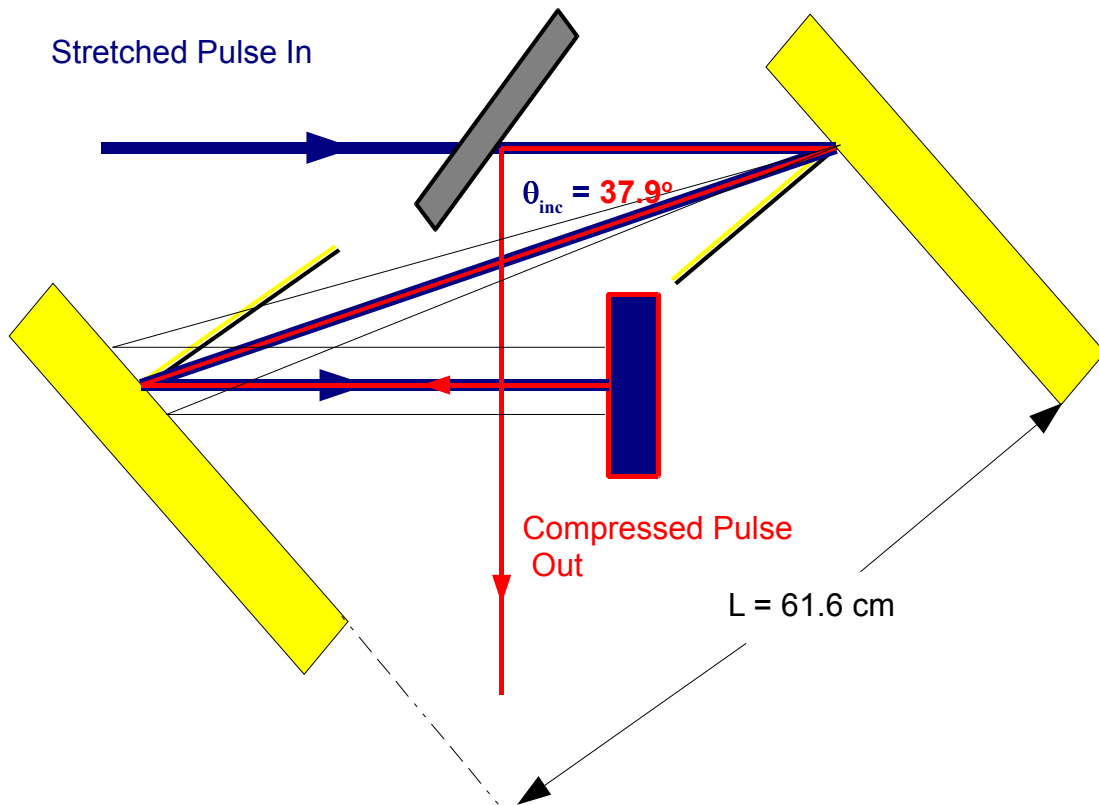
Figure C.1: A simple diagram of the Raman grating compressor. The yellow blocks are the gratings themselves, the blue lines represent the incident beam until it reaches the rooftop mirror (blue and red rectangle), the red line the the beam after reflection from the rooftop mirror, and the black and gray rectangle is the mirror (positioned above the incident stretched pulse but in the path of the exiting compressed pulse). The gratings have a perpendicular separation of L = 61.6 cm, with the angle of incidence is θ_{inc} 37.9°. The yellow-black lines are perpendicular to the gratings, and the thin black lines are to show that the beam does not diffract from each grating as a singe ray but rather that it disperses spatially between the two gratings. The diagram is not drawn to scale.
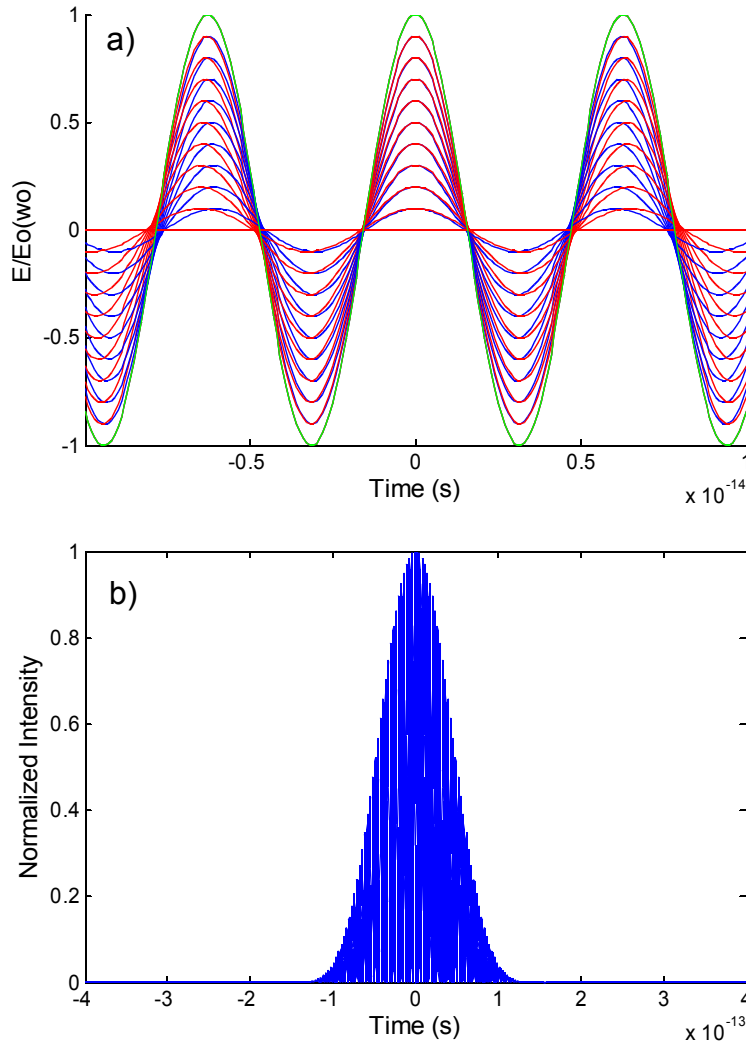
Figure C.2: Normalized intensity of a compressed pulse. This pulse is created by adding together 2001 spectral components, with a central frequency $\omega_0 = 1\times10^{15}$ s^{-1} and a bandwidth of $\Delta\omega = 4\times10^{13}$ s^{-1} FWHM ($\omega/\Delta\omega = 4\%$). Each spectral component is shifted by $\delta\omega = 0.004\%$ ω_0, and the amplitude decreases by 0.1% of E_0 for each frequency shift. a) Every hundredth pulse is plotted, with the red pulses being the lower frequency components, the blue pulses being the higher frequency components, and the green pulse being the component at ω_0. These pulses have been normalized the E-field amplitude of the central frequency. b) The FWHM duration in this case is ~100 fs.

287

Pulse compression involves setting the spectral phase equal to zero (meaning, all spectral modes have identical phase). The spectral phase of the pulse can be Taylor expanded about the central frequency:

$$\phi(\omega-\omega_0)=\phi_0+\phi_1(\omega-\omega_0)+\frac{\phi_2}{2!}(\omega-\omega_0)^2+\frac{\phi_3}{3!}(\omega-\omega_0)^3+... \tag{C.1.1}$$

The coefficient of the linear term in this expansion, ϕ_1 gives the group delay, which pertains to the arrival time of each spectral mode. The coefficient of the quadratic term, $\phi_2/2!$, gives the group delay dispersion (GDD), which is typically positive for materials in the normal dispersion regime[xxiii]. The next coefficient, $\phi_3/3!$, is the third order delay (TOD), which in addition to stretching a pulse adds a ringing effect to the pulse compression[215]. A grating compressor can be made to compensate for these three terms by controlling the spacing of the gratings, their diffraction angle, and their groove spacing.

The Raman compressor—and for that matter, the main beam compressor—consists of a pair of diffraction gratings placed parallel to each other. The pulse diffracts from the first, then from the second, is raised by a rooftop mirror pair, and then diffracts back through both gratings, after which it is picked off by a mirror placed at the height of the pulse form the second pass, and sent to the target chamber. The angle of diffraction θ_{dif} (between the incident beam and the diffracted beam) is determined by the grating equation

---

xxiii Plasmas are anomalously dispersive, and so are an exception to this rule.

$$\sin(\theta_{inc} - \theta_{dif}) = \frac{\lambda}{d} - \sin(\theta_{inc})$$

(C.1.2)

Where d is the grating's groove spacing, θ_{inc} is the angle of incidence of the pulse on the grating, and λ is the optical wavelength. The group delay between a given wavelength and the center wavelength is determined by the difference in optical path length traveled. It is given by

$$T_g = \frac{l(\lambda)}{c}(1 + \cos\theta_{dif}) = \frac{L/c}{\sqrt{1 - (\lambda/d - \sin\theta_{inc})^2}}(1 + \cos\theta_{dif})$$

(C.1.3)

where $l(\lambda)$ is the slant distance traveled by the pulse's center wavelength,

$$l(\lambda) = \frac{L}{\cos(\theta_{inc} - \theta_{dif})} = \frac{L}{\sqrt{1 - \sin^2(\theta_{inc} - \theta_{dif})}}$$

(C.1.4)

Therefore, by differentiating Eqn. (C.1.4) and its derivatives, we can obtain the different ϕ_n. It is convenient to first define $x \equiv \lambda/d$ and $y \equiv \sin\theta_{inc}$, and then to find the second and third order-terms, since the subsequent derivatives can be defined in terms of these:

$$\phi_1 = \frac{L}{c} \frac{1 + \cos(\theta_{inc} - \sin^{-1}(x - y))}{\sqrt{1 - (x - y)^2}}$$

(C.1.5a)

$$\phi_2 = \frac{-L d x^3}{\pi c^2}\left(1 - (x - y)^2\right)^{-3/2}$$

(C.1.5b)

Note that Eqns. (C.1.4) and (C.1.5a) are equivalent via Eqn. (C.1.2), and that that the derivative taken is

$$\frac{\partial}{\partial\omega} = \frac{\lambda_0}{c_0}\frac{\partial}{\partial\lambda}$$

(C.1.6)

where λ_0 is the wavelength corresponding to ω_0, that is, the central wavelength (or frequency) of the Taylor expansion in Eqn. (C.1.1). The next three terms—third-, fourth-, and fifth-order terms—are given by

$$\frac{\phi_3}{\phi_2} = \frac{-3dx}{2\pi c} \frac{1+y(x-y)}{1-(x-y)^2} \equiv \zeta \tag{C.1.7a}$$

$$\frac{\phi_4}{\phi_2} = \left(\frac{\phi_3}{\phi_2}\right)^2 + \frac{3d^2x^2}{4\pi^2c^2} \frac{x^2+(1+y(x-y))^2}{(1-(x-y)^2)^2} \equiv \zeta^2 + \zeta' \tag{C.1.7b}$$

$$\frac{\phi_5}{\phi_2} = \zeta^3 + 4\zeta\zeta' - \frac{3d^3x^3}{4\pi^3c^3} \frac{(1+y(x-y))(3x^2+(1+y(x-y))^2)}{(1-(x-y)^2)^3} \equiv \zeta^3 + 4\zeta\zeta' + \zeta'' \tag{C.1.7c}$$

The angle of incidence (θ_{inc}) and the grating separation (L) can then be solved for using the second- and third-order terms, e.g. by setting the ratio in Eqn. (C.1.7a) to some constant by proper choice of incident angle, then solving for the grating separation to provided the desired ϕ_2.

This determines the phase for which the compressor gratings compensate to third-order. To compress pulses, this must be equal to the phase added by the pulse stretcher plus any phase from material dispersion (and the fourth-order and higher terms must be relatively small). In practice, the effective stretcher and initial material dispersion was determined by reverse-engineering the Thales' main compressor: 1480 lines/mm with a separation of 46.2 cm and an incident angle of 46.3°, nominally. This compensates for the stretcher between the XPW and Booster Amplifier plus the material dispersion for amplification in the Booster Amplifier, the Pre-Amplifier, and the Power Amplifier (see Appendix A for a description of the primary laser system). However, material dispersion

from the Raman system itself must be taken into account. This consists of several lenses, three 5-cm-long barium nitrate crystals, 6 passes in the Ti:Sapph crystal, a window to the compressor chamber, and approximately 20 meters' worth of air. The phase added from each of these elements can be determined from the Sellmeier equations[216] for that material, each of which has the form

$$\eta^2(\lambda) = 1 + \sum \frac{B_i \lambda^2}{\lambda^2 - C_i} \approx 1 + \frac{B_1 \lambda^2}{\lambda^2 - C_1} + \frac{B_2 \lambda^2}{\lambda^2 - C_2} + \frac{B_3 \lambda^2}{\lambda^2 - C_3} \qquad \text{(C.1.8)}$$

The rightmost hand side is the typical form in which this equation is specified, with the middle form being a more general equation. The B and C coefficients are typically specified for the wavelength λ in microns; for example, for fused silica, a common optical material and the material of which most of the lenses and windows in the Raman system are composed, the coefficients are[217] $B_1 = 0.6961663$, $B_2 = 0.4079426$, $B_3 = 0.8974794$, $C_1 = 4.6791826 \times 10^{-3}$ μm^2, $C_2 = 1.35120631 \times 10^{-2}$ μm^2, and $C_3 = 97.9340025$ μm^2; for barium nitrate, the Sellmeier equation is[218],[219] given by

$$\eta^2(\lambda) \approx 2.4069 + \frac{0.01992}{\lambda^2 - 0.03773 \, \mu m^2} - 0.006166 \lambda^2 \mu m^{-2} \qquad \text{(C.1.9)}$$

The phase orders in Eqn. (C.1.1) can then be found by differentiating the Sellmeier equations:

$$\phi_1 = \frac{\eta(\lambda_0)}{c} z - \frac{\lambda_0}{c} \frac{\partial \eta}{\partial \lambda} z \qquad \text{(C.1.10a)}$$

$$\phi_2 = \frac{\lambda_0^3}{4 \pi c^2} \frac{\partial^2 \eta}{\partial \lambda^2} z \qquad \text{(C.1.10b)}$$

291

$$\phi_3 = \frac{\lambda_0^4}{8\pi^2 c^3}\left(\frac{\partial^2 \eta}{\partial \lambda^2} + \frac{\lambda_0}{3}\frac{\partial^3 \eta}{\partial \lambda^3}\right) z \qquad\qquad\qquad (C.1.10c)$$

where all the derivatives are evaluated at λ_0.

C.2 ALIGNMENT OF THE RAMAN COMPRESSOR

What follows is a description of the alignment procedure used to set-up the Raman system compressor. A basic diagram of the compressor is shown in Fig C.1. The compressor itself consists of a pair of 1200 lines/mm diffraction gratings which are oriented parallel to each other, plus a rooftop-retroreflector; additionally, a pair of irises is placed at the entrance to the compressor for repeatable alignment.

In practice, it is normally sufficient to align the laser through the two irises at the input to the system. However, on occasion the gratings get bumped by other users, and over time the gratings do have to be realigned; furthermore, the correct settings of the grating compressor can change, in particular if a different Raman mode is to be compressed (e.g. 2 Stokes at 938 nm instead of 1 Stokes at 873 nm). The alignment procedure is therefore:

1. Rotate CG1 so that it retroreflects the 0th order (reflected) beam.

2. Now rotate from this position so that the specular reflection of CG1 is in the m = 1 diffraction direction in order to align CG2.

3. Rotate CG2 so that it retroreflects the specular reflection from CG1.

4. Now rotate CG2 from that position so that its specular reflection is in the m = 1 diffraction direction in order to align the rooftop retroreflector.

292

5. Retroreflect from the rooftop mirrors.

6. Rotate CG2 to set it for pulse compression.

7. Rotate CG1 for pulse compression.

The settings obtained using this procedure for each grating are presented in Table C.2.1, using light at 873 nm. The direction of the m=1 diffraction order is obtained using

$$\sin\theta_m = \frac{m\lambda}{d} + \sin\theta_{inc} \qquad\qquad\qquad (C.2.1)$$

and the specular reflection angle is found from

$$\theta_{spec} = \frac{1}{2}\left(\theta_{-1} + \theta_{inc}\right) \qquad\qquad\qquad (C.2.2)$$

For the Raman compressor at First Stokes—which has λ = 873 nm, $1/d$ = 1200 lines/mm —the CG1 retroreflection occurs at ϕ_{ret1} = 1º5' (this is the angle on the compressor grating's rotation mount at which retroreflection occurs). The desired incident angle is θ_{inc} = 37.9º ~37º55', which means that the actual angle at which the CG1 mount should be set to obtain the desired incident angle is ϕ_{CG1} = ϕ_{ret} - θ_{inc} = 1º5' + 37º55' = 39º0'. The specular reflection angle obtained from Eqn. (C.2.2) is θ_{SPEC} = ½ (-25.7º + 37.9º) = 6º10', which is applicable to both gratings; the actual angle to which the mount for CG1 must be set is ϕ_{SPEC1} = ϕ_{ret1} + θ_{SPEC} = 1º5' + 6º10' = 7º15'.

Grating	Retroreflection Angle	Specular Reflection Angle	Compression Angle
CG1	1°5'	7°15'	39°
CG2	11°40'	5°30'	37°15'

Table C.2.1: The angular settings for the rotation mounts for the two compressor gratings. The perpendicular separation is 61.67 cm and the angle of incidence is 37.9°.

The settings for the second grating, CG2, can be found similarly. Retroreflection occurs at $\phi_{ret2} = 11°40'$, so $\phi_{SPEC2} = \phi_{ret2} + \theta_{SPEC} = 11°40' - 6°10' = 5°30'$ and $\phi_{CG2} = \phi_{ret} - \theta_{-1} = 11°40' - (-25°35') = 37°25'$. In practice, the actual angle of the second grating's mount is about 10' off, however.

Appendix References

[213] E. B. Treacy, "Optical Pulse Compression With Diffraction Gratings," IEEE Journal of Quantum Electronics, Vol. Qe-5, No. 9, September 1969.

[214] C. W. Siders, "An Experimental Demonstration of the Laser Wakefield 'Photon Accelerator': Longitudinal Interferometric Diagnostics for Plasma Based Accelerators," Doctoral Dissertation, University of Texas at Austin, 1996.

[215] V. Chauhan, "Pulse Dispersion and Compression Control in Ultrafast Optics." Doctoral Dissertation, Georgia Institute of Technology, 2010.

[216] W. Sellmeier, *Ann. Phys. Chem*. Vol. **143**, 271 (1871).

[217] I. H. Malitson, "Interspecimen comparison of the refractive index of fused silica", J. Opt. Soc. Am. 55 (10), 1205 (1965).

[218] P.G. Zverev, T.T. Basiev, V.V. Osiko, A.M. Kulkov, V.N. Voitsekhovskii, and V.E. Yakobson, "Physical, chemical, and optical properties of barium nitrate Raman crystal," *Opt. Mat.* Vol. **11**, No. 4, pp 315-334 (1999).

[219] P.G. Zverev, T.T. Basiev, and A.M. Prokhorov "Stimulated scattering of laser radiation in Raman crystals," *Opt. Mat.* Vol. **11**, No. 4, pp 335-352 (1999).

Appendix D

System Stability

In this appendix, I discuss the overall stability of both the primary and the Raman laser systems. I have already included a few histograms earlier in this work, to give some sense of shot-to-shot stability. Here I consider stability over longer time-spans, hours, days, or even months[xxiv].

D.1   STABILITY OF THE FRONT END AND PRIMARY LASER SYSTEM

The front-end is in theory a turnkey terrawatt system: theoretically, we never need to open the covers to have access to the laser. The covers shipped with bolts to secure everything in place—just turn the key and push a few buttons and the laser system turns on and is ready to go. In practice, the laser system requires maintenance regularly, from basic alignment at startup to more serious maintenance when optics are damaged.

There are a few regular sources of instability in the front end. These are due to a number of effects, some of which can be mitigated somewhat and some of which cannot:

- Stability of the oscillator, which is the very front-end of the system.

- Pointing stability.

- Stability of the Jade laser which pumps the 9-pass and Booster amplifiers.

---

xxiv For what it is worth, our current laser schedule gives me about 9 days of beam time once every month.

- Mode-matching stability between pumps and 800 nm laser.

- Changes to mode and spectrum after especially the XPW.

- Changes to the pump modes/energy in the SAGA and Continuum pump lasers.

I will discuss each of these briefly in turn.

The main oscillator at the front of the system has a number of instabilities, most of which cannot be mitigated. Instability can be caused by vibrations in the room, especially from the machine shop directly above the lab. These actually are for the most part mitigated by the fact that the optics tables are all floated so as to damp out vibrations However, there are also some vibrations in in the chilling water supply, in particular over time. These sometimes occur because the water supply begins to run low, and sometimes are because the load on the whole of the water circuit gets to be too great.

Another significant reason is that over time some algae will begin to grow in the chilling water lines. When this occurs, the lines must be flushed and cleaned, which in turn results in the phase-matching of the Millenium laser being altered. Thus, upon startup the crystal must be re-adjusted before the oscillator can be made to work. Therefore, the chiller to the oscillator should only be turned off as a last resort.

Another factor which has some effect if not mitigated is changes in air temperature, humidity, and pressure. However, the ambient conditions of the clean-room are for the most part stably controlled, with temperature fluctuations of ~2° F over days or even weeks of continuous monitoring. Nevertheless, the oscillator stability has been known to change with the weather, and may at times requires cavity length adjustments.
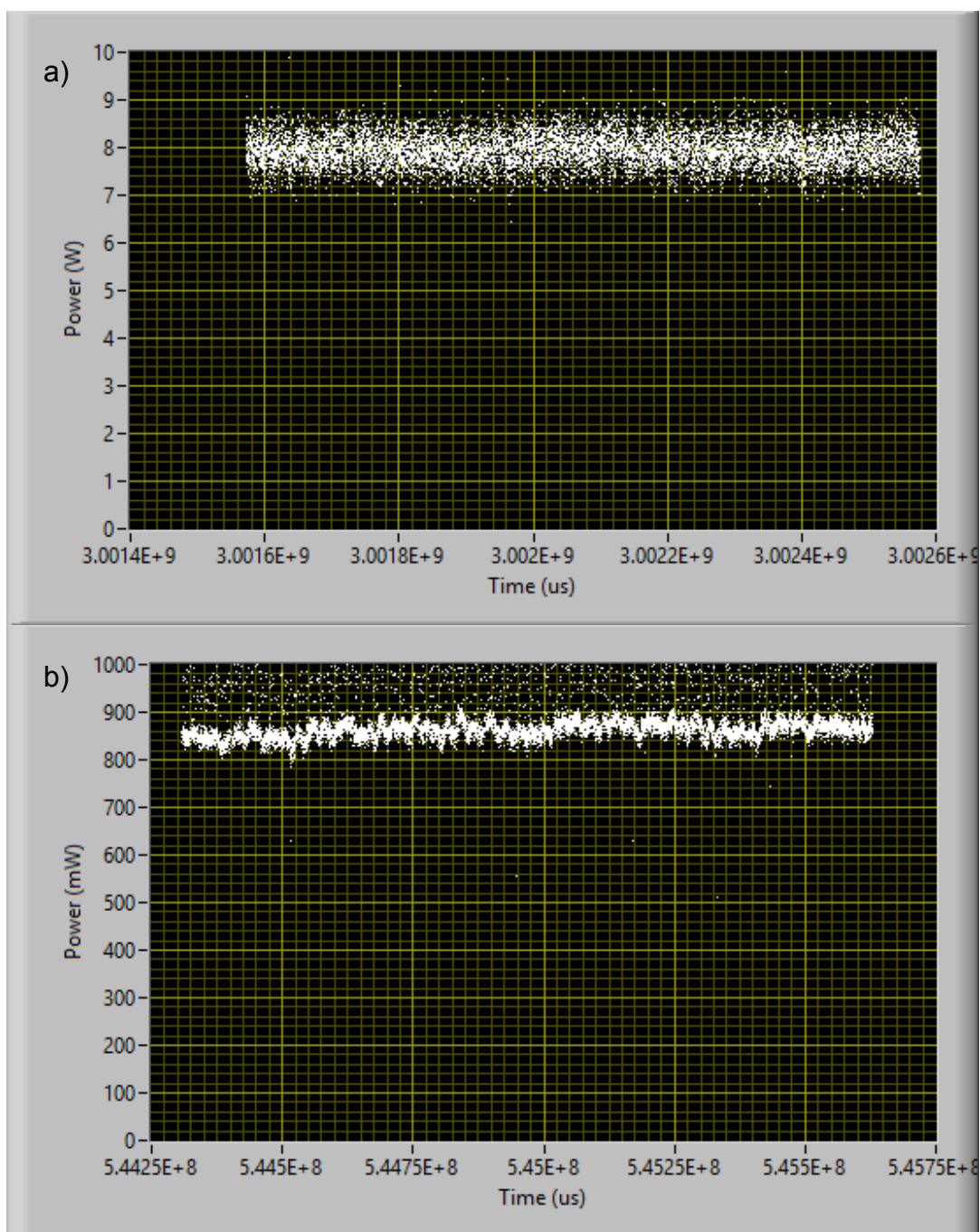
Figure D.1: Energy stability of the Jade pump and 9-pass Femtolaser Ti:Sapph amplifier. a) Shot-by-shot history of the Jade pump power split to pump the 9-pass amplifier, and b) the resulting Ti:Sapph output power. These two are not taken simultaneously, but it is evident that the slight oscillation in pump power leads to a more dramatic amplified pulse power variation.

The Jade laser's stability directly affects the stability of the 9-pass amplifier and the Booster amplifier. The greatest cause of instability here is the rapid fluctuations caused by vibrations (and cavitation) in the chilling line, and also by the longer-term sinusoidal fluctuations due to changes in chilling water temperature. Ideally, the temperature control would keep the water at a constant temperature, which would in turn result in the Jade's diode packs (pumps) operating at a constant energy and wavelength. However, the actual chilling system attempts to maintain a constant water temperature by monitoring the water's temperature *in situ*, and either heating or cooling the water as necessary to maintain the desired temperature. The result is a sow rise then fall of the temperature, which means a slow rise and fall in the green light coupled out through the Jade's doubling crystal. The doubling crystal's phase-matching condition is highly sensitive to the wavelength of the wavelength of the light out from the Yt:YAG crystals, and these are in turn sensitive to the wavelength at which they are pumped by the diode packs, which is ultimately determined (by design) by the water temperature. Small fluctuations in the water temperature thus means fluctuations in the pump laser's output power, and thus in turn on the Ti:Sapph amplifiers' performance.

It should be noted that the data shown in Fig. D.1 were taken after extensive optimization of the 9-pass amplifier system. This was done over the course of three weeks' time following the replacement of a damaged Ti:Sapphire crystal and a deteriorated Jade laser head and in conjunction with a service visit from the Thales lasers

299

specialist. Thus, the Jade laser was delivering ~8W to the Ti:Sapph crystal, whose output power was in turn ~800 mW average, meaning that the average shot power was 800 µJ with 1 kHz repetition rate; some shots here exceeded 1 mJ in energy. Over the course of the next year and a half, this output power slowly degenerated so that the typical out power was reduced to ~330 mW. This reduction in power is due in part to the fact that the system can run with so little as 300 mW output power, and hence most users stop "optimizing" upon achieving 350-400 mW. However, the surface of the Ti:Sapphire crystal also slowly degenerates, and the crystal itself gets damaged over time and has to be translated so that the pump is moved away from the damaged spot. The mode from the optimized system is shown in Fig. D.2, and may be contrasted with the "typical" mode shown in Fig. A.3b (see Appendix A).

Pointing stability is nominally controlled by two pointing-stabilized mirrors in the front end, one of which no longer works. Essentially, these mirrors are centered on a pair of diodes, and then some pizo motors keep the pointing on the same location on these diodes. These are located before and after the 9-pass amplifier, and even without the second mirror's correct operation still do improve the beam's performance. The diodes also act as an effective iris for alignment purposes. However, there is also some pointing drift downstream, in particular in the mirrors in the XPW. The output mirrors need to be re-adjusted approximately every 4-5 hours as they drift and thus cause a dramatic decline in the Booster output power (typically from 150 mW to 30 mW over 4 hours)
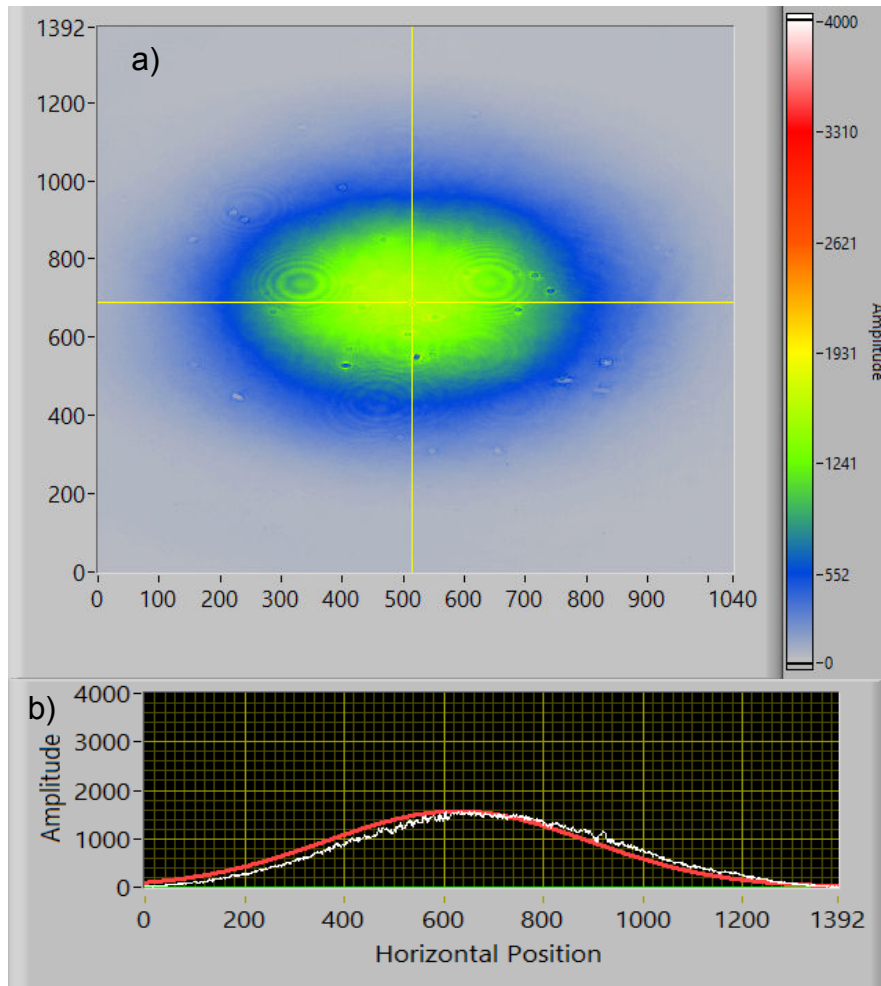
Figure D.1.2: Mode and lineout of the optimized 9-pass Femtolaser Ti:Sapph amplifier. This figure is taken approximately 18 months before Fig. A.3 in Appendix A.

Longer term, the phase-matching conditions of the doubling crystals in the pump lasers may drift slightly, which in turn means that the crystals need slight adjustments from time to time. This is done by entering the password "device" into the Jade control software provided by Thales, but it must be done very carefully. Only the small-angle tuning should ever be done, and this only ever by few steps because the doubling crystal

also acts as the output coupler or the Jade's cavity: if too little light is coupled out then the Jade will be damaged (typically in the amplifiers, though sometimes luck prevails an it is only one of the mirrors which gets damaged).

This can change the laser's mode somewhat, as can shifts in polarization (the splitter between 9-pass and Booster is essentially a piece of glass placed at the Brewster angle to send one polarization to the 9-pass and the other to the Booster). A change in the mode can result in a poorer mode match hence, less power output), or even a poorer-quality mode out of the 9-pass (or Booster) amplifier, or on occasion can cause damage to the 9-pass Ti:Sapph crystal. This crystal also gets damaged on occasion from the accumulation of moisture in its cooling cell: this moisture can condense on the crystal's face, or even freeze into small ice crystals which act as lenses to the laser.

When this crystal is damaged, it is typically shifted, but its top and bottom are in thermal contact with some indium foil for greater thermal conductivity. Thus, when the crystal is shifted care must be taken that this foil does not fall int the beam's path, or it will ablate, coat the crystal's face, and cause further damage to the crystal. Furthermore, both faces of the crystal (and both windows of the chamber) are Brewster cut, so care must be taken to not rotate the crystal or the chamber if either need to be moved.

Small changes to the beam's optical pathlength also means that the prism compressor separation must be adjusted to compensate for differences in GVD (refer to Appendix C). Such adjustments affect both the output power and spectrum from the XPW, and hence of the rest of the system. Changes in the beam energy and mode out

form the 9-pass have a similar effect, though the expanding lens pair before the XPW as well as the crystal positions within it can help mitigate this particular issue.

All of these effects collectively require some adjustments in the laser system alignment-wise. This is especially true when one of the optics (usually, the amplifier crystals) gets damaged. If the damaged spot is small and to the side, the crystal may merely be translated slightly to avoid the damaged spot, but in the case of the Pre-Amplifier and Power-Amplifier crystals, it is often necessary to order entirely new crystals. These in turn must be oriented along the correct axis for maximum gain, and may ultimately result in lesser (or sometimes greater) power output.

Furthermore, these little adjustments can cumulatively affect not only the energy output, but also the mode quality and the spectral output. The mode output in particular is of concern because of its effects on the Raman system. Often, the adjustment of a lens (or lens pair) upstream in the front-end can result in a poorer mode-match between pump and seed in the Raman system second stage (for example). Moreover, because the mode itself evolves somewhat from output of the front-end to input at the location of the Raman crystals, changes in the system which have no effects on other users can result in a drastically changed Raman beam.

The mode sizes in the final amplifier have been increased for both pumps and amplified beam. This is to avoid damaging the Ti:Sapphire crystal, a problem which was endemic in original design. The drawback to enlarging the spots sizes is that the power

output of this amplifier drops correspondingly, since the pump intensity is decreased as a result of the larger spot size.

One final factor is the mode and energy output of the SAGA and Continuum pump lasers for the Pre-Amplifier and the Power Amplifier. As the flashlamps in these laser age, the output power decreases and the mode-quality drops. Additionally, the doubling crystals may need to be tuned as a result of thermal phase-matching, which changes somewhat with the thermal load from the laser drops as a result of its power's declining.

D.2   STABILITY OF THE RAMAN LASER SYSTEM

The Raman laser stability and functionality has a strong dependence on the stability and quality of the front-end system used to generate the Raman beam. For example, when the beam drifts so that the Booster power drops from 150 mW to 30 mW, the Power Amplifier's power may drop by 50% (it is running near saturation), but the Raman beam's power will decrease by as much as 95%. Re-aligning the Booster means that the Pre- and power-Amplifiers must also be re-aligned (usually a relatively quick process), and then so must be the Raman system (typically a process which can consume hours). Furthermore, the compressors and everything downstream from them are under a vacuum which typically requires approximately 3 hours to establish.
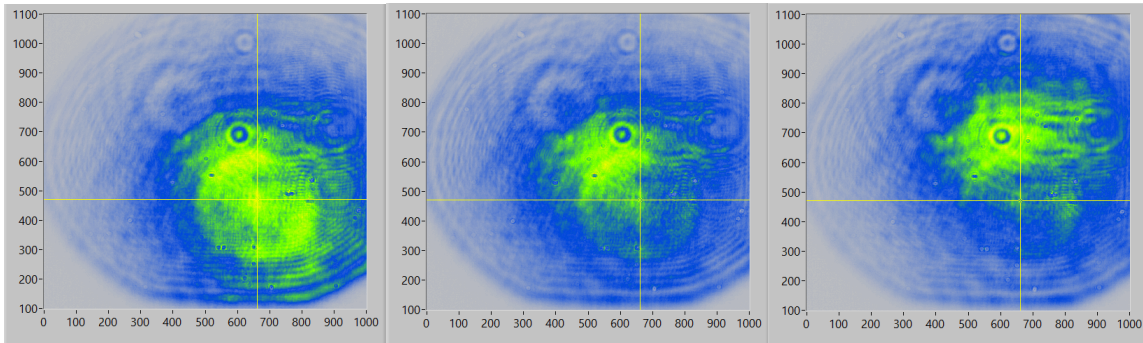
Figure D.3: Raman system post-compressor leakthrough pointing monitor. The system itself consists of the light leaked through a high-reflecting (R>99%) mirror and then imaged via a lens to the position of the mirror through which it was leaked. Three different shots are show to give some idea of shot-to-shot pointing stability of the system.

To help mitigate the realignment pointing problems, I have placed a leakthrough monitoring system after the first mirror following the Raman compressor system. This ccd monitors the pointing of the Raman system in conjunction with a set of two separate pair of irises (each separated by >2 m), one at the input to the Raman system's beamsplitter, and one after the 6-pass Final Amplifier. Typically, adjusting the mirrors at input to the first pair of irises and then centering the Raman beam on the ccd suffices to approximately optimize the Raman beam alignment to the target chamber, though a mirror with controllable mirrors inside the vacuum system allows for final fine-adjustment on target in conjunction with the post-target relay-imaging system described in Chapter 4 (Sec. 4.7). Some frame-grabs from the ccd pointing monitor system are shown in Fig. D.3.

However, these re-alignments often result in a slightly weaker-than-optimum beam through the 6-pass Ti:Sapph. For example, the Ti:Sapph may initially be aligned to 160 mJ average energy, and then after re-aligning will yield only 120 mJ. More thorough

alignment may improve the energy output back to 160 mJ, but could take hours; and after the next re-alignment the energy may re-improve to 150 mJ, then again to 115 mJ, and so on. Typically, by the end of the week the output power is consistently lower on average by ~25% than at the beginning of the week if a thorough re-alignment is not undertaken each time.

Also, the Quanta Ray Pro-350 typically has a long (> 10 minutes) warm-up time, after which the Raman laser is at its best power; then both slowly decrease in power over time for the next 30-45 minutes. This is likely not the effect of merely alignment drift, since the power typically levels off for an hour or two at least, and this at > 90% of the initial "peak" laser output.

Longer-term, the Raman laser will slowly degrade in quality. This happens over the course of many laser runs (each ~ 1 month apart), and can be due to a number of factors, most of which have been discussed above. However, the barium nitrate crystals also slowly degrade, in part because they absorb water at the surface. This is mitigates by place the crystals inside of a sealed housing with desiccant, but the desiccant eventually saturates and the crystals then begin to absorb water at the surface, which becomes cloudy and cannot be cleaned (acetone, methanol, and isopropanol solutions all contain plenty of water), resulting eventually in surface or even bulk damage to the crystals.

This in turn leads to messier modes and lower output energies from all stages over time. Therefore, it is recommended that the desiccants be changed every few months, and that new crystals be purchased every few years as needed.

Appendix E

Various Target Chamber Configurations

In this appendix, I will show the different recommended configurations of the wakefield target chamber to accomplish a variety of the two-color experiments discussed in this dissertation. The current layout of the Wakefield Target Chamber is Sown in Fig. E.1.
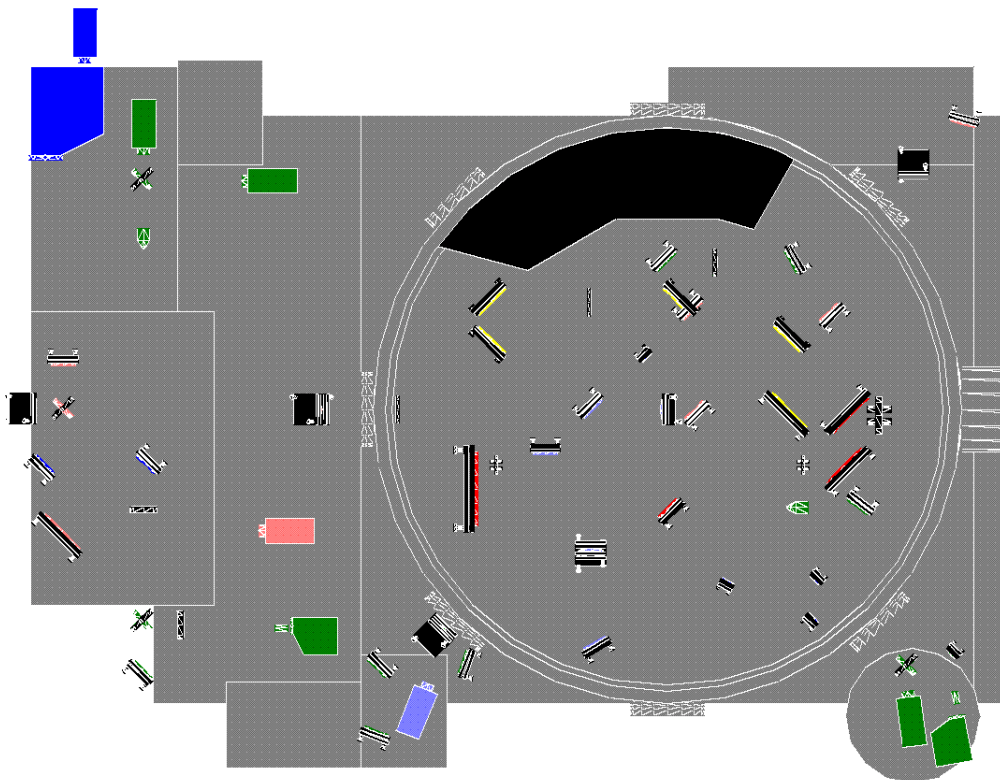
Figure E.1: Current layout of the Wakefield Target Chamber (WTC). The optics are color-coded by relevant purpose: red = Main and Raman line to target, gold = colliding pulse optics, green = relay imaging (and spectrum) optics, dark blue = FDH probe, pink = transverse probe, and steel blue = Thompson scattering optics.

E.1 CONFIGURATION FOR RXPM, SFRS, AND EMC EXPERIMENTS

These are the recommended first set of experiments for this laser system. The RXPM experiment essentially requires a high intensity pump to set up the plasma density modulation, and then a long probe (the Raman beam) to be modulated over many plasma lengths. The stimulated forward Raman scattering (SFRS) experiment and the electromagnetic cascading (EMC) experiment both require the Main and Raman beams to be ~ matched in duration and overlapping in time: the major differences between the two set-up wise is in the diagnostics. SFRS involves looking for Raman amplification and the generation of electrons; EMC involves looking at spectral broadening and also pulse compression, with a 3rd order autocorrelator[220] or preferably a FROG[221] or SPIDER[222] capable of resolving a high repetition of compressed ultrashort pulses, each of whose duration is <10 fs.

This is the default (i.e. current) set-up for the system anyway: it uses the same beam path as other users of the Wakefield Target Chamber, albeit with a different set of mirrors which are broad enough in bandwidth to reflect at both the fundamental and the 1 Stokes' wavelengths. In this case, the two beams are combined via dichroic mirror in the compressor chamber's exit, and then a pair of Thorlabs 4" broadband coated (700 nm-900 nm) mirrors are used to steer the two beams jointly to the off-axis parabola, which reflects at a 15° angle to a 2" diameter Newport mirror (also coated for 700 nm – 900 nm, but with a higher nominal damage threshold), and from there to its focus on the front of the gas jet. The set-up and beampaths are shown in Fig. E.2.
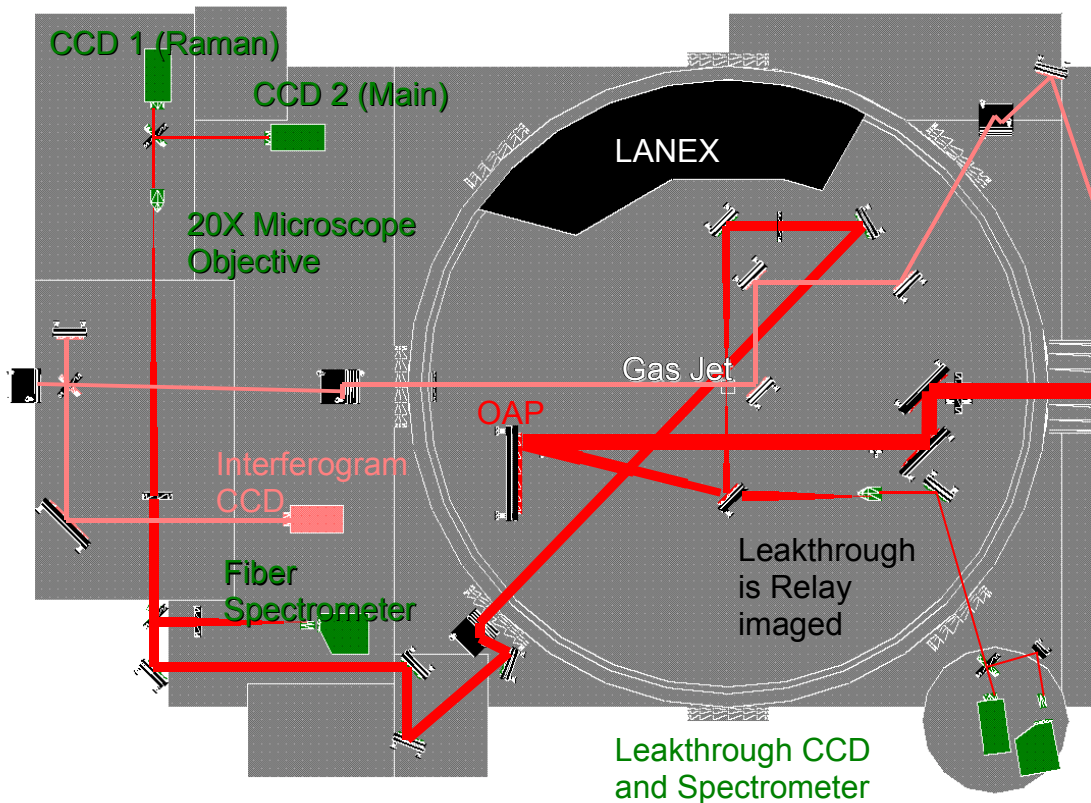
Figure E.2: Beamlines for the SFRS and RXPM experiments. The red beam is the primary (fundamental) and secondary (Raman) beams (they are combined through a dichroic in an earlier chamber) which enters from the right. The red optics are the broadband high-reflecting mirrors and the off-axis parabola (OAP) prior to the target gas jet. The green optics are for relay imaging and also recording spectrum before (via leakthrough) and after the interaction with the plasma. The salmon-colored beam (and optics) is for the transverse probe (interferogram or shadowgraph). The EMC experiment would add another beam splitter after the reflection of the first beam splitter in the output relay line, which transmits to the fiber spectrometer and reflects to a FROG.

In this set-up, the Main beam and Raman beam enter from the right and are reflected from a pair of 4" diameter mirrors; the beams have a diameter of ~5 cm at this point. Irises for alignment are setup as follows: 1) before the first mirror, to align the

dichroic; 2) after the second mirror a pair of irises is in place to align into the OAP; 3) one iris immediately after the 2" steering mirror (which is mounted on a translation stage after the OAP but before the gas jet) and one just before the attenuator mirror (first mirror after the gas jet): these are to align the steering mirror (the near one determine translation stage position, the far one the mirror's pointing).

The OAP is a gold-coated 8" diameter 15° off-axis parabola mirror whose focal length is 60 cm (an f/12 focusing optic). Typically, the OAP is aligned by direct viewing of the beam using an objective lens placed at the focus followed by a ccd; the beam energy must be dramatically attenuated first, usually by first turning the main beam's energy to minimum and blocking the Raman beam upstream, then placing a 0° mirror in the chamber prior to the first 4" broadband mirror; if this attenuation process is not carried out, the objective lens will be destroyed. Alignment consists mostly of optimizing the beam's focus if necessary. Once this is done, the 0° mirror, objective lens, and ccd are all removed and the steering mirror can be aligned on the two irises described above.

The first mirror in the relay-imaging line (first mirror after the gas jet) is on a motorized mount and can be raised into the beam path for relay-imaging the laser, or lowered out of the beam path to allow electrons to pass into the LANEX. The mirror itself is an attenuator which transmits ~96% of the Main and Raman light and reflects the remaining 4%. This is done to avoid creating a large B-integral in the lens which follows it[xxv], which has a 25 cm focal length. The beam is sent through a window to a periscope,

---

xxv In the EMC experiment, that lens would need to be replaced with a curved mirror and the mirrors re-arranged accordingly so as not to stretch the pulse duration, but the beam would still need to be attenuated to avoid a large B-Integral through the output window.

and from there is sent to a beam splitter (T = 2%, R = 98%). The transmitted portion of the beam is then focused by a lens with 50 cm focal length, which is imaged by a 20X microscope objective lens placed at the focus. This focus spot is then split by another beam splitter which sends the beam to a pair of ccds. An interference filter which passes 880 nm (80 nm FWHM bandwidth) and rejects other wavelength (O.D. > 3.0) can be placed on one ccd to view only the Raman beam with another interference filter which passes 800 nm (40 nm bandwidth) and rejects other wavelength (O.D. > 3.0) can be placed on the other ccd to view only the Main beam. The objective lens is mounted on a translation stage, and if the interference filters are removed and one beam then the other is blocked, the relay imaging system can be used to transversely overlap the two beams.

The reflected portion from the T98/R2 beamsplitter is currently sent to a fiber spectrometer to measure any spectral effects of the plasma on the lasers. In the EMC experiment, a second beamsplitter which reflects to a FROG (or equivalent device) and transmits to the spectrometer would be needed to enable accurate pulse duration measurements. Even then the FROG would still measure some phase effects from the window out of the chamber: ideally is could be placed inside the target chamber, with a beamsplitter transmitting to the relay imaging system and reflecting to the FROG placed prior to the window.

Depending on one's choice of a steering mirror between the OAP and the gas jet, it is possible to use leak through from the steering mirror to image the mode(s) and spectrum of the Raman and Main laser prior to the interaction with the gas jet. This can

311

be done *in situ* with the relay-imaged modes and spectrum taken downstream from the gas jet for the sake of shot-by-shot comparisons. However, certain companies (Thorlabs, Newport) may use a mirror whose back side is not polished—such is the case with the broadband mirrors currently in place. Therefore, if input modes and spectra are desired, the leak through from an earlier mirror can be taken, albeit without having both beams combined.

The transverse probe line (Fig. E.2, salmon-colored line and optics) consists of a 800 nm (or 400 nm if desired) ~100 fs pulse with ~10 mJ energy. It passes transversely through the gas jet, exits through a window at the left of the chamber, and enters a beam-splitter. One arm of the splitter uses a pair of rooftop mirrors to flip the beam vertically, and the beam is then interfered with itself on a ccd. This arm of the interferometer may be blocked if a shadowgraph is desired instead.

E.2 CONFIGURATION FOR TWO-COLOR COLLIDING PULSE INJECTION EXPERIMENT

The two-color colliding-pulse experiment will require two counter-propagating beam lines, along with either a pair of Faraday isolators or a pair of interference filters to prevent damage to the front end of the laser system. The recommended set up and beam paths are shown in Fig. E.3. In this case, the two beams do not necessarily need to co-propagate along a single axis into the chamber. Instead, they enter the chamber along parallel axis at the same height, and both hit a dichroic mirror which transmits the 873 nm Raman beam while reflecting the 800 nm Main beam, which therefore splits the two beams.
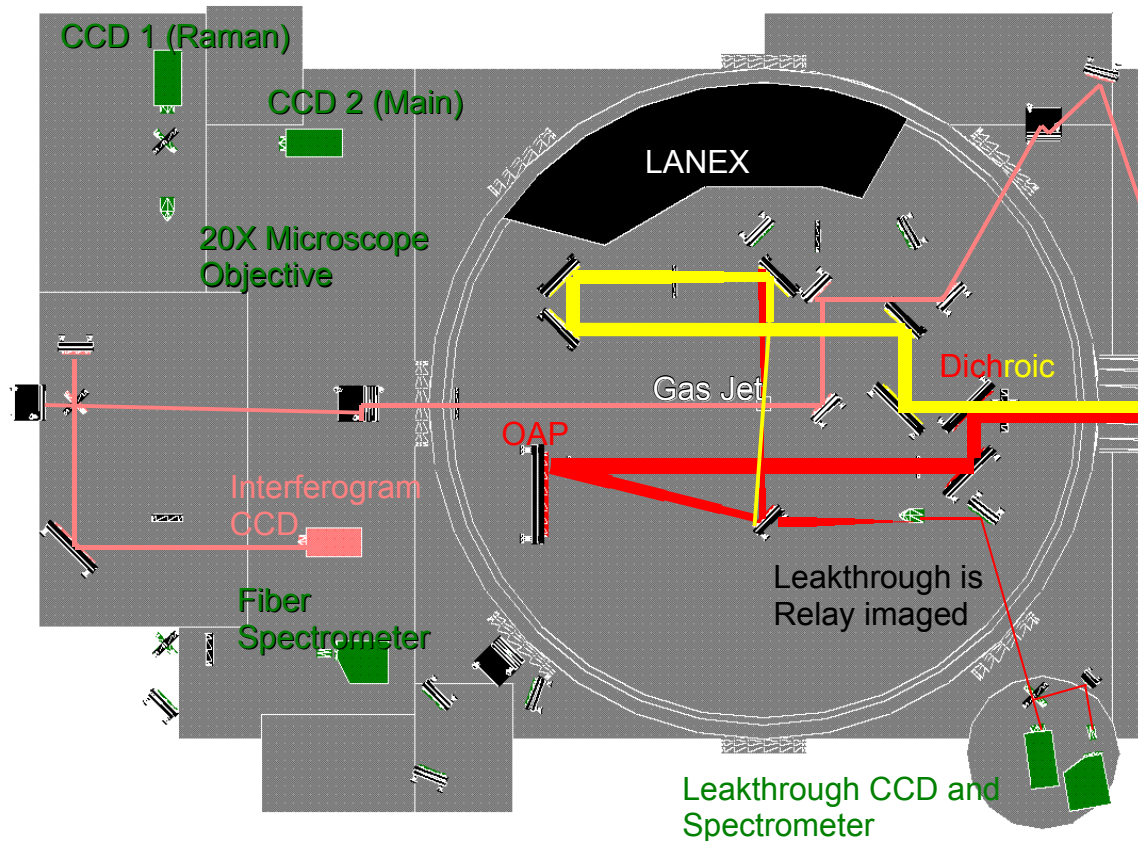
Figure E.3: Recommended set-up for the two-color colliding pulse experiment. The Raman beam (yellow) and the Main beam (red) initially propagate into the chamber parallel to each other from the right. The first mirror is a dichroic beam splitter, which reflects 800 nm and transmits 873 nm at 45° incidence. The transverse probe line (salmon) is still used as in the SFRS/RXPM/EMC experiments, though it now becomes the primary diagnostic to check beam overlap.

While the two do not in principle need to share an axis prior to the dichroic beam splitter, there are two practical considerations which might make this desirable: first, that the aperture size of the beam tube is fixed at 6" in diameter, and second that the dichroic beam splitter has a 4" diameter and will need to have the two beams enter at a 45°

incident angle for the coating to be maximally effective. Therefore, if the two beams do not co-propagate along a single axis, the Raman beam risks clipping on either the beam tube or the edge of the dichroic beam splitter.

The primary beam and transverse probe line operate as before, though the transverse probe line takes on new importance. Since the primary and secondary beams do not propagate collinearly to the gas jet, the ccd relay imaging system can no longer be used to ensure overlap between the two beams. Therefore, the images of the ion channels created by both the primary and the secondary beam on either the interferogram or the less sensitive shadowgraph become the most straightforward means of overlapping the two beams in the gas jet.

Furthermore, if a scan of electron bunch energy vs overlap position is desired, it is advisable for the secondary beam's mode size to be ~constant over the length of the gas jet. Therefore, a larger focal spot size is indicated. This can be accomplished by using a longer focal-length lens—the feasibility of which is unlikely given space constraints inside the chamber, or to use a smaller initial secondary beam waist. This option is more feasible since all the mirrors in the secondary beam line may be dielectric, which has a higher damage threshold that metal-coated mirrors such as the OAP. It has the added advantage of not needing the larger 4" mirrors (which are also more expensive than mirrors of the 2" variety), and of then allowing parallel propagation without clipping on the beam tube or the dichroic beamsplitter.

Relay imaging of the main beam after the gas jet can still be accomplished provided that the last mirror in the secondary beam's counter-propagation line is also

dichroic (transmitting 800 nm and reflecting 873 nm) or provided that it is offset such that the counter-propagation is not collinear[223]. If the counter-propagation is to be collinear, then this last mirror in the Raman line must have a hole through which any accelerated electrons can pass to arrive at the LANEX.

E.3 CONFIGURATION FOR CONTROLLED RSF EXPERIMENTS

The controlled RSF experiments require a larger spot size than any of the previously mentioned experiments. Whereas the other experiments work reasonably well with a beam waist of ~10 μm, the recommended focal waist in the RSF suppression experiment is 25 μm; this experiment is also very delicately balanced between power, intensity, the requirement that the beams interact over several plasma lengths, and the dependence of beam guiding on the guide beam's waist. The effect is very sensitive to the spot size (and phase front curvature) at the entrance to the gas jet[224].

As discussed in Sec. E.2, this can be accomplished by using a smaller pre-focused beam waist. However, doing so will likely result in damage to the OAP, which is gold-coated rather than dielectric, and whose damage threshold is therefore comparable to the intensity of the beam with the requisite pre-focused waist. Therefore, a focusing optic with longer focal length was needed: in this case, a spherical mirror with a 60-inch focal length replaces the OAP with 60 cm focal length. In order to accommodate this longer focal length, an extension must be mounted to the WTC, as shown in Fig. E.4.
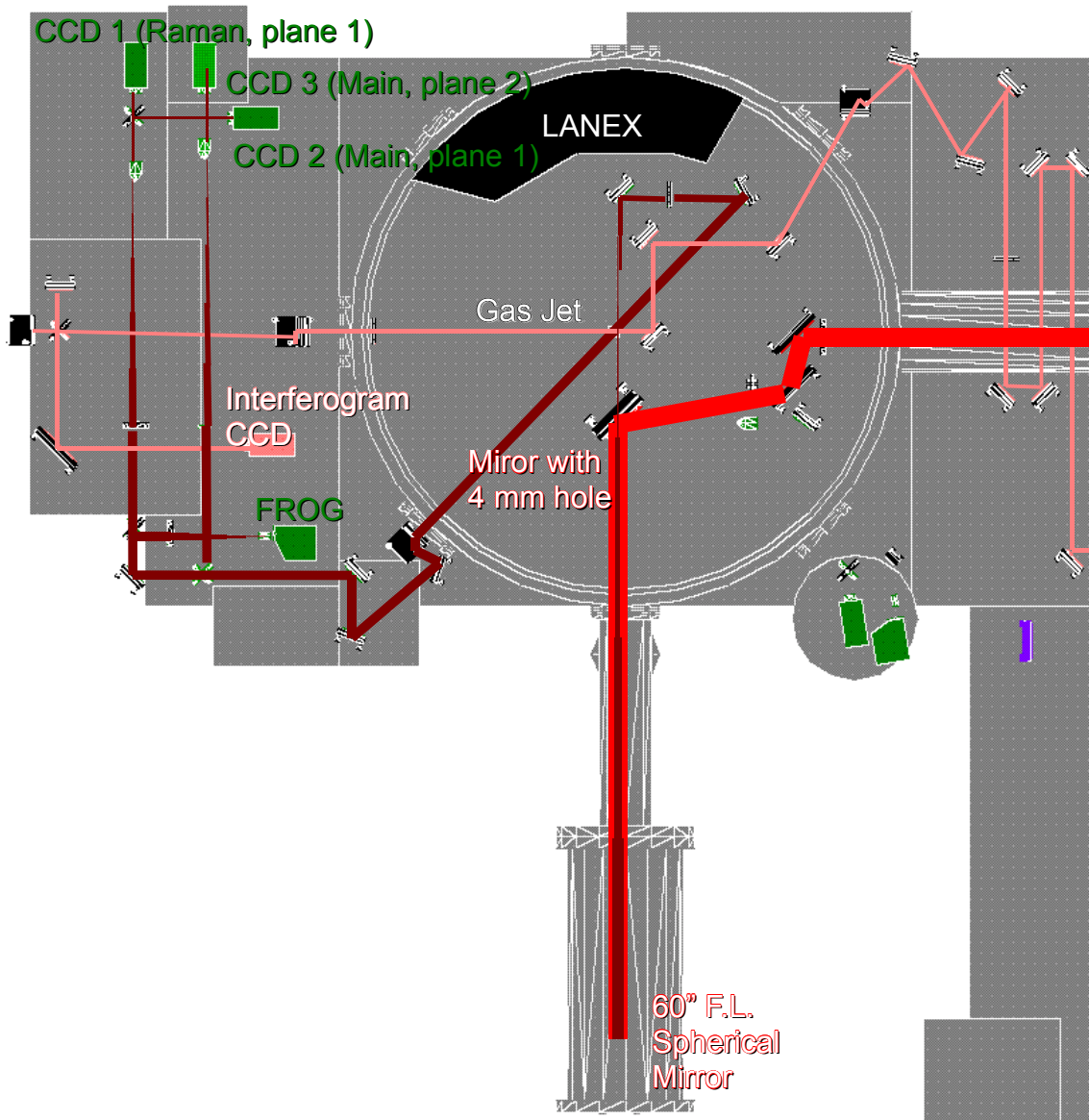
Figure E.4: Recommended WTC set-up for RSF control experiments. An extension tube with a 60" focal-length spherical mirror has been added to the south side of the WTC. The regular steering mirror has been replaced with a 4" diameter mirror with a 4 mm hole drilled through the middle. The Raman and Main beams enter from the right (light red), are reflected at 0° incidence to the spherical mirror, which then focuses them (dark red) such that the beams' waists fit through the 4 mm hole and are focused on the front of the gas jet. The transverse probe line remains unaffected.
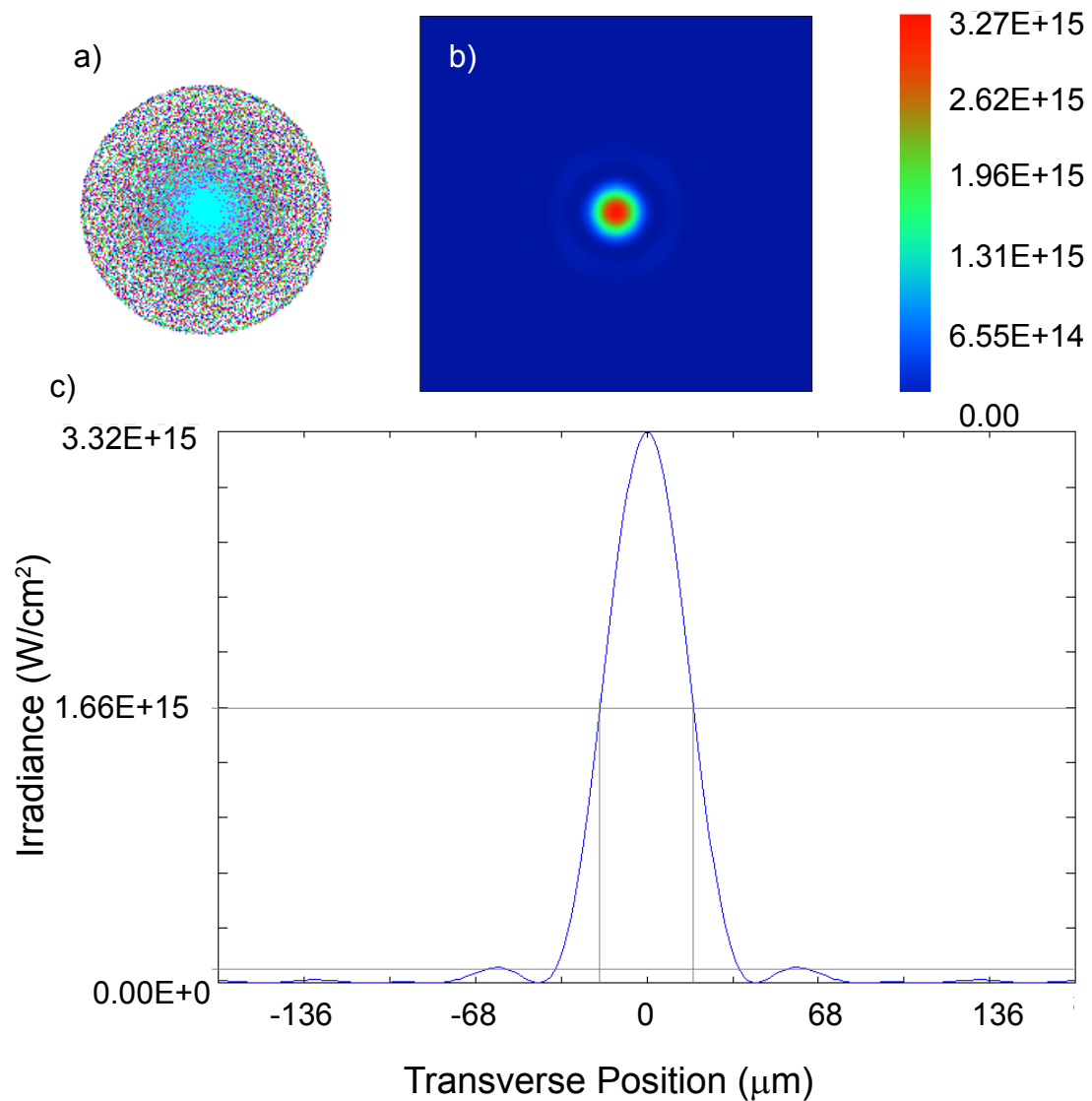
Figure E.5: ZEMAX simulations of the spot at focus after reflecting from and then passing back through the mirror with a hole. a) Ray trace diagram for 780, 800, 820, 860, 875, and 890 nm,showing the focal spot shape. b) The transverse mode profile assuming an initially tophat mode at 800 nm, 2 mm hole radius and a 30 mm initial waist for the beam prior to focusing. c) Intensity lineout in the horizontal direction shows a ripple of <3% of the main peak intensity and an expected FWHM size of 29 μm at focus. Approximately 98% of the initial beam's energy incident on the steering mirror initial arrives on target.

The chamber extension provides sufficient length to focus the two-color laser to a spot waist of 25 μm, with the focus being on the front of the gas jet target. In order to avoid astigmatism, the beams must be incident at 0° to the spherical mirror. This places the steering mirror directly in the path of the reflected and focusing light. Therefore, a 4 mm hole is drilled through the center of this mirror, so that the light reflected from the spherical mirror can pass through with minimal clipping. The hole is sufficiently small to avoid both energy loss on the mirror and a significantly distorted diffracted beam. The focused beam profiles from a ZEMAX trace of the beam after reflecting from the mirror with the hole to the spherical mirror, an the back through the hole are shown in Fig. E.5.

The focused spot is free spherical of astigmatism, and 98% of the energy arrives on-target. The expected spot size is 29 μm FWHM ($1/e^2$ radius is 24.5 μm) with a ~sinc profile and <3% intensity ripple.

Appendix References

[220] J. Collier, C. Hernandez-Gomez, R. Allott, C. Danson, and A. Hall, "A single-shot third-order autocorrelator for pulse contrast and pulse shape measurements," *Laser and Particle Beams*, Vol. **19**, No. 02, pp 231-235 (2001).

[221] D. J. Kane and R. Trebino, "Characterization of arbitrary femtosecond pulses using frequency-resolved optical gating", *IEEE J. Quantum Electron.*, Vol. **29**, No. 2, 571 (1993).

[222] C. Iaconis and I. A. Walmsley, "Spectral phase interferometry for direct electric-field reconstruction of ultrashort optical pulses", *Opt. Lett.*, Vol. **23** No. 10, 792 (1998).

[223] J. Faure, C. Rechatin, A. Ben-Ismail, J. Lim, X. Davoine, E. Lefebvre, V. Malka, "Physics of colliding laser pulses in underdense plasmas," *C. R. Physique*, Vol. **10**, 148–158 (2009).

[224] S. Kalmykov (personal communication, May 30 and June 4, 2012).

Appendix F

Raman Secondary Booster Amplifier

In this appendix, I present a brief plan for safely boosting the output energy of the Raman laser system which serves as the secondary beam line on the UT^3 laser.

A number of two-color experiments would be aided by access to a more powerful second color. For example, the RSF suppression experiment would ideally have 100 mJ on-target from the Raman beam. After accounting for losses on all optics and especially through the compressor, this would require approximately half again as much energy as the current 6-pass Ti:Sapph final amplifier output.

One possible method for extracting more energy is to add more passes to this final amplifier. However, as discussed in Chapter 4 (Sec. 4.6), there are a few problems with doing this. The first is that the gain begins to saturate, so that adding more passes does not dramatically increase the output energy. The second is that the beam already has self-focusing/filamentation-hotspot problems, for which reason the output energy has been intentionally limited.

These hotspots disappear in the event than an iris is placed in the beam as a sort of spatial filter before the amplifier. This comes at the expense of further loss of energy in the beam, however.

Nevertheless, there is a possible method for achieving higher energy at the output of the amplifier, which is to add a second Ti:Sapph amplifier stage before this final amplifier. In the simplest configuration, this other amplifier is a two-pass retroreflection amplifier which uses lower pump energy and a smaller spot size for amplification.

Simulation and experience both suggest that as much as an order of magnitude may be gained at 873 nm using such a set-up. The Booster amplifier at the front-end of the UT³ laser system is such a retrofreflected amplifier, pumped by ~10 W average power at 1 kHz (10 mJ per pulse), the effect of which is to amplify a pulse whose initial energy is ~1 μJ at kHz rep rates to up to ~200 μJ at the same repetition rate, which is fully two orders of magnitude in amplification after 2 passes (once through and then retroreflected).
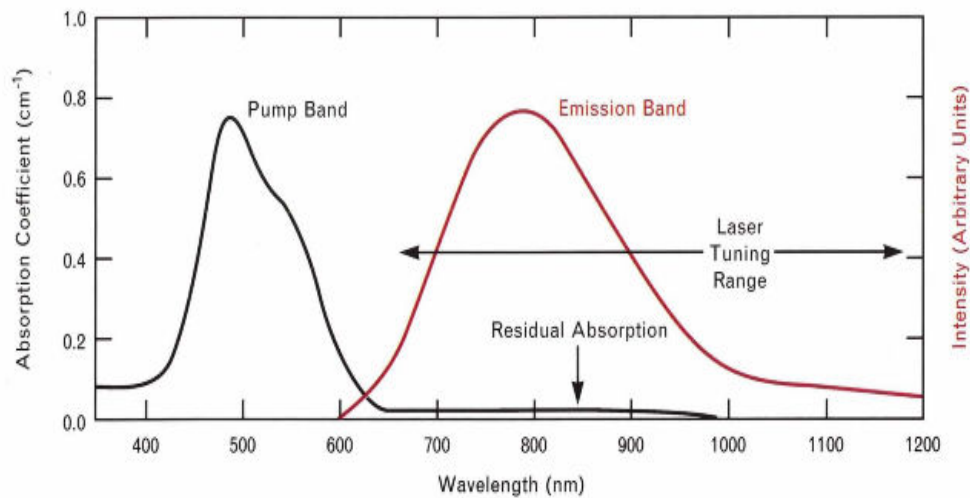
Figure F.1: The absorption and gain curves for titanium-doped sapphire[225].

Such is the case when the seed pulse is centered at 800 nm, which is near the peak of the gain curve[225] for Ti:Sapph, as shown in Fig. F.1. With that said, the amplification of the 873 nm Raman pulse from ~1 mJ to up to ~300 mJ (albeit with hotspots) in 6 passes suggests an average per-pas gain of 2.59, meaning that after each pass in the 6-pass final amplifier the 873 nm pulse is amplified by a factor of 2.59 (on average). In practice, the per-pas gain is not actually constant, with earlier passes at lower energy having a greater fractional gain than later passes at high energy. For example, the first two passes in the current 6-pass Ti:Sapph system regularly result in a measured amplification factor of 3.5-4.0 and 3.0-3.5 (respectively), meaning that the combined amplification for two passes at low energy is a factor of ≈ 12.

Granted, the pump energy is ≈ 1.05-1.10 J when these measurements were made, but the pump's spot size is also $w_{pump} \approx 0.35$ cm with a seed size of $w_{0seed} \approx 0.30$ cm at the entrance to the amplifier. Under these conditions—choose 1.05 mJ for the pump—and for a 0.5 mJ seed with 9% per-pass loss (which is the measured loss of the Ti:Sapph amplifier), the simulation predicts a total output energy of 6.86 mJ, an amplification by a factor of 13.72 in 2 passes. Under the same conditions with a 0.455 mJ seed energy incident on the Ti:Sapph amplifier, the measured output energy at 873 nm after 2 passes was 5.75 mJ, which is an amplification by a factor of 12.6. The difference in amplification here can be attributed to uncertainty in pump beam energy. For example, if the pump is reduced from 1.05 mJ to 1.03 mJ, and change of $\approx 2\%$, the simulated output energy is 6.52 mJ or a factor of 13.04 amplification; and the pump energy does tend to oscillate somewhat even after warming up, as discussed in Appendix D.

If the beam is irised to clean up the transverse profile and remove any hotspots, then the typical energy through the iris is ≈0.1-0.2 mJ with a waist of 0.1-0.15 cm. Using 0.1 cm waist and 0.1 mJ seed energy, and a pump whose waist is also 0.1 cm nd whose energy is 0.1 J, a two-pass amplifier should yield ≈2.0 mJ. Using the same pump but with a 0.15 cm waist and the seed with 0.2 mJ and 0.15 cm initial energy and waist should yield only 0.7 mJ, so it is best to use the smaller lower energy seed and the smaller more intense pump for this stage. However, the fluence from this pump size and energy is 3.2 J/cm^2, which is approximately the damage threshold for a Ti:Sapph crystal. Increasing the pump energy to 0.15 J with a 0.15 cm waist and using the 0.15 cm, 0.2 mJ seed pulse yields ~1.5 mJ from two passes, with a pump fluence of ~2.1 J/cm^2. If this 1.5 mJ pulse is then uses to seed the 6-pass final amplifier pumped with 1.05 J, assuming that the beam's waist has been doubled to approximately match the pump's waist, then the predicted output energy is ≈260 mJ. This is sufficient to have ≈100 mJ on-target, which is enough energy for experiment such as the colliding-pulse injector and the RSF suppression experiments.

There are three possible sources for this pump energy in the current UT^3 system— in other words, three places from which to get 0.15 J without buying an additional pump laser system:

1. Split ≈10-15% of the energy from the existing Pro-350 pump which is used for pumping the 6-pass Final Amplifier.

2. Use the transmitted pump light from the Ti:Sapph crystal.

3. Use a doubling crystal to generate additional light at 532 from the transmitted fundamental of the Pro-350 pump laser.

I will now consider each of these in turn.

The first option is the easiest, most straightforward option. It would require only that a 15/85 or 10/90 (R/T) beamsplitters be placed in the path of the pump beam in each arm before arriving at the amplifier crystal, and a pair of lens to resize the pump beam. However, it also reduces the amount of energy with which the 6-pass amplifier is to be pumped. For example, if the pump beam initially has only 1.05 mJ available, and 150 mJ are removed to pump the Secondary Booster Crystal, the remaining 0.90 J left to pump the Final Amplifier result in an output of 178 mJ, which is only a marginal improvement over the current system, which regularly sees average energies in excess of 150 mJ and a shot-to-shot energy tail extending above 200 mJ.

The second option is to use the light transmitted by the Ti:Sapph crystal. The measured transmission of this crystal for 532 nm at 1 J is ≈10%. Therefore, the energy available—≈100mJ—falls well short of the 150 mJ needed to pump the Secondary Booster crystal. However, if this 100 mJ pumps a spot size of 0.12 cm and a mode-match 0.14 mJ seed—an attainable parameter—then the output from the Secondary Booster is calculated as 1.12 mJ, which can then be amplified to ≈245 mJ in the final amplifier.

The difficulty with the second option is that the pump mode must be re-sized and re-imaged. Since it is actually focusing, there is also no convenient location where it can be safely picked up by optic to be sent to the Secondary Booster crystal.

The third option is to "re-double" the 1064 light from the pump laser. Essentially, Nd:YAG lases at 1064 nm. This light is the sent to a nonlinear frequency-doubling crystal (typically KTP, KDP, or KD*P), where some portion of the light is doubled. For example, in the SAGA pump lasers used by the UT[3] laser, the output in 1064 light is $\approx$2.4-2.5 J per pulse. The laser nominally uses a KTP crystal to frequency double this light, with a resulting output of 1.6 J in doubled light at 532 nm; the remaining 0.8 J of unconverted ght is simply wasted, dumped into a beam block in the laser. However, this beam block can be removed, and the 0.8J of unconverted light can then be sent to a second doubling crystal—it has already been separated from the frequency-doubled light using a dichroic mirror. That 0.8 J can be used to generated ~200-300 mJ of doubled light with good mode quality in a second crystal. The UT[3] laser's primary beam line is in fact already doing this with the three SAGA lasers, though the KTP crystal has been replaced with a lower efficiency but higher damage threshold KD*P crystal.

This can therefore be used on the Quanta Ray Pro-350 pump laser to "redouble" the unconverted 1064 light which it normally dumps, with an expected output of $\approx$300 mJ in doubled light. If this is used to pump the Secondary Booster crystal with a spot size of 0.2 cm, and pumps the seed at 0.2 mJ and 0.15 cm incident, the calculated output would be 1.9 mJ; or it could be attenuated to 200 mJ (to avoid damage) and used to pump a spot of size 0.15 cm, resulting in a total output of 2.9 mJ. These would give anticipated Final Amplifier energies of 270 mJ and 289 mJ, respectively.

Further, the attenuation can be via beamsplitter. This allows the transmitted part to be sent to pump the Secondary Booster Amplifier and the reflected part to be sent to pump the 6-pass Final Amplifier. Such a scheme would further increase the anticipated output energy of the 6-Pass Final Amplifier.

The biggest drawback to this method is that space constraints would require that the current pump beam line be reconfigured. It would also require the purchase of another doubling crystal and its housing, a significant expense.

Pump Method #	Seed Energy (mJ)	2-Pass Pump Energy (mJ)	Mode Size (cm)	2-Pass Output Energy (mJ)	6-pass Pump Energy (mJ)	6-Pass Output Energy (mJ)
1	0.1	0.1*	0.1	1.92	0.95	211
1	0.2	0.15	0.15	1.44	0.9	170
2	0.1	0.1*	0.1	1.92	1.05	265
2	0.1	0.1	0.15	0.73	1.05	218
3	0.2	0.3	0.2	1.85	1.05	264
3	0.2	0.2	0.15	2.79	1.15	324
3	0.1	0.1*	0.1	1.92	1.25*	361
3	0.2	0	0.15	0.2	1.35*	334
3	0.2	0	0.15	0.2	1.05	138

Table F.1: Summary of output energies from Secondary Booster Amplifier and 6-Pass Final Amplifier. An asterisk (*) means that the total fluence exceeds the Ti:Sapph damage threshold of 3 J/cm², though it should be noted that only ~half of this fluence is incident on each face of the crystal. Methods are as described in text: 1) split energy directly from pump, thereby reducing Final Amplifier pump in order to pump Secondary Booster Amplifier; 2) use transmitted 532 light from Final Amplifier to pump Secondary Booster; 3) use secondary doubling of Pro-350 to pump Secondary Booster and Final Amplifier.

Table F.1 shows a summary of the simulated output energies using this 2-pass Secondary Booster Amplifier. The best option—meaning, the one which provides the most output energy—is to use secondary doubling of the Pro-350 pump, splitting this with 100 mJ to pump a Secondary Booster and 200 mJ (125 mJ total) to pump the Final amplifier, though sending 200 mJ (with a slightly larger spot size) to pump the Secondary Booster Amplifier and 1.15 J (1.05 J primary doubling + 100 mJ secondary doubling) to pump the 6-pass Final Amplifier sacrifices < 10% final energy in exchange for keeping the total fluence below the damage threshold for the crystals, noting of course that there is a built-in safety margin of a factor of 2 (since half of the fluence is incident on each face).

Finally, both methods 2 and 3 will provide adequate amplified energies out of the 6-Pass Final Amplifier. Method 3 appears to be the best overall method, though it will require the purchase of a doubling crystal (KTP or KD*P) and mount.

Appendix References

[225] T.F. Wall and A. Sanchez, "Titanium Sapphire Lasers," *The Lincoln Laboratory Journal*, Vol. **3**, No. 3, (1990).

References

A.I. Akheizer and R.V. Polovin, "Theory of wave motion of an electron plasma," *Sov. Phys. JETP,* Vol. **3**, pp 696-705 (1956).

F. Amiranoff, S. Baton, D. Bernard, B. Cros, D. Descamps, F. Dorchies, F. Jacquet, V. Malka, J.R. Marques, G. Matthieussent, P. Mine, A. Modena, P. Mora, J. Morillo, and Z. Najmudin, "Observation of Laser Wakefield Acceleration of Electrons," *Phys. Rev. Lett.*, Vol. **81**, No. 5 (1998).

F. Amiranoff, M. Laberge, J.R. Marques, F. Moulin, E. Fabre, B. Cros, G. Matthieussent, P. Benkheiri, F. Jacquet, J. Meyer, Ph. Mine, C Stenz, and P. Mora, "Observation of Modulational Instability in Nd-Laser Beat-Wave Experiment," *Phys. Rev. Lett.* Vol. **68**, No. 25, pp. 3710-3713 (1992).

M. Amosov and N. Delone, "Tunnel Ionization of complex atoms and atomic ions in electromagnetic field," SPIE Vol. **664**, 138-140, High Intensity Laser Processes (1986).

Anonymous, Handbook of Optics, 3rd edition, Vol. 4. McGraw-Hill (2009).

Anonymous, "Optical Glass Data Sheets," Schott Glass, 19 April 2010, pdf available at http://www.schott.com/advanced_optics/us/abbe_datasheets/schott_datasheet_all_us.pdf

Anonymous, "The Relativistic Heavy Ion Collider Run-9: 250 GeV Polarized Proton Operation," *Brookhaven National Laboratory, Collider-Accelerator Department*, 02 April, 2009.
http://www.agsrhichome.bnl.gov/AP/Spin2009/

Anonymous, "File:Breakdown of the cumulative number of industrial accelerators according to their applications.png," *Wikipedia*, 21 February 2013.
http://en.wikipedia.org/wiki/File:Breakdown_of_the_cumulative_number_of_industrial_accelerators_according_to_their_applications.png

T.M. Antonsen, Jr. and P. Mora, "Self-focusing and Raman scattering of laser pulses in tenuous plasmas," *Phys. Rev. Lett.*, Vol. **69**, pp. 2204-2207 (1992).

J. A. Armstrong, "Measurement of picosecond laser pulse widths", *Appl. Phys. Lett.*, Vol. **10** No. 1, 16 (1967).

S. Augst, D.D. Meyerhofer, D. Strickland, and S.L. Chin, "Laser ionization of noble gases by Coulomb-barrier suppression," *J. Opt. Soc. Am. B*, Vol. **8**, No. 4, pp. 858-867 (1991).

M. Belkin, personal communication, November 3 2011. M. Belkin, "Spontaneous and stimulated Raman scattering" [pdf], November 3, 2011, retrieved from http://blackboard.utexas.edu

R.S. Bennink, V. Wong, A.W. Marino, D.L. Aronstein, R.W. Boyd, C.R. Stroud, Jr., S. Likishova, and D.J. Gauthier, "Honeycomb Pattern Formation by Laser-Beam Filamentation in Atomic Sodium Vapor," *Phys. Rev. Lett.*, Vol. **88**, 113901 (2002).

B. Bernstein and I. Smith, "Aurora, an electron accelerator," *IEEE Trans. Nucl. Science* Vol. **3**, 294-300 (1973).

N. Bloembergen, "The stimulated Raman effect," *Am. J. Phys.*, Vol. **35**, 989 (1967).

Ian Blumenfeld, Christopher E. Clayton, Franz-Josef Decker, Mark J. Hogan, Chengkun Huang, Rasmus Ischebeck, Richard Iverson, Chandrashekhar Joshi, Thomas Katsouleas, Neil Kirby, Wei Lu, Kenneth A. Marsh, Warren B. Mori, Patric Muggli, Erdem Oz, Robert H. Siemann, Dieter Walz, and Miaomiao Zhou, "Energy doubling of 42 GeV electrons in a metre-scale plasma wakefield accelerator," *Nature*, Vol. **445**, 05538, 741-744 (2007).

A.B. Borisov, A.V. Borovskiy, V.V. Korobkin, A.M. Prokhorov, O. B. Shiryaev, X.M. Shi, T.S. Luk, A. McPherson, J.C. Solem, K. Boyer, and C.K. Rhodes, "Observation of Relativistic and Charge-Displacement Self-Channeling of Intense Subpicosecond Ultraviolet (248 nm) Radiaton in Plasmas," *Phys. Rev. Lett.*, Vol. **68**, No. 15, 2309-2312 (1992).

A.B. Borisov, A.V. Borovskiy, O.B. Shiryaev, V.V. Korobkin, A.M. Prokhorov, J.C. Solem, T.S. Luk, K. Boyer, and C.K. Rhodes, "Relativistic and charge-displacement self-channeling of intense ultrashort laser pulses in plasmas," *Phys. Rev. A*, Vol. **45**, No. 8, pp. 5830-5845 (1992).

R.W. Boyd, *Nonlinear Optics, Second Edition*, Elsevier, Academic Press (2003).

S.V. Bulanov, I. N. Inovenkov, V.I. K.M. Naumova, and S.A. Sakharov, "Nonlinear depletion of ultrashort and relativistically strong laser pulses in an underdense plasma" Phys. Fluids B4 1935 (1992).

S. Bulanov, N. Naumova, F. Pegoraro, and J. Sakai, "Particle injection into the wave acceleration phase due to nonlinear wake wave breaking," *Phys. Rev. E*, Vol. **58**, R5257 (1998).

M. Burza, A. Gonoskov, K. Svensson, F. Wojda, A. Persson, M. Hansson, G. Genoud, M. Marklund, C.-G. Wahlstro and O. Lundh, "Laser wakefield acceleration using wire produced double density ramps,", *Phys. Rev. STAB*, Vol. **16**, 011301 (2013).

A. Buter, D.J. Spece, and S.M. Hooker, "Guiding of high-intensity laser pulses with a hydrogen-filled capillary discharge waveguide," *Phys. Rev. Lett.*, Vol. **89,** 185003 (2002).

V. Chauhan, "Pulse Dispersion and Compression Control in Ultrafast Optics." Doctoral Dissertation, Georgia Institute of Technology, 2010.

P. Chen, J.M. Dawson, R.W. Huff, and T. Katsouleas, "Acceleration of Electrons by the Interaction of a Bunched Electron Beam with a Plasma," *Phys. Rev. Lett.*, Vol. **54**, 693 (1985).

R.Y. Chiao, E. Garmine, and C.H. Townes, "Self-Trapping of Optical Beams," *Phys. Rev. Lett.*, Vol. **13**, 479, 1964.

C.E. Clayton, C. Joshi, C. Darrow, and D. Umstadter, "Relativistic Plasma-Wave Excitation by Collinear Optical Mixing," *Phys. Rev. Lett.*, Vol. **54**, No. 21, pp. 2343-2346 (1985).

C. E. Clayton, K. A. Marsh, A. Dyson, M. Everett, A. Lal, W. P. Leemans, R. Williams, and C. Joshi, "Ultrahigh-gradient acceleration of injected electrons by laser-excited relativistic electron plasma waves," *Phys. Rev. Lett.* Vol. **70**, No. 1, 37-40 (1993).

C.E. Clayton, J.E. Ralph, F. Albert, R.A. Fonseca, S.H. Glenzer, C. Joshi, W. Lu, K.A. Marsh, S.F. Martins, W.B. Mori, A. Pak, F.S. Tsung, B.B. Pollock, J. S. Ross, L.O. Silva, and D.H. Froula, "Self-guided laser wakefield acceleration beyond 1 GeV using ionization-induced injection," *Phys. Rev. Lett*. Vol. **105**, 105003 (2010).

B.I. Cohen, A.N. Kaufman, and K.M. Watson, "Beat Heating of a Plasma," *Phys. Rev. Lett.*, Vol. **29**, No. 9, pp. 581-584 (1972).

J. Collier, C. Hernandez-Gomez, R. Allot, C. Danson, and A. Hall, "A single-shot third-order autocorrelator for pulse contrast and pulse shape measurements," *Laser and Particle Beams,* Vol. **19**, No. 02, pp 231-235 (2001).

S. Corde, C. Thaury, A. Lifschitz, G. Lambert, K Ta Phuoc, X. Davoine, R. Lehe, D. Douillet, A. Rousse, and V. Malka, "Observation of longitudinal and transverse self-injection in laser-plasma accelerators," *Nature Communications*, Vol. **4**, 1501 (2013).

C.A. Coverdale, C.B. Darrow, C.D. Decker, W.B. Mori, K.-C. Tzeng, K.A. Marsh, C.E. Clayton, and C. Joshi, "Propagation of Intense Subpicosecond Laser Pulses through Underdense Plasmas," *Phys. Rev. Lett.*, Vol. **74**, No 23, pp. 4659-4663 (1995).

X. Davoine, E. Lefebre, J. Faure, C. Rechatin, A. Lifschitz, and V. Malka, "Simulation of quasimonoenergetic electron beams produced by colliding pulse wakefield acceleration," *Phys. of Plasmas*, Vol. **15**, 113102 (2008).

C.D. Decker, W.B. Mori, T. Katsouleas, and D.E. Hinkel, "Spatial temporal theory of Raman forward scattering," *Phys. Plasmas*, Vol. **3**, No. 4, pp. 1360-1372 (1996).

N. B. Delone and V. P. Krainov, "Tunneling and barrier-suppression ionization of atoms and ions in a laser radiation field," *Physics-Uspekhi*, Vol. **41**, No. 5, 469-485 (1998).

M.C. Downer, personal communication, March 12, 2009.

E. Esarey, R.F. Hubbard, W.P. Leemans, A. Ting, and P. Sprangle, "Electron Injection into Plasma Wake Fields by Colliding Laser Pulses," *Phys. Rev. Lett*. Vol. **79**, No. 14, 2682-2685 (1997).

E. Esarey and M. Pillof, "Trapping and acceleration in nonlinear plasma waves," *Phys. Plas.* Vol. **2**, 1432 (1995).

E. Esarey, C.B. Schroeder, and W.P. Leemans, "Physics of laser-driven plasma-based electron accelerators," *Rev. Mod. Phys.*, Vol. **81**, No. 3, pp. 1229-1285 (2009).

E. Esarey, C.B. Schroeder, W.P. Leemans, and B. Hafizi, "Laser-Induced electron trapping in plasma-based accelerators," *Phys. of Plasmas*, Vol. **6**, 2262 (1999).

E. Esarey, P. Sprangle, J. Krall, and A. Ting, "Overview of Plasma-Based Accelerator Concepts," *IEEE Trans. Plasma Sci.*, Vol. **24**, No. 2 (1996).

J. Faure, Y. Glinec, A. Pukhov, S. Kiselev, S. Gordienko, E. Lefebre, J.-P. Rousseau, F. Burgy, and V. Malka, "A laser-plasma accelerator producing monoenergetic electron beams," *Nature*, Vol. **431**, 541-544 (2004).

J. Faure, C. Rechatin, A. Ben-Ismail, J. Lim, X. Davoine, E. Lefebvre, V. Malka, "Physics of colliding laser pulses in underdense plasmas," *C. R. Physique,* Vol. **10**, 148–158 (2009).

J. Faure, C. Rechatin, O. Lundh, L. Ammoura, and V. Maka, "Injection and acceleration of quasimonoenergetic relativistic electron beams using density gradients at the edges of a plasma channel," *Phys. of Plasmas,* Vol. **17**, 083107 (2010).

J. Faure, C. Rechatin, A.F. Lifschitz, X. Davoine, E. Lefebre, and V. Malka, "Experiments and Simulations of the Colliding Pulse Injection of Electrons in Plasma Wakefields," *IEEE Trans. Plasma. Phys.,* Vol. **36**, No. 4, pp. 1751-1759 (2008).

J. Faure, C. Rechatin, A. Norlin, A. Lifschitz, Y. Glinec, and V. Malka, "Controlled injection and acceleration of electrons in plasma wakefields by colliding laser pulses," *Nature*, Vol. **444**, 737-739 (2006).

N. Ebrahim, P. Lavigne, and S. Aithal, "Experiments on the plasma beat-wave accelerator," *IEEE Trans. Nucl. Sci.*, Vol. **32**, No. 5, pp. 3539-3541 (1985).

G. Eckhardt, R.W. Hellwart, F.J. McClung, S.E. Schwartz, D. Weiner, and E.J. Woodbury, "Stimulated Raman Scattering from Organic Liquids," *Phys. Rev. Lett.*, Vol. **9**, 455-457, 1962.

M. Fomyts'kyi, C. Chiu, M. Downer, and F. Grigsby, "Controlled plasma wave generation and particle acceleration through seeding the forward Raman scattering instability," *Phys. Plasmas*, Vol. **12**, No. 2, 023103 (2005).

M. Fomyts'kyi, C. Chiu, M. Downer, and F. Grigsby, "LWFA with Low Energy Raman Seeded Pulses," *CP737, Advanced Accelerator Concepts: 11th Workshop*, Ed. Vitaly Yakimenko, pp. 846-852 (2004).

G. Fubiani, E. Esarey, C.B. Schroeder, and W.P. Leemans, "Beat wave injection of electrons into plasma waves using two interfering laser pulses," *Phys. Rev. E*, Vol. **70**, No. 1, 016402 (2004).

E. W. Gaul, T. Ditmire, M. D. Martinez, S. Douglas, D. Gorski, G. R. Hays, W. Henderson, A. Erlandson, J. Caird, C. Ebbers, I. Iovanovic, and W. Molander, "Design of the Texas Petawatt Laser," *OSA/QELS Conf. Proc.*, JFB2 (2005).

Erhard W. Gaul, Mikael Martinez, Joel Blakeney, Axel Jochmann, Martin Ringuette, Doug Hammond, Ted Borger, Ramiro Escamilla, Skylar Douglas, Watson Henderson, Gilliss Dyer, Alvin Erlandson, Rick Cross, John Caird, Christopher Ebbers, and Todd Ditmire, "Demonstration of a 1.1 petawatt laser based on a hybrid optical parametric chirped pulse amplification/mixed Nd:glass amplifier," *J. Appl. Optics*, Vol. **49**, No. 9, 1676-1681 (2010).

C. G. R. Geddes, K. Nakamura, G. R. Plateau, Cs. Toth, E. Cormier-Michel, E. Esarey, C. B. Schroeder, J. R. Cary, and W. P. Leemans, "Plasma-Density-Gradient Injection of Low Absolute-Momentum-Spread Electron Bunches," *Phys. Rev. Lett.*, Vol. **100**, 215004 (2008).

C.G.R. Geddes, Cs. Toth, J. van Tilborg, E. Esarey, C.B. Schroeder, D. Bruhwiler, C. Nieter, J. Cary, and W.P. Leemans, "High-quality electron beams from a laser wakefield accelerators using plasma-channel guiding," *Nature,* Vol. **431**, 538-541 (2004).

M. Geissler, J. Schreiber, and J. Meyer-ter-Vehn, "Bubble acceleration of electrons with few-cycle laser pulses," *New J. of Phys.*, Vol. **8**, 186, (2006).

P. Gibbon, "The self-trapping of light waves by beat-wave excitation," *Phys. Fluids B*, Vol. **2**, No. 9, pp. 2196-2208 (1990).

P. Gibbon and A.R. Bell, "Cascade Focusing in the Beat-Wave Accelerator," *Phys. Rev. Lett.*, Vol. **61**, No. 14, pp. 1599-1602 (1988).

S. Gordienko and A Pukhov, "Scalings for ultrarelativistic laser plasmas and quasimonoenergetic electrons", *Phys. Plasmas*, Vol. **12**, 043109 (2005).

R.A. Van de Graaff, *Phys. Rev.*, Vol. **38**, 1919 (1931).

F.B. Grigsby, "Chirped Pulse Raman Amplifier," Doctoral Dissertation, University of Texas at Austin (2009).

F. Grigsby, P. Dong, and M.C. Downer, "Chirped-pulse Raman amplification for two-color, high-intensity laser experiments," *J. Opt. Soc. Am.* B/Vol. **25**, No. 3, 346-350 (2008).

F. Grigsby, P. Deng, and M.C. Downer, "Development of 873 nm Raman Seed Pulse for Raman-seeded Laser Wakefield Acceleration," Conf. Proc. AAC 11, 559-563 (2004).

F. Grigsby, P. Deng, and M.C. Downer, "Stimulated Raman Scattering and Compression of Chirped TW Laser Pulses for Two-Color High Intensity Experiments," *QELS Conf. Proc.*, JthD2, 1546-1548 (2005).

R.W. Hamm and M.E. Hamm, *Industrial Accelerators and Their Applications,* World Scientific. ISBN 978-981-4307-04-8 (2012).

H. Hamster, A. Sullivan, S. Gordon, W. White, and R.W. Falcone, "Subpicosecond, electromagnetic pulses from intense laser-plasma interaction," *Phys. Rev. Lett.*, Vol. **71**, No. 17, 2725-2728 (1993).

R.W. Hellwarth, "Theory of stimulated Raman scattering," *Phys. Rev. A*, Vol. **130**, 1850, 1963.

T. Hosokai, K Kinoshita, T. Wanatabe, K. Yoshii, T. Ueda, A. Zhidokov, M. Uesaka, K. Nakajima, M. Kando, H. Kotaki, "Supersonic gas jet target for generation of relativistic electrons with 12TW-50fs laser pulse," *Proceedings of EPAC*, Paris, France, pp. 981-983 (2002).

C. Iaconis and I. A. Walmsley, "Spectral phase interferometry for direct electric-field reconstruction of ultrashort optical pulses", *Opt. Lett.*, Vol. **23** No. 10, 792 (1998).

T.P.A. Ibbotson, N. Bourgeois, T.P. Rowlands-Rees, L.S. Caballero, S.I. Bajlekov, P.A. Walker, S. Kneip, S.P.D. Mangles, S.R. Nagel, C.A.J. Palmer, N. Delerue, G. Doucas, D. Umer, O. Chekhlov, R.J. Clarke, E. Divall, K. Ertel, P.S. Foster, S.J. Hawkes, C.J. Hooker, B. Parry, P.P. Rajeev, M.J.V. Streeter, and S.M. Hooker, "Laser-wakefield acceleration of electron beams in a low density plasma channel," *Phys. Rev. STAB*, Vol. **13**, No.3 031301 (2010).

C. Joshi, T. Tajima, J.M. Dawson, H.A. Baldis, and N.A. Ebrahim, "Forward Raman Instability and Electron Acceleration," *Phy. Rev. Lett.*,Vol. **47**, 1285 (1981).

S. Kalmykov (personal communication, May 30 and June 4, 2012).

S. Y. Kalmykov, S.A. Reed, S.A. Yi, A. Beck, A.F. Lifschitz, X. Davoine, E. Lefebvre, V. Khudik, G. Shvets, P. Dong, X. Wang, D. Du, S. Bedacht, Y. Zhao, W. Henderson, A. Bernstein, G. Dyer, M. Martinez, E. Gaul, T. Ditmire, and M.C. Downer, "Laser wakefield electron acceleration on Texas Petawatt facility: Towards multi-

GeV electron energy in a single self-guided stage," *High Energy Density Physics*, Vol. **6**, no. 2, pp. 200-206 (2010).

S.Y. Kalmykov, B.A. Shadwick, and M.C. Downer, "All-optical Control of Nonlinear Self-Focusing in Plasmas Using Non-Resonantly Driven Plasma Wave," *AIP Conf. Proc. Advanced Accel. Conc. 14*, Vol. **CP1299**, pp. 752-757 (2010).

S. Kalmykov and G. Shvets, "Compression of laser radiation in plasmas via electromagnetic cascading," *Phys. Plasmas*, Vol. **13**, No. 5, 056707 (2006).

S. Kalmykov and G. Shvets, "Guiding of Laser Beams in Plasmas by Radiation Cascade Compression," *AIP Conf. Proc. Advanced Accel. Conc. 12*, Vol. **CP877**, pp. 395-401 (2006).

S. Kalmyov and G. Shvets, "Nonlinear evolution of the plasma beat wave: Compressing the laser beat notes via electromagnetic cascading," *Phys. Rev. E*, Vol. **73**, No. 4, 046403 (2006).

S. Y. Kalmykov, S. A. Yi, and G. Shvets, "All-optical suppression of relativistic self-focusing of laser beams in plasmas," *Phys. Rev. E* Vol. **78**, No. 4, 057401 (2008).

S. Kalmykov, S. A. Yi, and G. Shvets, "All-optical control of nonlinear focusing of laser beams in plasma beat wave accelerator," *Plasma Phys. Control. Fusion*, Vol. **51**, 024011 (2009).

S. Karsch, J. Osterhoff, A. Popp, T.P. Rowlands-Rees, Zs. Major, M. Fuchs, B. Marx, R. Horlein, K. Schmid, L. Veisz, S. Becker, U. Schramm, B. Hidding, G. Pretzler, D. Habs, F. Gruner, F. Krausz, and S.M. Hooker, "GeV-scale electron acceleration in a gas-filled capillary discharge waveguide," *New J. of Phys.*, Vol. **9**, No. 11, 415 (2007).

S.J. Karttunen and R.R.E. Salomaa, "Electromagnetic Field Cascading in the Beat-Wave Generation of Plasma Waves," *Phys. Rev. Lett.*, Vol. **56**, No. 6, pp. 604-607 (1986).

T. Katsouleas and W.B. Mori, "Wave-breaking amplitude of relativistic oscillations in a thermal plasma," *Phys. Rev. Lett.,* Vol. **61**, pp 90-93 (1988).

R. Keinigs and M.E. Jones, "Two-dimensional dynamics of the plasma wakefield accelerator," *Phys. Fluids*, Vol. **30**, pp. 252-263 (1987).

L. V. Keldysh, "Ionization in the field of a strong electromagnetic pulse," *Sov. Phys. JETP*, Vol. **20**, 1307 (1965).

D.W. Kerst, "Acceleration of Electrons by Magnetic Induction," Phys. Rev., Vol. **58**, No. 9 (1940).

D.W. Kerst, "The Acceleration of Electrons by Magnetic Induction," Phys. Rev., Vol. **60**, 47–53 (1941).

F. L. Kien, K. Hakuta, and A.V. Sokolov, "Pulse compression by parametric beating with a prepared Raman coherence," *Phys. Rev. A*, Vol. **66**, No. 2 023813 (2002).

F. L. Kien, J.Q. Liang, M. Katsuragawa, K. Ohtsuki, K. Hakuta, and A.V. Sokolov, "Subfemtosecond pulse generation with molecular coherence control in stimulated Raman scattering," *Phys. Rev. A*, Vol. **60**, No. 2, 1562-1571 (1999).

Y. Kitagawa, T. Matsumoto, T. Minamihata, K. Sawai, K. Matsuo, K. Mima, K. Nishihara, H. Azechi, K.A. Tanaka, H. Takabe, and S. Nakai, "Beat-Wave Exceitation of plasma Wave and Observation of Accelerated Electrons," *Phys. Rev. Lett.*, Vol. **68**, No. 1 (1992).

S. Kneip, S.R. Nagel, S.F. Martins, S.P.D. Mangles, C. Bellei, O. Chekhov, R.J. Clarke, N, Delerue, E.J. Divall, G. Doucas, K. Ertel, F. Fiuza, R. Fonseca, P. Foster, S.J. Hawkes, C.J. Hooker, K. Krushelnick, W.B. Mori, C.A.J Palmer, K. Ta Phuoc, P.P. Rajeev, J.Schreiber, M.J.V. Streeter, D. Urner, J. Vieira, L.O. Silva, and Z.Najmudin, "Near-GeV Acceleration of Electrons by a Nonlinear Plasma Wave Driven by a Self-Guided Laser Pulse," *Phys. Rev. Lett.,* Vol. **103**, No. 3, 035002 (2009).

H. Kotaki, I. Daito, M. Kando, Y. Hayashi, M. Jinglong, L.-M. Chen, T. Z. Esirkepov, Y. Fuduka, T. Homma, A. Pirozhkov, J.K. Koga, K. Nakajima, H. Daido, and S.V. Bulanov, "Improvement of the Quality and Stability of Electron Bunch Using Countercrossing Laser Beam," *IEEE Trans. Plasma Phys.*, Vol. **36**, No. 4, pp. 1760-1764, 2008.

H. Kotaki, S. Masuda, M.Kando, J.K. Koga, N. Nakajima, "Head-on injection of a high quality electron beam by the interaction of two laser pulses," *Phys. Plasmas*, Vol. **11**, 3296 (2004).

K. Koyamaa, A. Yamazakia, A. Maekawaa, M. Uesakaa, T. Hosokaib, M. Miyashitac, S. Masudad, E. Miura, "Laser-plasma electron accelerator for all-optical inverse Compton X-ray source," *Nucl. Instrum. Methods A*, Vol. **608**, S51 (2009).

337

J. Krall, A. Ting, E. Esarey, P. Sprangle, and G. Joyce, "Enhanced acceleration in a self-modulated laser wakefield accelerator," *Phys. Rev. Lett.*, Vol. **48**, pp. 2157-2161 (1993).

D. J. Kane and R. Trebino, "Characterization of arbitrary femtosecond pulses using frequency-resolved optical gating", *IEEE J. Quantum Electron.*, Vol. **29** No. 2, 571 (1993).

G. Landsberg and L. Mandelstam, "A new occurrence in the light diffusion of crystals," *Naturwissenchaften*, Vol. **16**, 557-558, 1928.

E. O. Lawrence, "Method and apparatus for the acceleration of ions," US patent 1948384, issued 1934-02-20.

S.P. LeBlanc, M.C. Downer, R. Wagner, S.-Y. Chen, A. Maksimchuk, G. Morour,and D. Umstadter, "Temporal Characterization of a Self-Modulated Laser Wakefield," *Phys. Rev. Lett.*, Vol. **77**, No. 27, pp. 5381-5384 (1996).

W.P. Leemans, B. Nagler, A.J. Gonsalves, Cs. Toth, K. Nakamura, C.G.R. Geddes, E Esarey, C.B Schroeder, and S.M. Hooker, "GeV electron beams from a centimetre-scale accelerator," *Nature Physics*, Vol. **2**, 696-699 (2006).

W.P. Leemans, P. Volbeyn, K.X. Guo, S. Chattopadhyay, C.B. Schroeder, B. A. Shadwick, P. B. Lee, J.S. Wurtele, and E. Esarey, "Laser-driven plasma-based accelerators: Wakefield excitation, channel guiding, and laser-triggered particle injection," *Phys. of Plasmas*, Vol. **5**, 1615 (1998).

W. P. Leemans, D. Rodgers, P. E. Catravas, C. G. R. Geddes, G. Fubiani, E. Esarey, B. A. Shadwick, R. Donahue, and A. Smith, "Gamma-neutron activation experiments using laser wakefield accelerators," *Phys. Plasmas*, Vol. **8**, No. 5 2510 (2001).

Z. Li, R. Zgadzaj, X. Wang, P. Dong, and M.C. Downer, "Frequency-domain streak camera for ultrafast imaging of evolving light-velocity objects," *Opt. Lett.*, Vol. **35**, No. 24, 4087-4089 (2010).

W. Lu, C. Huang. M. Zhou, W.B. Mori, and T. Katsouleas, "Nonlinear Theory for Relativistic Plasma Wakefields in the Blowout Regime," *Phys. Rev. Lett.*, Vol **96**, 165002 (2006).

W. Lu, M. Tzoufras, C. Joshi, F.S. Tsung, W.B. Mori, J. Vieira, R.A. Fonseca, and L.O. Silva, "Generating multi-GeV electron bunches using single laser wakefield acceleration in a 3D nonlinear regime," *Phys. Rev. STAB*, Vol. **78**, 061301 (2007).

P. Maine, D. Strickland, P. Bado, M. Pessot, and G. Mourou, "Generation of Ultrahigh Peak Power Pulses by Chirped Pulse Amplification" *IEEE J. Quantum Electron.*, Vol. **24** No. 2, 398 (1988).

I. H. Malitson, "Interspecimen comparison of the refractive index of fused silica", J. Opt. Soc. Am. 55 (10), 1205 (1965).

V. Malka, "Review of Laser Wakefield Accelerators," *Proceedings of IPAC* (2013).

V. Malka, J. Faure, C. Rechatin, A. Ben-Ismail, J.K. Lim, X. Davoine, and E. Lefebre, "Laser-driven accelerators by colliding pulses injection: A review of simulation and experimental results," *Phys. of Plasmas*, Vol. **16**, 056703 (2009).

V. Malka, S. Fritzler, E. Lefebvre, M.-M. Aleonard, F. Burgy, J.-P. Chambaret, J.-F. Chemin, K. Krushelnick, G. Malka, S. P. D. Mangles, Z. Najmudin, M. Pittman, J.-P. Rousseau, J.-N. Scheurer, B. Walton, A. E. Dangor, "Electron Acceleration by a Wake Field Forced by an Intense Ultrashort Laser Pulse," *Science*, Vol. **298**, 1596-1600 (2002).

V. Malka and P. Mora, "Principles of Laser-Plasma Accelerators," *C.R. Physique*, Vol. **10**, pp 106-115 (2009).

S. P. D. Mangles, C. D. Murphy, Z. Najmudin, A. G. R. Thomas, J. L. Collier, A. E. Dangor, E. J. Divall, P. S. Foster, J. G. Gallacher, C. J. Hooker, D. A. Jaroszynski, A. J. Langley, W. B. Mori, P. A. Norreys, F. S. Tsung, R. Viskup, B. R. Walton & K. Krushelnick, "Monoenergetic beams of relativistic electrons from intense laser–plasma interactions," *Nature*, Vol. **431**, 535-538 (2004).

S.P.D. Mangles, A.G.R. Thomas, M.C. Kaluza, O. Lundh, F. Lindau, A. Persson, F.S. Tsung, Z. Najmudin, W.B. Mori, C.-G. Wahlstrom, and K. Krushelnick, "Laser-Wakefield Acceleration of Monoenergetic Electron Beams in the First Plasma-Wave Period," *Phys. Rev. Lett.*, Vol. **96**, 215001 (2006).

N.H. Matlis, S. Reed, S.S. Bulanov, V. Chvykov, G. Kalintchenko, T. Matsuoka, P. Rousseau, V. Yanovsky, A. Maksimchuk, S. Kalmykov, G. Shvets, and M.C. Downer, "Snapshots of laser wakefields," *Nature Physics*, Vol. **2**, 749-753 (2006).

N. Minkovski, S. M. Saltiel, G. I. Petrov, O. Albert and J. Etchepare, "Polarization rotation induced by cascaded third-order processes," *Opt. Lett.* Vol. **27**, No. 2, pp. 2025-2027 (2002).

A. Modena, Z. Najmudin, A.E. Dangor, C.E. Clayton, K.A. Marsh, C. Joshi, V. Malka, C.B. Darrow, and C. Danson "Observation of Raman Forward Scattering an Electron Acceleration in the Relativistic Regime," *IEEE Trans. Plas. Phys.*, Vol. **24**, No. 2, pp. 289-295 (1996).

A. Moderna, Z. Najmudn, A.E Danger, C.E. Clayton, K.A Marsh, C. Joshi, V. Malka, C.B. Darrow, C. Danson, D. Neely, and F.N. Walsh, "Electron acceleration from the breaking of relativistic plasma waves," *Nature*, Vol. **377**, 606 (1995).

W.B. Mori, C.D. Decker, D.E. Hinkel, andT. Katsouleas, "Raman forward scattering of short high-intensity lasers," *Phys. Rev. Lett.*, Vol. **72**, pp. 1482-1485 (1994).

J.T. Murray, W.L. Austin, and R.C. Powell, "Intracavity Raman conversion and Raman beam cleanup," *Opt. Mat.*, Vol. **11**, 353-371 (1999).

Z. Najmudin, C.A.J. Palmer, N.P. Dover, I. Pogerelsky, M. Babzien, A.E. Dangor, G.I. Dudnikova, P.S. Foster, J.S. Gree, M. Ispiriyan, D. Neely, M.N. Polyanskiy, J. Schreiber, P. Shkolnikov, and V. Yakimenko, "Observation of impurity free monoenergetic proton beams from the interaction of a CO_2 laser with a gaseous target," *Phys. Plasmas*, Vol. **18**, 056705 (2011).

K. Nakajima, D. Fisher, T. Kawakubo, H Nakanishi, A. Ogata, Y. Kato, Y. Kitagawa, R. Kodama, K. Mima, H. Shiraga, K. Suzuki, K. Yamakawa, T. Zhang, Y. Sakawa, T. Shoji, Y. Nishida, N. Yugami, M. Downer, and T. Tajima, "Observation of Ultrahigh Gradient Electon Acceleration by a Self-Modulated Intense Short Pulse," *Phys. Rev. Let.* Vol. **74**, Number 22, May 1995.

K. Nakajima, T. Kawakubo, H Nakanishi, A Ogata, Y Kato, Y Kitagawa, R Kodama, K Mima, H Shiraga, K Suzuki, T Zhang, Y Sakawa, T Shoji, Y Nishida, N Yugami, M Downer, D Fisher, B Newberger and T Tajima, "A proof-of-principle experiment of laser-wakefield acceleration" *Physica Scripta*, **T52**, 61 (1994).

G. Neil and L. Merminga, "Technical approaches for high-average-power free-electron lasers," *Rev. Mod. Phys.*, Vol. **74**, 685-701 (2002).

A. Ogata, "Status and Problems of Plasma Accelerators," *ICFA Beam Dynamics Newsletter*, No. 11, August 1996.

A. Pak, K. A. Marsh, S. F. Martins, W. Lu, W. B. Mori, and C. Joshi, "Injection and Trapping of Tunnel-Ionized Electrons into Laser-Produced Wakes," *Phys. Rev. Lett.*, Vol. **104**, 025003 (2008).

G.I. Petrov, O. Albert, N. Minkovski, J. Etcepare, and S.M. Saltiel, "Experimental and theoretical investigation of generation of a cross-polarized wave by cascading of two different second-order processes," *J. Opt. Soc. Am. B*, Vol. **19**, No. 2, pp. 268-279 (2002).

I.V. Pogorelshy, V. Yakimenko, M. Polyanskiy, P. Sholnikov, M. Ispiryan, D. Neely, P. McKenna, D. Carrol, Z. Najmudin, L. Willingale, "Ultrafast CO2 laser technology--Application in ion acceleration," *Nuclear Instruments and Methods in Physics Research A*, Vol. **620**, No. 1, pp. 67-70 (2010).

B.B. Pollock, J.S. Ross, G.R. Tynan, L. Divol, S.H. Glenzer, V. Leurent, J.P. Palastro, J.E. Ralph, D.H. Froula, C.E. Clayton, K.A. Marsh, A.E. Pak, T.L. Wang, and C. Joshi, "Two-screen method for determining electron beam energy and deflection from laser wakefield acceleration," *Proceedings of the 2009 Particle Accelerator Conference* (Vancouver, 2009).

D. Panaenko and Y. Fainman, "Interferometric Correlation of Infrared Femtosecond Pulses with Two-Photon Conductivity in a Silicon CCD," *Applied Optics*, Vol. **41**, No. 18, pp. 3748-3752 (2002).

M. Polyanskiy, "Refractive Index Database," Web. 10 February 2014. http://refractiveindex.info/

A. Pukhov and J. Meyer-ter-Vehn, "Laser wake field acceleration: the highly non-linear broken-wave regime," *Appl. Phys. B*, Vol. **74**, 355-361 (2002).

C.-H. Pai, M.-W. Lin, L.-C. Ha, S.-T. Huang, Y.-C. Tsou, H.-H. Chu, J.-Y. Lin, J. Wang, and S.-Y. Chen, "Backward Raman Amplification in a Plasma Waveguide," *Phys. Rev. Lett.*, Vol. **101**, 065005 (2008).

C.V. Raman, "A new radiation," *Indian J. Phys.,* Vol. **2**, 387-398 (1928).

C.V. Raman and K.S. Krishnan, "A New Type of Secondary Radiation," *Nature,* Vol. **121**, 501-502 (1928).

C. Rechatin, J. Faure, A. Ben-Ismail, J. Lim, R. Fitour, A. Specka, H. Videau, A. Tafzi, F. Burgy, and V. Malka, "Controlling the Phase-Space Volume of Injected Electrons in a Laser-Plasma Accelerator," *Phys. Rev. Lett.*, Vol. **102**, No. 16, 164801 (2009).

D. M. Riffe and A. J. Sabbah, "A compact rotating-mirror autocorrelator design for femtosecond and picosecond laser pulses", *Rev. Sci. Instrum.*, Vol. **69** No. 9, 3099 (1998).

T. P. Rowlands-Rees, C. Kamperidis, S. Kneip, A. J. Gonsalves, S. P. D. Mangles, J. G. Gallacher, E. Brunetti, T. Ibbotson, C. D. Murphy, P. S. Foster, M. J. V. Streeter, F. Budde, P. A. Norreys, D. A. Jaroszynski, K. Krushelnick, Z. Najmudin, and S. M. Hooker, "Laser-Driven Acceleration of Electrons in a Partially Ionized Plasma Channel," *Phys. Rev. Lett.*, Vol. **100**, 105005 (2008).

J. B. Rozenzweig, B. Breizman, T. Kasouleas, and J. J. Su , "Acceleration and focusing of electrons in two-dimensional nonlinear plasma wake fields" *Phys. Rev. A*, Vol. **44**, No. 10, R6189-R6192 (1991).

J.B. Rosenzweig, D.B. Cline, H. Figueroa, W. Gai, R. Konecny, J. Norem, P. Schoessow, and J. Simpson, "Experimental Observation of Plasma Wake-Field Acceleration," *Phys. Rev. Lett.*, Vol. **61** No. 1 (1988).

W. Rudolph, M. Sheik-Bahae, A. Bernstein, and L. F. Lester, "Femtosecond autocorrelation measurements based on two-photon photoconductivity in ZnSe," *Optics Letters*, Vol. **22**, No. 5, pp. 313-315 (1997).

J.C. Sanders, R. Zgadzaj, and M.C. Downer, "Two-color terawatt system for high-intensity laser-plasma experiments," *AIP Conf. Proc. AAC 14th Workshop*, Vol. **1507**, 882 (2012).

K. Sala, G. Kenney-Wallace, and G. Hall, "CW autocorrelation measurements of picosecond laser pulses", *IEEE J. Quantum Electron.*, Vol. **16** No. 9, 990 (1980).

F. Salin, P. Georges, G. Roger, and A. Brun, "Single-shot measurement of a 52-fs pulse," *Applied Optics*, Vol. **26**, No. 21, pp. 4528-4531 (1987).

K. Schmid, A. Buck, C.M.S. Sears, J.M. Mikhailova, R. Tautz, D. Herrmann, M. Geissler, F. Krausz, and L. Veisz, "Density-transition based electron injector for laser driven wakefield accelerators," *Phys. Rev. STAB*, Vol. **13**, 091301 (2010).

C.B. Schroeder, P.B. Lee, J.S. Wurtele, E. Esarey, and W.P. Leemans, "Generation of ultrashort electron bunches by colliding laser pulses," *Phys. Rev. E*, Vol. **59**, pp. 6037-6047 (1999).

W. Sellmeier, *Ann. Phys. Chem*. Vol. **143**, 271 (1871).

B.A. Shadwick, C.B. Schroeder, and E. Esarey, "Nonlinear laser energy depletion in laser-plasma accelerators," *Phys. of Plasmas*, Vol. **16**, 056704, 2009; Paper D12 3, *Bull. Am. Phys. Soc.*, Vol. **53**, 77 (2008).

B.A. Shadwick, C.B. Schroeder, E. Esarey, and W.P. Leemans, "Nonlinear Pump Depletion and Electron Dephasing in Laser Wakefield Accelerators," *Proceedings of the Advanced Accelerator Concepts Workshop, AIP Conf. Proc.* Vol. **737**, 578 (2004).

G. Shvets, personal communication, November 23, 2011.

M.Y. Shverdin, D.R. Walker, D.D. Yavuz, G.Y. Yin, and S.E. Harris, "Generation of a Single-Cycle Optical Pulse," *Phys. Rev. Lett.*, Vol. **94**, No. 3, 033904 (2005).

C. W. Siders, "An Experimental Demonstration of the Laser Wakefield 'Photon Accelerator': Longitudinal Interferometric Diagnostics for Plasma Based Accelerators," Doctoral Dissertation, University of Texas at Austin, 1996.

A.E. Siegman, *Lasers*, Mill Valley, CA, University Science Books (1986).

R.E. Slusher and C.M. Surko, "Study of density fluctuations in plasmas by small-angle CO_2 laser scattering," *Phys. Fluids*, Vol. **23**, No. 3, 472 (1980).

I.D. Smith and H. Aslin, "Pulsed Power for EMP Simulators," *IEEE Trans. Antennas and Prop.*, Vol. **AP-26**, No. 1, pp. 53-59 (1978).

A.V. Sokolov, D.R. Walker, D.D. Yavuz, G.Y. Yin, and S.E. Harris, "Raman Generation by Phased and Antiphased Molecular States," *Phys. Rev. Lett.*, Vol. **85**, No. 3, pp. 562-565 (1999).

A.V. Sokolov, D.D. Yavuz, and S.E. Harris, "Subfemtosecond pulse generation by rotational molecular modulation," *Opt. Lett.*, Vol **24**, No. 8, pp. 557-559 (1999).

D.J. Spence and S.M. Hooker, "Investigation of a hydrogen plasma waveguide," *Phys. Rev. E*, Vol. **63,** 015401 (2001).

P. Sprangle, E. Esarey. J. Krall, and G. Joyce, "Interaction of ultrahigh laser fields with beams and plasmas," *Phys. Fluids B*, Vol. **4**, pp. 2241-2248 (1992).

P. Sprangle, E. Esarey. J. Krall, and G. Joyce, "Propagation and guiding of intense laser pulses in plasmas," *Phys. Rev. Lett.*, Vol. **69**, pp. 2200-2203 (1992).

P. Sprangle, E. Esarey, A. Ting, and G. Joyce, "Laser wakefield acceleration and relativistic optical guiding," *Applied Phys. Letters*, vol. 53, pp 2146-2148 (1988).

P. Sprangle, E. Esarey, and A. Ting, "Nonlinear interaction of intense laser pulses in plasmas," *Phys. Rev. A.*, Vol. **41**, pp. 4463-4469 (1990).

P. Sprangle, C.M. Tang, and E. Esarey, "Relativistic Self-Focusing of Short-Pulse Radiation Beams in Plasmas", *IEEE Trans. Plasma Sci.*, Vol. **15**, 145 (1987).

A. Smekal, "Zur Quantentheorie der Dispersion," *Naturwissenchaften*, Vol. **11**, 873-875 (1923).

M. Suzuki, "Recombination luminescence from ionization tracks produced by alpha particles in high pressure argon, krypton and xenon gases," *Nucl. Instr. and Methods in Phys. Research*, Vol. **215**, No. 1–2, pp. 345–356 (1983).

T. Tajima and J. M. Dawson, "Laser Electron Accelerator," *Phys. Rev. Lett.*, Vol. **43** No. 4 (1979).

S. Totchitsky, J. Pigeon, D. Haberberger, and C. Joshi, "Amplification of High-Power Picosecond 10-μm Pulses in Atmospheric CO_2 laser," *Conf. Proc.* CLEO 2012.

E. B. Treacy, "Optical Pulse Compression With Diffraction Gratings," IEEE Journal of Quantum Electronics, Vol. Qe-5, No. 9 (1969).

D. Umstadter, S.-Y. Chen, A. Maksimchuk, G. Mourou, and R. Wagner, "Nonlinear Optics in Relativistic Plasmas and Laser Wake Field Acceleration of Electrons," *Science*, Vol. **273**, No. 5274, pp. 472-475 (1996).

D. Umstadter, J.K. Kim, and E. Dodd, "Laser Injection of Ultrashort Electron Pulses Into Wakefield Plasma Waves," *Phys. Rev. Lett.*, Vol. **76**, No. 12, 2073-2076 (1996).

T.F. Wall and A. Sanchez, "Titanium Sapphire Lasers," *The Lincoln Laboratory Journal*, Vol. **3**, No. 3, (1990).

X. Wang R. Zgadzaj, S.A. Yi, V. Khudik, W. Henderson, N. Fazel, Y.-Y Chang, R. Korzekwa, H.-E. Tsai, C.-H. Pai, Z. Li, E. Gaul, M. Martinez, G. Dyer, H. Quevedo, A. Bernstein, M. Donovan, G. Shvets, T. Ditmire, and M.C. Downer "Self-injected Petawatt Laser-driven Plasma Electron Acceleration in 10^{17} cm^{-3} Plasma," *Las. Appl. Phot. Application*, *OSA Conf. Proc, Quant. El. and Las. Sci. Conf*, QMJ3 (2011), and *J. Plasma Phys.*, Vol. **78**, No. 4, p 413-419 (2012).

X. Wang, D. Du, S.A. Yi, S. Kalmykov, E. D'avignon, N. Fazel, R. Zgadzaj, S. Reed, P. Dong, W. Henderson, G. Dyer, A. Bernstein, E. Gaul, M. Martinez, G. Shvets, T. Ditmire, and M. Downer, "Multi-GeV Electron Generation Using Texas Petawatt Laser," *AIP Conf. Proc.* **1299**, 209 (2010).

X.Wang, R. Zgadzaj, N. Fazel, S. A. Yi, X. Zhang, W. Henderson, Y.-Y. Chang, R. Korzekwa, H.-E. Tsai, C.-H. Pai, Z. Li, H. Quevedo, G. Dyer, E. Gaul, M. Martinez, A. Bernstein, T. Borger, M. Spinks, M. Donovan, S. Y. Kalmykov, V. Khudik, G. Shvets, T. Ditmire and M. C. Downer, "Petawatt-laser-driven wakefield acceleration of electrons to 2 GeV in 1017cm-3 plasma," *AIP Conf. Proc. AAC*, **1507**, 341-344 (2012).

Xiaoming Wang, Rafal Zgadzaj, Neil Fazel, Zhengyan Li, S. A. Yi, Xi Zhang, Watson Henderson, Y.-Y. Chang, R. Korzekwa, H.-E. Tsai, C.-H. Pai, H. Quevedo, G. Dyer, E. Gaul, M. Martinez, A. C. Bernstein, T. Borger, M. Spinks, M. Donovan, V. Khudik, G. Shvets, T. Ditmire & M. C. Downer, "Quasi-monoenergetic laser-plasma acceleration of electrons to 2 GeV," *Nature Communications*, Vol. **4**, 2988 (2013).

X. Wang, R. Zgadzaj, W. Henderson, N. Fazel, Y.-Y. Chang, R. Korzekwa, A.S. Yi, V. Khudik, H.-E. Tsai, Z. Li, H. Quevedo, G. Dyer, E. Gaul, M. Martinez, A. Bernstein, T. Borger, M. Spinks, M. Donovan, G. Shvets, T. Ditmire, and M.C. Downer, "Generation of Dark-current-free Quasi-monoenergetic 1.25 GeV Electrons by Laser Wakefield Acceleration," *Quant. Elect. And Laser Sci. Conf. Proc.*, QW3F (2012).

R. Widerøe, "Ueber Ein Neues Prinzip Zur Herstellung Hoher Spannungen". *Archiv fuer Elektronik und Uebertragungstechnik* , Vol. **21**, No. 4, 387 (1928).

E.J. Woodbury and W.K. Ng, *Proc. I.R.E.*, Vol. **50**, 2367, 1962.

G. Xinan, Lambsdorff, J. Kuhl, and W. Biachang "Fast-scanning autocorrelator with 1-ns scanning range for characterization of mode-locked ion lasers", *Rev. Sci. Instrum.*, Vol. **59** No. 9, 2088 (1988).

A. Yariv, *Quantum Electronic, Third Edition*, New York, John Wiley and Sons (1989).

N. Zhavoronkov, F. Noack, V. Petrov, V. P. Kalosha, and J. Herrmann, *Opt. Let.* **26**, 47–49 (2001).

P.G. Zverev, T.T. Basiev, V.V. Osiko, A.M. Kulkov, V.N. Voitsekhovskii, V.E. Yakobson, "Physical, chemical and optical properties of barium nitrate Raman crystal," Optical Materials, Vol. 11, 315-334 (1999).

P.G. Zverev, T.T. Basiev, and A.M. Prokhorov "Stimulated scattering of laser radiation in Raman crystals," *Opt. Mat.* Vol. **11**, No. 4, pp 335-352 (1999).

P. G. Zverev, W. Jia, H. Liu, and T. T. Basiev, "Vibrational dynamic of the Raman-active mode in barium nitrate crystal," Optics Letters, Vol. 20, No. 23, 2378-2380 (1995).

Vita

James C. "JC" Sanders was born in August of 1984 in Grants Pass, Oregon, the first son of Lonnie and Cindy Sanders. He spent his early years on his parents' farm, first in Myrtle Creek and then later in Tenmile, Oregon. He spent most of his youth and childhood riding horses and showing sheep and cattle at the local county fairs. He attended Douglas High School in Winston and Umpqua community college in Winchester before transferring to Roseburg High School during the second half of his junior year.

After graduating high school in 2002, he moved to Corvallis and studied physics at Oregon State University during the school years. He was a member of the University Honors College, the Society of Physics Students, and the undergraduate Senate and wrote a semi-weekly column for the underground paper. He also learned ballroom-, latin-, and country western-, and most importantly swing-dancing. He graduated *Magna Cum Laude* after 4 years, earning an honors bachelor of science degree in physics with an optics option.

During the summer, he worked at a mill, then in subsequent summers was a Princeton national undergraduate fellow in plasma physics and fusion research at Los Alamos National Laboratory, an undergrad research assistant at Lawrence Livermore National Laboratory, and finally a graduate research assistant at LLNL. The first internship at LLNL became the basis for his undergraduate honors thesis: asteroid interdiction.

After the second internship in Livermore, he drove to Austin, where he enrolled a the University of Texas as a Ph.D. student. He met his future wife, Rebecca Alessa

Friemel, at the University Catholic center the week after his first spring break, after which all the dance classes he took as an undergraduate finally paid off. He proposed to her on a volcano in Oregon, and they were wed on June 19, 2010. They have had one daughter together so far, and they still find time to go swing dancing on occasion.

Permanent address (or email): james.c.sanders@gmail.com

This dissertation was typed by the author.